

PHOTOELECTRON SPECTROSCOPY OF SOME
METALS AND ALLOYS IN THE LIQUID STATE

MARTYN K. GARDINER

A thesis submitted to the University of
Leicester for the degree of Doctor of
Philosophy.

December
1983

UMI Number: U346577

All rights reserved

INFORMATION TO ALL USERS

The quality of this reproduction is dependent upon the quality of the copy submitted.

In the unlikely event that the author did not send a complete manuscript and there are missing pages, these will be noted. Also, if material had to be removed, a note will indicate the deletion.



UMI U346577

Published by ProQuest LLC 2015. Copyright in the Dissertation held by the Author.
Microform Edition © ProQuest LLC.

All rights reserved. This work is protected against
unauthorized copying under Title 17, United States Code.



ProQuest LLC
789 East Eisenhower Parkway
P.O. Box 1346
Ann Arbor, MI 48106-1346



Thesis

17.4.1984

CONTENTS

Acknowledgements

Abstract

	Page
<u>Chapter 1</u> <u>Introduction</u>	1
1.1 Disorder in Metals.	2
1.2 The Determination of the Structure of Liquid Simple Metals.	3
1.3 Models and Theories of the Liquid State.	6
1.4 The Electronic Structure of the Liquid Simple Metals.	9
1.5 The Ziman Theory.	10
1.6 The Thermoelectric Power.	14
1.7 The Density of States at the Fermi Level. The Knight Shift.	15
1.8 The Density of States below the Fermi Level.	16
1.9 Liquid Semiconductors.	19
1.10 Amorphous Metals and Alloys.	24
 <u>Chapter 2</u> <u>The Theory of Photoemission</u>	 26
2.1 Introduction.	27
2.2 The Primary Electron Distribution.	27
2.3 Optical Matrix Elements.	29
2.4 The Three Step Model of Photoemission.	32
2.5 The Unscattered Primary Distribution of Photoemitted Electrons.	33
2.6 The Energy Distribution of Inelastically Scattered Electrons.	36
2.7 The Total Energy Distribution of Emitted Electrons.	42

	Page
2.8 The Calculation of an Optical Density of States.	43
<u>Chapter 3</u> <u>Experimental</u>	44
3.1 Introduction.	45
3.2 The Ultraviolet Photoelectron Spectrometer: Vacuum Chambers and Pumping System.	45
3.3 The Ultraviolet Light Source.	46
3.4 The Power Supply for the Lamp.	48
3.5 The Argon Sputter Ion Gun.	48
3.6 The Electron Energy Analyser.	48
3.7 The Signal Detection System.	52
3.8 Signal Averager Based on a Microprocessor.	52
3.9 Auger Electron Spectroscopy.	56
3.10 Sample Preparation - General.	58
3.11 Details of the Pouring Mechanism for the Lithium and Lithium Based Alloys.	59
3.12 The Manipulator Tube and Sample Boat.	61
3.13 Preparation of the Silver-Germanium Alloys.	61
3.14 The Experimental Arrangement for the Silver- Germanium Alloys.	62
3.15 The Vapour Source for Lead and Tin.	62
3.16 Magnetic Shielding of the Source Chamber.	63
3.17 The (Old) Vacuum System.	63
3.18 Sample Preparation and Sample Crucible Arrangement.	64
3.19 The Electron Energy Analyser and Electronic Detecting System.	64
3.20 The Light Source.	65
3.21 Measurement of the Yield.	66

	Page
<u>Chapter 4</u> <u>Lithium</u>	67
4.1 Introduction.	68
4.2 The Photoemission Spectrum of Liquid Lithium at $h\nu = 21.2$ eV.	69
4.3 The Optical Density of States of Liquid Lithium at $h\nu = 21.2$ eV.	70
4.4 The Photoemission Spectrum of Liquid Lithium at $h\nu = 7.87$ eV.	71
4.5 Surface Photoemission.	72
4.6 The Optical Density of States of Liquid Lithium at $h\nu = 7.87$ eV.	73
4.7 The Effect of the Matrix Elements.	74
4.8 Summary.	75
 <u>Chapter 5</u> <u>The Lithium-Lead and Lithium-Tin Alloy Systems</u>	 77
<u>A Review of their Properties and Photoemission Results from the Alloys and Pure Metals</u>	
5.1 The Phase Diagrams.	78
5.2 Atomic Structure and Thermodynamic Behaviour of the Lithium-Lead System.	79
5.3 Electronic Properties of the Lithium-Lead and Lithium-Tin Systems.	84
5.4 Models of the Electronic Structure.	87
5.5 The Ionic Model of Liquid Semiconductors:- The Caesium-Gold System.	89
5.6 The Photoelectron Spectra of the Lithium- Lead System.	91
5.7 The Photoelectron Spectra of the Lithium-Tin System.	94
5.8 A Discussion and Interpretation of the Photoemission Data of the Lithium-Lead and Lithium-Tin Systems.	96
5.9 A Model for Lithium-Lead and Lithium-Tin.	101

	Page
5.10 The Optical Density of States of Liquid Lead at 21.2 eV.	102
5.11 The Optical Density of States of Liquid Tin at 21.2 eV and 16.8 eV.	104
<u>Chapter 6</u> <u>Germanium, Silver and Silver-Germanium</u>	107
6.1 Germanium:- Structure and Other Properties.	108
6.2 Photoemission Spectra.	109
6.3 The Optical Density of States of Liquid Germanium.	111
6.4 Photoemission and Structure and Concluding Remarks.	113
6.5 Silver:- Introduction.	115
6.6 The Photoemission Spectrum of Liquid Silver.	116
6.7 The Optical Density of States of Liquid Silver.	117
6.8 The Photoemission Spectrum of Liquid Silver at $h\nu = 16.8$ eV.	118
6.9 Metallic Glasses and the Silver-Germanium System.	119
6.10 The Photoelectron Spectra of the Silver-Germanium System.	122
6.11 A Discussion and Interpretation of the Photoemission Data of the Silver-Germanium System.	123
<u>Chapter 7</u> <u>Summary, Conclusions and Suggestions for Further Work.</u>	127
References	133
Appendix A:- Computer Program for ODS calculation.	142
Appendix B:- Microprocessor Program.	155
Appendix C:- Electropolishing of Molybdenum.	161

ACKNOWLEDGEMENTS

I would like to thank my supervisor, Dr. C. Norris, for his continued guidance and support throughout the course of this work.

I would also like to thank the S.E.R.C. for the provision of a studentship which allowed the commencement of this work and the D.H.S.S. whose support allowed its completion.

My thanks go to Mr. J. S. G. Taylor for his technical skills, to Mr. R. Cox and his workshop staff for their expertise and to Dr. T. Harris and his workshop staff for help with electronic equipment.

I have benefitted from discussions with many people and would like to especially acknowledge Dr. C. Binns and Dr. R. A. Howe for clarifying particular points. Special thanks are due to Dr. D. Colbourne.

Many of the diagrams in this work result from the skills of Mrs. R. Littler and Mr. J. Kerruish to whom thanks are due. Finally I would like to thank Mrs. S. M. Sherlock for her careful and neat typing of this thesis.

ABSTRACT

Ultraviolet photoelectron spectroscopy measurements are presented from a variety of metals and alloys in the liquid state. For the metals, the optical density of states function is extracted from the photoemission data, by using an extended version of the three step model of Berglund and Spicer and compared to theoretical liquid density of states calculations based on a weak scattering approach which show only small deviations from the free electron parabola. The experimentally derived results for liquid lead and liquid tin reveal deviations from the simple picture with some of the solid state density of states features persisting into the liquid phase. By contrast, liquid lithium is shown to adhere more closely to the free electron model, showing a weaker deviation from the parabolic form for its experimentally derived density of states, while the same function for liquid silver is shown to be a smeared version of the solid state curve which, as explained, is not unexpected because of structural considerations. Photoemission data from liquid germanium is presented and discussed in comparison with published data for crystalline and amorphous germanium in terms of local atomic ordering.

Data is presented from the liquid semiconducting lithium-lead alloy system and the similar lithium-tin alloy system which is shown incompatible with a simple ionic bonding model, and a stoichiometric structure is proposed where the unlike atom bonding is taken to be more covalent in character.

Photoemission spectra are also presented from the silver-germanium alloy system which has a deep eutectic composition indicating enhanced glass forming qualities. Some change with composition can be seen in the valence band region but this cannot account for the above behaviour.

CHAPTER 1

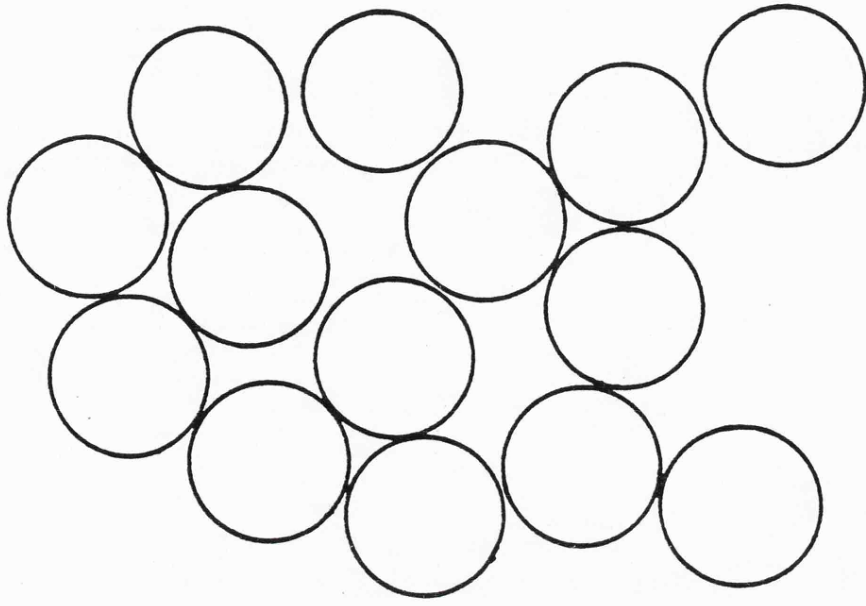
INTRODUCTION

Liquid simple metals are characterized by their good electrical and thermal conductivity and lack of long range atomic order. Liquid semiconductors show anomalies in their electrical behaviour, as a function of composition, which cannot be explained within a weak scattering formalism, even though the two constituents themselves may be classified as "liquid simple metals". This chapter gives a review of the properties of liquid simple metals and liquid semiconductors are introduced. Some binary alloys formed from a noble metal and a semiconductor show an enhanced glass forming ability. The known properties of one such system, silver-germanium, are summarized.

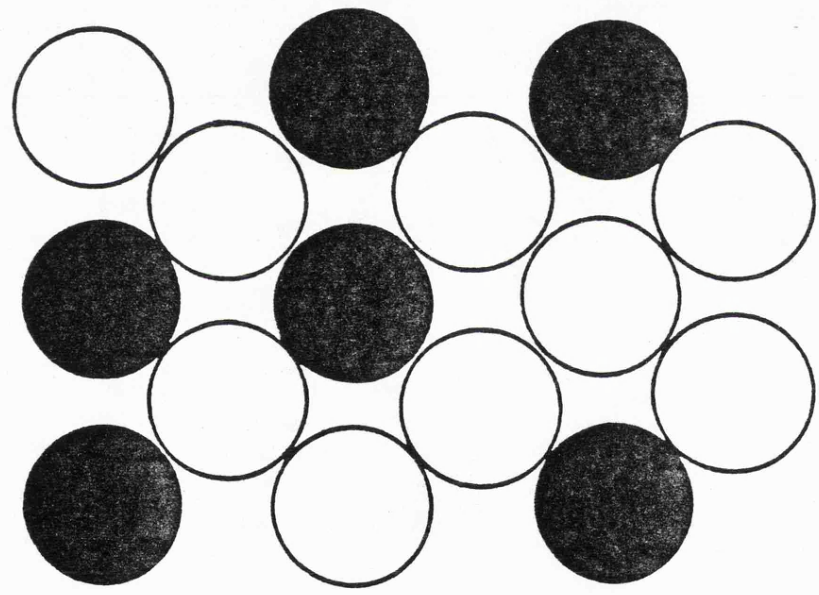
1.1 Disorder in Metals

Single crystals of pure metals at absolute zero are characterized by long range periodic ordering of the constituent atoms. Although the crystal may be finite in size and contain defects in the lattice, the translational symmetry is not seriously affected, leading to a considerable simplification in the theoretical description. Thus Bloch's theorem allows the one electron wavefunctions to be written in terms of a single momentum vector \mathbf{k} , and the eigenfunctions of the wave equation solved for a periodic potential are of the form of the product of a plane wave and a function with the periodicity of the lattice. Extensive theoretical and experimental studies have been undertaken yielding information on the ionic structure and electron states of ordered systems.

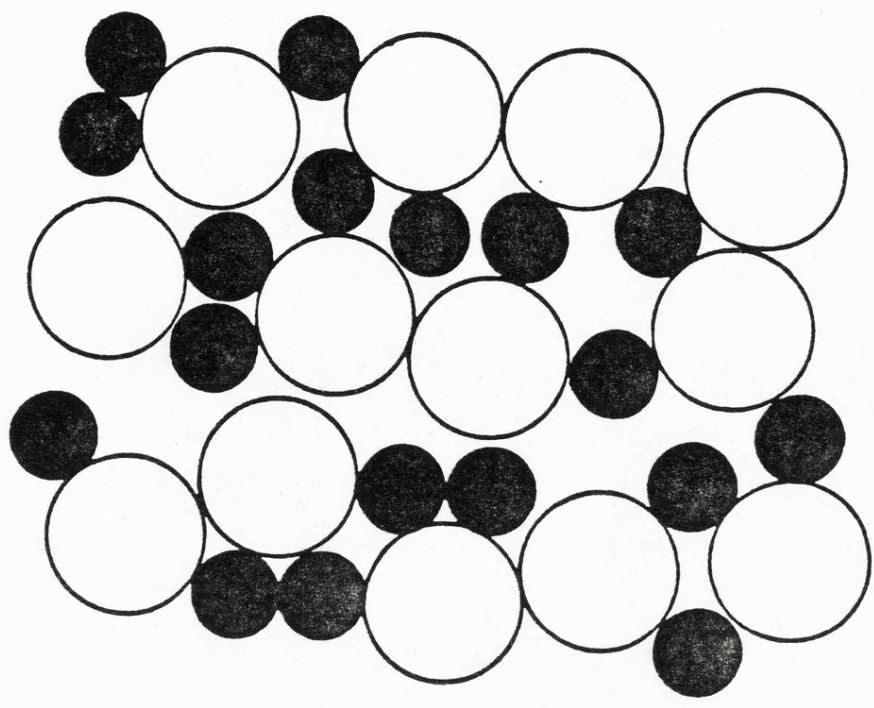
Increasingly, interest is being directed to the study of disordered metallic systems where long range translational symmetry has been destroyed. Three patterns of metallic disorder may be distinguished and these are illustrated in figure 1-1. Amorphous and liquid metals are characterized by positional disorder. In principle the solid amorphous phase which can be prepared by splatt cooling or the super-cooling of evaporated films should provide an attractive field of study because it should reproduce the main features of the liquid state without the problems of high temperature and sample containment. Unfortunately it is found that the degree of disorder is specimen dependent and thus the liquid phase gives a more reproducible state. Historically the study of solid random alloys provided a convenient and easily prepared form of disordered metal. In these systems the lattice ordering remains, although site substitution has occurred.



(a) amorphous or liquid metal



(b) random binary alloy



(c) liquid alloy

Three forms of disorder in metals

Figure I-I

Examples of these systems are Cu-Zn and Cu-Ag over limited concentration ranges. Theoretical descriptions of the electronic properties have been developed in agreement with experimental data (Stocks et al., 1973). The last case is that of liquid alloys where both positional and substitutional disorder occur. They represent the most difficult case to consider especially if they exhibit a tendency for short range ordering; alloys of this category form a major part of this work.

1.2 The Determination of the Structure of Liquid Simple Metals

Simple metals fall into the classification of those not having tightly bound d or f orbitals close to the Fermi level. The atomic structure in the solid state is simplified by the existence of long range periodic ordering which enables a crystal structure to be defined. For a liquid metal this is not possible and the structure is normally discussed by reference to the distribution functions $g_n(R)$. The first and most important of these is the pair distribution function, $g_2(R)$, defined such that if there is one molecule with its centre at the point $\underline{R} = 0$, the probability of finding another at the same instant with its centre inside a small element of volume $d\underline{R}$ is given by:-

$$N g_2(R) d\underline{R} / \Omega \quad (1.1)$$

where a volume Ω contains N molecules. This definition in terms of a probability implies that an ensemble average of the structure is being considered, that is an average over a large number of replicas of the system, with the same volume and temperature but not necessarily the same microscopic configuration; a time average of a single system is identical. Since a liquid is on the average

isotropic, $g_2(R)$ depends on the magnitude but not the direction of \underline{R} . It is normalised so that it tends to unity for large values of R ; for small R it must go to zero because it is energetically unfavourable for molecules to overlap.

Although the pair distribution function is of great importance, it alone cannot express all the details of a liquid structure and it is necessary to define a whole series of higher order distribution functions, $g_3(\underline{R}, \underline{R}')$, $g_4(\underline{R}, \underline{R}', \underline{R}'')$ etc. The three body function is defined such that if a molecule is located at the origin, then the probability of finding two others at the same instant with their centres in the small elements of volume $d\underline{R}$ and $d\underline{R}'$ is given by:-

$$(N / \Omega)^2 g_3(\underline{R}, \underline{R}') d\underline{R} d\underline{R}' \quad (1.2)$$

The higher order distribution functions are defined in a similar manner. It is possible (within certain limitations) to determine $g_2(R)$ experimentally but there is no way of determining $g_3(R)$ directly and naturally this applies to the higher order distribution functions as well. Only indirect inference can yield information concerning $g_3(R)$.

The direct experimental probe of atomic structure consists of irradiating a specimen with a parallel beam of monochromatic radiation which has a wavelength λ comparable to atomic dimensions and measuring the intensity scattered through an angle 2θ by a detector which subtends a small solid angle at the specimen. In principle both neutrons and X-rays can be used although the latter method is not so common for liquid metals because of the very strong absorption effect.

The justification for using these techniques lies in the fact

that $g_2(R) - 1$ is the Fourier transform of the interference function $a(q) - 1$. Whereas the structure factor, defined by:-

$$F(\underline{q}) = \sum_i \exp(-i\underline{q} \cdot \underline{r}_i) \quad (1.3)$$

where \underline{q} is the scattering vector and \underline{r}_i denotes the position of the i^{th} ion, determines how the amplitude of waves scattered from an assembly of identical molecules is modulated by the effects of coherence between wavelets scattered from molecules at different sites, it is the interference function that determines how the intensity of the scattered waves is modulated by coherence effects and hence is, in principle, a measurable quantity. The interference function is defined by the ensemble average:-

$$a(\underline{q}) = N^{-1} \sum_{ij} \exp i \underline{q} \cdot (\underline{r}_j - \underline{r}_i) \quad (1.4)$$

and is determined from the experimental data via a series of approximations to allow for the effects of multiple scattering, incoherent scattering and absorption by the sample container in the case of neutrons (see, for example, Enderby 1969). The most important approximation is the static approximation which assumes that the initial and final wavevectors of the scattered particle are identical in magnitude, thus ignoring any recoil of the atoms. The magnitude of the scattering vector is then given by:-

$$|\underline{q}| = \frac{4\pi}{\lambda} \sin \theta \quad (1.5)$$

For X-ray diffraction this is almost certainly true but for neutron studies serious doubts have been cast upon it. To partially overcome this, use is generally made of the Placzek corrections (Placzek, 1952).

The determination of the pair distribution function from the experimentally evaluated interference function follows from Fourier transform theory. It may be shown that (Faber, 1972):-

$$a(q) - 1 = \frac{4\pi N}{\Omega} \int_0^{\infty} (g_2(R) - 1) \frac{\sin qR}{qR} R^2 dR \quad (1.6)$$

$$\text{and } g_2(R) - 1 = \frac{\Omega}{2\pi^2 N} \int_0^{\infty} (a(q) - 1) \frac{\sin qR}{qR} q^2 dq \quad (1.7)$$

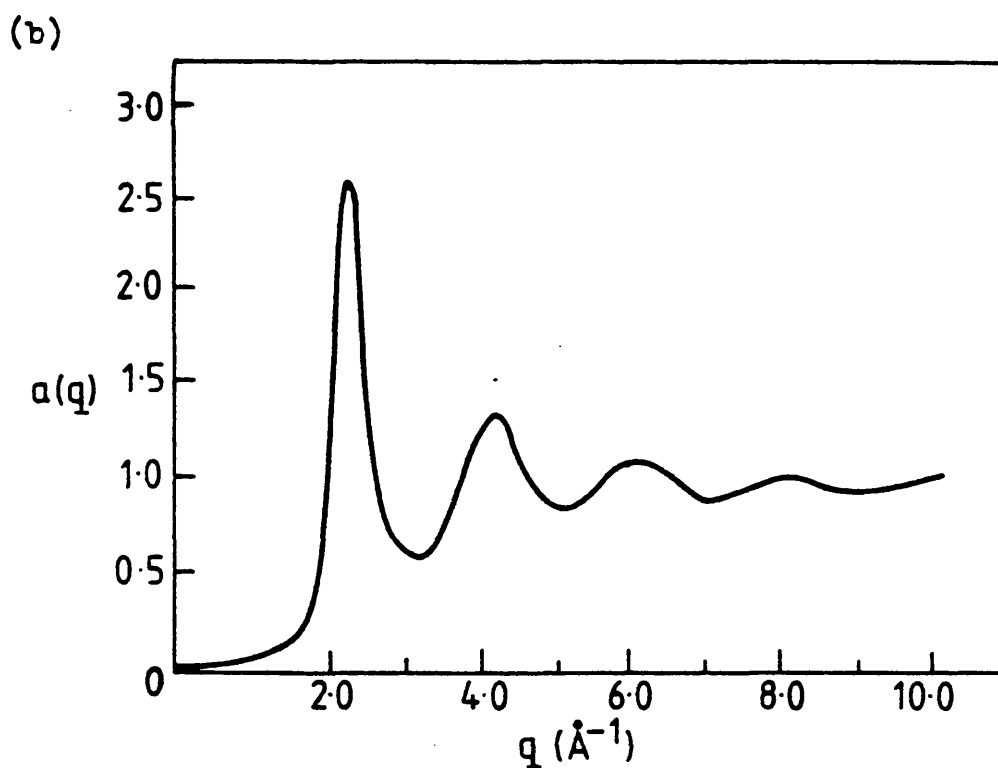
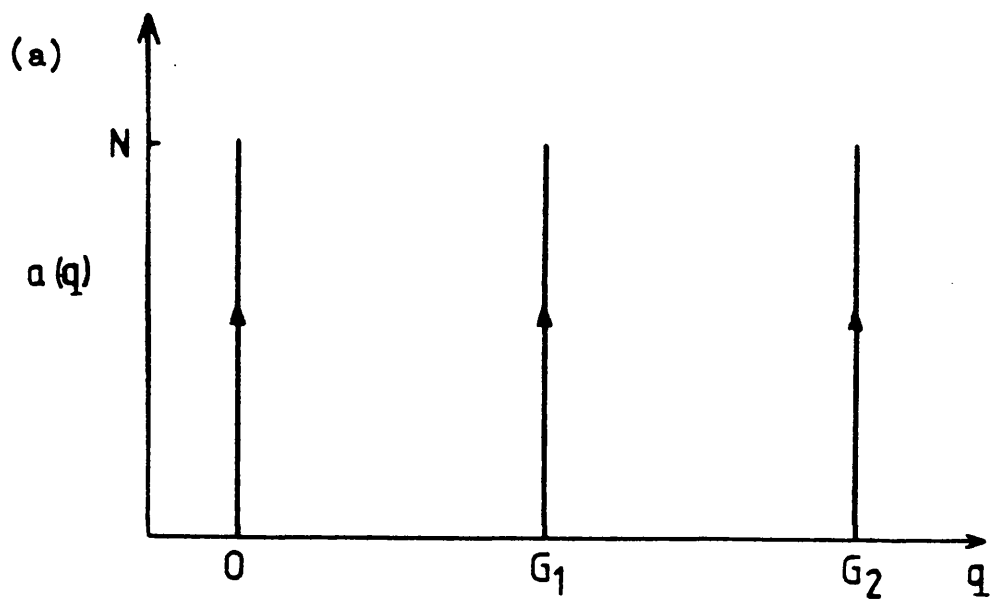
The major difficulty in calculating $g_2(R)$ lies in the existence of truncation errors; the finite upper limit of q is typically 12 \AA^{-1} and the random errors in $a(q)$, although usually small at any given value of q , give rise to a cumulative error in the transform which appears as a sharp increase in the magnitude of $g_2(R) - 1$ at values of R less than about 1 \AA .

It is interesting to consider the form of the interference function for a perfectly regular solid when there are no effects caused by thermal agitation of the molecules. The value of $a(q)$ is then zero apart from when q equals one of the reciprocal lattice vectors, G , at which values $a(q)$ becomes equal to N (figure 1-2).

The interference function for any liquid simple metal has the same basic form as shown in figure 1-2; the value of $a(q)$ rises from a minimum at small values of q , peaks at a certain value of q then proceeds to oscillate and decay about the value of $a(q) = 1$ as q becomes larger. Thus, short range ordering does exist in these systems, otherwise $a(q)$ would have the value unity, characteristic of a completely random gas like structure, for all q values. There are, however, subtle differences between the interference function curves for the liquid simple metals and it is necessary to examine models and theories of the liquid metal state to try to explain these.

1.3 Models and Theories of the Liquid State

Although there has been much experimental and theoretical work devoted to the structure of molten simple metals, there is still no



Interference function for (a) perfectly regular
solid at $T=0$

(b) liquid metal (Pb at 340°C)

Figure I-2

one all-embracing theory which can be considered to be completely successful. Approaches to the problem have ranged from a quasi-crystalline model, where the local coordination just above the melting point is treated as the same or very similar to the structure applicable to the solid phase just below the melting point, to the opposite extreme, consisting of the random close packed (RCP) spheres model of Bernal (1965).

It is instructive to consider the entropy of liquid metal systems and examine how this parameter changes on melting. A measurement of the increase of entropy, ΔS , may be made from the latent heat of melting, and when expressed in units of k_B /atom (where k_B is the Boltzmann constant), shows a systematic variation in its magnitude from one group of substances to the next. For the rare gases it is $1.7k_B$, for the b.c.c. metals (eg: Li, Na, Cs) it is $0.85k_B$, and the value is about $1.15k_B$ for the close packed metals (eg: Cu, Ag, Mg). The most significant group, however, are those which are semiconducting or semi-metallic (eg: Ga, Bi, Ge, Si) in the solid state for which ΔS is in excess of $1.15k_B$ /atom, thus indicating a more ordered assembly. It is also interesting to compute the total entropy of the liquid phase and subtract from it the value for the entropy of a perfect gas at the same temperature and volume; this gives the excess entropy for a variety of substances and may be denoted S_E . In comparison to the values for ΔS which exhibit a trend, the variations of S_E seem to be unsystematic and relatively small. It is the view of Faber that this entropy data undermines the quasi-crystalline approach.

The RCP model has been studied on the macroscopic scale by

pouring rigid spheres into an irregular container and agitating them until the minimum volume is reached. However, such an approach being effectively static in nature, yields little useful information about real systems. Of more fundamental use is the method of molecular dynamics, where a computer is used to calculate the positions and movements of a set number of molecules, interacting via a specified pair potential $\omega(R)$, and following motions allowed by Newton's Laws. Such an approach, although limited in practice to about 10^3 molecules and expensive in computer time has allowed a better understanding of the thermodynamic properties of simple liquid metals.

Approximate theories of the liquid state do exist which enable $\omega(R)$ to be coupled to $g_2(R)$, the best known theories being the Born - Green and Percus - Yevick formulations. Although an exact relation does exist between $g_2(R)$ and $\omega(R)$, it involves the unknown three body distribution function $g_3(R)$. The Born - Green theory of liquids (Green, 1960) relies upon the superposition approximation, first proposed by Kirkwood, which expresses $g_3(R)$ by the equation:-

$$g_3(\underline{R}, \underline{R}') = g_2(\underline{R}) g_2(\underline{R}') g_2(|\underline{R} - \underline{R}'|). \quad (1.8)$$

However, results deduced from the Born - Green theory when compared both to experimental data and computer simulations have proved to be less successful than the Percus - Yevick theory even though the latter may be considered to be largely empirical.

The fit between the Percus - Yevick theory solved within the rigid sphere model to the experimental data of $a(q)$ for liquid metals at their melting temperatures has been examined by Ashcroft and Lekner (1966). Although not perfect the theory is able to reproduce the

position and shape of the first peak with fair accuracy although the spacing between the first peak and the second peak is slightly overestimated by the model. The corresponding value for the packing fraction (defined as the fraction of the total volume occupied by the rigid spheres) is about 0.46. Overall though, the model provides a good approximation for liquid metals at their melting points and results obtained from the Percus - Yevick theory for the hard sphere model compare well to computer models for various values of the packing fraction. However, detail differences do exist between the interference functions for liquid metals and it is likely that these are caused by differences between the exact forms of the pair potential $\omega(R)$; differences in the repulsive core and the long range (Friedel) oscillations.

The direct and indirect evidence available for simple systems shows that on melting the crystal structure relaxes substantially although some short range ordering remains. Good review accounts of both the experimental methods and theoretical approaches have been given by Faber (1972) and more recently Shimoji (1977) for liquid metal systems.

1.4 The Electronic Structure of the Liquid Simple Metals

The historical development of the understanding of the electron behaviour in liquid metals has paralleled that of the crystalline, solid state by initially attempting to describe theoretically various trends in transport phenomena. The simplest possible approach is to consider that the induced disorder has reduced the scattering potential, thus rendering the electrons completely free. Within this model it is quite simple to derive the transport properties. The

Hall effect, which measures the transverse electric field in the presence of a magnetic field H , for a thin sample can be written simply in terms of a Hall coefficient given by:-

$$R_H = \frac{-1}{ne} \quad (1.9)$$

where n is the number density of current carriers of charge e . In table 1.1 the experimentally determined values of R_H with respect to the free electron value R_0 , given by the above equation, are shown for a selection of liquid simple metals. It is immediately apparent that with the exception of the heavy polyvalent metals Tl, Pb and Bi, this ratio is approximately unity. It is significant that other heavy liquid metals (Ag, Cu, Au) do not show such deviations from the simple model. These results imply that the Fermi surface may be described by a free electron sphere and indeed, the Hall coefficient is more a measure of Fermi surface sphericity rather than a probe of the electrons at this energy.

With the apparent success of the free electron picture an application to the resistivity for a nearly free electron (NFE) situation, provided an appropriate testing ground.

1.5 The Ziman Theory

For a NFE system the resistivity may be written down as:-

$$\rho_L = \frac{m}{ne^2 \langle \tau \rangle} \quad (1.10)$$

where $\langle \tau \rangle$ represents the average relaxation time. For an ordered solid the calculation of τ has been well developed, however, for liquid metals the induced disorder produces obvious complications for a description of the electron scattering. Although it was probably Bhatia and Krishnan (1948) who first realised that the information

Liquid	Temp (K)	R_H/R_0	ρ (expt) $\mu\Omega\text{ cm}$	ρ (theory) $\mu\Omega\text{ cm}$	S (expt) $\mu V/K$	S (theory) $\mu V/K$	L (Å)
Na	400	0.98 1.0	0.0965	0.094	-9.9	-8.3	157
Rb	340	1.0	0.22	0.139	-7.1	-5.7	121
Al	1000	1.0	0.247	0.245	-2.8	-3.9	18
Ga	600	0.97	0.295	0.32	-0.5	—	17
Hg	320	0.99 0.98	0.98	0.772	-5.0	1.38	7
Tl	675	0.76	0.75	0.596	-0.5	-4.87	8
Pb	650	0.88 0.73	0.96	0.77	-5.0	-4.5	6
Bi	600	0.60 0.69	1.289	1.09	-1.4	-3.5	4
Li	460	—	0.24	—	21.7	17.7	40

A selection of the transport properties of some liquid simple metals

Table I.1

required was contained in the interference function, $a(q)$, it was Ziman (1961) who first developed the formal theory in terms of scattering by weak pseudopotentials.

In a real metal, as opposed to a jellium, the positive charge is obviously concentrated in ions and the conduction electrons penetrate the ion cores to experience an attractive potential that becomes, near the nucleus, very strong compared to the kinetic energy component of the total Fermi energy. Although the conduction electrons, when removed from the ion cores, may be described by plane wave functions, inside a core there will be oscillations making the true wave function in this region resemble a valence wave function for the free atom rather than a plane wave. This means that the phase shifts caused by the ionic potential are large but, fortunately, they are usually close to an integral number of π and if the major interest is the extent to which an ion scatters an incident plane wave (and in this case that is so), then it can be described by an effective potential which is comparatively weak. It is this fact which makes the free-electron model a good basis from which to launch a better theory of metals. The effective potentials which are used in practice to describe the interaction of electrons with metallic ions are then known as the pseudopotentials. The methods for their derivation have been well covered in the literature (Heine (1970), Cohen and Heine (1970)).

Following Faber (1972), the effective relaxation time for an electron contributing to the total mean current density is given by:-

$$\frac{1}{\tau} = \frac{m}{\pi \hbar^3} \frac{N}{\Omega} k_F \int_0^1 a(q) |u(q)|^2 4 \left(\frac{q}{2k_F} \right)^3 d \left(\frac{q}{2k_F} \right) \quad (1.11)$$

where $u(q)$ is the pseudopotential due to a single ion and k_F is the radius in k space of the Fermi surface in the free electron model, given by:-

$$k_F = (3\pi^2 n)^{\frac{1}{3}} \quad (1.12)$$

where n is the number of electrons per unit volume. If there are N atoms in a volume Ω , each of valency z , then n is given by:-

$$n = Nz/\Omega \quad (1.13)$$

Thus, substitution of (1.11) into (1.10) using (1.12) shows:-

$$\rho_L = \frac{3\pi m^2}{h^3 e^2} \frac{N}{\Omega k_F^2} \int_0^{2k_F} a(q) |u(q)|^2 q^4 \left(\frac{q}{2k_F} \right)^3 dq \quad (1.14)$$

which is Ziman's formula for the resistivity of a liquid metal.

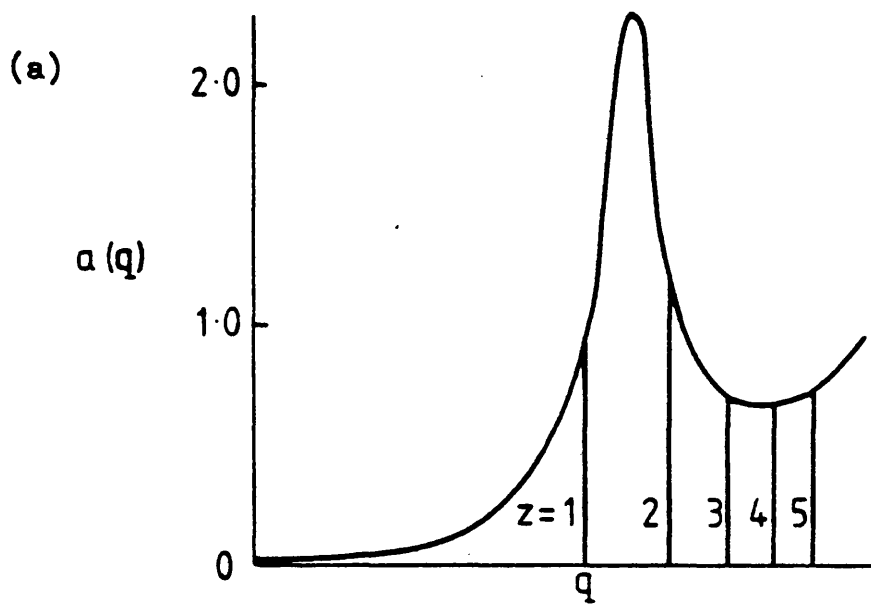
The success of this simple model is illustrated by reference to table 1.1 where theoretical and experimental values of ρ_L are shown taken largely from the early work of Sundström (1965). The calculation of ρ_L from Ziman's formula requires a knowledge of how $|u(q)|^2$ and $a(q)$ vary with q in the range from 0 to $2k_F$. The pseudopotential due to a single ion is largest near the origin but $|u(2k_F)|^2$ may be only about 10^{-2} times $|u(0)|^2$. However, $a(2k_F)$ is typically of order unity whereas $a(0)$ is usually about 10^{-2} . Hence the product $|u(q)|^2 a(q)$ has about the same value at each end of the range of integration thus the value of ρ_L depends mostly on how the product is evaluated mid-range; the position of the main peak of the interference function affects the calculated value of ρ_L considerably. Since k_F changes with valence as $z^{\frac{1}{3}}$, then the resistivity should increase as the valence does which is the situation found experimentally.

For monovalent liquid metals the limit of integration lies just to the left of the main peak of $a(q)$, for divalent metals just to its right and for higher valent metals further to the right, as shown in figure 1-3(a). Experiments show that the main peak in the interference function becomes broader but decreases in amplitude as the temperature is raised; the value of q where the peak lies remaining almost unchanged. In view of the weighted form of the integral in Ziman's formula, the resistivity can be larger with increasing temperature except for divalent metals, ie:- the temperature coefficient of resistivity of liquid metals is expected to be positive, and thus the temperature dependence of many liquid metals has reasonably been predicted. For divalent metals the integral may decrease with increasing temperature, explaining the negative value of the temperature coefficient of the resistivity observed for zinc (Bradley et al, 1962). However, the calculation of realistic values of the resistivity depends on having good pseudopotentials and accurate forms for the interference function; this is especially true for the monovalent liquid metals because the integration limit lies in a region of low q where the statistical uncertainty present in both X-ray and neutron diffraction data can be largest.

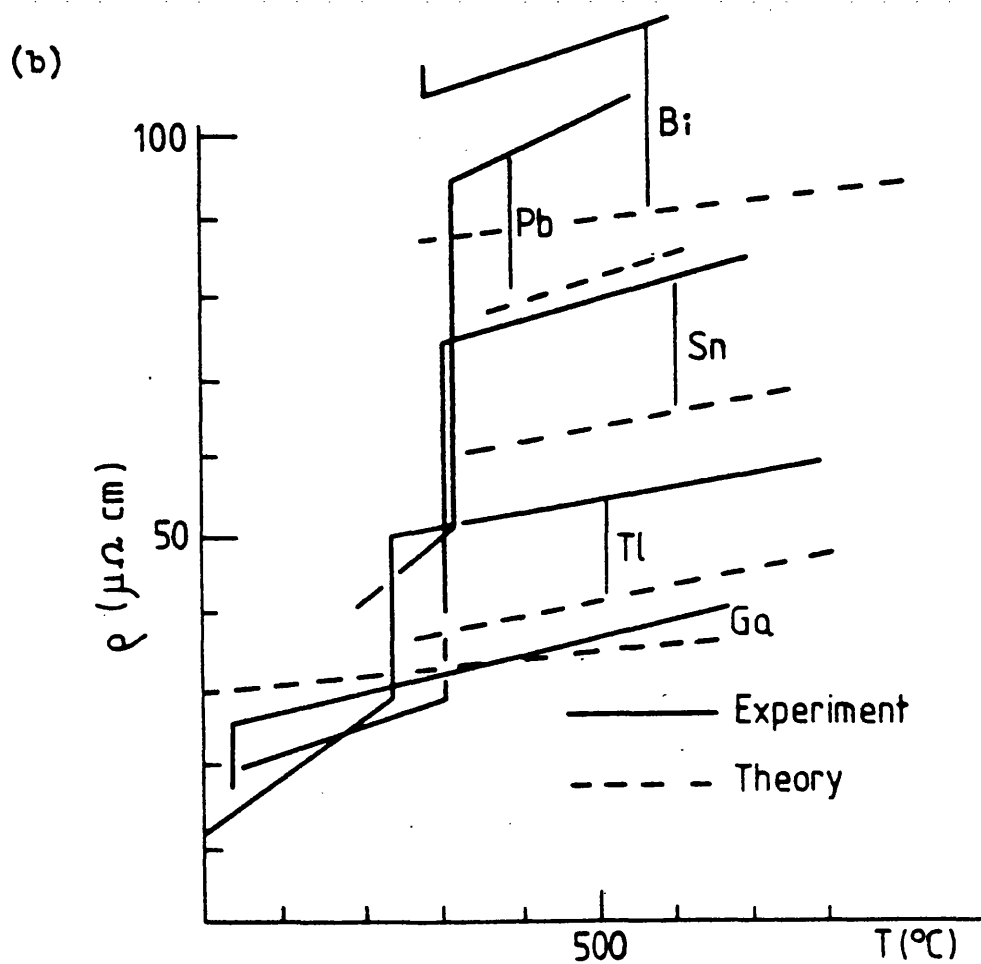
From the knowledge that the Fermi surface and the constituent electrons are nearly free, the concept of a mean free path can be developed by writing this quantity as:-

$$L = V_F < \tau > \quad (1.15)$$

where V_F is the Fermi velocity calculated from free electron theory and $< \tau >$ is available from (1.11). This quantity is shown in table 1.1 for some liquid simple metals which shows that liquid Tl, Pb and Bi are relatively strong scatterers. The concept of the mean



Vertical lines mark the limit of integration in Ziman's formula corresponding to $q=2k_F$



The resistivity of some liquid simple metals

Figure I-3

free path will be mentioned later in connection with the metal alloy systems which show a change, dependent on relative concentration, to semiconducting behaviour.

1.6 The Thermoelectric Power

When the electron distribution of a nearly free electron system is displaced in k space, there is not only an electric current but also a flux of energy Q . For this type of system at absolute zero all the energy is carried by electrons at energy E_F , but at finite temperatures, this is not strictly true. For two different metals in contact, a charge flows to equate the Fermi energies, thus setting up a potential difference. If a current is forced to flow across this, an amount of heat is released which is the so-called Peltier heat. This enables the Peltier coefficient to be defined by:-

$$\Pi = \frac{\pi^2 (k_B T)^2}{3e} \frac{\sigma'}{\sigma(0)} \quad (1.16)$$

for each metal, where k_B is Boltzmann's constant, T the absolute temperature, e the electronic charge and σ' and $\sigma(0)$ refer respectively to the derivative of $\sigma(\delta)$ and the value of the conductivity, $\sigma(0)$, when $\delta = 0$ where $\delta = (E - E_F)$, E_F being the Fermi energy and E the cut off energy of an element of the Fermi distribution function removed from E_F by the influence of thermal broadening.

Thus the thermoelectric power, S , which is a measurable quantity can be defined by:-

$$S = \frac{\Pi}{T} \quad (1.17)$$

By differentiating Ziman's formula with respect to k_F shows that for a liquid metal:-

$$S = \frac{\pi^2 k_B^2 T}{3e K_F} \left[\frac{3 - 2|u(2k_F)|^2 a(2k_F)}{\langle |u|^2 a \rangle} - \frac{\langle k_F (\partial |u|^2 / \partial k)_F a \rangle}{\langle |u|^2 a \rangle} \right] \quad (1.18)$$

where K_F is the kinetic energy component of the total Fermi energy and the brackets $\langle \rangle$ refer to an integration of a function of q over the range 0 to $2k_F$, weighted towards the upper end of this range by a factor q^3 . A trivial simplification is to write the bracket as δ , the thermoelectric parameter. A less trivial simplification used by some authors is to ignore the final term in δ which is inappropriate for several systems. Thus, for example, the Evans potential for mercury (Evans, 1970) gives a considerable improvement in the calculated value for the thermopower of mercury and this is due to the inclusion of the last term in (1.18), ie:- the k -dependence of the pseudopotential.

Compared to the case of resistivity, theoretical values of thermoelectric power are quite sensitive to the details of the pseudopotential at $q = 2k_F$. The calculation of the thermoelectric power is thus rendered difficult and the agreement between theory and experiment may, at best, be considered to be reasonable.

1.7 The Density of States at the Fermi Level.

The Knight Shift

This effect is a shift $\Delta\nu$ in the frequency ν_0 at which nuclear magnetic resonance (NMR) is observed for a given field, when the nuclei form part of a metal. It is measured relative to the resonance frequency for an isolated nucleus which is obtained from NMR experiments on non-metallic compounds. The Knight shift is due to a hyperfine contact interaction between a nucleus and the surrounding conduction electrons (Knight, 1956). The standard formula for the Knight shift K is given by:-

$$K = (8\pi/3) \chi_p V \langle |\psi_k(0)|^2 \rangle_{FS} \quad (1.19)$$

where χ_p is the Pauli spin susceptibility, V is the atomic volume and $V \langle |\psi_k(0)|^2 \rangle_{FS}$ is the electron density of conduction electrons at the nuclear site averaged over the Fermi surface, called the contact density. Although an exact interpretation of the Knight shift is difficult, it forms a useful guide to changes in electronic structure on, for example, melting and alloying for χ_p is proportional to $N(E_F)$, the density of states at the Fermi level and $V \langle |\psi_k(0)|^2 \rangle_{FS}$ is determined primarily by the S component of the atomic part of ψ_k and it may change if the character of the wave functions at E_F changes with temperature or composition.

It is experimentally known that the Knight shift in many metals is changed by only a small amount on melting (table 1.2). The two factors in (1.19) are governed by the characteristic arrangement of ions in space, consequently it was inferred (Knight et al, 1959) that the ionic arrangement in the liquid phase is not locally different from that in the solid phase; that the electronic structure at the Fermi level in the solid and liquid phases is largely the same; the corollary to this being that the band structure effects in the solid are carried over into the liquid phase. This result thus contradicts the NFE model where in the liquid state the density of states is supposed to resemble that of the free electron model parabola (or show only small deviations from it) leading to a description of the transport parameters in terms of scattering from weak pseudopotentials.

1.8 The Density of States below the Fermi Level

The density of states function for sodium and potassium has been calculated by Itami and Shimoji (1972) and the resulting $N(E)$ curves

Metal	$\Delta K/K$ (expt)
Li	-0.012
Na	0.022
K	0.020
Rb	0.012
Cs	-0.021
Cu	0.05
Hg	0.00
Al	0.00
In	-0.04
Tl	0.00
Sn	-0.03
Pb	-0.01

ΔK is the change in the Knight shift on melting;

$$K_{\text{liquid}} - K_{\text{solid}}$$

Knight Shift change on melting
(from Shimoji (1977))

Table I.2

were found to be close to the free electron value or parabolic form. Liquid sodium and potassium may be regarded as representatives of the NFE metal. Presumably then the same is true for these two metals in the solid phase for the Knight shift change on melting is very small. The situation appears different in the case of lithium where the Knight shift change on melting is also very small. However, according to the perturbation calculation of Shaw and Smith (1969), the densities of states in both the solid and liquid phases coincide with each other, despite their considerable deviations from free electron behaviour. The density of states of some liquid polyvalent metals has also been evaluated (using the Green function method). The results for zinc and aluminium (Ballentine, 1966), lead and tin (Itami and Shimoji, 1972), indium (Chan and Ballentine, 1972) are very close to the free electron values.

The experimental situation is, however, somewhat different. Probably the best probe of electronic structure below the Fermi level is provided by the conceptually simple tool of photoemission spectroscopy. In these experiments the absorption of an incident photon causes excitation of an initial, valence band electron to a final conduction band state. If this energy is above the work function, the electron has the possibility of travelling to the surface and escaping into the surrounding vacuum. A measure of the number of electrons which have escaped against their energy should give information on the initial density of states from which the electrons were derived. This process will be discussed in more detail in chapter two. The first measurements for liquid metals were reported by Koyama and Spicer (1971) who found that for indium, a feature in the solid state spectrum persisted into the liquid state. This was

interpreted in terms of a crystalline band structure and provided some evidence that the density of states was in contradiction to the NFE model. A review by Norris (1977) presents photoemission results for the heavy polyvalent metals lead and bismuth. The photoemission results for lead, confirmed in this work, clearly show two separate bands superposed on a background of secondary electrons. A similar correspondence between structure in the liquid spectra and details of the band structure of the solid have also been argued for aluminium and mercury (Norris et al, 1974). Photoemission measurements on liquid lithium, at two photon energies, will be presented in this work which show closer agreement to the free electron model.

A brief summary of liquid simple metals would conclude that the atomic structure may be ascertained using diffraction techniques, and upon melting the crystal structure relaxes substantially although short range ordering remains. The liquid structure may be described by reference to distribution functions and the pair potential. A description in terms of hard spheres results in an interference function which provides a good approximation for the liquid aluminium group to which most of the liquid simple metals belong (the main exceptions to this being the molten divalent metals zinc, mercury and cadmium which when compared to the hard sphere result deviate substantially at large q). The electronic structure (for transport properties) may conveniently be described within a nearly free electron formalism relying on scattering by weak pseudopotentials but photoemission measurements reveal deviations from the weak-scattering model for liquid simple metals beyond groups I and II. There is, unfortunately, little other spectroscopic work (eg:- using X-rays as a primary photon source) on liquid metals to provide further evidence. The

description of electronic structure for some liquid metals is thus not yet fully understood.

1.9 Liquid Semiconductors

A rough guide as to what constitutes a liquid semiconductor is provided in the pioneering review article of Ioffe and Regel (1960):- liquid semiconductors are electronically conducting liquids with electrical conductivities less than the usual range for liquid metals. The distinction from molten salts and molecular liquids, which do not conduct electronically, is thus made, although it is always possible that electronic conduction and ionic conduction may occur in parallel in molten salts and either one may dominate in some systems depending on conditions (eg:- temperature). As noted by Ioffe and Regel the electrical conductivity σ of an ionic liquid is not likely to be greater than about $1 \Omega^{-1} \text{ cm}^{-1}$ because of the limited ionic mobility so that liquids with higher conductivities must conduct electronically. When σ is lower than that, other considerations, such as measured ionic transport numbers or the chemical nature, must be used to establish the extent of electronic conductivity.

At the other end of the conductivity range the boundary with liquid metals is somewhat arbitrary. Ioffe and Regel suggested that liquids with electronic conductivities less than about $10,000 \Omega^{-1} \text{ cm}^{-1}$ (the value for liquid mercury) should be regarded as liquid semiconductors. The situation is clouded by the fact that semi-conducting liquids in the high conductivity range ($> 100 \Omega^{-1} \text{ cm}^{-1}$) are statistically degenerate and obey Fermi - Dirac statistics: they may thus be regarded as metals although the name liquid semiconductor is normally used - this arose because such liquids show a strong increase

in conductivity with temperature, in contrast to typical liquid metals, but akin to solid semiconductors in the classical definition. However, according to Cutler (1971), such behaviour cannot always be attributed to excitation of carriers across a gap or out of traps but must be the result of a change in chemical structure with temperature, therefore the physical mechanisms responsible for the temperature dependence of the electrical conductivity may well be very different from conventional semiconductors.

Ioffe and Regel emphasized the fact that in semiconducting liquids, in contrast to liquid metals, the mean free path is of the order of the interatomic distance, whereas in liquid metals the scattering is weak and the Ziman theory is applicable where the conductivity exceeds about $3,000 \Omega^{-1} \text{ cm}^{-1}$ (section 1.5). Thus, following Mott and Davis (1979) the conductivity spectrum may be divided into three main regions:-

Regime 1. This is the so-called weak scattering limit where Ziman's theory applies. Many liquid metals and alloys fall into this category. The mean free path L is large ($k_F L \gg 1$). The conductivity is given by:-

$$\sigma = \frac{S_F e^2 L g^2}{12 \pi^3 \hbar} \quad (1.20)$$

where k_F is the wavevector at the Fermi energy E_F ,

$$g = \frac{N(E_F)}{N(E_F)_{\text{FREE}}},$$

and S_F is the Fermi surface area ($4\pi k_F^2$). The thermoelectric power can be related to the conductivity by:-

$$S = \frac{\pi^2}{3} k_B^2 T / E \left[\frac{d(\ln \sigma)}{dE} \right]_{E = E_F} \quad (1.21)$$

and the Hall coefficient is given by $R_H = -1/ne$ as shown previously.

Regime II. Following the theoretical work by Anderson (1958), Mott concluded that a lower limit for σ must exist below which conduction by processes involving extended electronic states is not possible. From plausible assumptions, Mott determines the value of σ_{\min} to be about $200 \Omega^{-1} \text{ cm}^{-1}$. For conductivities above this value but below about $3,000 \Omega^{-1} \text{ cm}^{-1}$, the scattering is so strong that $L \sim a$ (where a is the inter-atomic spacing) and the density of states at the Fermi energy rather than the mean free path controls the conductivity which is given by:-

$$\sigma = \frac{S_F e^2 a g^2}{12 \pi^3 \hbar} \quad (1.22)$$

where g is in the range from 1 to 0.3. The thermoelectric power is given by:-

$$S = \frac{\pi^2}{3} \frac{k_B^2}{e} T \frac{2d(\ln g)}{dE} \quad (1.23)$$

The approximate relationship $\sigma \approx \{N(E_F)\}^2$ is to be expected where $N(E_F)$ may be deduced from the Knight shift.

Regime III. For g values less than about 0.3, Mott suggests that states at the Fermi energy become Anderson localized and the liquid behaves as a semiconductor, the conductivity being given by:-

$$\sigma = \sigma_{\min} \exp(-\mathcal{E}/k_B T) \quad (1.24)$$

where \mathcal{E} is the energy required to excite an electron to the mobility edge given by $\mathcal{E} = E_c - E_F$. The thermopower is given by:-

$$S = (k_B/e) \left(\mathcal{E}/k_B T + A \right) \quad (1.25)$$

Theory predicts that A should have the value unity but negative values are sometimes found for an unknown reason.

Thus it may be seen that using the conductivity as a guide to classification results in an indistinct boundary between liquid metals and liquid semiconductors. Cutler (1977) has written that for $10,000 \gtrsim \sigma \gtrsim 1000 \Omega^{-1} \text{ cm}^{-1}$ investigators whose main concern is liquid metals or liquid semiconductors may feel equally at home.

It is instructive to pause at this point and consider what substances can be regarded as liquid semiconductors. Among the elements, molten selenium and molten tellurium fall into this category; the conductivity of liquid tellurium is around $2000 \Omega^{-1} \text{ cm}^{-1}$ near the melting point and rises with temperature (Tieche and Zareba, 1963). The conductivity of liquid selenium is very small; it has been measured at as low a value as $10^{-8} \Omega^{-1} \text{ cm}^{-1}$ (Glazov et al, 1969) but shows a positive temperature coefficient (Gobrecht et al, 1971).

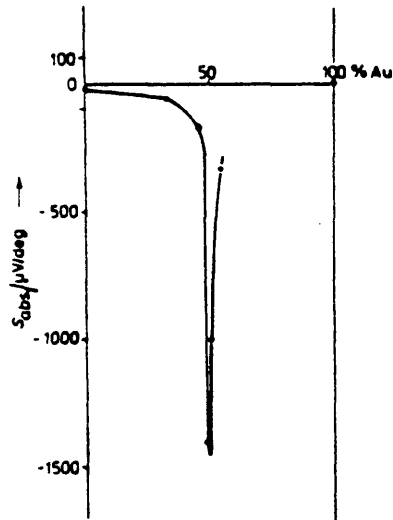
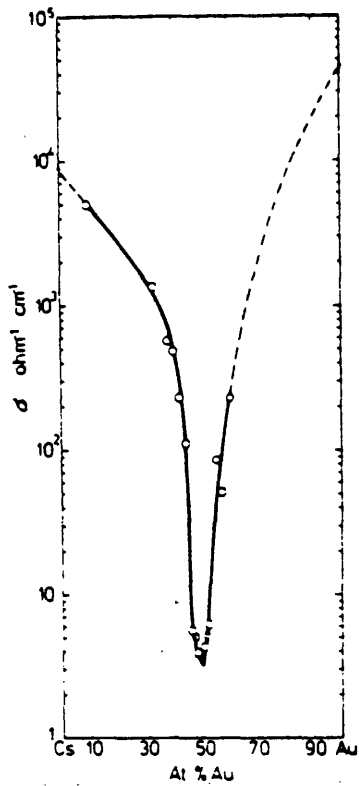
There are many alloy systems which can be classified as liquid semiconductors, many of which are composed from a metallic component and a chalcogen component (sulphur, selenium and tellurium). Some examples of such systems are shown in table 1.3. Obviously very many tertiary or even more complex alloy systems would fall into this category but the study of such systems does not at the moment yield any further information on the basic questions concerning liquid semiconductors, the answers to which are incomplete for binary systems anyway.

Some liquid binary alloys show semiconducting behaviour even though their constituents exhibit strongly metallic behaviour in the pure state. Examples of such systems are:- magnesium - bismuth, magnesium - antimony, lithium - bismuth and caesium - gold. Figure 1-4 reproduces

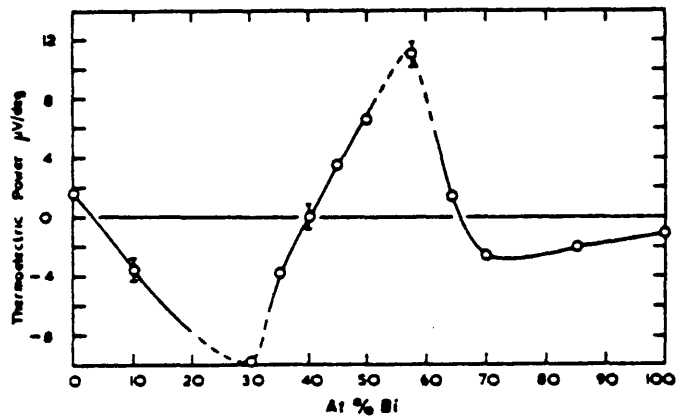
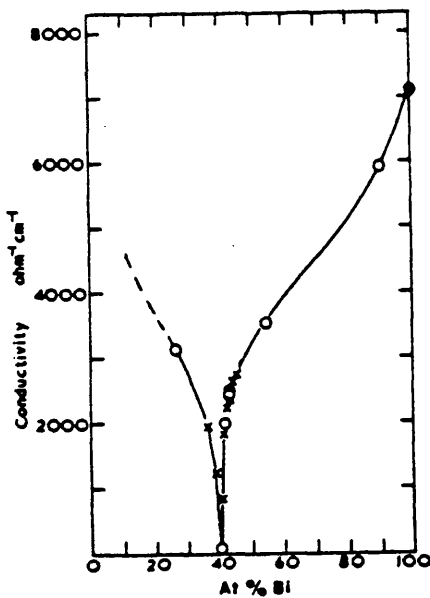
Liquid	Conductivity($\Omega^{-1}\text{cm}^{-1}$)	Thermopower($\mu\text{v/K}$)
CuO	0.4	
Cu ₂ S	50	
Cu ₂ Se	200	
CuTe	1920	60
Ag ₂ S	200	
AgTe	600	130
ZnTe	40	
CdTe	40	
HgSe	25	
HgTe	630	
GaTe	700	
InSe	0.3	-100
In ₂ Te ₃	25	20
Tl ₂ S	2.3	-300
Tl ₂ Se	3	-100
Tl ₂ Te	70	-100
GeS	1.4	
SnS	24	
SnTe	1400	28
PbS	110	
PbSe	400	
PbTe	1100	
Sb ₂ Se ₃	2	2
Bi ₂ Mg ₃	800	
Bi ₂ Se ₃	900	-35
FeO	180	20
FeS	400	
BiS	600	

Electrical conductivities of some semiconducting liquids (from Shimoji (1977))

Table I.3



(a) Conductivity and thermoelectric power of Cs-Au system (Schmutzler et al, 1976)



(b) Conductivity and thermoelectric power of Mg-Bi system (Enderby and Collings, 1970)

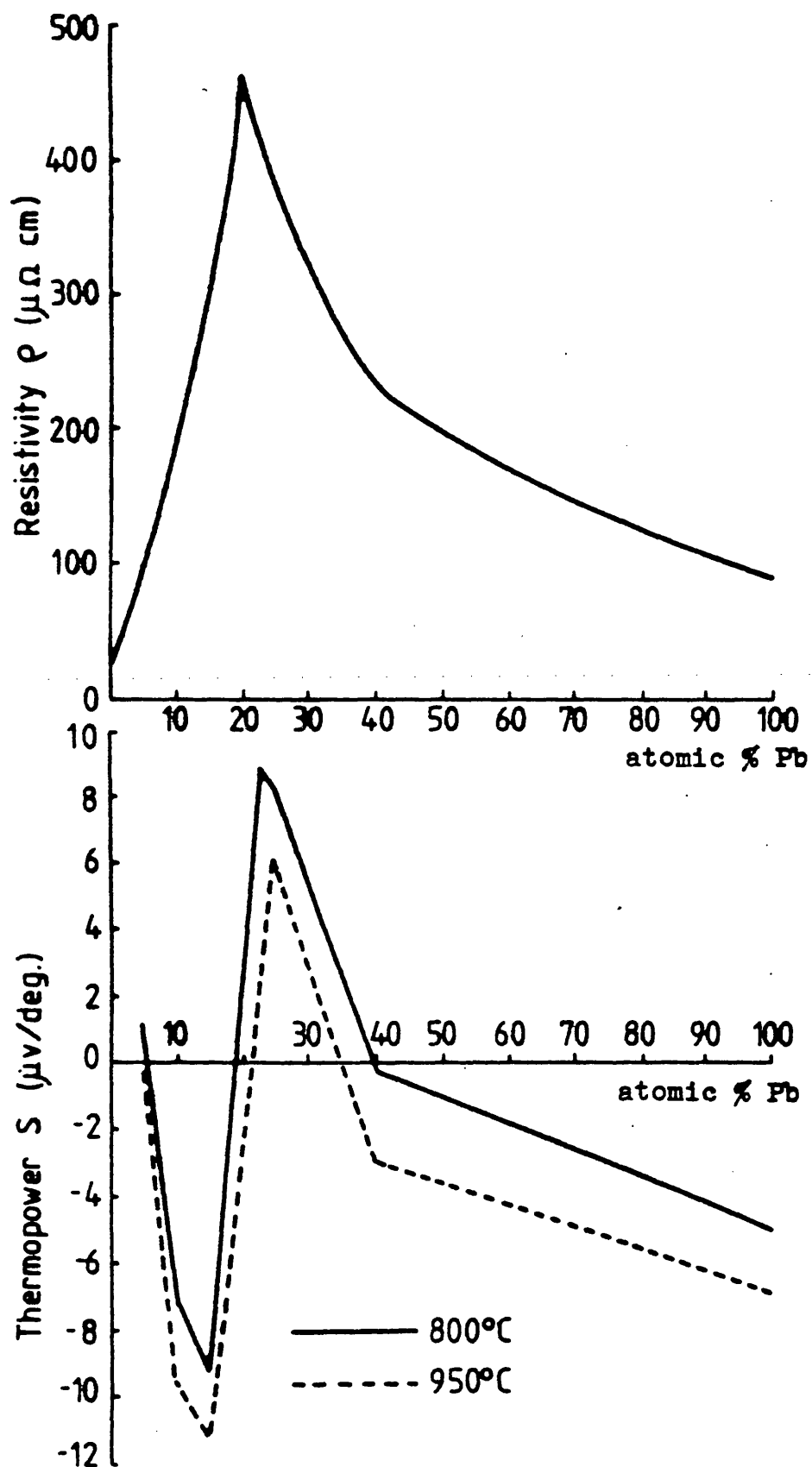
Figure I-4

the conductivity against composition curves for the molten alloy systems magnesium-bismuth and caesium-gold, where it can be seen that the conductivity changes dramatically at a composition which corresponds to elementary valence considerations. However, there are differences between these systems for the thermoelectric power of magnesium-bismuth passes through zero at the composition corresponding to the minimum in the conductivity whereas for the caesium-gold system at the same point, the thermoelectric power rises to a maximum value.

Such behaviour poses questions which need to be answered if the properties of these systems are to be understood. These may be summarized as:-

1. What is the change in atomic structure on alloying?
2. What is the change in the electronic density of states function on alloying?
3. What is the bonding mechanism between constituent entities in semiconducting binary alloys?

Photoemission spectroscopy being a tool which directly probes electronic structure provides evidence for the second question and indirect evidence for the third and accordingly was used on two binary alloy systems, one of which (lithium-lead) is known to exhibit anomalies in its electronic and thermodynamic properties near the stoichiometric composition Li_4Pb and the other (lithium-tin) is suspected of doing so because of the similarity in the chemical properties of tin and lead and also because of the similarity in the change on alloying of the Knight shift of the lithium-lead and lithium-tin systems, (Van der Marel et al, 1980). Lithium-tin also offers the possibility of Mössbauer measurements (Hubberstey - private communication). Figure 1-5 shows the measured resistivity curve and thermopower plot for the



Resistivity and thermopower of the Li-Pb system

Figure I-5

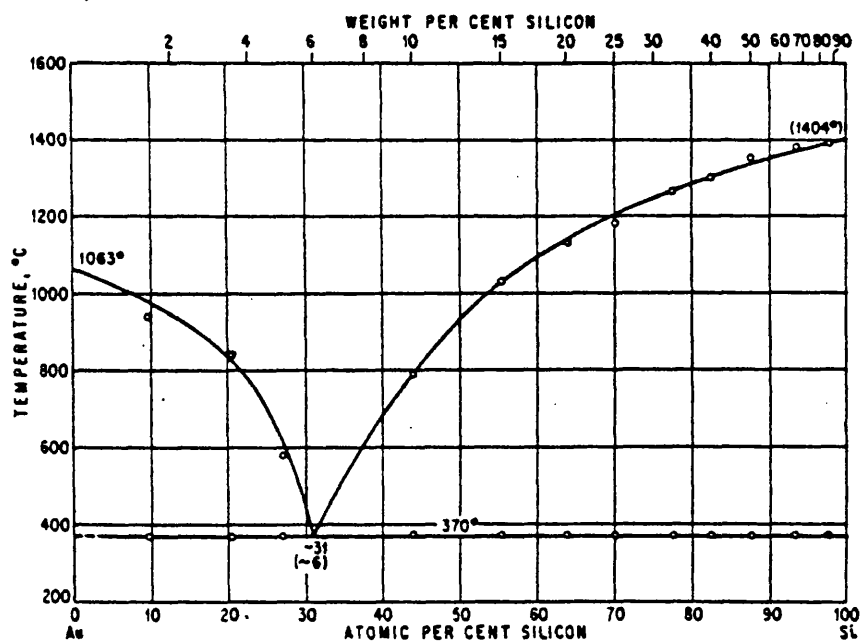
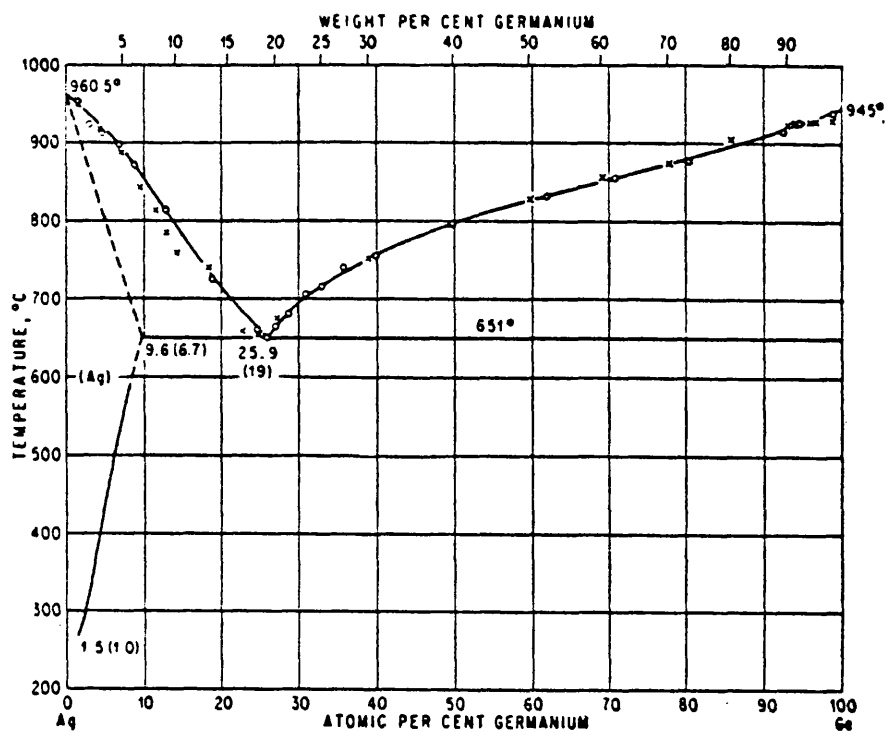
lithium-lead system (Nguyen and Enderby, 1977) although a full description of the properties of the system will be reserved for a later chapter where the photoemission results will be discussed in relation to theories of the bonding mechanism and the electronic structure.

1.10 Amorphous Metals and Alloys

The glass state may be considered to be an amorphous solid formed by continuous hardening of a liquid and may be regarded as having properties and structures characteristic of a metastable liquid which is, naturally, frozen.

Although no pure metals have been prepared practically in completely amorphous form by cooling from the melt, certain alloys formed by composing noble metals with semiconductors, such as the binary alloys silver-germanium and gold-silicon, show enhanced glass forming qualities, when their composition is at a eutectic value. At this composition, the melting temperature of the alloy is relatively far removed from that of the pure elements, see figure 1-6 (Hansen, 1958). The silver-germanium alloy system, the one chosen for study in this work, shows further thermodynamic properties which are interesting. Thus the enthalpy of mixing is negative (Castanet et al, 1969) and the excess volume of mixing has been measured in the range 0-40 atomic % Ge (Martin - Garin et al, 1975) and found to be negative and minimal for the eutectic composition.

Similar questions pose themselves for these glassy systems as for liquid semiconductors regarding the changes in atomic structure and bonding on alloying and the form of the density of states curve throughout the composition range. Information on the structure side has been provided by the neutron diffraction work of Bellissent - Funel et al, (1977 and 1979) which reveal predominant atomic



Phase diagrams of the Ag-Ge and Au-Si systems

Figure I-6

interactions between silver and germanium and abnormal q - dependent small angle scattering which cannot be explained by the density and concentration fluctuations of a classical binary liquid alloy. Work has also been reported on the nucleation of the eutectic silver-germanium alloy by Lemaignan et al (1979 and 1980). No work has been reported on the electronic structure which consequently was investigated in this work by photoemission spectroscopy; the results will be presented in a later chapter and a full discussion of the known properties of the silver-germanium system will be reserved for that section.

This completes the introductory chapter. In chapter two the theory of photoemission is detailed while chapter three explains the experimental equipment and techniques used. The results from lithium are presented in chapter four while the results from lithium-lead and lithium-tin as well as the pure metals lead and tin and a discussion of the properties of the alloys are given in chapter five. Chapter six contains work on pure germanium and silver followed by a discussion on silver-germanium alloys complemented by photoemission data. The volume is concluded by chapter seven which gives a brief summary and offers suggestions for further work.

CHAPTER 2

THE THEORY OF PHOTOEMISSION

This chapter divides into two sections. The first explains the formal theory of photoemission while the second details the three step model which was used in the analysis of the photoemission data in this work.

2.1 Introduction

In essence, low energy photoemission spectroscopy is a simple probe of electronic states below the Fermi level in which the absorption of an incident photon causes the excitation of an electron to a final, empty state. If the energy of this state is greater than the work function, the electron may then escape and travel into the surrounding vacuum and be detected.

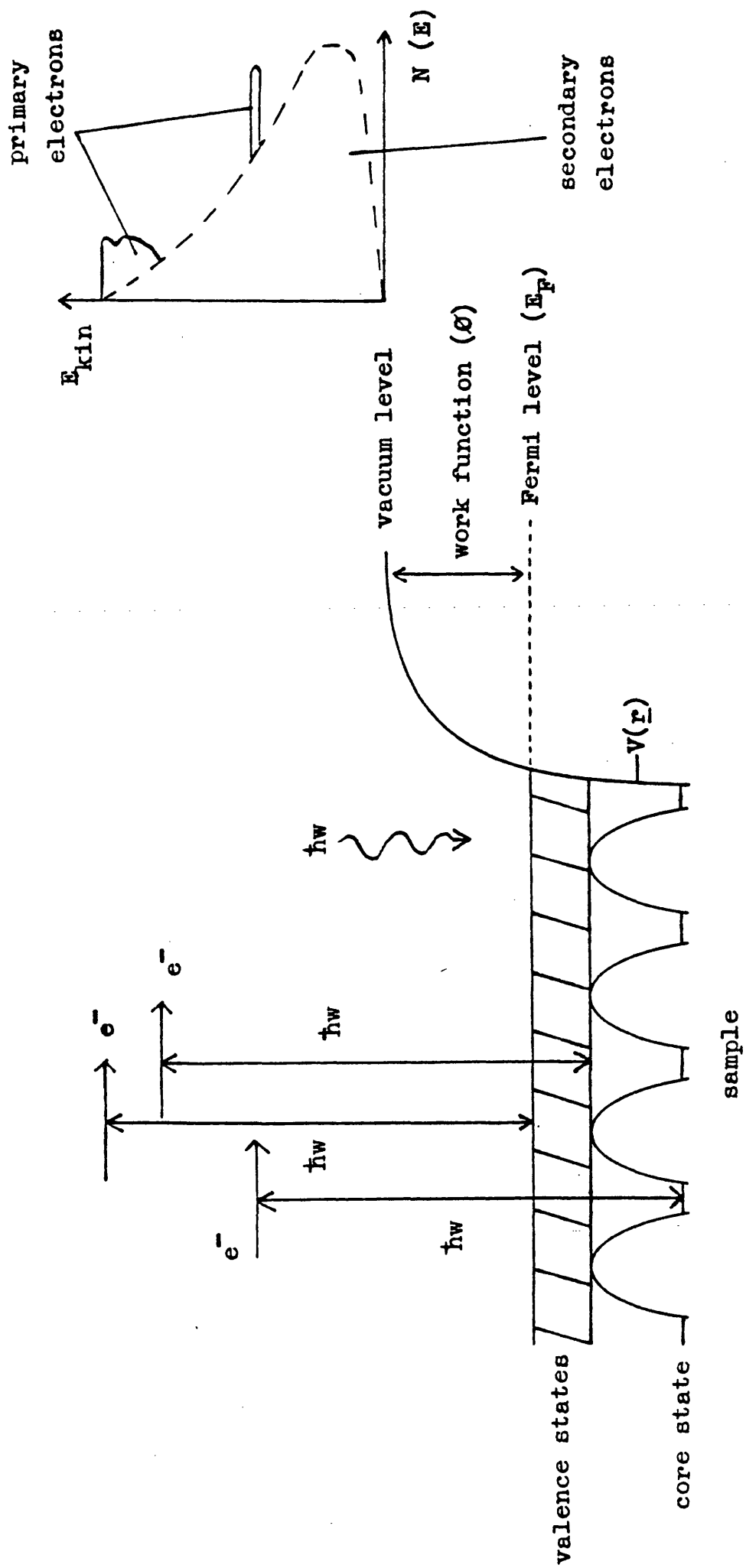
In reality this simple picture is clouded because of the effects of the decay of the hole left after the photoexcitation process and the scattering of the excited electrons. For some transition metals, hole decay can lead to lifetime broadening of the initial state by $\sim 1\text{eV}$, thus questioning the basis of the one electron band picture, where each electron is taken as moving under the influence of the background potential of the ions and the other $(N - 1)$ electrons $(V(\underline{r}))$. Usually, however, the effect is much smaller. Scattering of excited electrons restricts the probe depth of the spectroscopy but also means that only a small fraction of the excited electrons reach the surface to produce the primary photocurrent; the majority are inelastically scattered and contribute to the background of secondary electrons. The measured photocurrent thus may be written:-

$$\begin{aligned} \text{Total photocurrent} = & \text{Primary current} + \\ & \text{Secondary (scattered) current} \end{aligned} \quad (2.1)$$

Information about the unperturbed electron states is then derived from the primary current signal. The simple model of photoemission is illustrated in figure 2-1.

2.2 The Primary Electron Distribution

An incident photon induces a transition between an initial one



The photoemission process

Figure 2-1

electron state $|i\rangle$ and a final state $|u\rangle$ which has a plane wave component in the vacuum, far removed from the sample. The time averaged photocurrent may be written in a Fermi "Golden Rule" form:-

$$\langle J \rangle = \frac{2\pi e}{\hbar} \sum_{iu} |\langle i | H' | u \rangle|^2 \delta(E_u - \hbar\omega - E_i) \quad (2.2)$$

$$\text{where } H' = \frac{ie\hbar}{2mc} \times (\underline{A} \cdot \nabla + \nabla \cdot \underline{A}) \quad (2.3)$$

is the perturbing Hamiltonian. The vector potential of the vector field, $\underline{A} = A \underline{\hat{e}}$, is related to the electric vector by:-

$$\underline{E} = -\frac{1}{c} \frac{\partial \underline{A}}{\partial t} \quad (2.4)$$

Usually the spatial variation of \underline{A} is ignored and the Hamiltonian becomes:-

$$H' = \frac{ie\hbar}{2mc} \underline{A} \cdot \nabla \quad (2.5)$$

The current matrix element $\langle i | \underline{A} \cdot \nabla | u \rangle$ may be rewritten in terms of the potential $V(\underline{r})$ as:-

$$\langle i | \underline{A} \cdot \nabla | u \rangle = \frac{-ic}{m\omega} \langle i | \underline{A} \cdot \nabla V(\underline{r}) | u \rangle \quad (2.6)$$

The following theory assumes that $\underline{\hat{e}}$ is parallel to the surface (ie:- the incident wave is normal to the surface), so contributions due to the surface potential barrier can be ignored.

A practical theory for solving (2.2) for ordered systems has been given by Pendry (1976) but for illustration it is simpler to factorize out the electron escape part:-

$$N(E, \omega) = \frac{d}{dE} \langle J \rangle = \text{constant} \sum_f |\langle i | \nabla | f \rangle|^2 \delta(E_f - E_i - \hbar\omega) \delta(E - E_f) T_{\text{eff}}(E) \quad (2.7)$$

where $T_{\text{eff}}(E)$ is the effective escape probability. The term $|f\rangle$ is a final one electron state of the unperturbed system, and $N(E, \omega)$

is the measured electron distribution.

2.3 Optical Matrix Elements

Initially as an approximation the contribution of $|\langle i | \nabla | f \rangle|^2$ in (2.7) may be taken as a constant, then away from the threshold where $T(E)$ is slowly varying, (2.7) reduces to:-

$$N(E, \omega) = \text{constant} \sum_{if} \delta(E_f - E_i - \hbar\omega) \delta(E - E_f) = \text{const. } N_v(E - \hbar\omega) N_c(E) \quad (2.8)$$

where $N_v(E - \hbar\omega)$ is the density of initial states and $N_c(E)$ is the density of final states which has little structure so that $N(E, \omega)$ reflects the density of initial states function $N_v(E - \hbar\omega)$ but modulated by the effect of the matrix element term. The significance of the latter may be illustrated by writing $|i\rangle$ in tight binding form (Shevchik, 1977):-

$$|i\rangle = \sum_{\underline{m}} \exp i \underline{k} \cdot \underline{R}_{\underline{m}} \phi(\underline{r} - \underline{R}_{\underline{m}}) \quad (2.9)$$

where ϕ is a localised atomic orbital, \underline{k} is the one electron momentum vector, and $\underline{R}_{\underline{m}}$ is the position vector of the m^{th} atom, and $|f\rangle$ as a single APW = $\exp i \underline{k}' \cdot \underline{r}$ ($r \geq a$)

(augmented plane wave)

$$= \sum_{\underline{m}'} \exp i \underline{k}' \cdot \underline{R}_{\underline{m}'} \theta(\underline{r} - \underline{R}_{\underline{m}'}) \quad (r < a) \quad (2.10)$$

where a is the muffin tin radius. Thus:-

$$\langle i | \nabla | f \rangle = \int \sum_{\underline{m}} \exp -i \underline{k} \cdot \underline{R}_{\underline{m}} \phi^*(\underline{r} - \underline{R}_{\underline{m}}) \nabla [\exp i \underline{k}' \cdot \underline{r} + \sum_{\underline{m}'} \exp i \underline{k}' \cdot \underline{R}_{\underline{m}'}, \\ \times \theta(\underline{r} - \underline{R}_{\underline{m}'})] d^3 \underline{r} \quad (2.11)$$

A consideration of the overlap of the wavefunctions implies that the contribution of the $\exp i \underline{k}' \cdot \underline{r}$ term to the integral is small and also that $m = m'$. Hence:-

$$\langle i | \nabla | f \rangle = N \sum_{\underline{m}} \exp i (\underline{k}' - \underline{k}) \cdot \underline{R}_{\underline{m}} \int \phi^*(\underline{r}) \nabla \theta(\underline{r}) d^3 \underline{r} \quad (2.12)$$

and:-

$$| \langle i | \nabla | f \rangle |^2 = N^2 \sum_{m,n} \exp i (\underline{k}' - \underline{k}) \cdot (\underline{R}_m - \underline{R}_n) \left| \int \phi^*(\underline{r}) \nabla \theta(\underline{r}) d^3 \underline{r} \right|^2 \quad (2.13)$$

where N is the total number of atoms.

Then, ignoring the constant term in front this reduces to:-

$$| \langle i | \nabla | f \rangle |^2 = a(\Delta k) \sigma_{if} \quad (2.14)$$

where σ_{if} is the square of the atomic matrix element calculated from the APW and:-

$$a(\Delta k) = \frac{1}{N} \sum_{m,n} e^{i \Delta k \cdot (\underline{R}_m - \underline{R}_n)} \quad (2.15)$$

is the familiar interference function that occurs in diffraction theory.

This allows three regimes to be distinguished:-

(i) Ordered systems at low photon energies ($\hbar\omega < 40$ eV)

Here, $a(\Delta k)$ is a series of delta functions located at the reciprocal lattice vectors, $\underline{G} = \underline{G}_1, \underline{G}_2$ etc. This gives the well known constraint that for ordered systems interband transitions between Bloch functions cannot take place unless:-

$$\underline{k}' = \underline{k} + \underline{G} \quad (2.16)$$

Now at low photon energies, Δk (ie:- q) is small and the spiky nature of $a(q)$ is a strong influence, there being few bands in the energy band diagram of $E - \underline{k}$ between which transitions can occur. Hence, the electron distribution ($N(E, \omega)$) is a complex function of the band structure; peaks appear and move as the frequency, ω , is varied. Low energy, angle resolved photoemission is a powerful probe of the $E - \underline{k}$ dispersion relation in crystalline materials.

(ii) Ordered systems at high photon energies ($\hbar\omega \sim 1000$ eV)

Now, Δk (ie: q) is large and $a(q)$ tends to a continuum. The uncertainty in \underline{k} due to final state scattering is significant hence:-

$$N(E, \omega) \sim \sum_{if} \sigma_{if} \delta(E_f - E_i - \hbar\omega) \delta(E - E_f) \sim N_V(E - \hbar\omega) \quad (2.17)$$

This is the so called "XPS limit". The measured spectrum reflects the density of initial states; the disadvantage is the poor resolution resulting from the high kinetic energies of the electrons.

(iii) Highly disordered systems (all photon energies)

For highly disordered systems (eg: liquids), a single value of k is not a good description of the electron states. The $a(q)$ function is continuous and may be treated as approximately constant. Then the term $|\langle i | \nabla | f \rangle|^2$ is approximately constant and equation (2.8) provides a good description, the measured spectrum reflects initial density of states information modulated by the effects of matrix elements. It is this interpretation that applies to the data analysis of this work.

The term σ_{if} appears in all cases although it has no effect at a fixed photon energy. It allows trends to be explained in photo-emission spectra, eg: the 4d band of silver is strong at low photon energies but then dies away as the photon energy is increased. Some calculations of σ_{if} are available as an example (Kennedy and Manson, 1972).

The term $T_{eff}(E)$, the effective probability of an electron reaching the surface without scattering then penetrating the surface barrier, is also important. Two main processes may be identified (in scattering). The first is electron-electron scattering in which the energy exchange may be from zero to $\hbar\omega$ eV. It is strongly energy dependent as shown by the form of the electron inelastic mean free path curve (Seah and Dench, 1978). The second is electron-ion scattering where the energy exchange is very low (≈ 0.04 eV) and the process is usually taken as elastic. For modelling the transmission

process, a semi-classical picture is normally used. In the following sections an analytical form is given for the various scattering processes and the transmission function.

2.4 The Three Step Model of Photoemission

In order to extract the optical density of states from the photoemission data, it is necessary to model the photoemission process, the scattering of the excited electrons and the transmission function. Although first principles quantum mechanical calculations have been reported (Mahan, 1970, Schaich and Ashcroft, 1970, Caroli et al, 1973) including surface and matrix element effects, no applications have been made to real systems because of the complexity of the methods. The application of such calculations to disordered systems is in practice impossible as each is evaluated for a well defined crystal lattice, although the method of Schaich and Ashcroft can be approximated to include structural disorder. The method of Pendry (1976) was applied to the photoemission curve from a copper single crystal. Thus an interpretation of photoemission spectra of liquid metals can only be given by the three step model of Berglund and Spicer (1964) in which the photoemission process is viewed as three sequential steps:

- (i) Optical absorption of the incident photon and the associated photoexcitation of the initial state electron.
- (ii) Transport of this electron towards the surface during which it may undergo scattering processes.
- (iii) Escape of the electron from the surface.

In the following sections the three step model is explained and developed to include higher order inelastic scattering processes (Auger, tertiary and plasmon loss). This model is the same as that described by Wotherspoon (1978) and a résumé is given here for completeness.

2.5 The Unscattered Primary Distribution of Photoemitted Electrons

(i) Optical absorption and photoexcitation.

If a photon flux of angular frequency ω is incident upon a sample surface, then the number of photons absorbed per unit area between a distance x and $(x + dx)$ of the surface is:-

$$dI(x, \omega) = -\alpha I(x, \omega) dx \quad (2.18)$$

so that:-

$$I(x, \omega) = I_0(\omega) e^{-\alpha x} \quad (2.19)$$

where $I_0(\omega)$ is the total flux penetrating the surface and $\alpha(\omega)$ is the absorption coefficient (absorption per unit length). Assuming each absorbed photon gives rise to an excited electron, the spatial distribution of photoexcited electrons is given by:-

$$G(x, \omega) = -\frac{dI(x, \omega)}{dx} = I_0 \alpha e^{-\alpha x} \quad (2.20)$$

The internal energy distribution of electrons must be found. This is the number of electrons excited to an energy E which are created within a distance x to $(x + dx)$ of the surface. It is:-

$$G(E, x, \omega) = G(x, \omega) G(E) \quad (2.21)$$

where $G(E)$ is the fractional number of electrons excited from the valence band to a final conduction band state of energy E . Following Krolikowski (1967), this function may be written as:-

$$G(E) = \frac{N_C(E) N_V(E - \hbar\omega)}{E_F + \hbar\omega} \quad (2.22)$$

$$\int_{E_F} N_C(E) N_V(E - \hbar\omega) dE$$

This assumes that the matrix elements are constant and the

transitions are non-direct (ie:- conservation of \underline{k} is not an important transition rule). Combining (2.21), (2.22) and (2.20) then gives:-

$$G(E, x, \omega) = \frac{N_C(E) N_V(E - \hbar\omega) I_0 \alpha e^{-\alpha x}}{\int_{E_F}^{E_F + \hbar\omega} N_C(E) N_V(E - \hbar\omega) dE} \quad (2.23)$$

This is the internal distribution of photoexcited electrons and for a given ω is proportional to the product of the initial and final densities of states, $N_C(E) N_V(E - \hbar\omega)$.

(ii) Escape from the surface.

Assuming that the photocreation of electrons is isotropic, then the condition for escape from the surface is:-

$$\frac{m(Vg^n)^2}{2} > E_F + \phi \quad (2.24)$$

where Vg^n is the group velocity of the electrons normal to the surface, m is the electron mass, E_F is the Fermi energy and ϕ is the work function. This gives:-

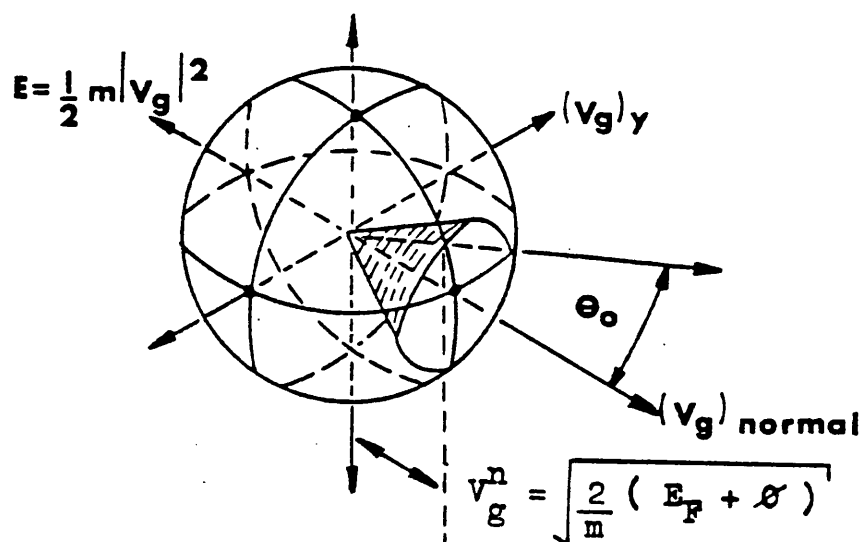
$$Vg^n > \sqrt{\frac{2}{m} (E_F + \phi)} \quad (2.25)$$

This restriction allows only a small fraction of the photoelectrons to escape. The situation is shown in figure 2-2a where the condition of (2.25) is represented by the escape cone lying within the total emission sphere. The proportion of electrons which escape is the area of the escape cone which intersects the emission sphere; it is called the semi-classical escape function and is given by:-

$$T_f(E) = \frac{1}{2} (1 - \cos \theta_0) \quad (2.26)$$

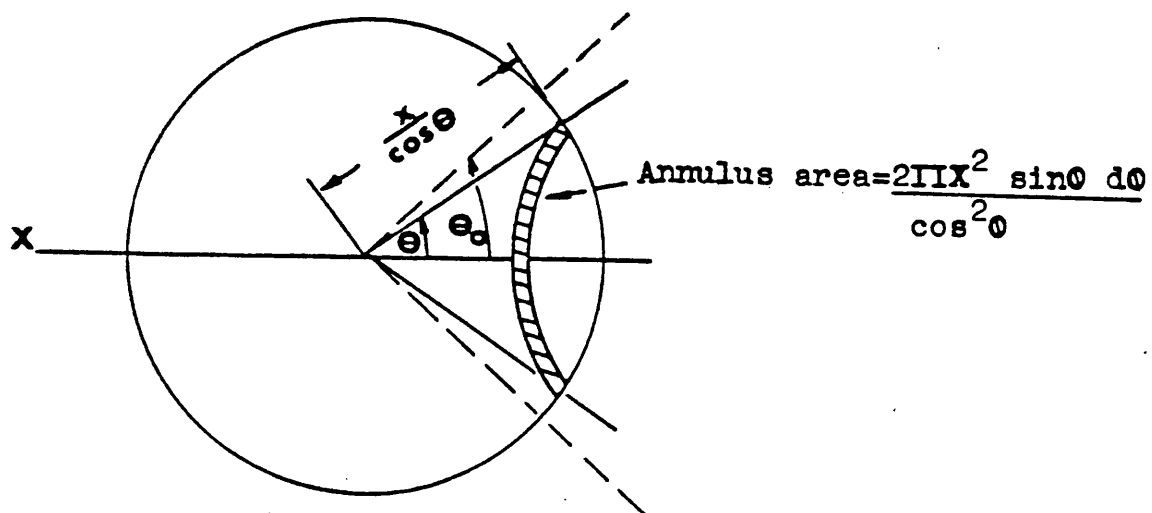
and substituting for θ_0 gives:-

(a)



The escape cone

(b)



The geometry of the escape process

Figure 2-2

$$T_f(E) = \frac{1}{2} \left[1 - \sqrt{\frac{E_F + \phi}{E_F + E}} \right] \quad (2.27)$$

(iii) Transport to the surface.

Let the photoexcitation process occur at a point $r_0(x_0, y_0, z_0)$ and let the electron travel to the surface at an angle θ with respect to the surface normal (defined to be in the x direction). The distance travelled is then:-

$$|x - x_0| = \frac{x}{\cos \theta} \quad (2.28)$$

during which the electron may collide with ion cores (taken to be elastic) or with conduction electrons, which will effect the emitted distribution of electrons. Defining an energy dependent inelastic mean free path as $L(E)$, the probability of travelling to the surface without scattering may be written as:-

$$P(x, \omega) = e^{-\frac{|x - x_0|}{L(E)}} = e^{-\frac{x}{L \cos \theta}} \quad (2.29)$$

A diagram of this process is shown in figure 2-2(b). The propagation of electrons between the angle θ and $(\theta + d\theta)$ is shown relative to the emission sphere so that the probability that these electrons escape, $P(\theta)$, is the ratio of the hatched annulus to the area of the sphere:-

$$P(\theta) = \frac{1}{2} \sin \theta \, d\theta \quad (2.30)$$

and therefore the probability that the photoexcited electron travels to the surface without scattering and escapes is given by the multiple of (2.29) and (2.30) integrated over the escape cone:-

$$F(E, x) = \int_0^{\theta_0} \frac{1}{2} \sin \theta \, e^{-\frac{x}{L \cos \theta}} d\theta \quad (2.31)$$

The emitted unscattered or primary distribution, $N_o(E, \omega)$, which is the number of electrons which are photoexcited to an energy E , travel to the surface and escape without scattering inelastically, is then given by the multiple of (2.23) and (2.31):-

$$N_o(E, \omega) = \frac{I_o \alpha e^{-\alpha x} N_c(E) N_v(E - \hbar\omega)}{E_F + \hbar\omega} \int_{E_F}^{\theta} \frac{1}{2} \sin \theta e^{-\frac{x}{L \cos \theta}} d\theta \quad (2.32)$$

After integrating this may be written as:-

$$N_o(E, \omega) = G(E) T_{eff}(E) \quad (2.33)$$

where $T_{eff}(E)$ is the effective threshold function and has the form:-

$$T_{eff}(E) = T_f(E) C[\alpha L, T_f] \left(\frac{\alpha L}{\alpha L + 1} \right) \quad (2.34)$$

and:-

$$C[\alpha L, T_f] = \left[\frac{\alpha L + 1}{\alpha L} - \frac{\alpha L + 1}{2T_f(\alpha L + 1)^2} \ln \left(\frac{\alpha L + 1}{\alpha L + 1 - 2\alpha T_f} \right) \right] \quad (2.35)$$

2.6 The Energy Distribution of Inelastically Scattered Electrons

(i) The inelastic mean free path.

The total inelastic mean free path, $L(E)$, may be written as:-

$$\frac{1}{L(E)} = \frac{1}{l_e(E)} + \frac{1}{l_{pl}(E)} \quad (2.36)$$

where $l_e(E)$ and $l_{pl}(E)$ represent the energy dependent mean free paths associated with the inelastic scattering processes of electron-hole pair creation and plasmon creation respectively.

The mean free path $l_e(E)$ has been calculated by Spicer and

Krolikowski (1970) using a first order perturbation expansion:-

$$\begin{aligned}
\ell_e(E) = L_0 & \frac{\sqrt{E}}{2E_F - E} \int_{E_F}^{E_V^0} d(E_V^0) \int_{E_F - E_V^0}^{\frac{1}{2}(E - E_V^0)} N_V(E_V^0) N_C(E - \Delta E) N_C(E_V^0 + \Delta E) d(\Delta E) \\
& \hspace{15em} (2.37)
\end{aligned}$$

where L_0 is a normalisation constant, fixing the value of ℓ_e at a particular final state energy E (8.6 eV above E_F), ΔE is the energy lost in the collision and E_V^0 represents the initial state energy.

The mean free path for the scattering of electrons through the creation of bulk plasmons has been calculated by Quinn (1962) using a self energy approach as:-

$$\ell_{pl}(E) = \frac{2a_0 E(p)}{\omega_p} 2\pi \left[\frac{(p_0^2 + 2m\omega_p)^{\frac{1}{2}} - p_0}{(p - [p^2 - 2m\omega_p]^{\frac{1}{2}})} \right]^{-1} \quad (2.38)$$

where p and p_0 are the momenta of the photoexcited electron with respect to the bottom of the valence band and Fermi level respectively, $E(p)$ is the kinetic energy of the electron before the scattering process, ω_p is the plasmon frequency and a_0 is the Bohr radius. Combining (2.36), (2.37) and (2.38) then allows the total inelastic mean free path to be evaluated.

(ii) The emission of electrons which have scattered once inelastically.

The transition probability for the scattering of electrons via the creation of electron-hole pairs may be written as:-

$$P = \frac{2\pi}{\hbar} | \langle \underline{k}', \underline{k}_0 | H' | \underline{k}, \underline{k}_1 \rangle |^2 \delta(E' - E - E_1 + E_0) \quad (2.39)$$

where an electron in a state (E', \underline{k}') is scattered to a state (E, \underline{k}) by the creation of an electron in a state (E_1, \underline{k}_1) and a hole in the state (E_0, \underline{k}_0) , the δ function conserves energy in the process and H' is the interaction Hamiltonian. The matrix element is assumed to be independent of the crystal momentum because the optical transitions are considered to be non-direct. Then the probability per second of an electron of energy E' scattering to an energy E via the creation of an electron-hole pair is given by:-

$$p_S(E', E) = N_c(E) \frac{2\pi}{h} |\langle H' \rangle|^2 \int_{-(E'-E)}^0 N_v(E_0) N_c(E_0 + E' - E) dE_0 \quad (2.40)$$

So the scattering rate for an electron of energy E' is simply:-

$$p_S(E') = \int_0^E p_S(E', E) dE \quad (2.41)$$

so that the distribution function for secondary electrons, $S(E', E)$ of energy E produced via electron-hole creation by unscattered primary electrons of energy E' can be written as:-

$$S(E', E) = \frac{2p_S(E', E)}{p_S(E')} = \frac{2N_c(E) \int_{-(E'-E)}^0 N_v(E_0) N_c(E_0 + E' - E) dE_0}{\int_0^E dE' N_c(E) \int_{-(E'-E)}^0 N_v(E_0) N_c(E_0 + E' - E) dE_0} \quad (2.42)$$

The factor 2 signifies that two secondary electrons are produced.

The contributions to the scattering probability from the spatial

position of the scattering process with respect to the surface are now determined. If the initially photoexcited electron has a final energy E' at a distance χ from the surface, the probability of scattering isotropically, $P_{\text{scat}}(E', E, \chi, \theta)$, to an energy E after travelling a distance r at an angle θ' is then given by:-

$$P_{\text{scat}}(E', E, \chi, \theta) = S(E', E) \frac{e^{-r/l'_e}}{l'_e} \frac{1}{2} \sin \theta' \quad (2.43)$$

where $l'_e = l_e(E')$ is given by (2.37). The external secondary distribution, $N_1(E, \omega)$ can now be found by multiplying (2.43) by the initial distribution of unscattered electrons, $G(E', \chi, \omega)$ and by the probability of escape, $F(E, \chi)$, after the scattering event. This gives after performing the integrations over the appropriate space:-

$$N_1(E, \omega) = T_{\text{eff}}(E) \int_E^{\hbar\omega} S_{ee}(E', E) G(E') C_2(\alpha, l'_e, L) dE' \quad (2.44)$$

$$\text{where:- } C_2 = \frac{1}{2} \left[\frac{l'_e}{L} \ln \left(1 + \frac{L}{l'_e} \right) + \frac{1}{\alpha L} \ln (1 + \alpha L) \right] \quad (2.45)$$

The C_2 function determines the fraction of the initial electron flux modified in energy as a consequence of the scattering mechanism under study.

(iii) Auger electron emission (see also section 3.9)

The Auger process is caused by the de-excitation of the valence band hole left after the photoexcitation process, in which a valence electron may recombine with this hole, the excess energy being taken up in the emission of an Auger electron from the valence band. Kane (1967) has derived the distribution function $S_{\text{he}}(E', E)$ which represents the production of Auger electrons at an energy E above the Fermi level produced by an initial state hole of energy E' :-

$$S_{he}(E', E) = N_c(E) \int_0^{\frac{(E+E')/2}{(E+E')/2}} N_c(E_0) N_v(E + E' - E_0) dE_0$$

$$- \int_0^{E'} dE'' N_c(E'') \int_{E''+E'}^0 dE_0 N_v(E_0) N_v(E'' + E' - E_0) \quad (2.46)$$

The external distribution of Auger electrons, $N_2(E, \omega)$, is then almost identical to (2.44) except that the function $G(E')$ must be replaced by $G(E' + \hbar\omega)$ where E' is the energy of the initial hole and $\hbar\omega$ the photon energy:-

$$N_2(E, \omega) = T_{eff}(E) \int_{-\hbar\omega}^E S_{he}(E', E) G(E' + \hbar\omega) C_2(\alpha, l_H, L) dE' \quad (2.47)$$

where $l_H(E)$ is the associated mean free path for the hole-hole scattering process, in which the Auger mechanism is modelled (where the hole created at (E', \underline{k}') is scattered to (E_1, \underline{k}_1) through recombination creating an electron hole pair at (E, \underline{k}) and (E_0, \underline{k}_0)) given by:-

$$l_H(E) = L_0 \frac{\sqrt{E'}}{\int_0^{E_H} dE N_c(E) \int_0^{(E_H-E_1)/2} dE_1 N_v(E_1) N_c(E_1 - E_0)} \quad (2.48)$$

where L_0 is assumed the same for both electron-electron and hole-hole scattering (Kane, 1967). C_2 is given by:-

$$C_2(\alpha, l_H, L) = \frac{1}{2} \left[\frac{l_H}{\alpha} \ln(1 + \alpha l_H) + \frac{L}{l_H} \ln(1 + \frac{l_H}{L}) \right] \quad (2.49)$$

(iv) The scattering of electrons via plasmon creation.

If the photon energy exceeds the plasmon threshold, photoexcited electrons may undergo plasmon creation and so contribute to the inelastically scattered background. The external distribution of such electrons, $N_3(E, \omega)$, has the familiar form:-

$$N_3(E, \omega) = T_{\text{eff}}(E) \int C_2(\alpha, l_{pl}, L) G(E') S_{pl}(E) dE' \quad (2.50)$$

where:-

$$C_2(\alpha, l_{pl}, L) = \frac{1}{2} \left[\frac{1}{\alpha l_{pl}} \ln(1 + \alpha l_{pl}) + \frac{L}{l_{pl}} \ln\left(1 + \frac{\alpha l_{pl}}{L}\right) \right] \quad (2.51)$$

The function $S_{pl}(E)$ is the plasmon distribution function which is the probability of an electron being scattered from an energy E' to E via the creation of a plasmon. This may be represented by a δ function conserving energy but because the plasmon has a finite width a Gaussian distribution is more appropriate:-

$$S_{pl}(E) = \frac{1}{1.77} \int_{\hbar\omega_p}^{\hbar\omega} e^{-(E' - \hbar\omega_p)^2} dE' \quad (2.52)$$

This has been normalised to unity with the plasmon full width at half maximum being 1.0 eV.

(v) Higher order losses.

At photon energies above approximately 11.0 eV, the background of scattered electrons is the dominant feature. To explain this it may be necessary to consider second order electron-hole pair creation mechanisms. The contributors to this will be the Auger, secondary and plasmon loss electrons before they escape. The analysis will be identical to that of the first order losses as described previously and therefore the external distribution of tertiary electrons,

$N_4(E, \omega)$, can be written as:-

$$N_4(E, \omega) = T_{\text{eff}}(E) \int_{E_F}^{E_F + \hbar\omega} S_{ee}(E', E) G^*(E') C_2(\alpha, l'_e, L) dE' \quad (2.53)$$

where:-

$$C_2(\alpha, l'_e, L) = \frac{1}{2} \left[\frac{1}{\alpha L} \ln(1 + \alpha L) + \frac{l'_e}{L} \ln\left(1 + \frac{L}{l'_e}\right) \right] \quad (2.54)$$

The distribution function $G^*(E')$ is modified in (2.53) since it must include the secondary, Auger and plasmon loss electrons, therefore:-

$$G^*(E') = \frac{1}{T_{\text{eff}}(E)} \sum_{i=1}^3 N_i(E, \omega) \quad (2.55)$$

(vi) Plasmon decay.

Supplementary to the analysis of Wotherspoon (1978), a term was included to allow for the effects of plasmon decay which Chung and Everhart (1977) showed was significant for aluminium. The distribution function was written as:-

$$N_5(E, \omega) = T_{\text{eff}}(E) \int_{E_F - 2\text{eV}}^{E_F + 2\text{eV}} G(E_{pl}, E) S_{pl}(E) \frac{N_3(E, \omega)}{T_{\text{eff}}} dE \quad (2.56)$$

where:-

$$G(E_{pl}, E) = \frac{N_c(E) N_v(E - \hbar\omega_p)}{E_F + E_{pl}} \int_{E_F}^{E_F + E_{pl}} N_c(E) N_v(E - \hbar\omega_p) dE \quad (2.57)$$

is the fractional number of electrons excited from the valence band to the conduction band and the term $N_3(E, \omega)/T_{\text{eff}}$ was included to represent the number of plasmons created. E_{pl} is the energy of the plasmon oscillation.

2.7 The Total Energy Distribution of Emitted Electrons

In units of electrons per absorbed photon per unit energy interval, the total energy distribution, $N(E, \omega)$, is the sum of the components derived previously, ie:-

$$N(E, \omega) = \sum_{i=0}^5 N_i(E, \omega) \quad (2.58)$$

This enables the number of electrons emitted per absorbed photon to be written as:-

$$Y(\omega) = \int_{\phi}^{\hbar\omega-\phi} N(E, \omega) dE \quad (2.59)$$

This quantity is called the quantum yield.

2.8 The Calculation of an Optical Density of States

The theory of sections 2.5 to 2.7 has been collected into a computer program listed in appendix A with the input parameters necessary for the calculation. The method of calculating an optical density of states (so called because in the derivation the matrix elements have been assumed constant, hence any density of states extracted from photoemission data will be an effective or optical density of states (ODS)) lies in initially estimating a form for the scattered background on the experimental photoemission curve. This enables a trial ODS to be formed which is then used in the program to calculate an energy distribution curve (EDC) which is compared to the original data. The calculation of an ODS then becomes an iterative process, changes being made to the trial ODS and input parameters to obtain the best fit between the experimental and calculated EDCS. When the best fit is achieved, the input ODS is then taken to be that of the sample under study.

CHAPTER 3

EXPERIMENTAL

The joint techniques of photoelectron spectroscopy and Auger electron spectroscopy demand the use of ultra high vacuum technology and low electrical signal detection. The application to the liquid phase of metals and alloys introduces problems of sample containment and preparation. This chapter describes the experimental apparatus, the preparation of the samples and all the signal measuring techniques employed in this study.

3.1 Introduction

Photoelectron and Auger electron spectroscopy involve the detection of electrons emitted from the first few atomic layers of the sample under study. In consequence, all experiments must be performed under ultra high vacuum (UHV) conditions. This follows from the kinetic theory of gases which shows that the average number, \bar{n} , of gas molecules colliding with a unit surface per second is given by:-

$$\bar{n} \approx 3.5 \times 10^{22} \frac{P}{\sqrt{MT}} \text{ s}^{-1} \text{ cm}^{-2} \quad (3.1)$$

where P is the gas pressure in torr, T the absolute temperature and M the molecular weight of the molecules. Taking M to be 28 for air and assuming that a molecule sticks on its first impact, then (3.1) shows that at 5×10^{-10} torr, approximately 100 minutes elapse before the surface becomes contaminated by a monolayer, hence UHV conditions are necessary to ensure sufficient time for performing an experiment.

Two vacuum systems were used in this study and these are now described beginning with the spectrometer used for measurements at helium I and neon I line energies.

3.2 The Ultraviolet Photoelectron Spectrometer: Vacuum Chambers and Pumping System

The spectrometer shown in figure 3-1 and plate 3-1 was designed to accommodate the properties of corrosivity and high vapour pressures of the samples at their melting points. The separation of the system into two chambers allowed the pouring process for sample preparation to be kept separate from the source chamber in which the measurements were made. The chambers were manufactured from stainless steel grade 321 and all the joints were argon arc welded. Flanges were sealed using

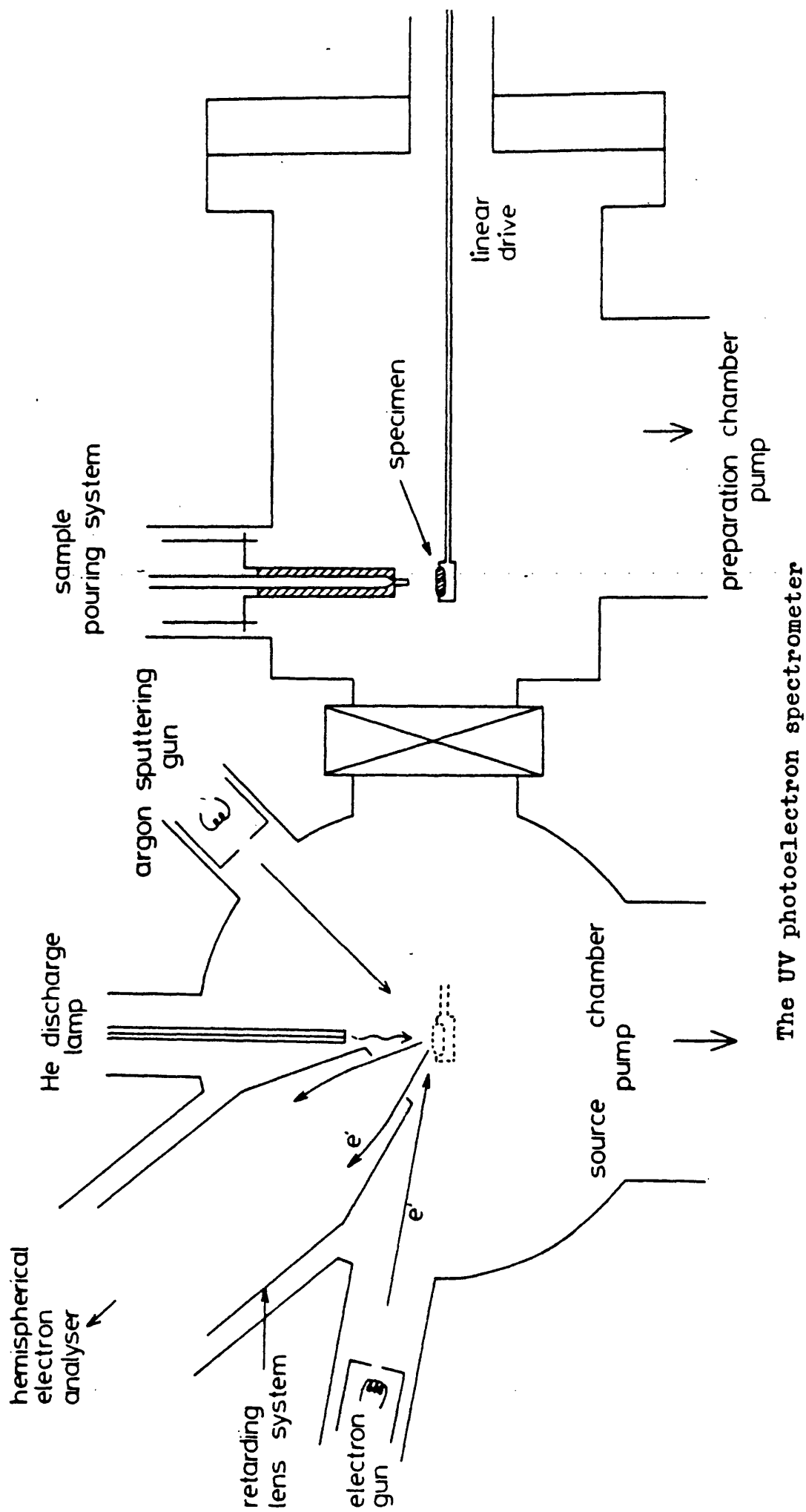
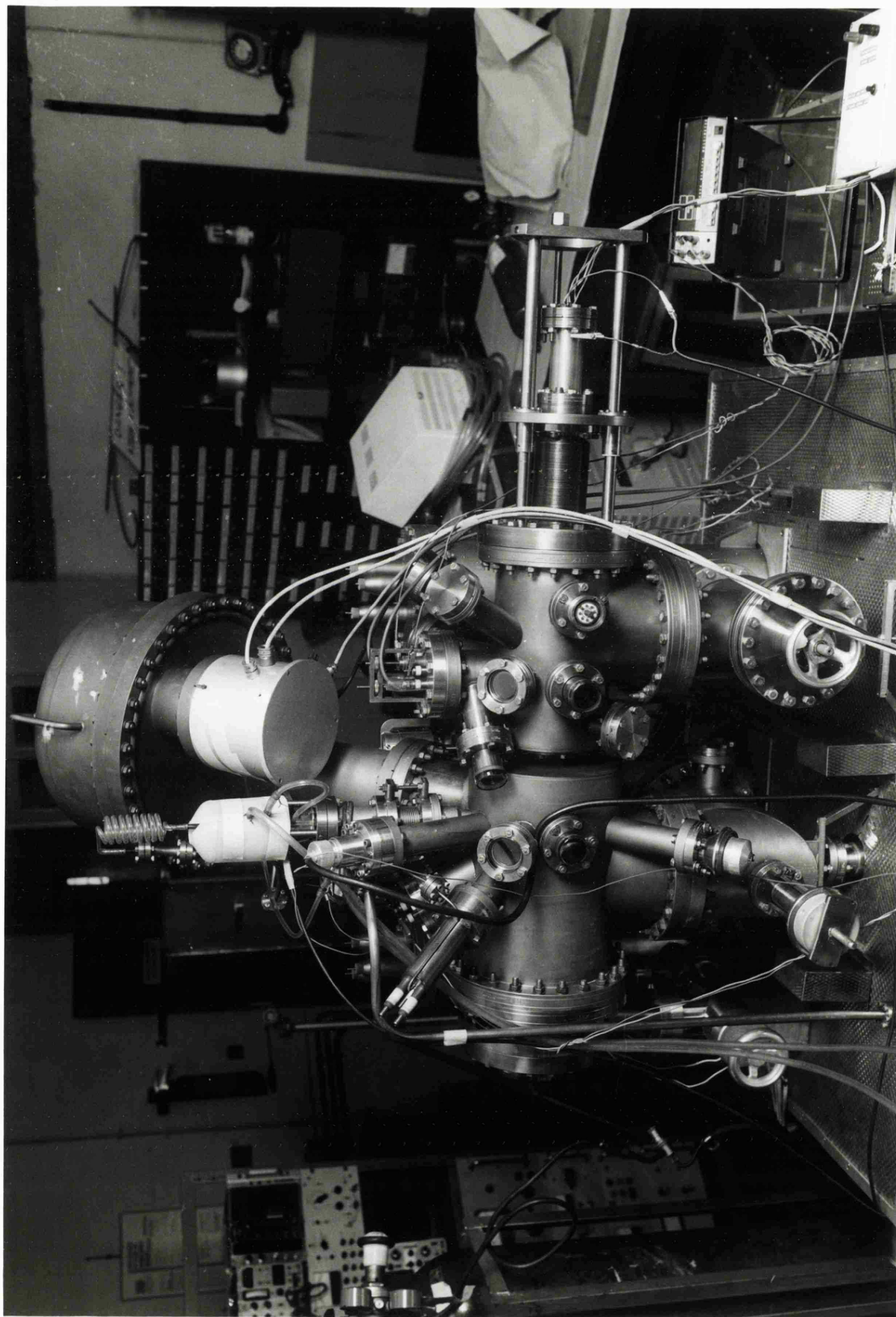


Figure 3-I

Plate 3-I

The ultraviolet photoelectron spectrometer



standard knife edge and oxygen free copper gasket seals.

Pumping of the chambers was achieved by two Edwards EO4 oil vapour diffusion pumps charged with Santovac 5 oil and fitted with liquid nitrogen traps manufactured by Leisk Engineering Ltd. Backing pressures were provided by two Edwards ES 200 rotary pumps mounted on anti-vibration pads. Automatic devices were incorporated to minimise damage in the event of power cuts or water flow failures. An Edwards EO2 oil vapour diffusion pump was used to provide high vacuum pumping of the discharge light source.

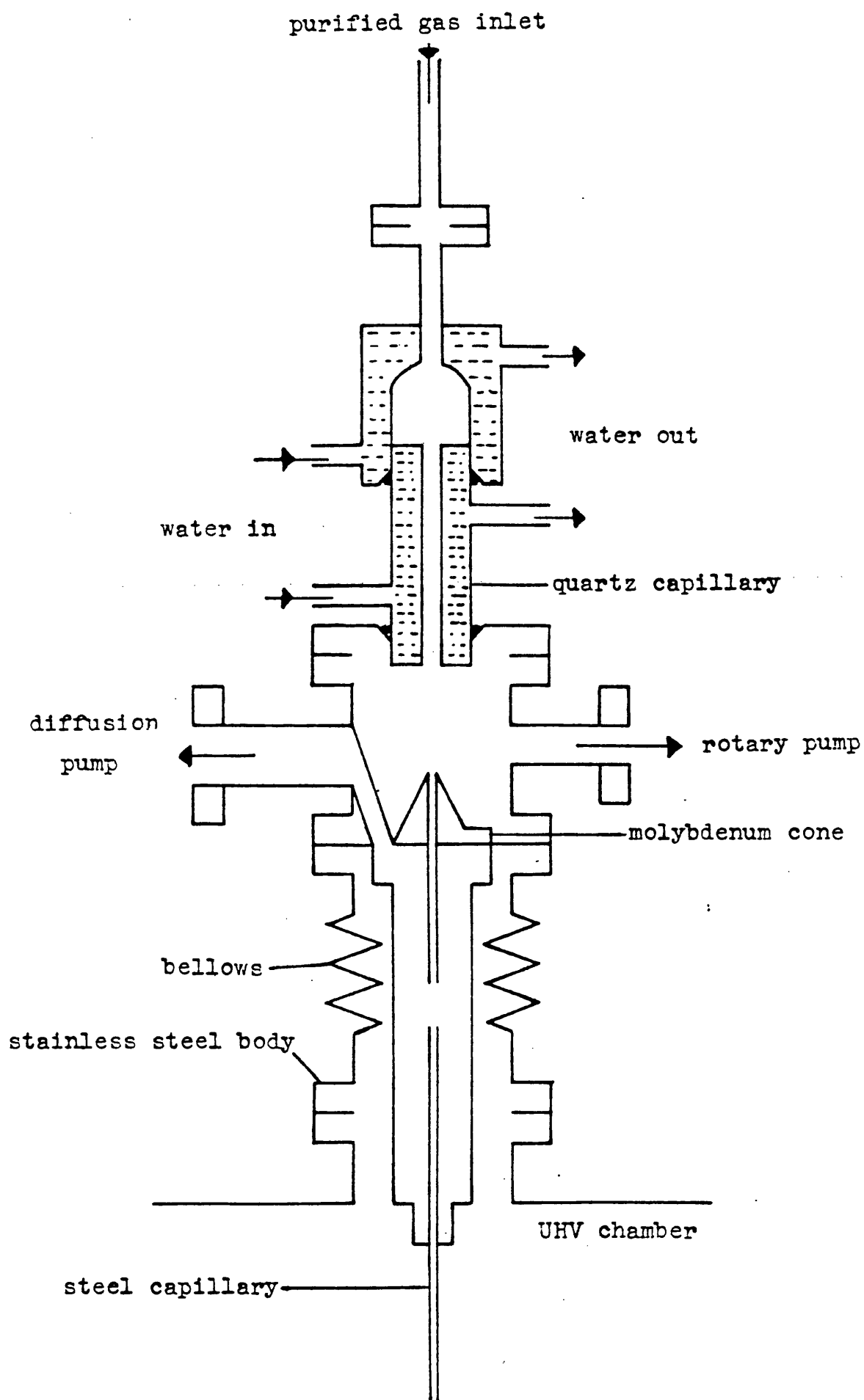
Pressures on the high vacuum side were monitored by three Bayard-Alpert ionization gauges linked to three Vacuum Generators (VG) IGP3 ionization gauge controllers. Two VG pirani gauges monitored the backing pressures.

The base pressure of the system (5×10^{-10} torr) was obtained after approximately three days pumping from atmospheric pressure inclusive of baking the system to 180°C for up to 36 hours. All filaments were outgassed at the termination of the bakeout.

A VG quadrupole (Q4) mass spectrometer showed the residual atmosphere to be composed mainly of nitrogen with smaller quantities of carbon dioxide, water vapour and certain hydrocarbons (CH_3 , C_3H_3 , C_3H_5), the latter being the break down products remaining from solvents used for cleaning. Very small quantities of oxygen and carbon were found present. The Q4 head also allowed leak testing of the system using helium as the tracer gas.

3.3 The Ultraviolet Light Source

Figure 3-2 shows schematically the light source used for the photoemission experiments carried out with the system described in



The rare gas discharge UV light source

Figure 3-2

section 3.2. Laboratory grade helium or neon was purified by passing the gas through a liquid nitrogen cooled activated alumina trap before entering the lamp through a leak valve. The discharge was struck across a water cooled quartz capillary tube, 80 mm long with 2.0 mm internal diameter, between a water cooled stainless steel cathode and stainless steel earthed lamp body. To maintain ultra high vacuum in the source chamber with one torr before the leak valve, differential pumping was used. The gas was pumped off by an Edwards ED100 rotary pump after the quartz capillary tube and by the ED2 diffusion pump from between the sections of the final stainless steel capillary which was split by a gap of 2.0 cm into two lengths of 4.0 cm and 9.0 cm, each having an inside diameter of 1.0 mm. The vacuum ultraviolet radiation was generated in the low pressure region (~ 0.1 torr) between the first and second capillaries. To focus the electron beam onto the axis of the latter and to protect it from the heating effect of the electron beam a molybdenum cone was fitted. For high yield the stainless steel capillary was internally polished with three grades of diamond paste (14, 6 and $1\mu\text{m}$) until it appeared bright to the eye and then all sections were assembled so that there was a clear line of sight through the lamp.

Discharge lines commonly used in photoelectron spectroscopy are listed in table 3.1 and the operating conditions employed for the lamp in this work are summarized in table 3.2. Normally the lamp was run in the helium I mode corresponding to an intense emission line at 21.22 eV photon energy and half width 40 meV (Samson, 1967). Using neon under the same conditions neon I radiation was obtained (a doublet at 16.67 and 16.85 eV). With care, a second series of lines, the brightest of which occurs at 40.81 eV (helium II), could be excited in singly ionized helium. To produce the helium II mode the lamp was first operated in the helium I mode giving its purplish-white discharge

Discharge Conditions	Transition	Wavelength (nm)	Energy (eV)	Approx. Intensity
~ 1.0 Torr	HeI 2p - 1s	58.435	21.217	$I_0 \sim 10^{10} - 10^{11} s^{-1}$
	HeI 3p - 1s	53.705	23.086	0.02 I_0
~ 0.5 Torr	HeII 2p - 1s	30.378	40.812	0.1 - 0.5 ($I_0/4$)
~ 0.5 Torr	NeI $3s(^3/2) - 2p^6$	74.372	16.670	0.4 I_1
	$3s(^1/2) - 2p^6$	73.590	16.848	$I_1 \sim 10^{10} - 10^{11} s^{-1}$
~ 0.1 Torr	NeII $2s2p(^6/2) - 2p^5(^1/2)$	46.239	26.813	0.05 I_1
	$2s2p(^6/2) - 2p^5(^3/2)$	46.073	26.910	0.1 I_1
~ 0.5 Torr	ArI $4s(^3/2) - 3p^6$	106.666	11.623	0.07 I_2
	$4s(^1/2) - 3p^6$	104.822	11.828	I_2
Impurities	O I	130.22	9.52	
	N I	113.41	10.93	
	H I (Ly α)	121.57	10.2	

Atomic line radiation important in photoelectron spectroscopy
Table 3.I

	Pressure in lamp line (Torr)	Pressure in source chamber (Torr)	Discharge current (mA)	Cathode voltage (V)
Helium I 21.22eV	5×10^{-6}	1×10^{-8}	70	800
Helium II 40.81eV	6×10^{-7}	3×10^{-9}	100	800
Neon I 16.67eV 16.85eV	5×10^{-6}	1×10^{-8}	70	800

Optimum conditions for discharge lamp
Table 3.2

colour in the quartz capillary. The leak valve was then slowly closed while simultaneously the discharge current was increased. As the pressure fell the colour changed to a bluish-green tint. The lamp became more stable in the helium II mode the longer it was run in that state. This was probably due to lower impurity levels caused by out-gassing of the walls in the discharge region by the higher energy electron beam.

3.4 The Power Supply for the Lamp

The supply was essentially provided by a transformed output rectified by a diode bridge circuit and subsequently smoothed. The lamp was series connected to the supply through a 25 k Ω ballast resistor chain. To initially strike a discharge took about 3 kV, after which the voltage across the lamp fell to about 800 V as the resistance of the gas lowered. The bulk of the voltage was then dropped across the resistor chain which then had to dissipate over 200 W necessitating the incorporation of forced air cooling.

3.5 The Argon Sputter Ion Gun

A VG model AG 2 argon sputter ion gun was mounted on the source chamber for in situ cleaning of samples, controlled by an AGS2 unit. Experience gained showed that lithium and the lithium based alloys could be prepared in a clean condition but the silver-germanium system could not be poured and needed ion bombardment cleaning. A typical cleaning cycle would need an argon (99.999% pure) gas pressure of 10^{-5} torr, a beam energy of 5 KeV and a focused beam current of 50 μ A for periods of up to two hours.

3.6 The Electron Energy Analyser

The electron energy analyser used for this work was a Leybold-

Heraeus design, model EA 10/100. The major consideration, for this series of experiments, was the choice of an analyser whose performance would not be impaired by contamination caused by evaporation from the samples. The chosen analyser featured a five element electron input lens incorporating an axial stop which prevented impurities from reaching the hemispheres. The basic layout of the analyser is shown schematically in figure 3-3. The analyser could be operated in one of two modes giving constant relative resolution or constant absolute resolution using retardation in the input lens system. The lens was designed using optimised computer ray tracing techniques so that the sample area examined remained constant throughout the duration of an energy scan. It was also highly desirable to achieve constant focusing and magnification throughout the energy range and under all retarding conditions which necessitated the use of a relatively complex lens. Such conditions cannot be achieved by a simple three element lens or a retarding slit system.

The transmission characteristics of the analyser obeyed the following equation, based on Liouville's theorem:-

$$E \times \Omega \times F = \text{a constant} \quad (3.2)$$

where E is the electron energy, Ω the acceptance angle and F the area.

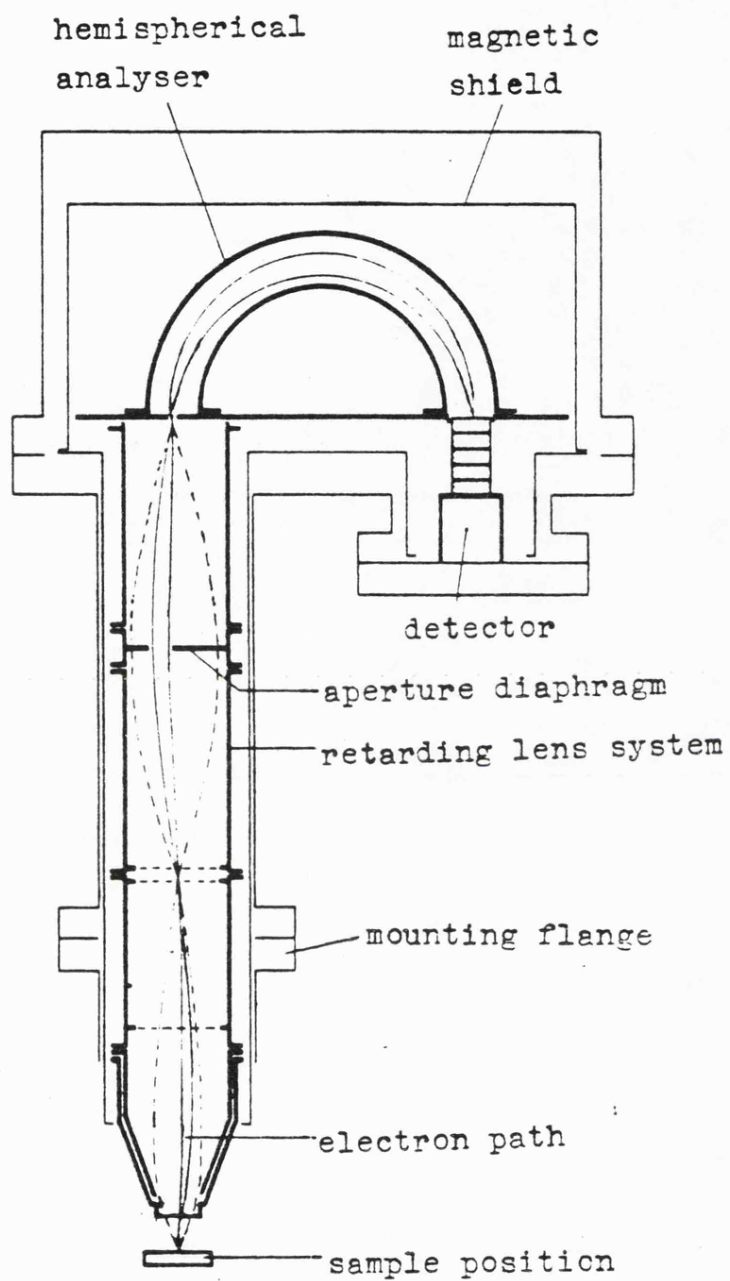
For optimum performance, all the electrons emitted from the sample and selected by the input system were injected into the analyser hemispheres, so that:-

$$E_{kin} \times F_S \times \Omega_S = E_o \times F_o \times \Omega_o \quad (3.3)$$

where E_{kin} = kinetic energy of the emitted electrons,

F_S = viewed area of sample,

Ω_S = acceptance angle at sample,



The electron energy analyser

Figure 3-3

E_o = pass energy of analyser hemispheres,

F_o = slit area,

Ω_o = solid angle of injection into the analyser.

For this lens, the magnification was defined to be an instrumental constant, ie:-

$$\frac{F_s}{F_o} = \text{constant} = 2 \quad (3.4)$$

This meant that the analysed area was twice the slit size. All electrons accepted by the lens were injected with the correct trajectory into the analyser. In effect this meant that the luminosity of the hemisphere system was defined in the input lens, or:-

$$\Omega_o = \text{constant}. \quad (3.5)$$

The étendue of the hemisphere system is defined as the product of the entrance area and entrance solid angle. Thus the étendue of the system has been defined:-

$$F_o \times \Omega_o = \text{constant}. \quad (3.6)$$

This allowed changes of resolution and transmission function to be performed electrically in the lens system without changes of slit size in the hemispheres and maintained a constant analysed area.

For a given slit size and shape the resolution in the hemispheres was a constant fraction of the pass energy:-

$$\Delta E = p \times E_o \quad (3.7)$$

where ΔE is the effective resolution in eV and E_o is the transmission (pass) energy (eV). The relative resolution, p , was an instrumental constant and was 1% for the used hemispheres with standard slits (20 mm x 1 mm).

The analyser was always used in the mode where it gave constant absolute resolution across an energy spectrum; reference to the above equation shows that the pass energy must then also be constant. The application of Liouville's theorem then shows that the acceptance angle, Ω_S , must become smaller as E_{kin} is swept to higher energies.

The measured intensity is given by:-

$$I(E_{kin}) = i(E_{kin}) \times F_S \times \Omega_S \times \Delta E \quad (3.8)$$

which varies proportional to Ω_S , where:-

$$\Omega_S = \frac{\Omega_0 \times \Delta E}{2 \times p \times E_{kin}} = \frac{const}{E_{kin}} \quad (3.9)$$

Hence:

$$I_{measured} \propto 1/E_{kin} \quad (3.10)$$

which defines the transmission function of the analyser when used in this mode.

Final detection of electrons in the analyser was initially performed by a Mullard channel electron multiplier ("channeltron") type B419 AL/01 which was later substituted by an EMI cascade electron multiplier type 9643/4B having a quoted current gain of 5×10^5 when operated at 2.85 KV.

The external casing of the analyser was manufactured from stainless steel and the whole unit was UHV compatible having a maximum bakeout temperature of 400°C . The effect of magnetic fields was reduced to a minimum by enclosing the input lens and the hemispheres as well as the electron detector system within a mumetal magnetic shield having a shielding efficiency for external magnetic fields up to 5 Oersted of 100.

The remanent internal magnetic field was quoted as being less than 5m Oersted (manufacturer's handbook). One further useful feature of the analyser was that it produced no electrostatic field at the sample for the first input grid of the electron lens was held at earth potential.

3.7 The Signal Detection System

Although the output from the lamp was intense in the helium I mode, the total photoelectron current, as measured using a Keithley model 427 current amplifier, was only about 1×10^{-10} amps. Such small currents demand circuitry of high gain but low noise.

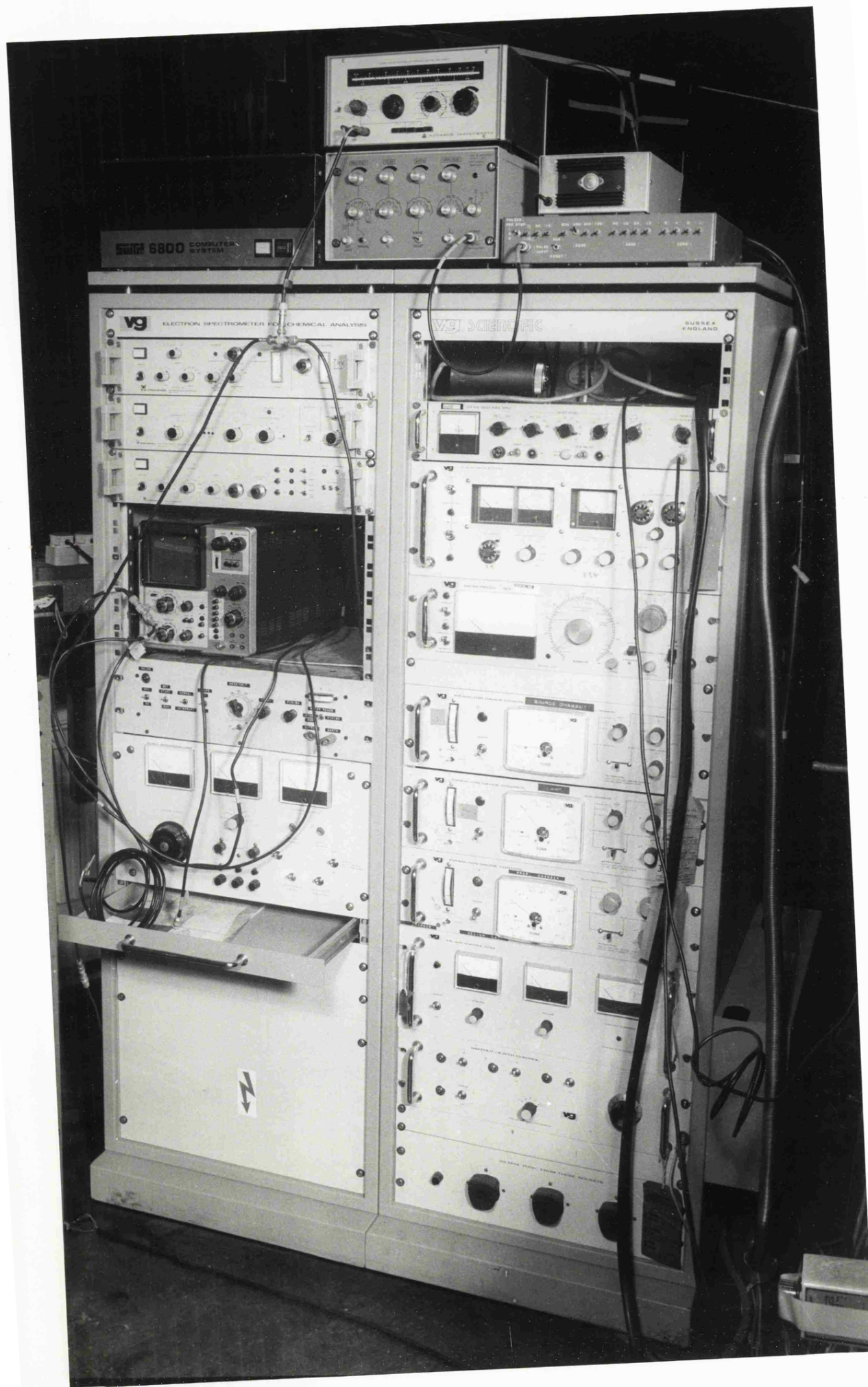
Acquisition of data was performed using three units manufactured by Leybold-Heraeus which can be seen in plate 3-2. The ratemeter/multiplier supply (NE-EA-10, mod 2230) was connected to the analyser by a detachable pre-amplifier unit. A ramping voltage was provided by the sweep generator (NA-EA-10, mod 2200) and the control of the analyser was performed by the electron energy analyser power supply (PS-EA-10, mod 2220). Data was outputted onto a Bryans 26000 A3 X-Y graph plotter and then digitised using the Ferranti Freescan digitiser table of the University's Graphics Centre. Computer routines were developed to interpolate, sum and finally plot the data.

3.8 Signal Averager Based on a Microprocessor

To obtain signal-averaged data a multi-scanning system was developed, based around a Motorola M6800 microprocessor. It can be shown (Hudgings and Dragt, 1972) that if the noise mixed with the photoemission signal is completely uncorrelated (ie:- random), then the improvement in signal to noise ratio after N sweeps is $\propto \sqrt{N}$. Alternatively, if the noise is periodic, for example 50 Hz mains

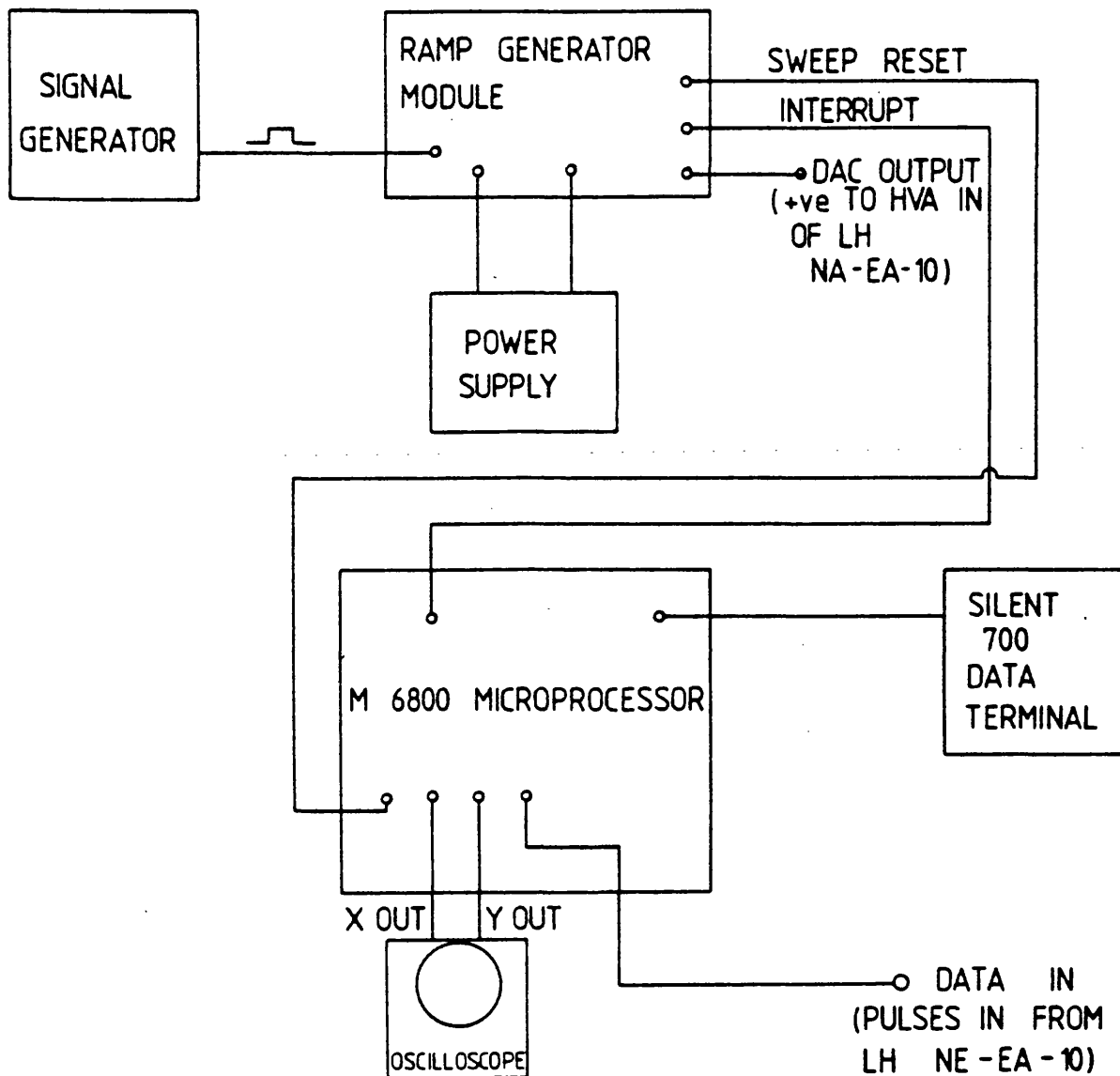
Plate 3-2

Spectrometer control rack



derived pick up, then the improvement in signal to noise produced by N sweeps is $\propto N$. The two major benefits of the computer based multi-scanning system are then seen to be that the signal to noise ratio is improved and the data is obtained in numerical form, making for easier data transfer and handling.

A block diagram of the microprocessor system is shown in figure 3-4. The timing of the system was performed by an external pulse generator, set to deliver +5V pulses at a typical frequency of 10Hz to the pulse input of the ramp generating box, which then produced a ramp voltage which increased as a function of time from a preset value. The base voltage of the ramp was set by a combination of fourteen switches on the ramp box, the difference between the actual base voltage and the indicated setting being a factor of twenty. The switches produced a binary coded decimal (BCD) signal which was added to the binary coded decimal signal derived from the number of input pulses received since the ramp was last reset. This BCD signal then passed via an inverter stage to the input of a digital to analogue converter which ultimately produced the ramp output. Although two ramp outputs were provided, only the positive one was used; its output was connected to the "high voltage amplifier in" (HVA in) connection of the Leybold-Heraeus ramp with which it was designed to be compatible. From the ramp box, the timing pulses were fed to the microprocessor via the interrupt line. The program for the microprocessor was organised into two parts; a display half and a data counting half. Normally, the display part of the program was in operation which drove an oscilloscope used in its x-y mode to show the stored spectrum in the microprocessor's memory. The oscilloscope was connected to the x and y outputs on the back of the microprocessor; the x output was connected with a $1\mu\text{F}$ capacitor to remove a large DC level. On the reception of a timing pulse on the



Block diagram of multi-scanning system

Figure 3-4

interrupt line, the second half of the program was used. During the time interval between this pulse and the last one, the number of pulses received on the "data in" line were counted by an eight bit input counter. The "data in" line of the microprocessor was connected to the TTL output connection of the Leybold-Heraeus ratemeter. On the reception of the timing pulse, the microprocessor then took the number of pulses from the input counter, added it to the number of pulses in the memory channel that it was in by a sixteen bit double precision addition, cleared the input counter, advanced the channel number by one and then returned to the display part of the program. This was continued channel by channel, building up the spectrum in energy increments until the end of the scan was reached. At this point, the microprocessor reset the ramp by sending a pulse down the sweep reset line to the ramp box which returned the ramp to its base value. The spectrum was then scanned through once again. Thus the width in eV of the scan taken by the microprocessor was dictated by the number of channels and the system was energy calibrated by arranging that the number of channels for one scan produced a ramp voltage which was equivalent to that produced by the Leybold-Heraeus unit.

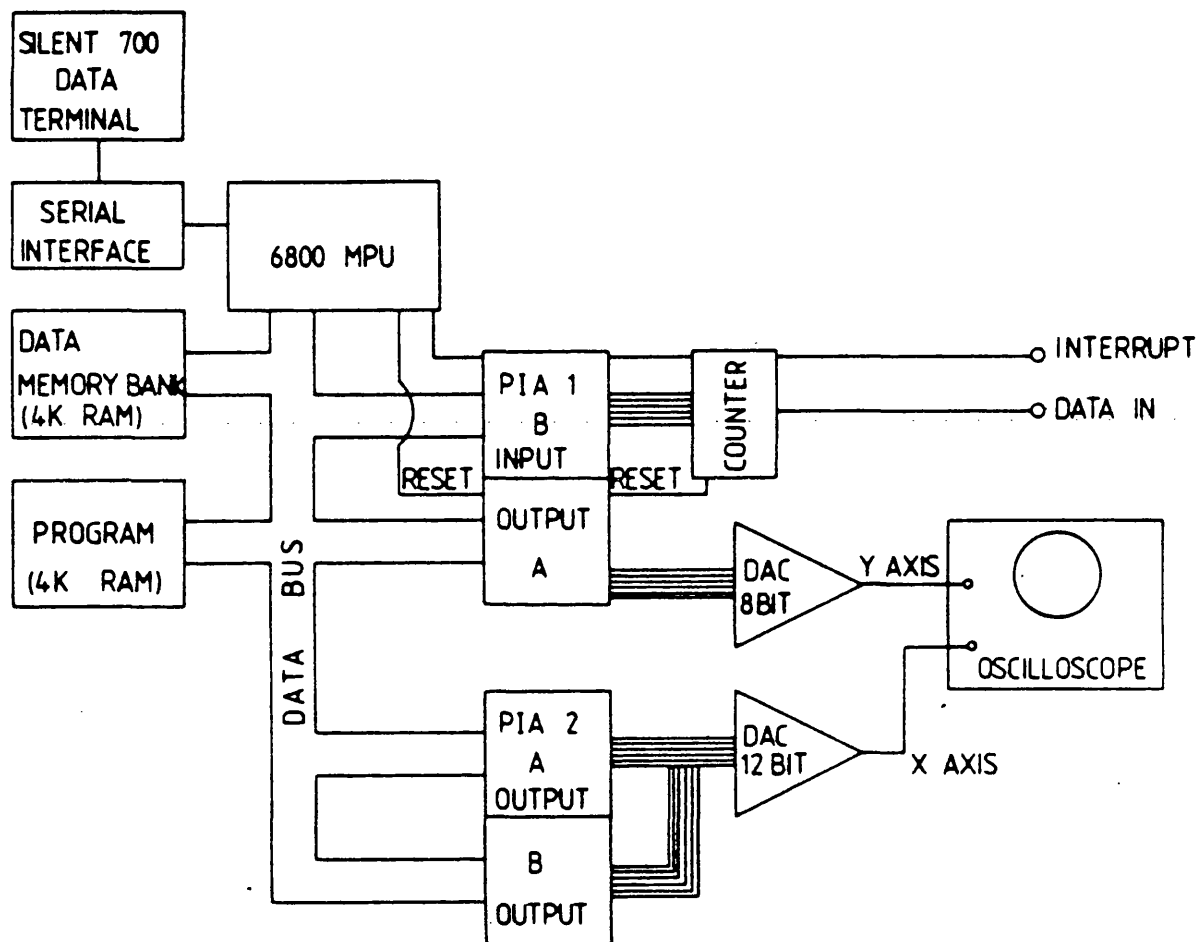
Communication with the microprocessor was achieved by using a Texas Instruments Silent 700 electronic data terminal. The program for the microprocessor was stored on magnetic digital cassette tape and was read in via the data terminal. At the completion of a multi-scan spectrum, the data stored in the microprocessor's memory was outputted to magnetic tape using the data terminal which was then read into the University computer for final analysis and plotting.

Although use of the multi-scan facility should have improved the quality of the data taken this was found not to be so for a variety of

reasons:-

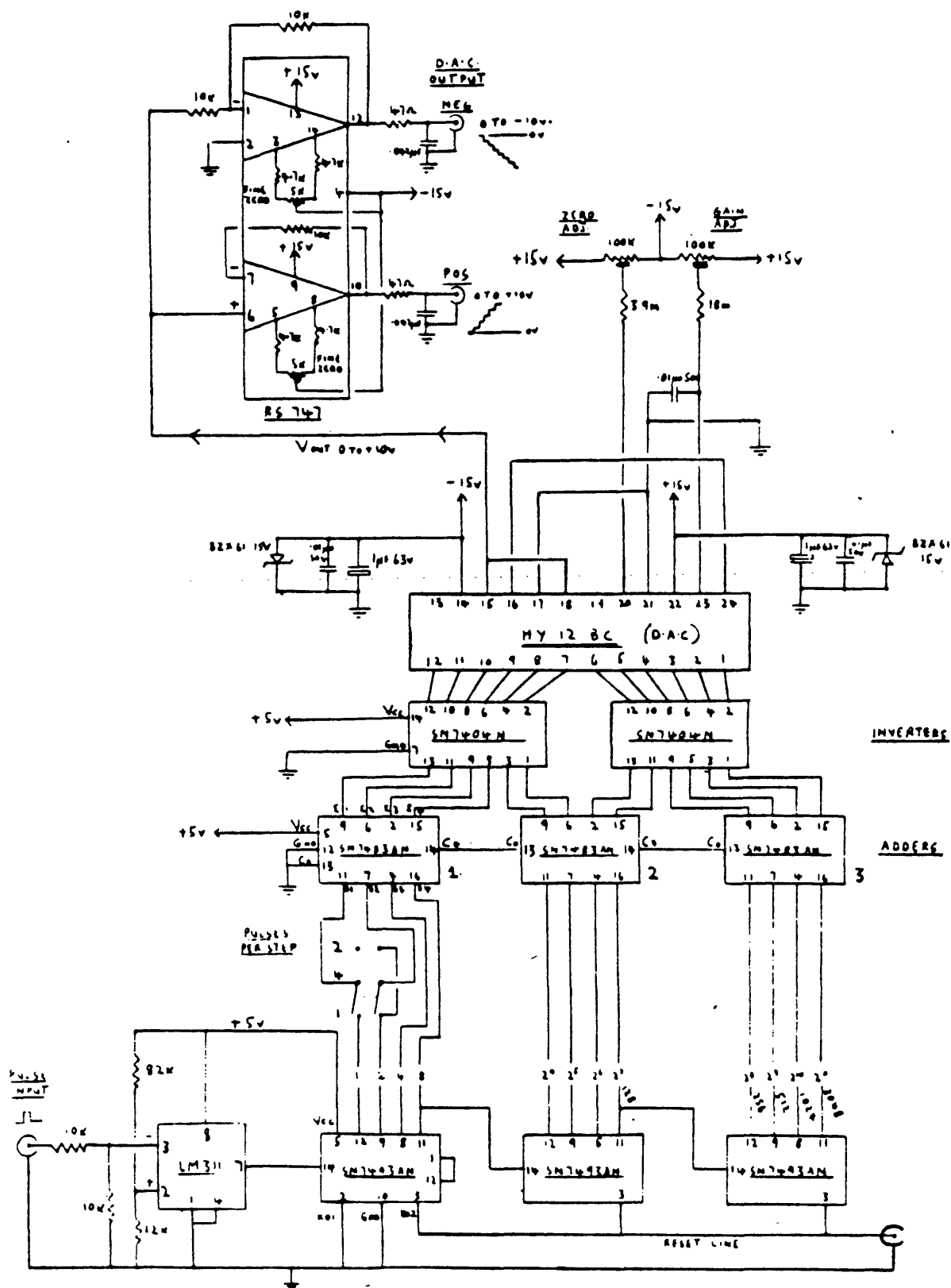
- (i) The input counter was built in as an 8 bit unit and therefore could only count a total of 256 pulses in one time interval. If the timing pulse generator was set at a frequency of 10Hz, then the maximum count rate which could be handled was 2560 counts/sec. If the count rate was larger than this, then the frequency of timing pulses had to be increased leading to shorter scan times and degrading the counting statistics in each energy channel. As the scan time decreased, the proportional quantity of dead time for the system increased, which further degraded the counting statistics.
- (ii) The ramp input voltage to the Leybold-Heraeus high voltage amplifier input terminal reset and then began to increase immediately allowing no time constant for voltage decay, leading to a degrading of the resolution of the multi-scanning system.
- (iii) The shape of the spectrum was found to vary with time, presumably with change in the sample surface curvature caused by sample loss through evaporation, and this could not be monitored while multi-scanning.
- (iv) The system was found to be susceptible to noise pick up which caused degradation of the resolution. One example of this was the cooling fan on the data terminal which consequently was turned off while multi-scanning was in progress.

For these reasons it was often found more convenient to take data with the analogue system described previously. Figures 3-5 and 3-6 show the organisation of the microprocessor system and the wiring diagram of the ramp generator respectively while a listing of the microprocessor program is given in Appendix B.



Internal organisation of the microprocessor system

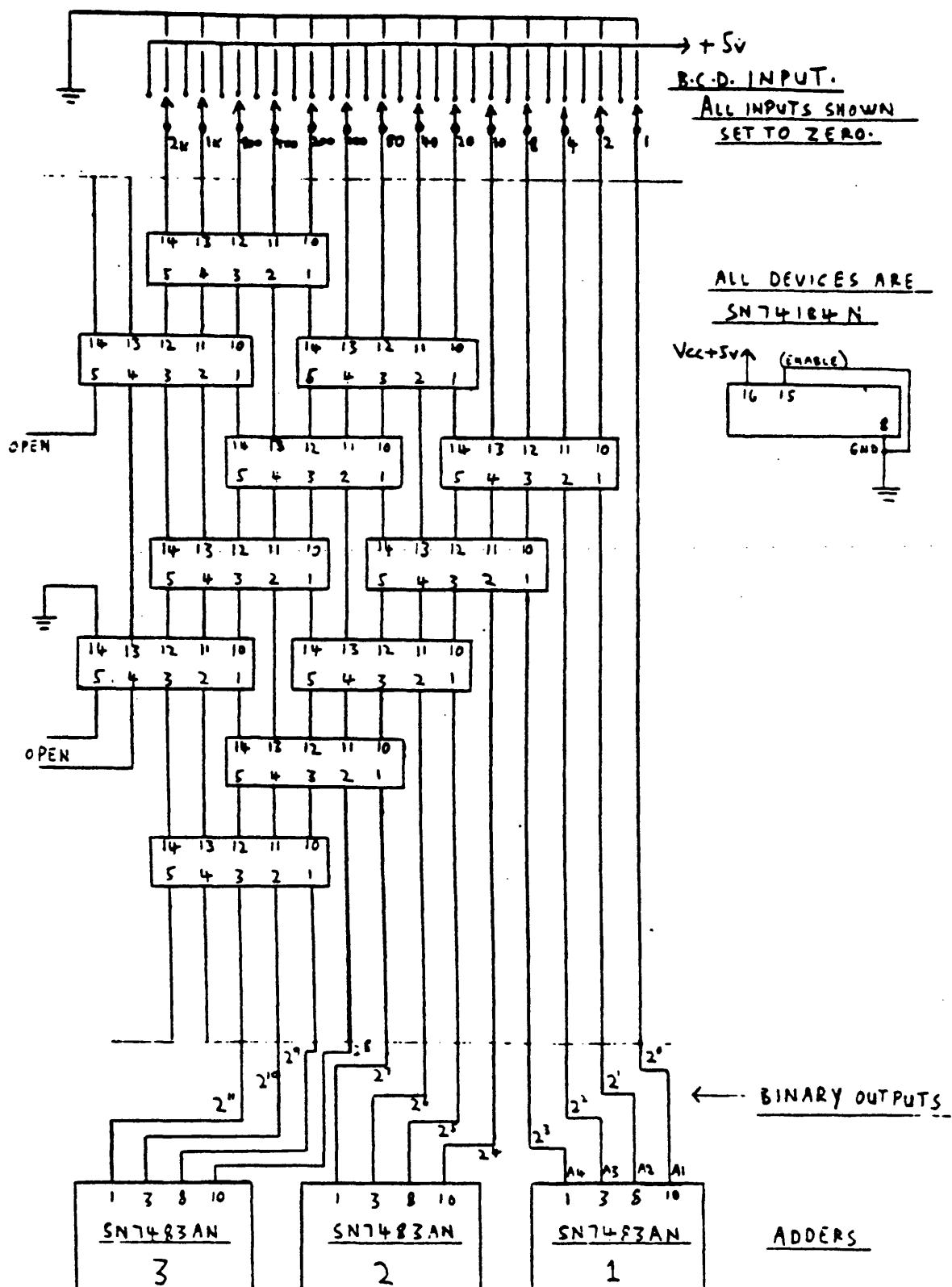
Figure 3-5



Rampbox wiring diagram (part I)

Figure 3-6

B.C.D. TO BINARY CONVERSION.



Rampbox wiring diagram (part 2)

Figure 3-6

3.9 Auger Electron Spectroscopy (AES)

The Auger process was first observed over fifty years ago (Auger, 1925), but has only more recently found widespread use as a surface chemical analysis technique following the work of Lander (1953) and Harris (1968).

The Auger process is normally envisaged as occurring in two stages. Initially an incident energetic particle ionises a core level of an atom located at or near the surface of the target material, and the core hole created in this way is then filled by an electron from a higher energy level. The difference in energy is then released by either a photon or by the ejection of another electron (termed the Auger electron). The incident particle causing ionisation may be any particle carrying sufficient energy to ionise the core level, but AES is now almost entirely performed using an incident beam of high energy electrons (typically 2.5 KeV). X-ray emission competes with Auger emission for de-excitation but has a much lower probability of occurring (less than one tenth) for all elements of the first two rows of the periodic table which includes all the common surface contaminants.

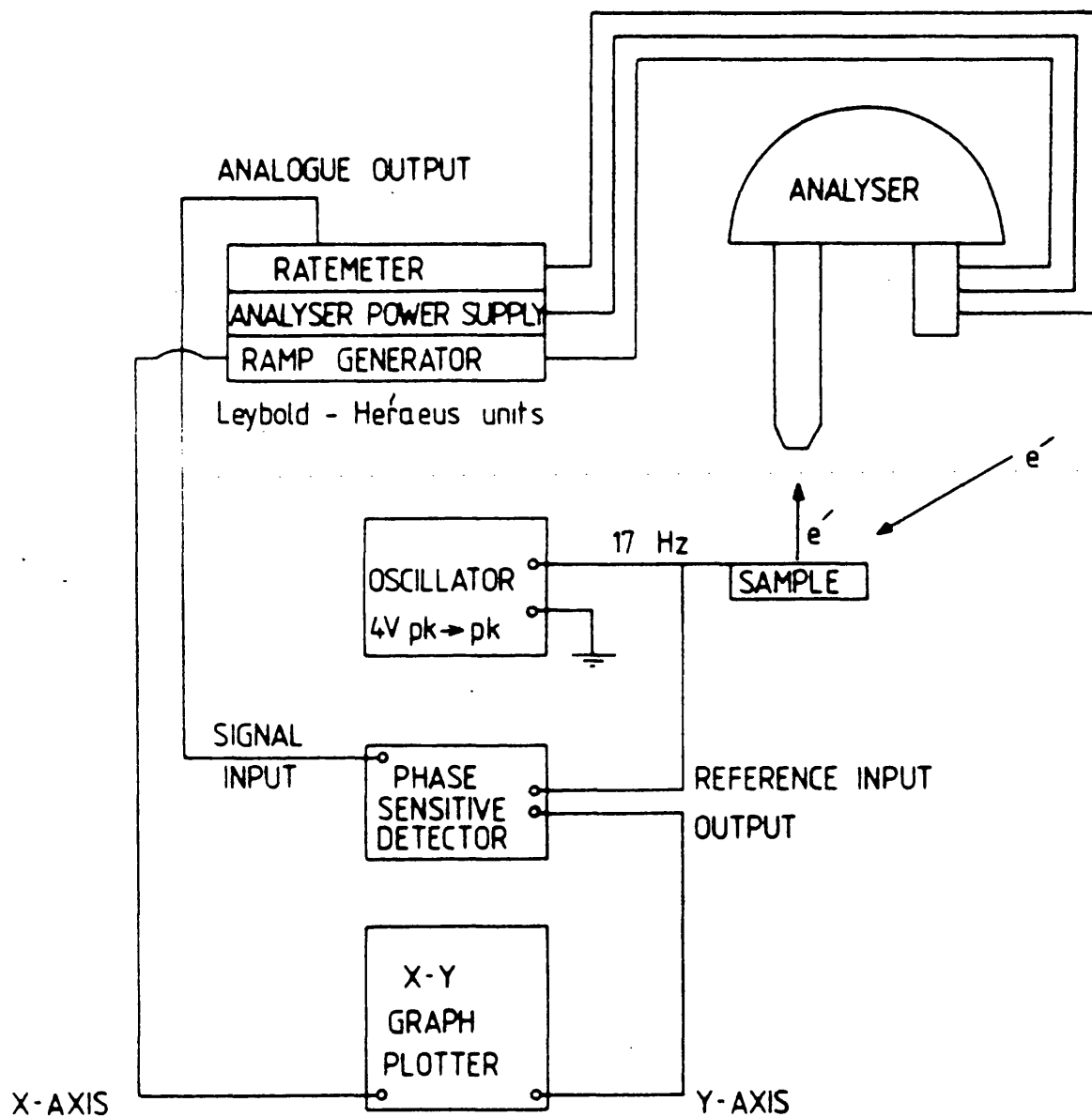
Auger peak widths can be twice the width of the valence band depending on from where the electron falls in energy to fill the core hole and from where the Auger electron is emitted. A further contribution to the width comes from lifetime broadening since any transition between two quantum states takes a finite time τ , the uncertainty principle introduces a corresponding energy uncertainty given by $\Delta E = \hbar/\tau$. As Auger transitions occur very quickly (typically 10^{-16} seconds), the corresponding energy is comparatively large (≈ 6 eV).

The energy of an Auger electron cannot be computed directly from the three neutral atom energy levels involved because following the initial ionisation, a redistribution of charge will occur which causes a shift in the energy levels. A simple expression due to Chung and Jenkins (1970) has been found to give accurate values of the energies of Auger electrons. For the case of emission from a solid, the work function must be subtracted to obtain the kinetic energy of the Auger electron in vacuum. A review of the general principles both fundamental and instrumental of Auger electron spectroscopy has been given by Chang (1971).

The source chamber was fitted with a VG Leg 31 glancing incidence electron gun powered by a model 326A stabilised unit for detecting surface contaminants and for estimating relative concentrations of surface components in binary alloys. The gun was outgassed after bake-out for about one hour at a filament current of up to $2\frac{1}{2}$ A, the maximum pressure in the source chamber being 5×10^{-8} torr. Under typical conditions of use, a beam current of 20 μ A with a beam energy of $2\frac{1}{2}$ KeV with a filament current of 2A provided sufficient signal for detecting Auger electron lines.

It is customary not to examine the primary $N(E):E$ spectrum in AES but to look at the first derivative, $dN(E)/dE:E$, by modulating the analysing energy and synchronously detecting the output current using a lock in amplifier. This allows for straightforward electronic differentiation and avoidance of noise by reducing the effective bandwidth.

Figure 3-7 shows a block diagram. Synchronous detection was performed by a Brookdeal model 9503 phase sensitive detector, and an Advance Instruments battery driven oscillator provided a modulation of



Block diagram of arrangement for AES

Figure 3-7

4.0 V peak to peak at 17 Hz between the sample and earth.

The operation of the system may be understood as follows. A perturbing voltage $\Delta E = K \sin \omega t$ is superposed on the energy of the electrons so that the analysed electron current $I(E)$ is energy modulated. Writing $I(E + \Delta E)$ in a Taylor expansion gives:

$$I(E + \Delta E) = I(E) + I'(E)\Delta E + \frac{I''(E)}{2} \Delta E^2 + \frac{I'''(E)}{3!} \Delta E^3 + \frac{I^{(4)}(E)}{4!} \Delta E^4 + \dots \quad (3.11)$$

where the prime denotes differentiation with respect to E . This may be re-arranged to give:-

$$I = I_0 + \left[I'K + \frac{I'''K^3}{8} + \dots \right] \sin \omega t - \left[\frac{I''K^2}{4} + \frac{I^{(4)}K^4}{48} + \dots \right] \cos 2\omega t + \dots \quad (3.12)$$

where I_0 is a time independent term.

$$\approx I_0 + I'K \sin \omega t - \frac{I''K^2}{4} \cos 2\omega t + \dots \quad (3.13)$$

where K^3 and higher order terms are neglected. The differential spectrum is thus obtained by allowing the lock in amplifier to pass only the in phase ω component.

One practical point requires mentioning. In use the electron gun was shuttered to prevent evaporated sample being deposited on the gun's insulating sections which would have led to high tension breakdown occurring and consequent damage to the power supply. This meant that the gun was never used to examine liquid surfaces. The shuttering system was also extended to cover two windows in the source chamber.

3.10 Sample Preparation - General

The typical probe depth in ultraviolet photoemission is about

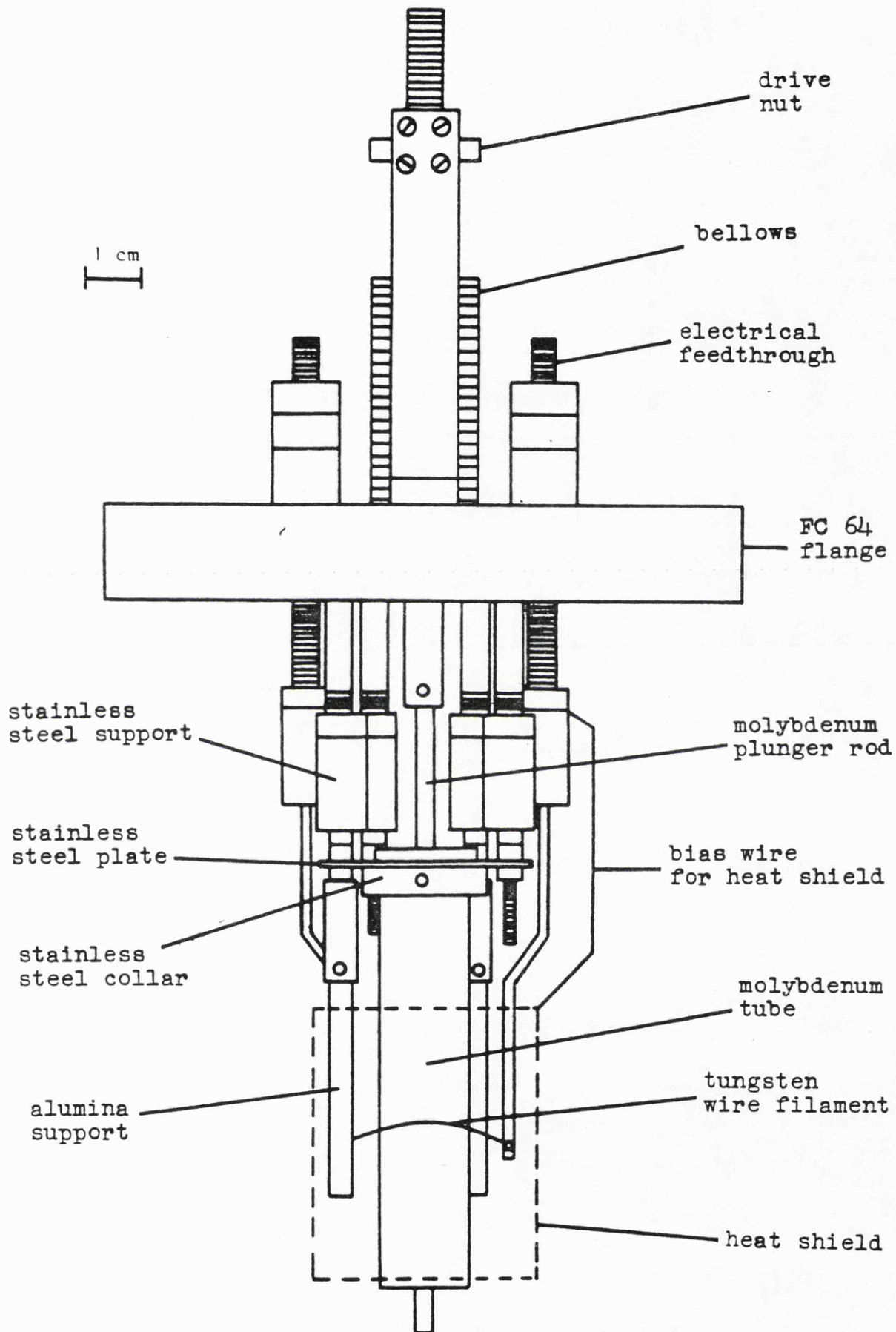
15 Å and thus spectra are sensitive to surface contaminants. For the solid phase, clean surfaces can be obtained by cleaving in vacuo for crystals or evaporating films for metals. For liquid metals the preparation was more complicated because a relatively large amount of sample was required.

For lithium and lithium based alloys, the technique used by Norris et al (1973) and Wotherspoon (1978) was used. By creating a column of liquid alloy sample in vacuo, contaminants (mainly oxide) separated out, allowing a clean specimen to be decanted from the centre of the melt. A pouring mechanism and a sample dish were thus required and these were constructed of pure molybdenum as supplied by Murex. Liquid metals are highly corrosive but the Liquid Metal Handbook (Jackson, 1955) showed that pure molybdenum is a suitable material for containing molten lithium alloys.

It was not practical to pour the silver-germanium alloys hence these were pre-formed in samples of the correct size and loaded directly on to the sample crucibles to be re-melted under UHV conditions and in situ cleaned by argon ion bombardment if necessary.

3.11 Details of the Pouring Mechanism for the Lithium and Lithium Based Alloys

The pouring mechanism is shown in figure 3-8 and plate 3-3 shows a partially dismantled pourer. The central feature was a molybdenum tube, suspended from the flange, and sealed at the bottom by a molybdenum rod which was ground to a tight fit using diamond paste. The rod was raised and lowered by a bellows and knurled wheel arrangement. The tube and plunger rod were thoroughly cleaned using scotchbrite, ultrasonic washing in acetone and methanol and electro-

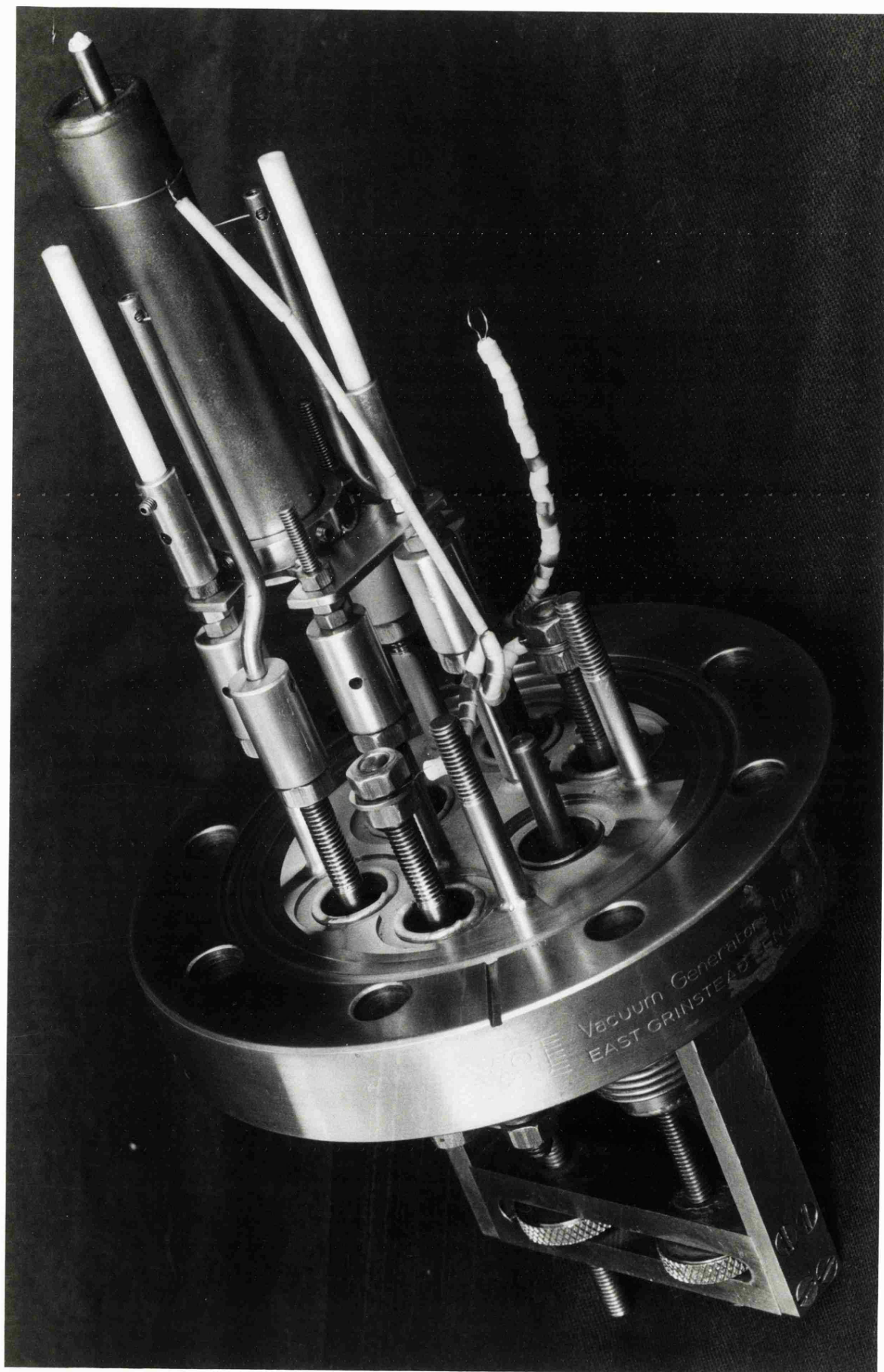


Sample pouring mechanism

Figure 3-8

Plate 3-3

Sample pouring mechanism



polishing (see Appendix C). Some samples (eg: lithium) were found to be so light (and the effects of surface tension correspondingly greater) that they would not fall through the exit hole of the nozzle in which cases the plunger rod was replaced with a molybdenum piston and the samples were pushed out.

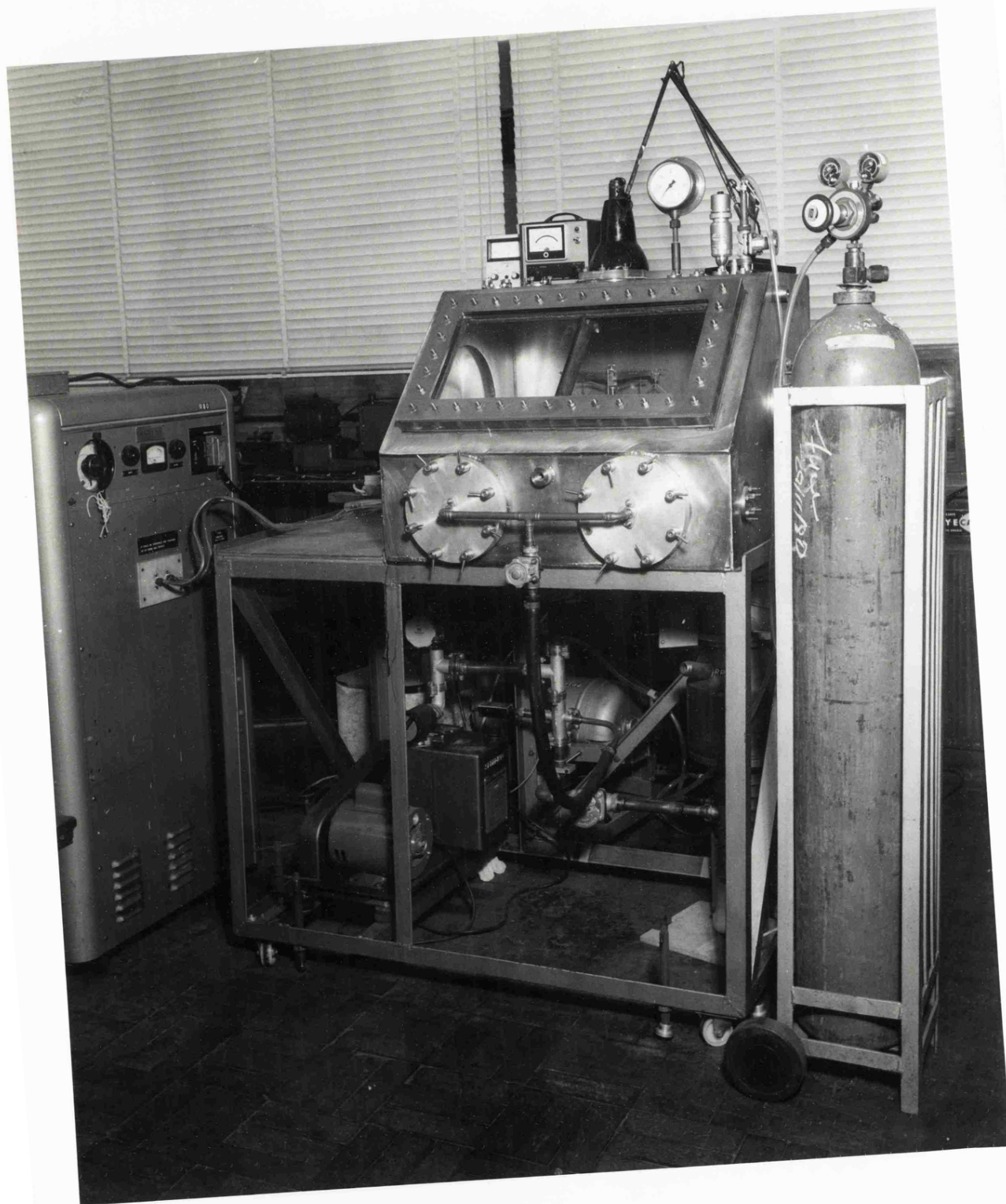
Heating of the tubes was achieved by electron bombardment. The 30 SWG plain tungsten filament was arranged to lie about 3 cm above the base of the tube to concentrate the heating at the top of the sample otherwise it was found that the tubes showed a tendency to crack. The tube temperature was monitored by a thermocouple junction clamped against the tube by stainless steel wire.

Normally during a run, three or four drips were poured into a drip tray before the sample was decanted into the sample boat. Pouring more from the centre of the melt was aided by the fact that the nozzle at the base of the tube was not flush but protruded upwards a distance of 6 mm.

The lithium based alloys were initially prepared in a glove box (plate 3-4) which had a base pressure of 10^{-5} torr. Tin rods (99.9999% pure) and lead rods (99.999% pure) supplied by Koch-Light Ltd were scraped and cut by clean steel knives, and pieces of lithium were cut from a $\frac{1}{4}$ lb ingot (99.8% pure from Koch-Light) using clean steel shears under one atmosphere pressure of commercial grade argon. The ingot was kept in a sealed, clean stainless steel container which was only opened under argon. The alloys were manufactured in the sample tube under the inert atmosphere of the glove box by heating using a "Radyne" radio frequency induction heater. After cooling, the sample tube was removed and assembled onto the pourer flange which was then bolted into the preparation chamber of the spectrometer and the equipment was then pumped down. This period of exposure to the air meant that the top and

Plate 3-4

The glove box



bottom of the sample became contaminated but the bulk of the sample (from which the experimental specimen was decanted) remained unaffected.

3.12 The Manipulator Tube and Sample Boat

A photograph of the complete manipulator tube is shown (plate 3-5) and an enlargement of the end which carried the sample boat is also reproduced (plate 3-6) which shows a specimen of frozen tin. The manipulator tube, which carried electrical connections for heating the crucible, temperature measurement by a thermocouple and for supplying a voltage to the sample, was mounted on the preparation chamber with a linear drive assembly allowing the sample crucible to be moved from underneath the pouring mechanism to the source chamber. The crucibles were heated by a tungsten filament wound non-inductively in the form of two spirals and sandwiched between two plates of re-crystallized alumina. The crucibles were made of pure molybdenum and were cleaned in the same way as the sample tubes.

3.13 Preparation of the Silver-Germanium Alloys

Small pieces of silver were cut from 99.999% pure rods (Metals Research Ltd.) with a clean hacksaw blade and small pieces of germanium were broken from small ingots (99.999% pure supplied by Koch-Light Ltd.) by wrapping them in aluminium foil and breaking them with a light hammer. The alloys were manufactured under an argon atmosphere in the glove box by heating the constituents together using the radio frequency induction heater inside clean graphite tubes. After cooling, the sample globules (of volume about 0.09 cm^3) were removed to the source chamber of the spectrometer using clean tweezers.

Plate 3-5

.....

The manipulator tube

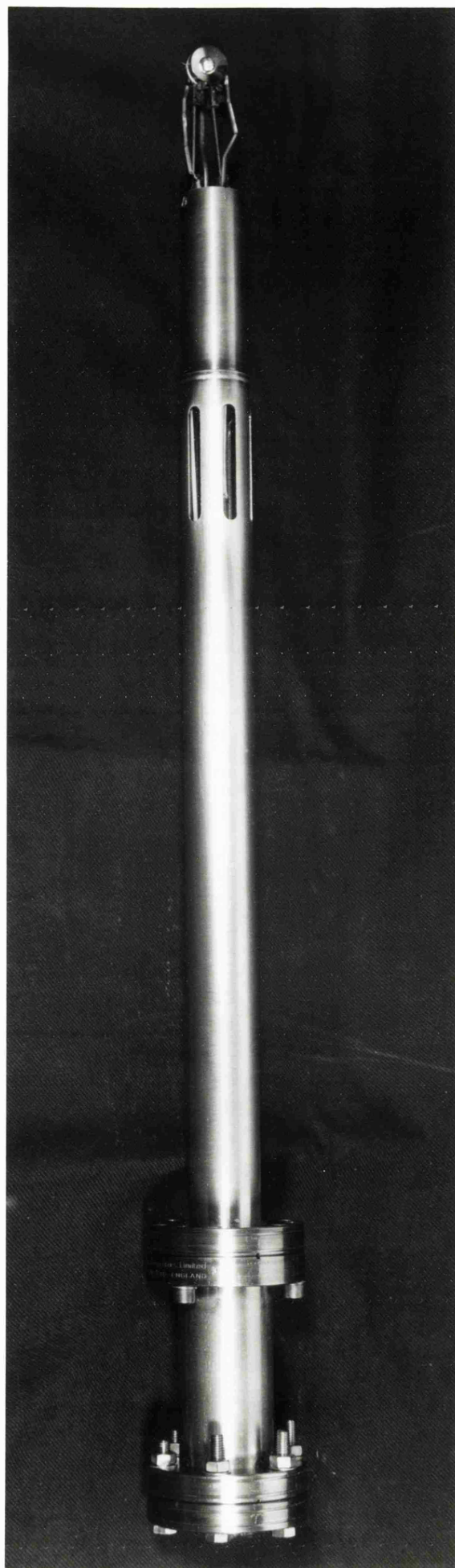
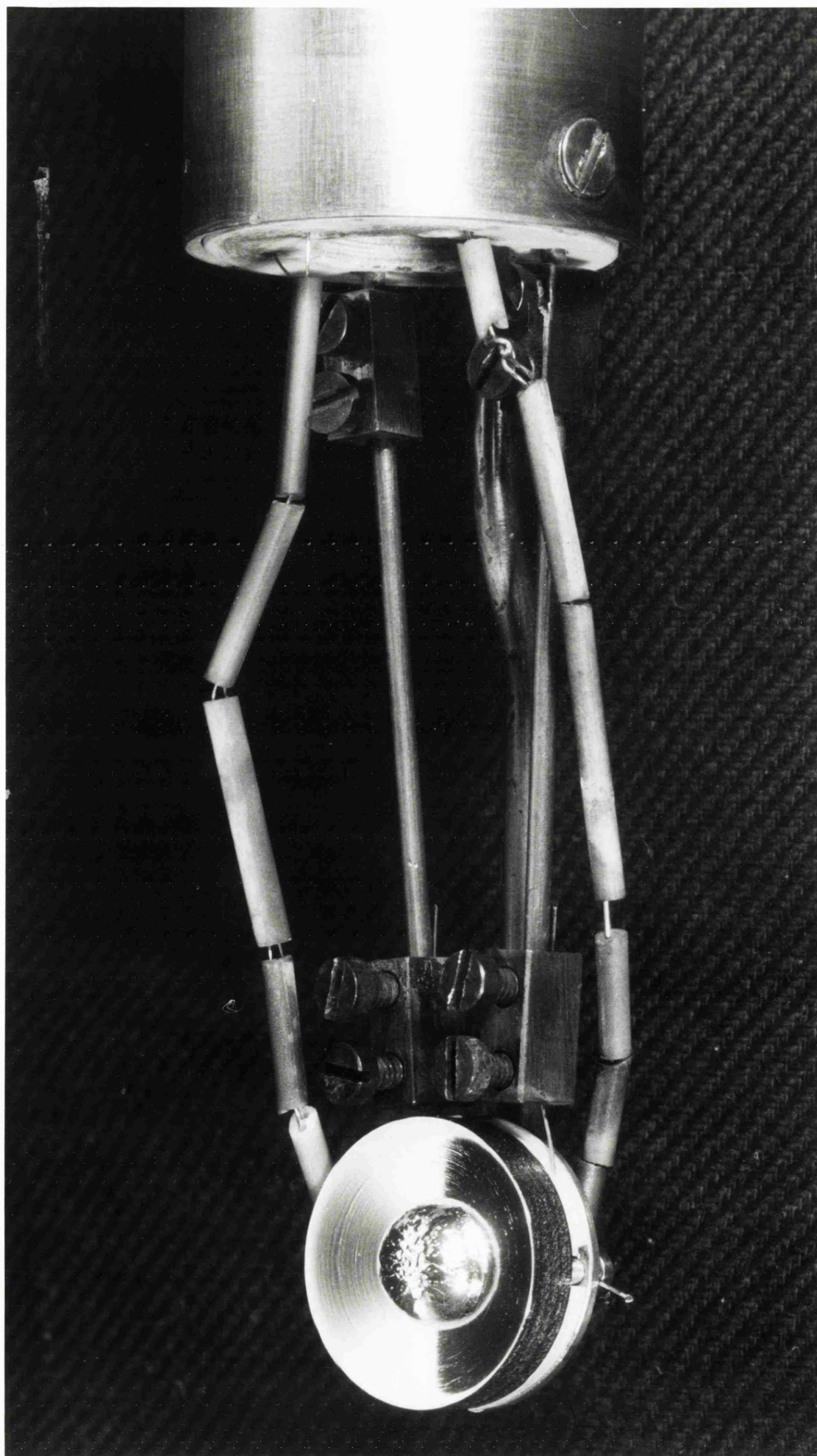


Plate 3-6

Sample crucible arrangement

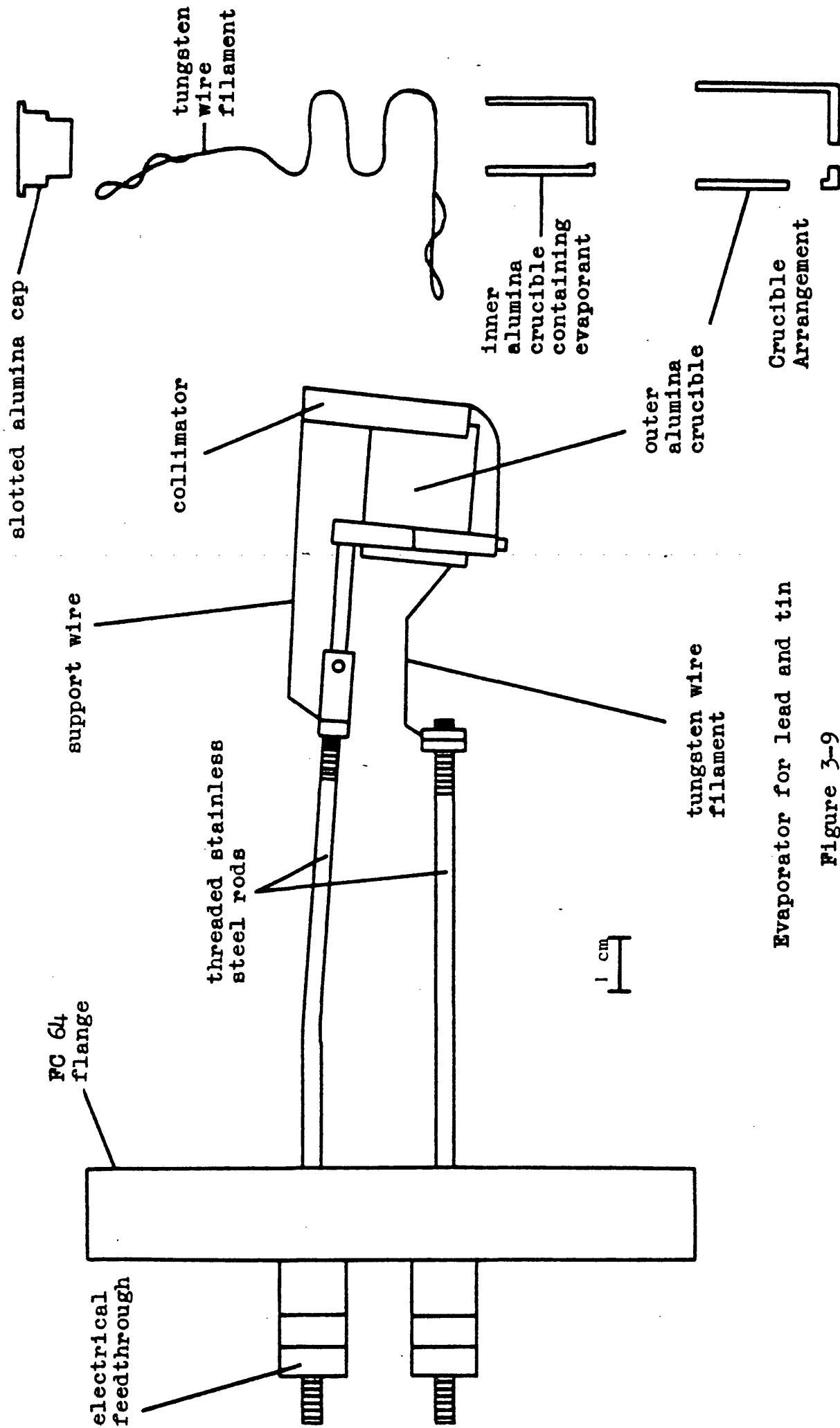


3.14 The Experimental Arrangement for the Silver-Germanium Alloys

The preparation chamber and manipulator tube were dispensed with and a flange substituted for the end window of the source chamber which carried a trolley on which three sample crucibles were held. The trolley slid on rails welded to the flange. Movement of the trolley was achieved by a soft iron plug, moved by an electromagnet, contained within a long glass tube and attached to the trolley. The flange carried electrical connections for heating the crucibles, temperature measurement using thermocouples and sample potential connections.

3.15 The Vapour Source for Lead and Tin

To estimate the surface concentration of the lithium based alloys, it was necessary to evaporate a covering layer of lead (tin) over the respective alloy samples. The evaporator for this purpose is shown in figure 3-9. It consisted of two alumina crucibles, the central one of which was heated by a tungsten filament. The crucibles were covered at one end by an alumina cap, the other end had a central hole of 3 mm diameter to allow the vapour flux to escape. A collimator was made by affixing a stainless steel plate a short distance away from the external crucible. The source of the samples for evaporation was as for the experiments. The temperature of the inner crucible was monitored by a thermocouple. The evaporator was outgassed for two hours at its running temperature before use. During the experiments, the evaporator was run for forty-five minutes which was found to be sufficient time to evaporate enough metal to be detectable on the sample to the naked eye.



Evaporator for lead and tin

Figure 3-9

3.16 Magnetic Shielding of the Source Chamber

The source chamber was internally fitted with a screen of mumetal which was treated by Telcon Metals Ltd. This reduced the effect of stray magnetic fields, including that of the earth, which a simple calculation shows is sufficient to cause low energy electrons to miss the analyser. The magnetic field inside the source chamber was reduced by a factor of nine by the magnetic shielding as measured by a Hewlett Packard model 428 B magnetometer.

Plate 3-7 shows a view inside the source chamber. This photograph illustrates the mumetal shielding, the shutters for the electron gun and windows, the evaporator, the analyser and its attendant shield, the sample crucible on the manipulator tube and a catch tray to prevent any spilt sample from falling into the valve below the chamber.

Another spectrometer was used to make photoemission measurements from liquid lithium at 7.87 eV. This equipment has been described by Wotherspoon (1978); a résumé will be given here.

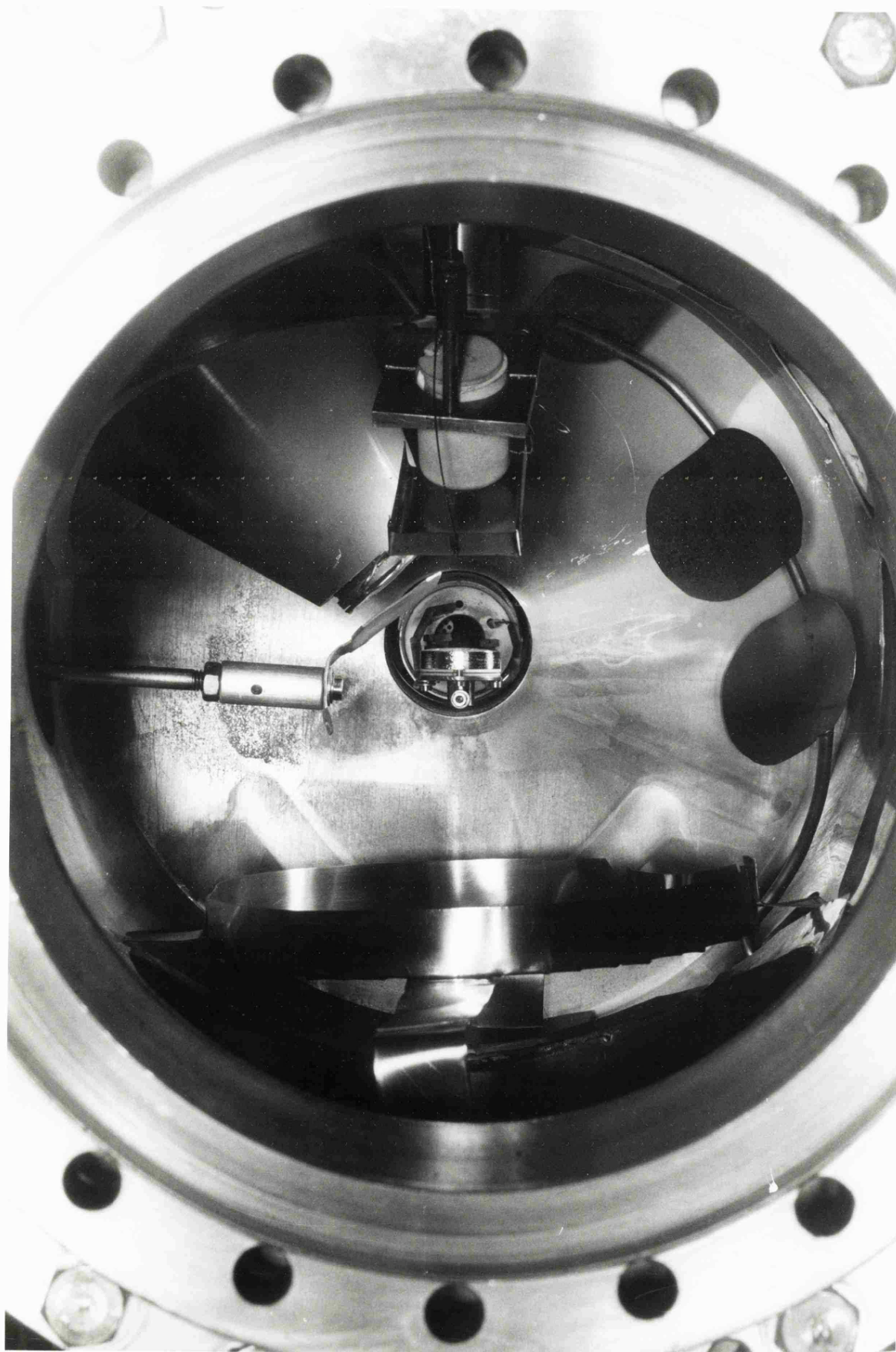
3.17 The (Old) Vacuum System

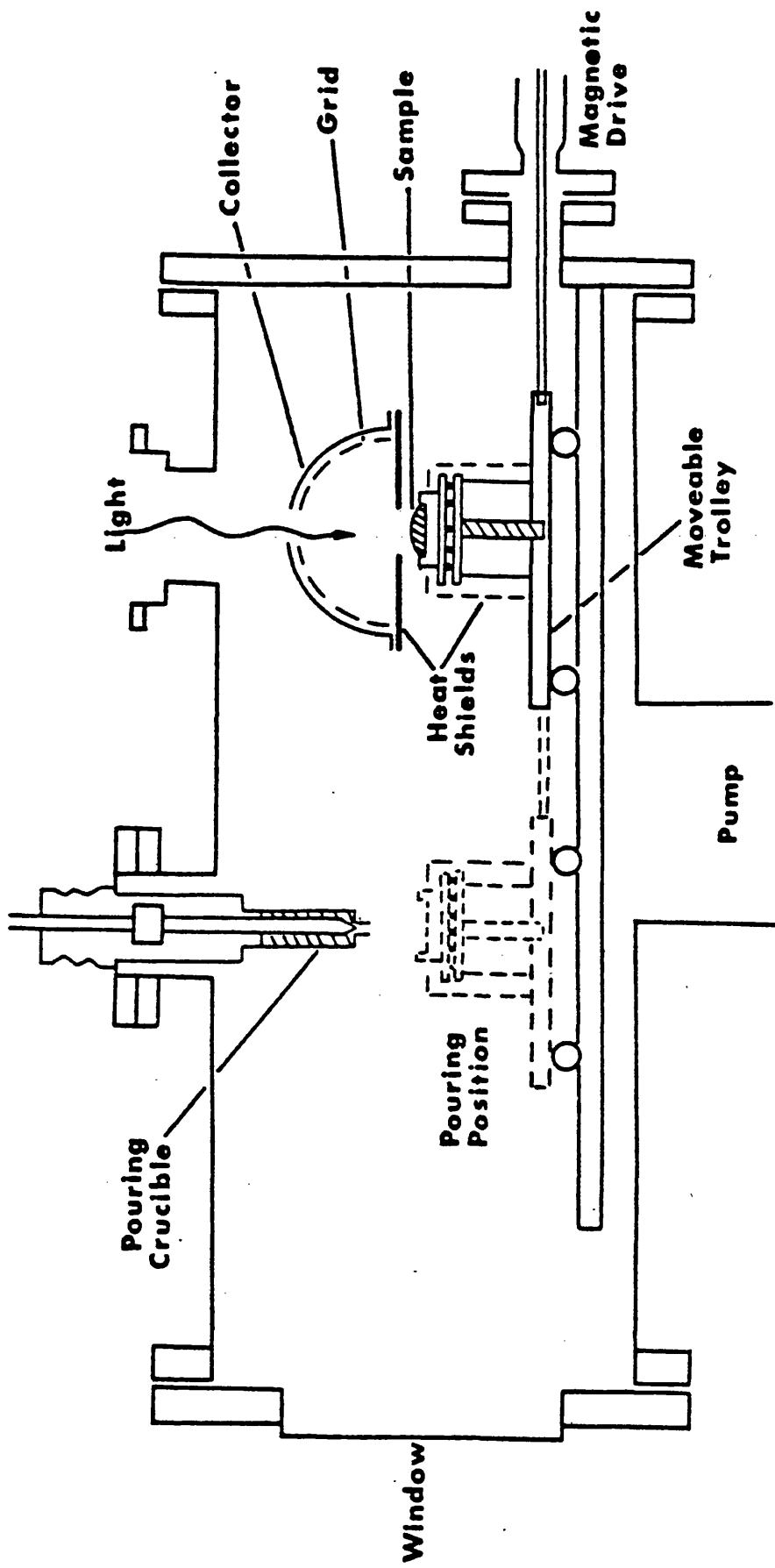
The ultra-high vacuum system is shown in plate 3-8 attached to the monochromator which provided the light source, and schematically in figure 3-10. It was manufactured from stainless steel and the flanges were sealed by knife edges and oxygen free copper gaskets. The main pumping for the chamber was a diode electrostatic ion pump, pressures being monitored by a nude ion gauge. After bakeout, the base pressure of 4×10^{-10} torr was reached; this vacuum was maintained by a titanium sublimation pump which was cycled for two minutes every four hours.

Plate 3-7

.....

Source chamber of spectrometer



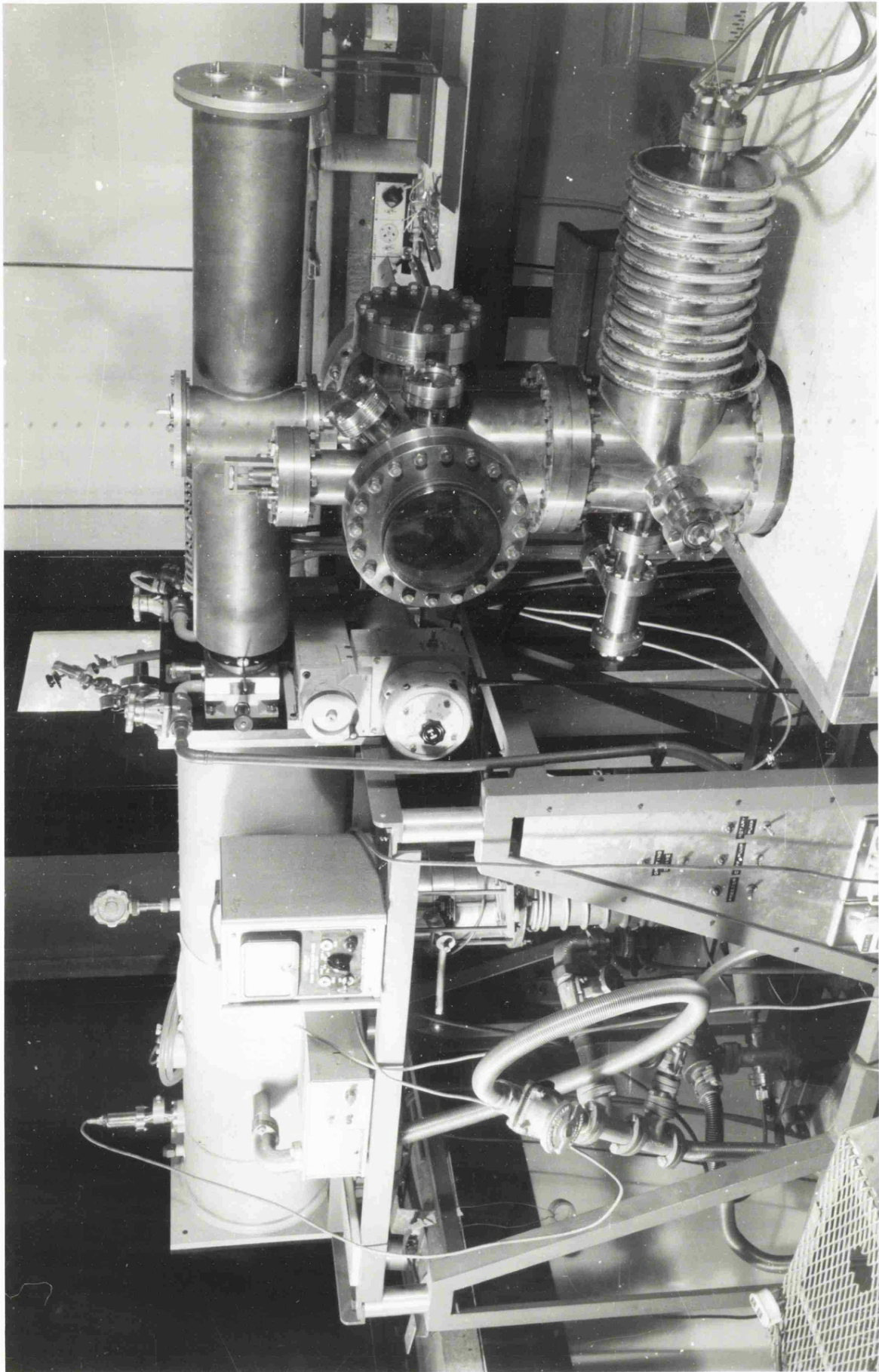


The vacuum chamber

Figure 3-10

Plate 3-8

The (old) vacuum system

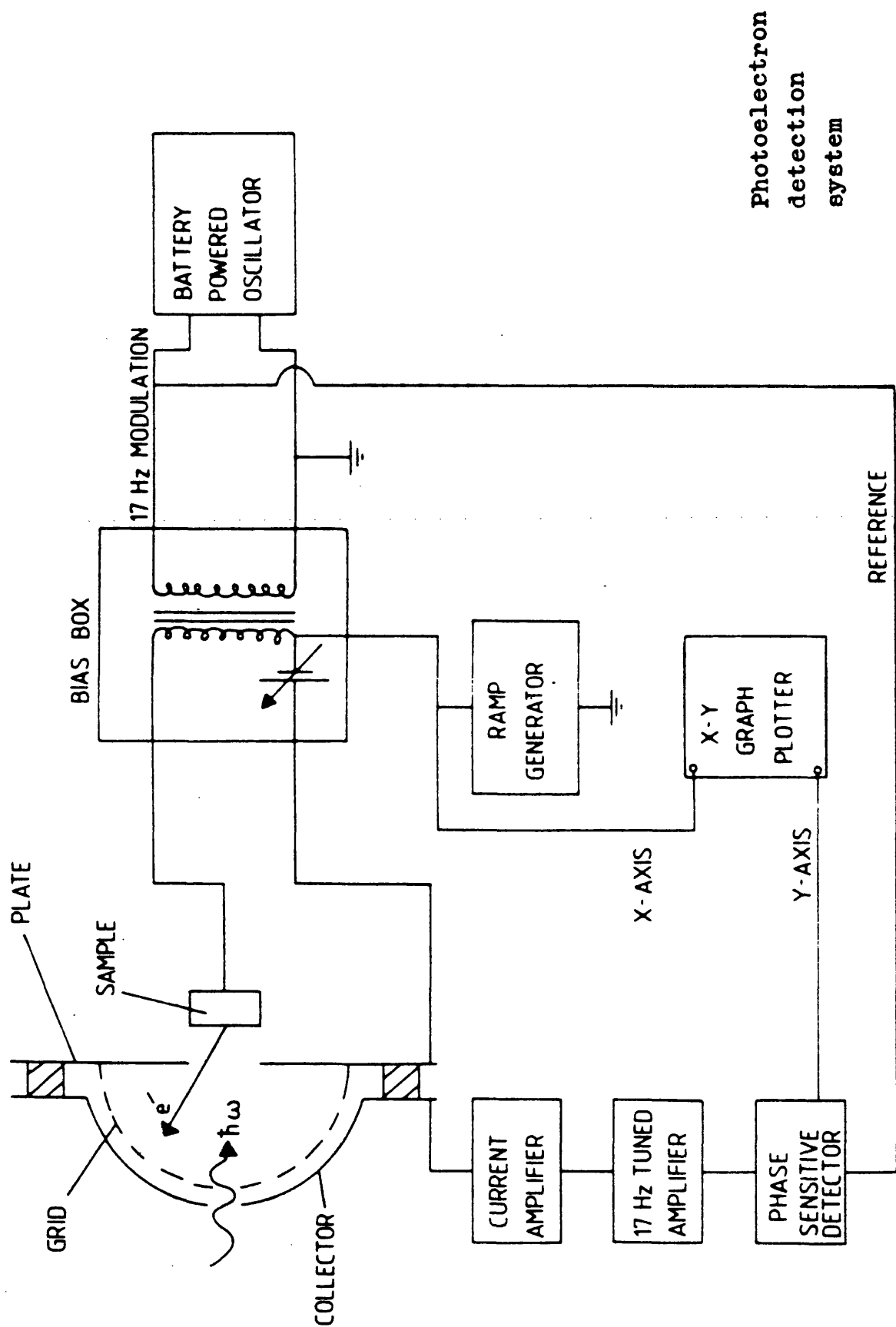


3.18 Sample Preparation and Sample Crucible Arrangement

The liquid lithium sample was prepared and poured as previously described (section 3.11). The molybdenum crucible was identical to those used in the other spectrometer, but was mounted on a trolley which ran on two rails welded to the end flange and was moved by an external electromagnet and a soft iron plug. A small, flat and clean stainless steel plate was also provided on the trolley for evaporating a film of gold over to be used as a calibration standard for obtaining the yield. Gold was evaporated from 99.999% pure gold wire suspended from a tungsten filament. The cleanliness of the evaporated film was monitored by taking a photoemission spectrum from it.

3.19 The Electron Energy Analyser and Electronic Detecting System

A retarding field electron energy analyser was used in this experiment. The light incident upon the sample caused electrons to be emitted and registered at the collector. Energy analysis of the electron spectrum was performed by ramping the sample slowly positive since only those electrons with sufficient kinetic energy were then capable of reaching the collector. However this meant that the collector current was the integral of the electron energy distribution and to obtain the number of electrons in a kinetic energy interval dE , it was necessary to electrically differentiate the collector current signal. This was performed by modulating the electron energy with a small AC signal and then synchronously detecting the output with a lock in amplifier. A block diagram of the circuit is shown (figure 3-11). Care was taken to avoid earth loops which could cause noise greater than the photoelectron signal. The use of synchronous detection reduced the bandwidth helping to eliminate noise to a large degree.



Photoelectron
detection
system

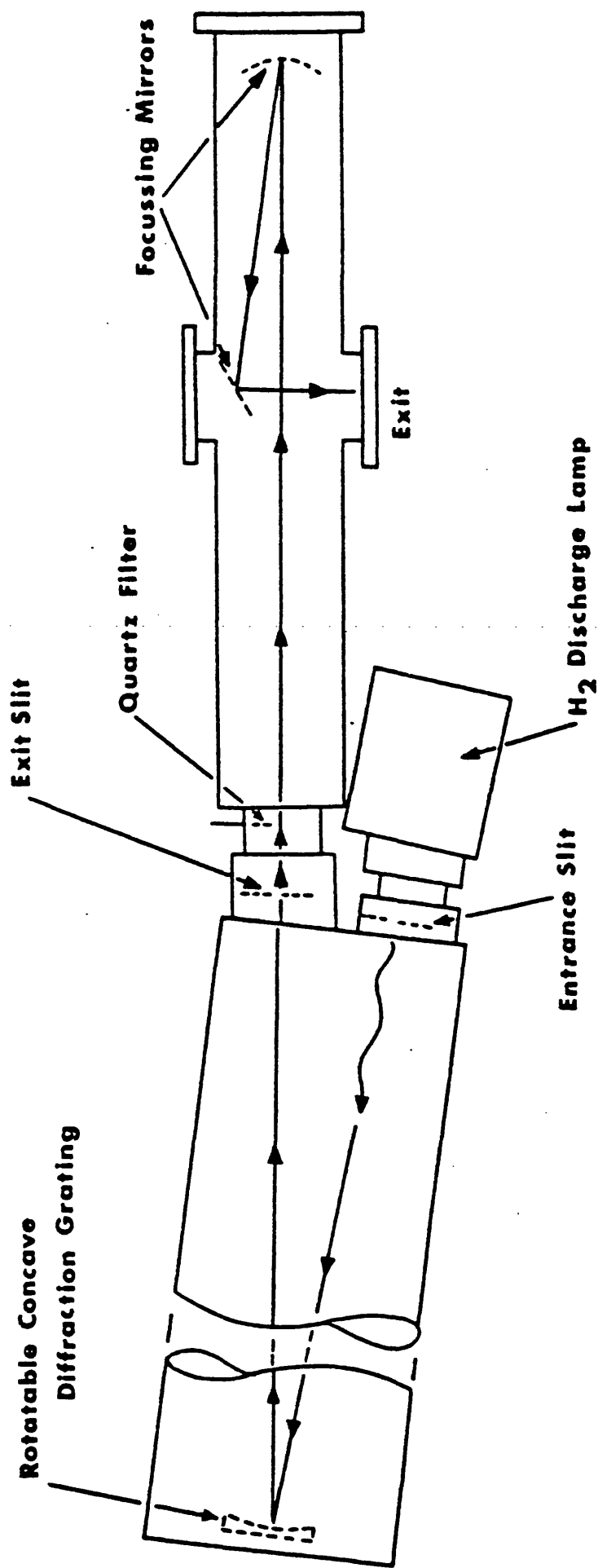
Figure 3-II

The photoelectron signal was passed through a Keithley 427 current amplifier and a sharply tuned 17 Hz amplifier to a Brookdeal 9503 lock in amplifier which drove the y-axis of a Bryans 26000 A3 X-Y plotter. The ramp generator simultaneously drove the x-axis and ramped the sample. Modulation was provided by an Advance Instruments battery driven oscillator. A bias voltage of 0 - 9 V between the grid and the sample compensated for the contact potential difference between the analyser and sample.

Although this analogue system produced spectra for molten lithium, the signal to noise ratio was poor so a signal averaging system based on a multi-channel analyser (Northern NS 905) was used to collect the spectrum used in this work. The working of the logic of the multi-scanning system has been described by Binns (1981). Basically a voltage to frequency convertor was connected to the output of the lock in amplifier to produce pulses for the multi-channel analyser. At the end of a scan the logic control produced a pulse to reset the ramp generator. An acceptable signal to noise ratio was obtained in seventeen scans.

3.20 The Light Source

Light in the energy range 3 - 11.6 eV was generated by a discharge in hydrogen in a water cooled quartz capillary which entered a monochromator (Hilger and Watts, 760) where it was wavelength (energy) selected by an accurately rotatable, concave diffraction grating. This was a Busch and Lomb three section replica grating, ruled at 600 lines per mm and blazed at 1500 \AA . Figure 3-12 shows a diagram of the monochromator. The selected light left the monochromator through a variable exit slit from where it was directed by mirrors in the light



The monochromator

Figure 3-I2

pipe to the exit. Pumping of the monochromator was by a cold trapped diffusion and rotary pump system; the monochromator was run at 4×10^{-5} torr. Coupling of the monochromator to the chamber was via a lithium fluoride window which has an ultraviolet cut-off at 11.6eV.

The intensity of the light source was monitored by coupling a photomultiplier to the exit slit. An intensity against photon energy plot is shown in figure 3-13. The most intense light occurred at 7.87 eV hence this energy was used for the liquid lithium experiment.

3.21 Measurement of the Yield

No direct calibration could be obtained for the incident photon flux and therefore a secondary standard was used by the evaporation of gold onto the stainless steel plate and measuring the total photocurrent from the sample and gold under the same conditions. The current amplifier was set to measure the total photocurrent and its output was sensed across the y-axis of the plotter for both the sample and gold with the exit slit open and closed. The common factor in each measurement was the incident photon flux, hence:

$$\frac{I_G}{Y_G(1-R_G)} = \frac{I_S}{Y_S(1-R_S)} \quad (3.14)$$

where I, R and Y refer to the photocurrent, reflectivity and yield per absorbed photon respectively and the subscripts S and G are the sample and gold film. The yield of gold over the range 3.0 - 11.0 eV is known (Krolikowski and Spicer, 1970) and thus the yield of the sample was calculated as the other variables were measured or computed.

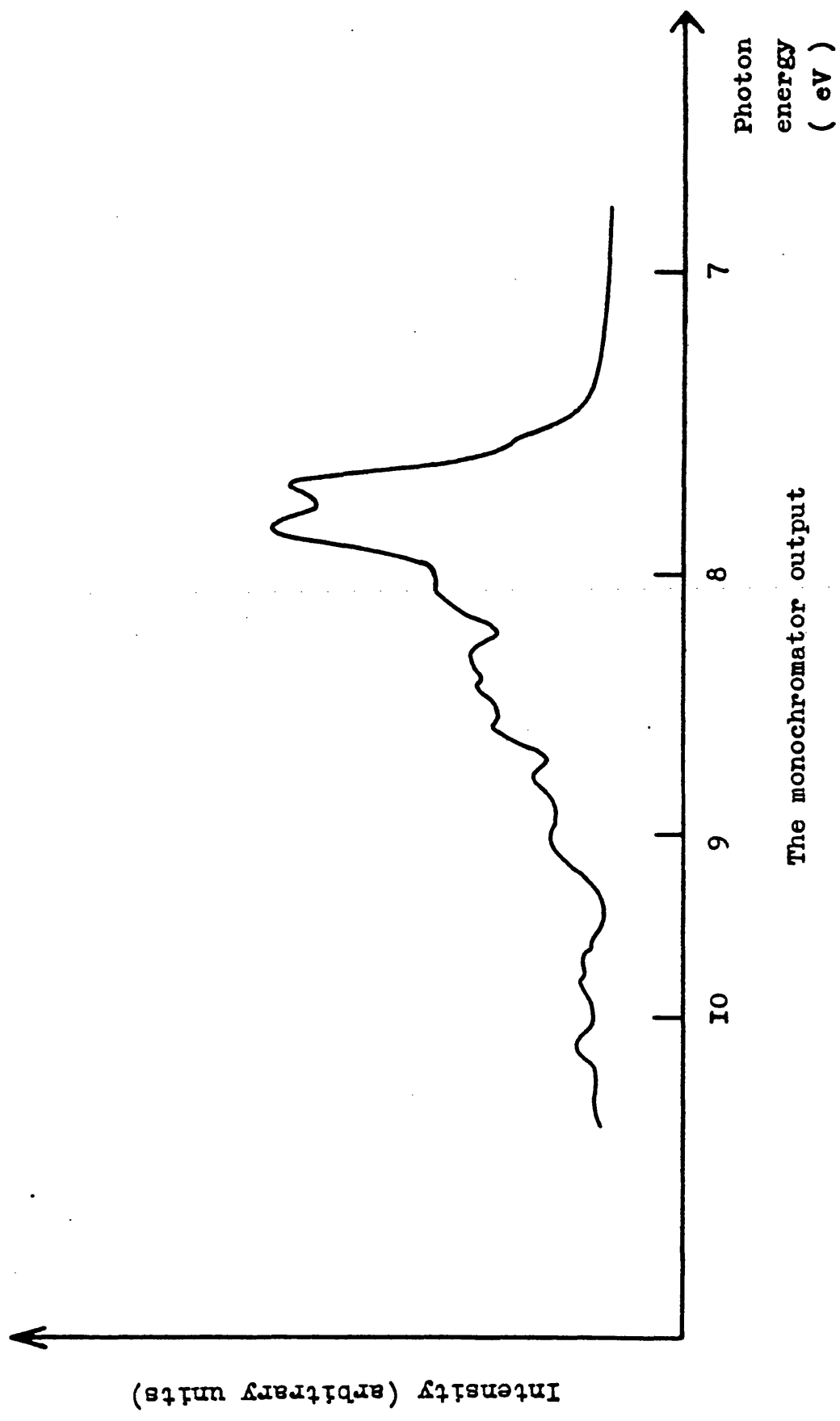


Figure 3-I3

CHAPTER 4

LITHIUM

Photoemission spectra at two photon energies are reported for liquid lithium. The analysis of this data allows the assumption of constant matrix elements to be tested. The optical density of states is extracted from the photoemission data and compared to calculations of the density of states. A deviation is found from the free electron parabola. Evidence is presented for the presence of surface photoemission.

4.1 Introduction

Lithium belongs to the class of alkali metals which are simple metals expected to exhibit free electron properties (Kittel, 1976). The structure of lithium in the crystalline and liquid phases is summarized in figure 5-2.

The electron band structure of lithium has been calculated by Ham (1962) using the quantum defect and the Green's function method, O'Keefe and Goddard (1969) using ab initio pseudopotentials and Rudge (1969) using the self-consistent augmented plane wave method.

The density of states of liquid lithium has been calculated by Shaw and Smith (1969) using a perturbation expansion of the electron energy and the full nonlocal form of the optimum model potential. Ichikawa (1973) calculated the density of states by a similar method and found a substantial deviation from the free electron parabola. Kuroha and Suzuki (1974) repeated the calculation using both the Green's function method and the perturbation theory method. They found good agreement to the result of Shaw and Smith despite the use of a local potential, but found their results to be in disagreement with the result of Ichikawa.

Little experimental work on lithium regarding density of states information is available. Enderby (1972) reported photoemission measurements on liquid lithium but it is certain that the surface was contaminated, rendering the results inconclusive. The lithium K absorption edge has been measured by yield spectroscopy (Petersen, 1975 and Petersen and Kunz, 1977), the results being interpreted in terms of a rising density of states at the Fermi level. This data

superseded earlier data (Petersen and Kunz, 1974) where EDC measurements were tried but the intensity was found insufficient to obtain measurements. Kowalczyk et al (1973) attempted X-ray photoemission from an evaporated lithium film but found that the lithium valence band cross section was too small to give usable spectra. The data presented in this chapter represents the first reported photoemission measurements from an uncontaminated liquid lithium sample.

4.2 The Photoemission Spectrum of Liquid Lithium at $\hbar\omega = 21.2$ eV

Figure 4-1 shows the photoemission result from liquid lithium corrected for the transmission function of the analyser and plotted against the energy of the initial state in electron volts; the Fermi energy being set at zero eV.

Structure visible from E_F to ≈ -3.2 eV is ascribable to transitions from the lithium 2s band, superposed on a background of secondary electrons. The weak peak centred at ≈ -5.3 eV is attributed to excitation of a surface plasmon. Surface plasmon loss peaks were observed by Smith and Spicer (1969 a) in photoemission measurements of evaporated films of potassium, rubidium and caesium.

The plasmon feature in figure 4-1 is displaced in energy by ≈ 4.9 eV from the maximum of the lithium 2s band, giving this value for the plasmon energy. This is in good agreement with the surface plasmon values of 4.8 eV deduced by Mathewson and Myers (1972) from infra-red absorption measurements on a lithium film and 4.7 eV deduced by Callcott and Arakawa (1974) from a study of the ultraviolet optical properties of an evaporated lithium film. Kittel (1976) quotes 7.12 eV as the lithium bulk plasmon energy, corresponding to a surface plasmon energy of 5.04 eV. This suggests that the feature in

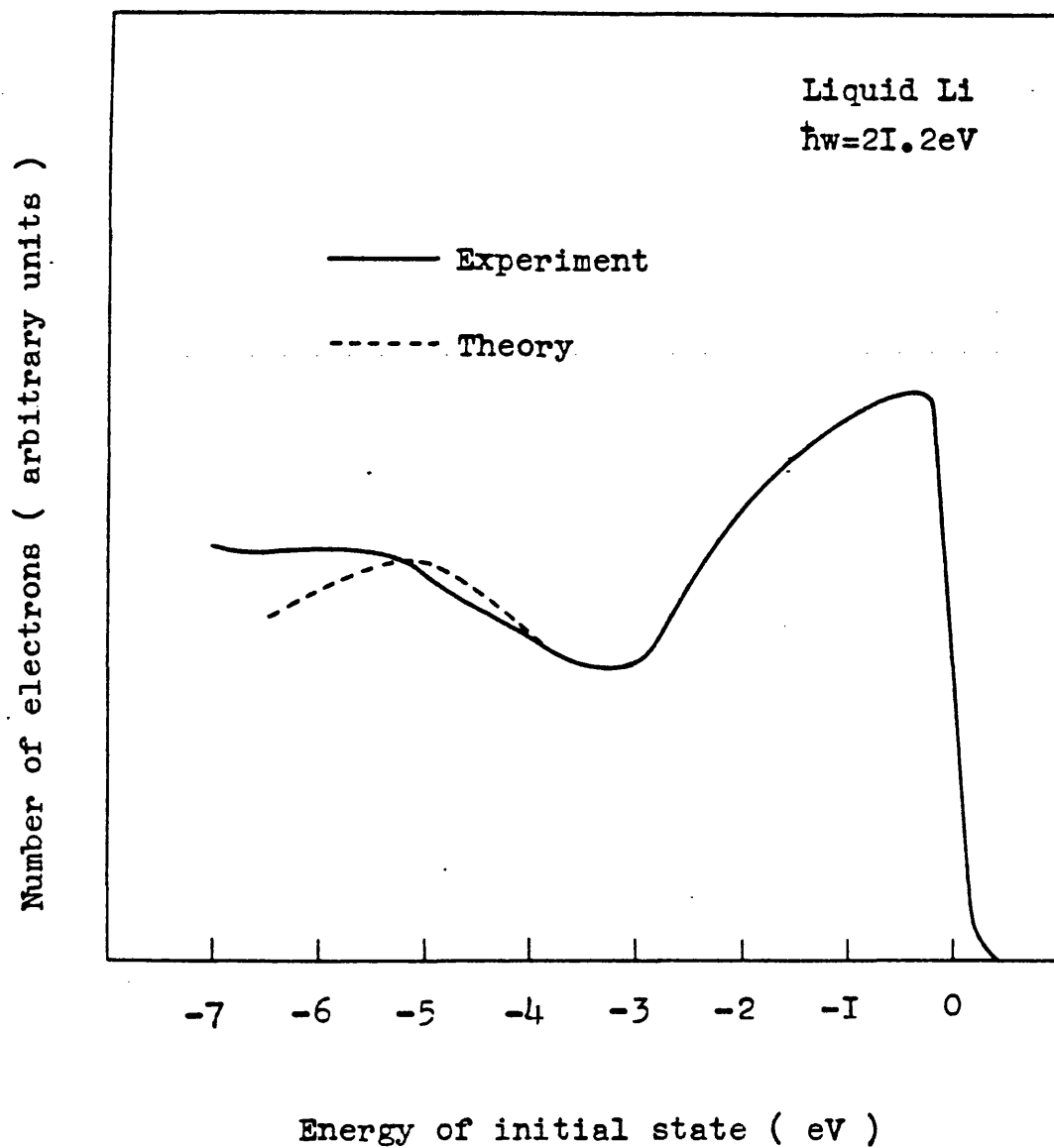


Figure 4-I

figure 4-1 is a surface plasmon loss mechanism and further suggests that surface photoemission is significant from liquid lithium. The consequences of this will be discussed later in this chapter.

4.3 The Optical Density of States of Liquid Lithium at $\hbar\omega = 21.2$ eV

The procedure described in chapter two was used to analyse the photoemission spectrum of figure 4-1 in order to extract the optical density of states (ODS) function. The energy distribution curve (EDC) generated by the computer simulation from the optimised ODS function is shown in figure 4-1. A comparison to the experimental EDC indicates that the plasmon loss feature is not perfectly modelled, but the overall agreement is good. The work function for the computation was taken from Weast (1979). The absorption coefficient of liquid lithium at $\hbar\omega = 21.2$ eV is not known (Kunz, private communication) and has not been reported at this photon energy for an evaporated lithium film, hence the absorption coefficient was used as an adjustable parameter. It proved impossible to fit the computer generated EDC to the experimental EDC using a value of the electron inelastic mean free path deduced from the universal curve (Seah and Dench, 1978) for the normalisation constant L_0 , and the computer simulations showed a lower value was more appropriate. Consequently the value 6\AA was calculated using the local density formalism of Lee and Beni (1977) based on the plasmon pole approximation for the dielectric function (Gurman, private communication).

The optimised ODS function is shown in figure 4-2 compared to the free electron parabola and the calculations of the density of states of liquid lithium of Shaw and Smith (1969) and Ichikawa (1973). Inspection shows that both calculated curves and the experimental

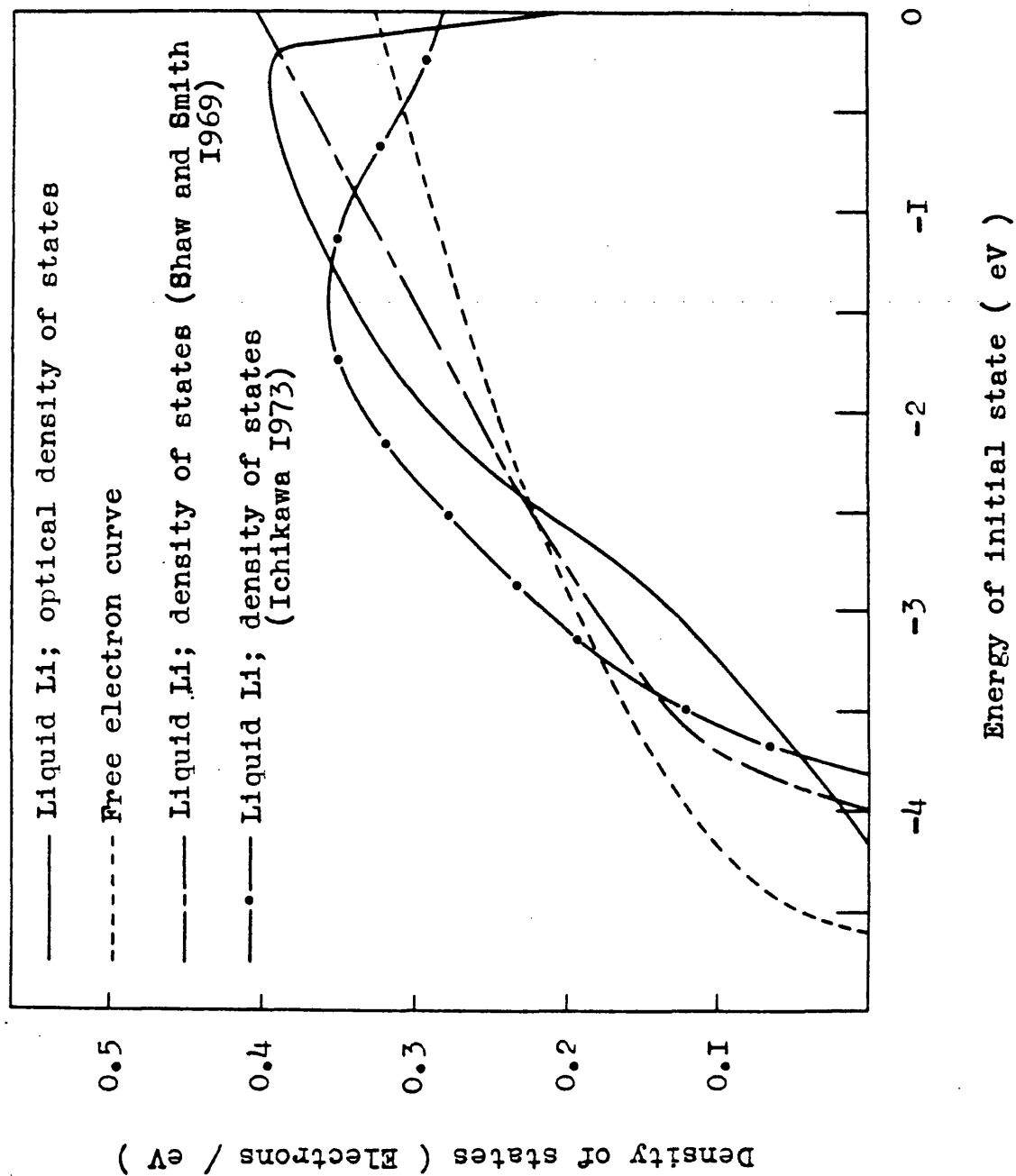


Figure 4-2

result show deviations from the free electron parabola. The experimental curve agrees in the value of the bandwidth to Shaw and Smith's result within 0.18 eV and within 0.35 eV to Ichikawa's result, but both calculations and the experimental result show a contraction over the value expected from the free electron theory.

The closest overall agreement with the experimental result is the calculation of Shaw and Smith; Ichikawa's result shows a broad maximum at ≈ -1.5 eV which is not shown by the experimental data and it also shows a decreasing density of states at the Fermi energy which contradicts the conclusions of Petersen (1975) and Petersen and Kunz (1977). Ichikawa's calculation is thus incompatible with the experimental data; Kuroha and Suzuki (1974) found that their calculations also did not agree with that of Ichikawa.

4.4 The Photoemission Spectrum of Liquid Lithium at $h\nu = 7.87$ eV

Figure 4-3 shows the photoelectron spectrum of liquid lithium at a photon energy of 7.87 eV. The vertical axis is calibrated in the number of electrons/absorbed photon/eV, using the procedure described in section 3-21. The reflectivity of gold at 7.87 eV was taken from the results of Canfield et al (1964). The reflectivity of liquid lithium is not known so a value was used for an evaporated film from the results of Rasigni and Rasigni (1976). The yield of gold was taken from the results of Krolikowski and Spicer (1970) and the total photocurrents from the lithium and gold specimens were measured as in section 3.21.

Figure 4-3 shows transitions from the lithium 2s band from E_F to ≈ -1.7 eV but the surface plasmon feature is not visible because of the reduced exciting energy. Figure 4-4 compares the EDCS of

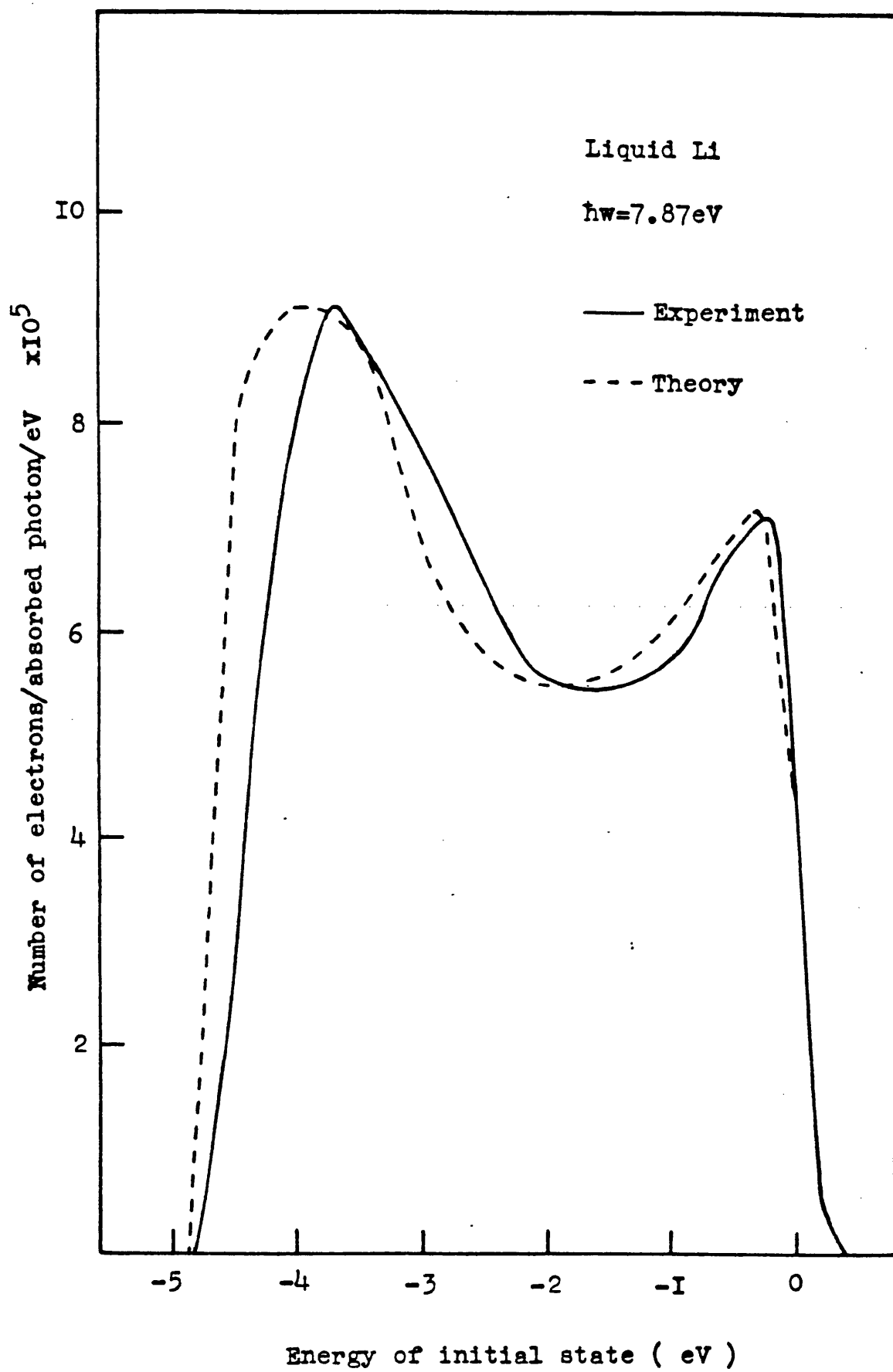


Figure 4-3

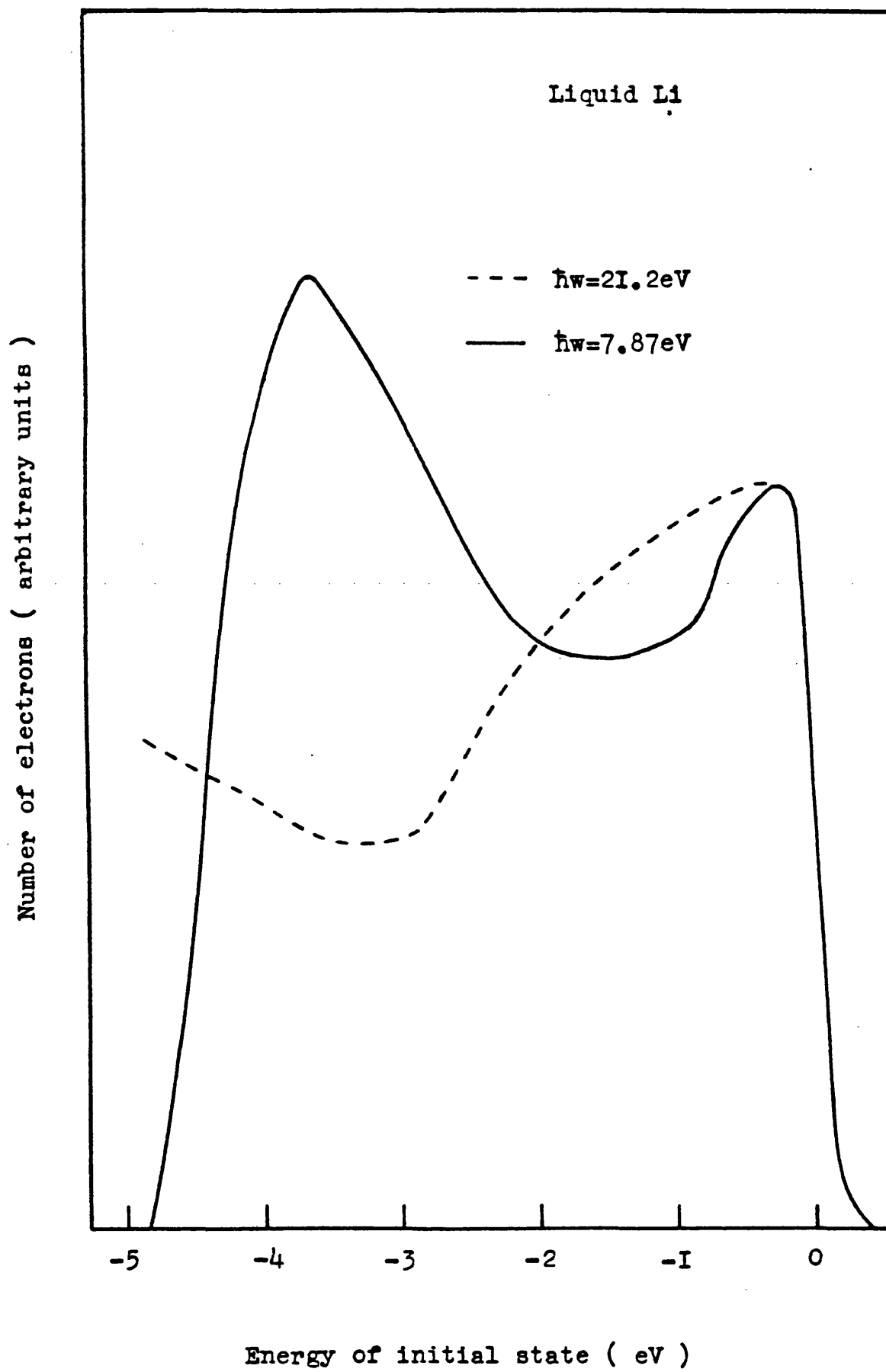


Figure 4-4

liquid lithium taken with the two photon energies, normalised to be of the same intensity at the Fermi level. The contraction of the peak attributed to primary electrons is clearly visible with decreasing photon energy; Smith and Spicer (1969 b) found the same effect in measurements on sodium and potassium in the form of evaporated films and explained it in terms of the direct (k conserving) nature of the optical transitions. In the framework of the analysis of chapter two the change of the matrix elements with photon energy (assumed constant) may be invoked to explain the change in the shape of the spectrum. A qualitative explanation of this effect is presented in section 4.7. A complete explanation of the effect is, however, complex because the data of section 4.2 suggests that surface photoemission occurs from liquid lithium (ie:- not all the signal originates from the bulk) and this is now briefly considered.

4.5 Surface Photoemission

Endriz (1973) performed calculations of the surface photoelectric effect, applied to aluminium but relevant to all nearly free electron metals at low photon energies where the relevant matrix element for surface excitation is (Petersen and Hagström, 1980):-

$$m = \text{const.} \int_{-\infty}^{+\infty} dz \left[A_z \frac{\partial \psi_i}{\partial z} + \frac{1}{2} \psi_i \frac{\partial A_z}{\partial z} \right] (\psi_f^+ - \psi_f^-) \quad (4.1)$$

where z is the direction normal to the surface, ψ_i and ψ_f are initial and final state wavefunctions, ψ^+ and ψ^- relate to whether the excited wave function is outgoing or incoming at large distances on the vacuum side of the metallic surface and A_z represents the z component of the vector potential of the exciting source. The second term in the matrix element accounts for the fact that there is a contribution

to the surface photocurrent which is caused by the changes of the electromagnetic field in the surface region, and photoyield measurements Petersen (1978) and Petersen and Hagström (1978) on aluminium have confirmed the significance of the $\frac{\partial A}{\partial z}$ term. This work suggests that a treatment including the field variations at the surface should be important for the interpretation of photoemission data whereas the three step model of chapter two assumes that the photoemitted signal originates from the bulk.

4.6 The Optical Density of States of Liquid Lithium at $\hbar\omega = 7.87$ eV

The optical density of states was extracted from the photoemission curve for liquid lithium (figure 4-3) using the procedure of chapter two. Input parameters for the calculation were used as in section 4.3 except for the absorption coefficient which was calculated from the optical properties of a lithium film (Callcott and Arakawa, 1974) and used as being the only data available.

It proved not possible to obtain a perfect fit between the experimental EDC and the computer simulation of the EDC; the best fit obtained is shown in figure 4-3 in which the relative intensities of the major features are correct but a detailed agreement is lacking. The ODS function used as an input is shown in figure 4-5 compared to the ODS function derived for liquid lithium at the higher photon energy (21.2 eV). The change in shape is explained qualitatively in the following section.

The ODS function of liquid lithium at $\hbar\omega = 7.87$ eV as shown in figure 4-5 reveals a deviation from the free electron parabola as may be expected from the $\hbar\omega = 21.2$ eV experiment, and similar comments apply to its functional form when compared to the theoretical

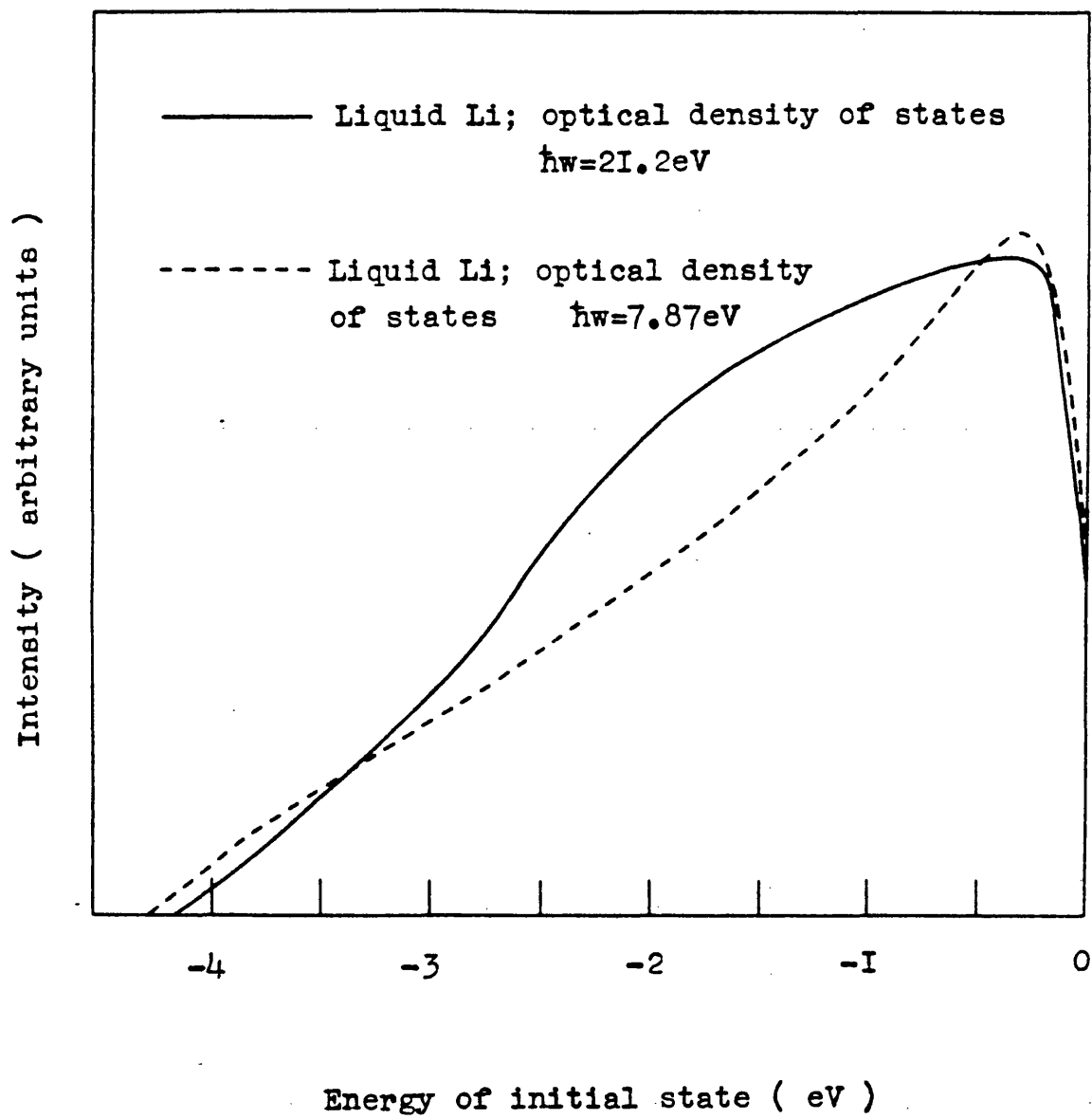


Figure 4-5

density of states calculations as in the case of the ODS derived in the higher photon energy experiment.

4.7 The Effect of the Matrix Elements

That the simple model of chapter two assuming direct transitions and constant matrix elements breaks down may be seen by reference to figure 4-6 which shows the computer generated EDC from the optimised ODS function derived from the $\hbar\omega = 21.2$ eV data compared to the experimental EDC from the $\hbar\omega = 7.87$ eV experiment. The simulation fails to predict the correct relative intensities of the primary and secondary electron peaks and also the dip in the EDC at ≈ -1.5 eV.

An explanation for the change in shape of the ODS function with photon energy (figure 4-5) may be given by reference to figure 4-7 and explained in terms of matrix element effects. If, as one extreme, the interference function for liquid lithium is taken to be of constant value, then the matrix element term can be ignored and the emitted electron distribution is principally governed by the initial density of states (equation (2.8)). At the other extreme, the interference function can be assumed to be dominated by the principal peak which for liquid lithium is located at $q = 2.4 \text{ \AA}^{-1}$ (Jacucci et al, 1976). It is then assumed for a transition that the momentum transfer must have this value, ie:-

$$| \underline{k}_f - \underline{k}_i | = 2.4 \text{ \AA}^{-1} \quad (4.2)$$

and also:-

$$E_f - E_i = \hbar\omega \quad (4.3)$$

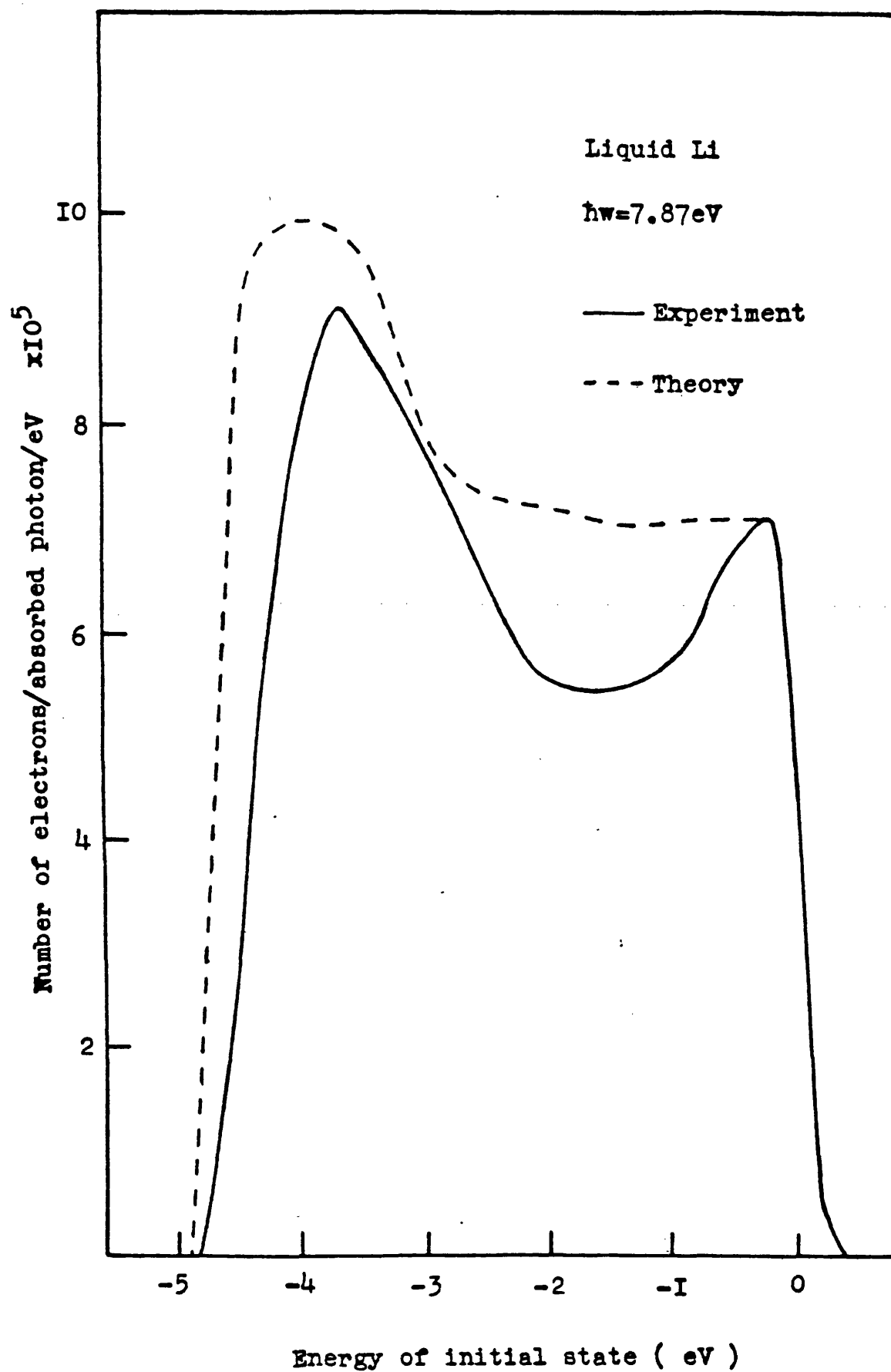


Figure 4-6

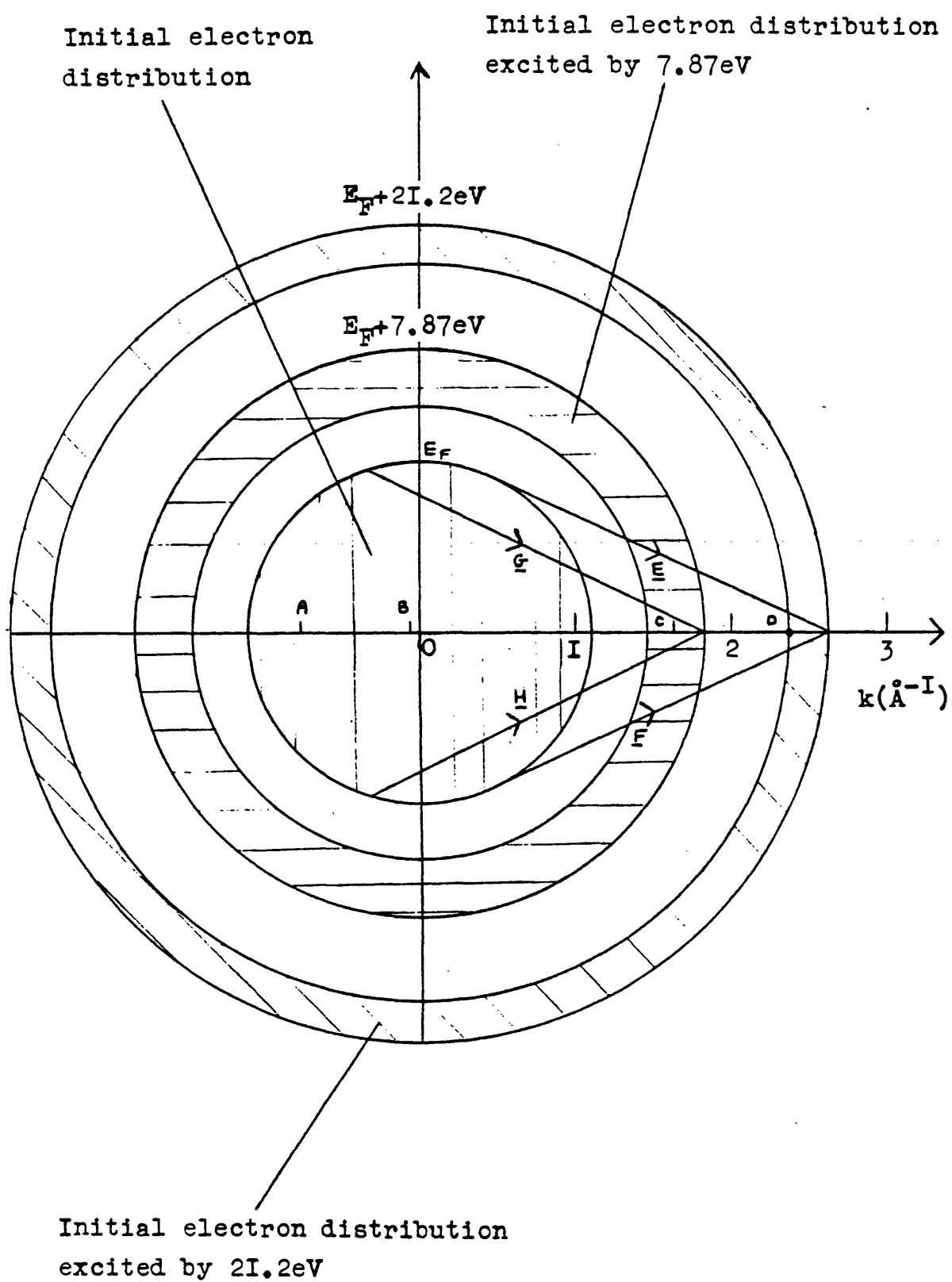


Figure 4-7

where the subscripts f and i refer to final and initial states. If liquid lithium is taken to be free electron like, then the constant energy surfaces are spheres in \underline{k} space as in figure 4-7 which shows the initial electron distribution and the initial electron distribution excited by 7.87 eV and 21.2 eV. In both cases, transitions are possible from E_F as shown by vectors \underline{E} , \underline{F} , \underline{G} and \underline{H} , which are all 2.4 \AA^{-1} long. For 21.2 eV emission, the initial distribution can be probed as far as point B which lies at a \underline{k} value corresponding to an energy of 0.008 eV. The \underline{q} vector representing the transition then connects point B to point D which lies very close to the bottom of the excited band which is drawn in both cases as though all the band can be probed. This vector obeys (4.2) and (4.3) and shows that for 21.2 eV, 99% of the band is accessible. For 7.87 eV radiation, the band can be probed as far as point A which corresponds to an energy of 2.25 eV, the \underline{q} vector representing this transition then connects point A to point C and 51% of the band is accessible. It is not possible to probe deeper without violating (4.2). This means that within the confines of this simple model, increasing the photon energy allows more of the band to be probed; in figure 4-5 this is represented by the increase in intensity of the 21.2 eV derived curve compared to the 7.87 eV curve at an energy corresponding to one half of the bandwidth, ie:- the 21.2 eV curve "bulges" more than the 7.87 eV curve.

4.8 Summary

The optical density of states functions of liquid lithium derived from photoemission experiments at two well separated photon energies reveal deviations from the free electron parabola. This

suggests that liquid lithium is not a good example of the NFE metal as liquid sodium and potassium are taken to be (Shimoji, 1977).

However, this analysis was performed using the three step model of photoemission which assumes bulk electron emission whereas part of the data of this chapter indicates that surface photoemission is not unimportant. The assumption of the constancy of the matrix elements has also been shown questionable and a simple, qualitative explanation of the effect of the change of the matrix elements has been given in relation to the photoemission data. Williams and Norris (1975) have also reported a model for aluminium where the effect of the matrix elements was included. These two factors suggest a more sophisticated model is desirable for a better interpretation of the data. Such a model may yield a better agreement between the experimental and theoretical EDCS of liquid lithium at $\hbar\omega = 7.87$ eV.

CHAPTER 5

THE LITHIUM-LEAD AND LITHIUM-TIN ALLOY SYSTEMS

A REVIEW OF THEIR PROPERTIES AND PHOTOEMISSION RESULTS FROM THE ALLOYS AND PURE METALS

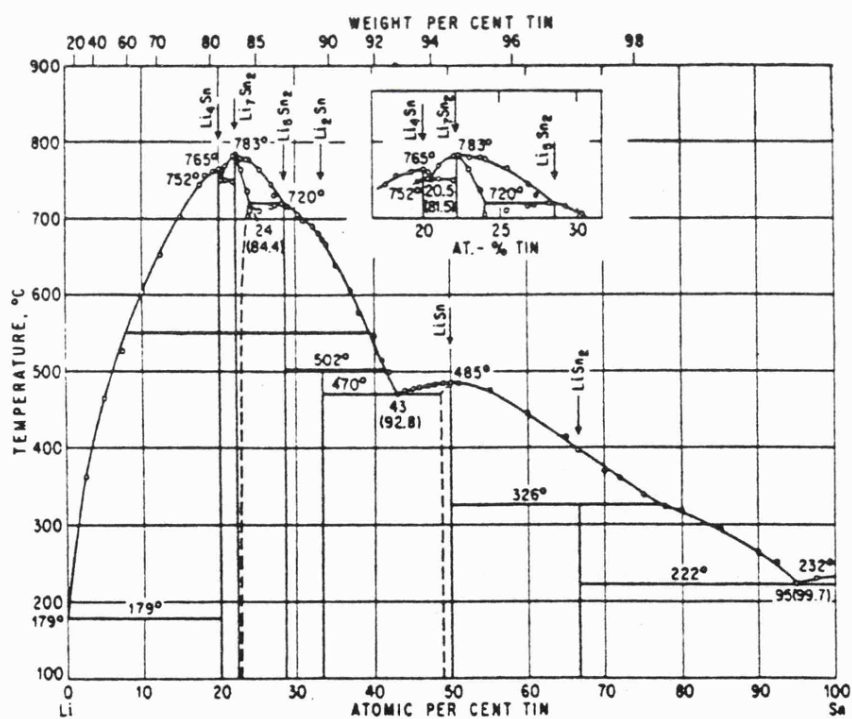
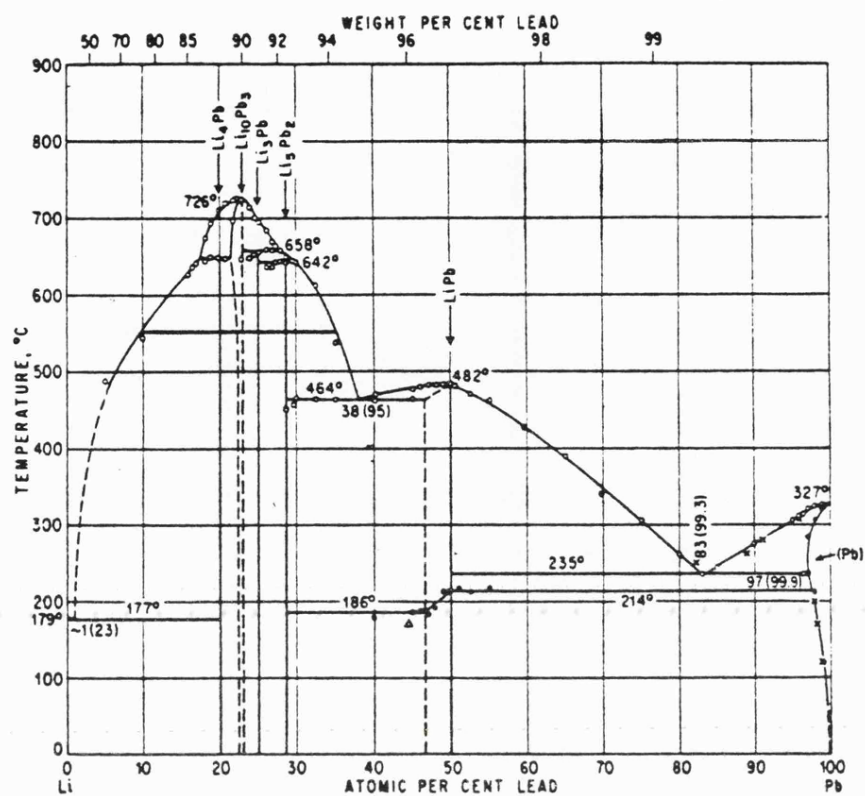
A review of the properties of the lithium-lead and lithium-tin alloy systems is given. Theories of the electronic structure of liquid semiconductors are presented and the ionic model, as exemplified by the caesium-gold system, is discussed. The photoemission results from both alloy systems are presented and analysed and finally the optical density of states function for lead and tin is extracted and compared to other spectroscopic data and theoretical calculations.

5.1 The Phase Diagrams

Figure 5-1 shows the phase diagrams for the lithium-lead and lithium-tin alloy systems (Hansen, 1958). The similarity in the liquidus curve for each system is striking; both curves showing a eutectic point at low lithium concentrations, a plateau at the equi-atomic concentration alloys, a kink close to the 40 atomic % mark (referred to the heavier element) and a maximum melting temperature close to the 20 atomic % composition. The similarity in the change of the magnitude of the liquidus temperature for both systems is expected because lead and tin exhibit like elementary chemical behaviour, both having a tendency to form compounds with valencies of two and four.

Figure 1-5, which shows the resistivity and thermopower for the lithium-lead system, illustrates that near the 20 atomic % concentration the resistivity and liquidus temperature both reach a maximum value and the thermopower passes through zero; there is thus a correlation between the electronic and thermodynamic properties.

The relatively high temperature of melting of the 20 atomic % composition of both alloy systems posed one important practical point which limited the experimental range. Although each constituent metal in its pure form at its melting point had a vapour pressure which caused no experimental problems, by virtue of being low (ie:- 6×10^{-9} torr for lead, 10^{-10} torr for lithium and even lower for tin), the vapour pressure of lithium rose steadily with temperature until it reached a value of 10^{-2} torr at a temperature of 550°C which represented the upper maximum which could be tolerated above which the sample loss through evaporation became too large.



Phase diagrams of the Li-Pb and Li-Sn systems

Figure 5-I

At this temperature the vapour pressure of lead was two orders of magnitude smaller and that of tin nine orders of magnitude smaller, thus the vapour pressure of lithium dominated, restricting the range of alloys which could be studied to those having melting points below 550 °C as indicated in figure 5-1.

5.2 Atomic Structure and Thermodynamic Behaviour of the Lithium-Lead System

There has been no probing of the structure and thermodynamic properties of the lithium-tin alloy reported in the literature, but lithium-lead has been extensively examined and a review is now given. General arguments, however, should also apply to the lithium-tin alloy.

Three basic models can be defined describing the atomic arrangement of a liquid binary alloy. The first model is an extension of the theory of a liquid simple metal where the atoms are considered as a system of randomly packed hard spheres. Thus in a binary alloy the two atomic species are distributed at random and deviations of physical and chemical properties are explained by a change of electronic states compared to the pure constituents.

Alternatively it has been argued (Cohen and Sak, 1972) that the special physical, chemical and metallurgical effects seen in some liquid alloys are related to the formation of compound clusters which are embedded into a largely disordered matrix but experimental and theoretical evidence has been presented against their existence (Turner, 1973).

An intermediate viewpoint is due to Wagner (1940) who pointed

out that for large negative deviations from Raoult's Law (eg: lithium-lead) the concept of a regular solution involving the random distribution of the constituent atoms is unrealistic. However the formation of groups of atoms into definite molecules having a long lifetime is also unlikely considering their non-existence in the crystal state, thus in liquid alloys the same type of short range order might exist as in solid, disordered solutions and according to Wagner the properties of the alloys depend strongly on the electronic state; the same electron distribution being possible in the liquid state and the corresponding solid phase.

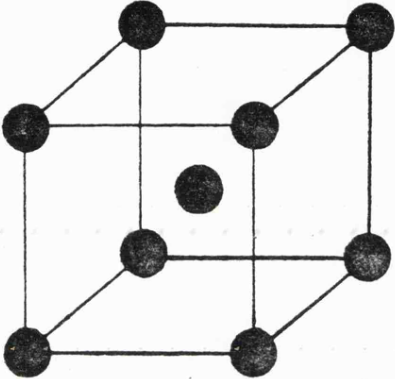
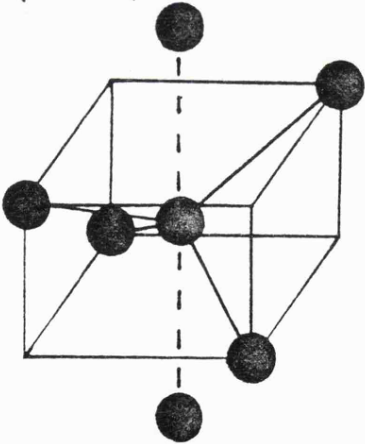
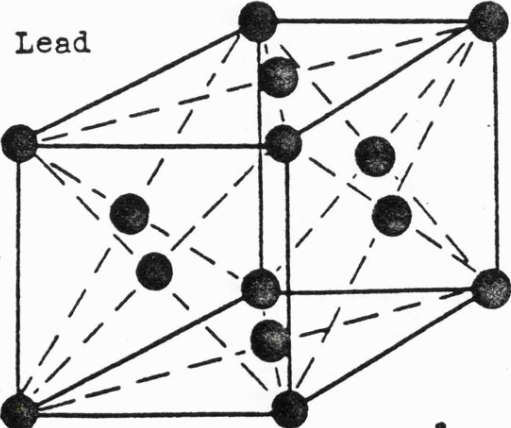
The structure of the lithium-lead system was probed by Ruppertsberg and Egger (1975) using neutron diffraction and Ruppertsberg and Reiter (private communication) using neutron and x-ray diffraction. Their conclusions support Wagner's hypothesis. The results showed at the 20 atomic % composition an unambiguous preference for unlike nearest neighbours with the same sort of short range order existing over a large concentration range. No evidence was found to support the idea of isolated Li_4Pb clusters existing in the melt; such a postulate was found incompatible with the radial concentration correlation function curve of liquid Li_4Pb and also incompatible with the large packing fraction of the liquid alloys (≈ 0.6) which is as large as that of simple liquid metals (≈ 0.61 to ≈ 0.63) thus leaving no space for a significant separation of Li_4Pb clusters from the matrix. The idea of clusters was also found inconsistent with the coherent scattering intensity at $q = 0$ ($q = 4\pi \sin \theta/\lambda$) for the Li_4Pb composition which, as demonstrated by Bhatia et al (1974), would then have a sharp minimum at that composition and would rise above the value of the ideal solution at higher lead contents which was

found not to be so. Other properties of the liquid lithium-lead alloy reported were a negative excess volume on mixing with a minimum value of $\approx 15\%$ at the 20 atomic % composition with a corresponding decrease, in the liquid phase, of the distance between unlike nearest neighbours compared to that expected from the mean of the corresponding distances of the pure components as shown in figure 5-2.

These observations correlate well to the data of Zalkin and Ramsey (1958) who completed the structure determination of the five lithium-lead intermetallic systems (Li Pb , Li_8Pb_3 , Li_3Pb , Li_7Pb_2 , $\text{Li}_{22}\text{Pb}_5$) by x-ray diffraction. They correctly labelled the most lithium rich compound as $\text{Li}_{22}\text{Pb}_5$ and not Li_4Pb as reported by Grube and Klaiber (1934) from thermal analysis data. The results of the investigations of Zalkin and Ramsey of the five intermetallics may be summarized as:-

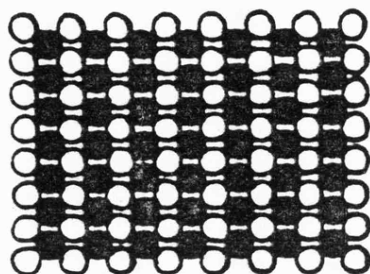
- 1) They all have almost the same over-all structure which is body-centred cubic as found in solid lithium.
- 2) The appropriate number of lithium atoms is substituted by lead atoms to prevent a direct contact between lead atoms where possible.
- 3) The formation of the compounds leads to a substantial reduction in volume as compared to the sum of the volumes of the pure constituents.

Lithium-lead distances as low as 2.82 \AA were found in the solid alloys showing a contraction over the interatomic distances of the pure components (figure 5-2), illustrating point (3) above and correlating well with the liquid structure. The atomic arrangements of the intermetallics are shown in figure 5-3:- in Li_8Pb_3 some lead atoms touch each other but this is the most efficient way of distributing the lead atoms given the 8/3 ratio and in $\text{Li}_{22}\text{Pb}_5$ there

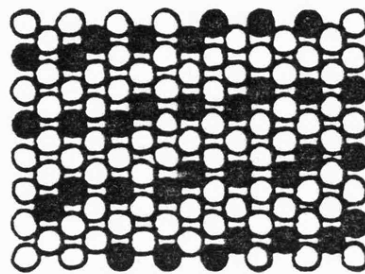
Structures of Pure Constituents		LIQUID	
SOLID (Wyckoff; 1963)		(a) Waseda; 1976 (b) Ruppersberg and Egger; 1975	
		Coordination Number	Nearest Neighbour Distance (\AA)
Lithium  <p>8 neighbours at 3.05 \AA</p> <p>body centred cubic</p>		9.5 (a)	3.15 (a) 3.0 (b)
Tin (white)  <p>4 neighbours at 3.02 \AA</p> <p>2 neighbours at 3.15 \AA</p> <p>body centred tetragonal</p>		10.9 (a)	3.23 (a)
Lead  <p>12 neighbours at 3.50 \AA 6 neighbours at 4.95 \AA</p> <p>face centred cubic</p>		10.9 (a)	3.33 (a) 3.4 (b)
		Figure 5-2	

○
Lithium

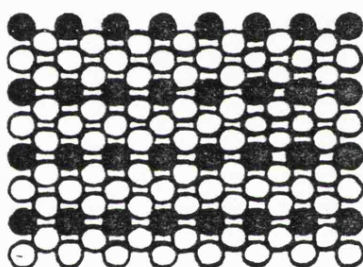
●
Lead



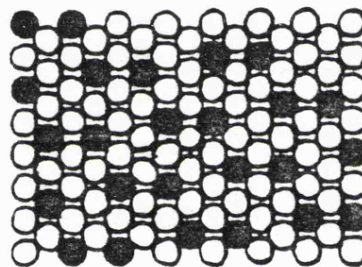
LiPb (rhombohedral and cubic)



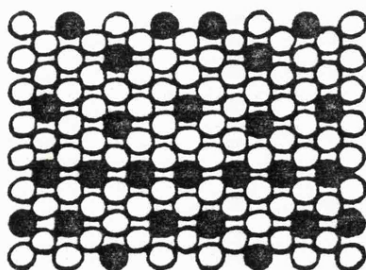
Li_8Pb_3 (monoclinic)



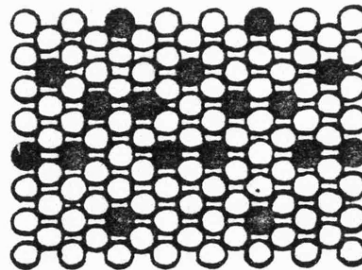
Li_3Pb (face centred cubic)



Li_7Pb_2 (hexagonal)



$\text{Li}_{22}\text{Pb}_5$ (face centred cubic)



Comparison of the atomic arrangements in the
compounds of the Li-Pb system

Figure 5-3

are two types of layers differing only in the number of lead atoms per layer, these layers then stacking to arrange a uniform distribution of the lead atoms.

A brief summary shows there are similarities in behaviour between the liquid state and the solid compounds; both exhibit a volume contraction over the pure constituents with a preference for unlike nearest neighbours, the liquid structure mirroring the solid structure with lead atoms replacing lithium to prevent direct contact between the lead atoms. Ruppersberg and Egger proposed that the origin of the short range order in the liquid phase was the rearrangement of the electronic states on mixing the pure components leading to a transfer of charge from lithium to lead (lead being the more electro-negative of the two elements), ie: partially saltlike bonding. The charge transfer postulate will be discussed later in this chapter.

Hoshino and Young (1980 a), however, proposed a model for the entropy of mixing of compound forming liquid binary alloys, applied to the lithium-lead system, where the formation of a "molecule" of Li_4Pb was assumed, although the authors pointed out that their use of the word molecule need not imply a simple molecule in the standard chemical sense. The two atomic species and the molecule were modelled as hard spheres; the diameter of the molecule was taken as an adjustable parameter. The large volume contraction of the alloy near the 20 atomic % concentration calculated from the experimental density data of Ruppersberg and Speicher (1976) was considered to be strong evidence for the formation of molecules. The concentration dependence of the entropy of mixing was calculated and compared to the experimental data of Demidov et al (1973) and Saboungi et al (1978) with good agreement using a value of 3 \AA for the hard

sphere diameter of the molecule. The formation of molecules was suggested as being responsible for the negative value of the entropy of mixing as the model predicted this result near the Li_4Pb concentration when neglecting the volume change on alloying in contrast to the case of the interpretation of the excess entropies of simple non-compound forming mixtures. The model was extended in a later publication (Hoshino and Young, 1980 b) and used to calculate the resistivity as a function of composition showing good agreement to the experimental results of Nguyen and Enderby (1977). The large negative temperature coefficient of the resistivity at the Li_4Pb composition was qualitatively explained by the stability of the molecules decreasing with increasing temperature.

The problem of the anomalous thermodynamic properties of liquid semiconducting alloys was tackled by Schirmacher (1980) with emphasis on the lithium-lead system. The isothermal compressibility, the partial volumes and the stability of liquid semiconducting alloys were presented in terms of the low wavenumber limit of the partial structure factors. By using the random phase approximation for the Ornstein - Zernike direct correlation functions, the quantities were shown to be composed of a hard core part and a part coming from the long range interatomic potentials which were assumed to be composed of a metallic part treated by pseudopotential theory plus an electronically screened attractive Coulomb interaction due to charge transfer. Using the additional assumption of a reduced electronic density of states near the Li_4Pb composition, the measured anomalies were qualitatively explained and reasonable agreement was found for the compressibility, volume change and stability with the data of Ruppertsberg and Speicher (1976), Saboungi et al (1978) and Ruppertsberg and Egger (1975). The

charge transfer was calculated as ≈ 0.8 electrons transferred to each lead site at the Li_4Pb composition.

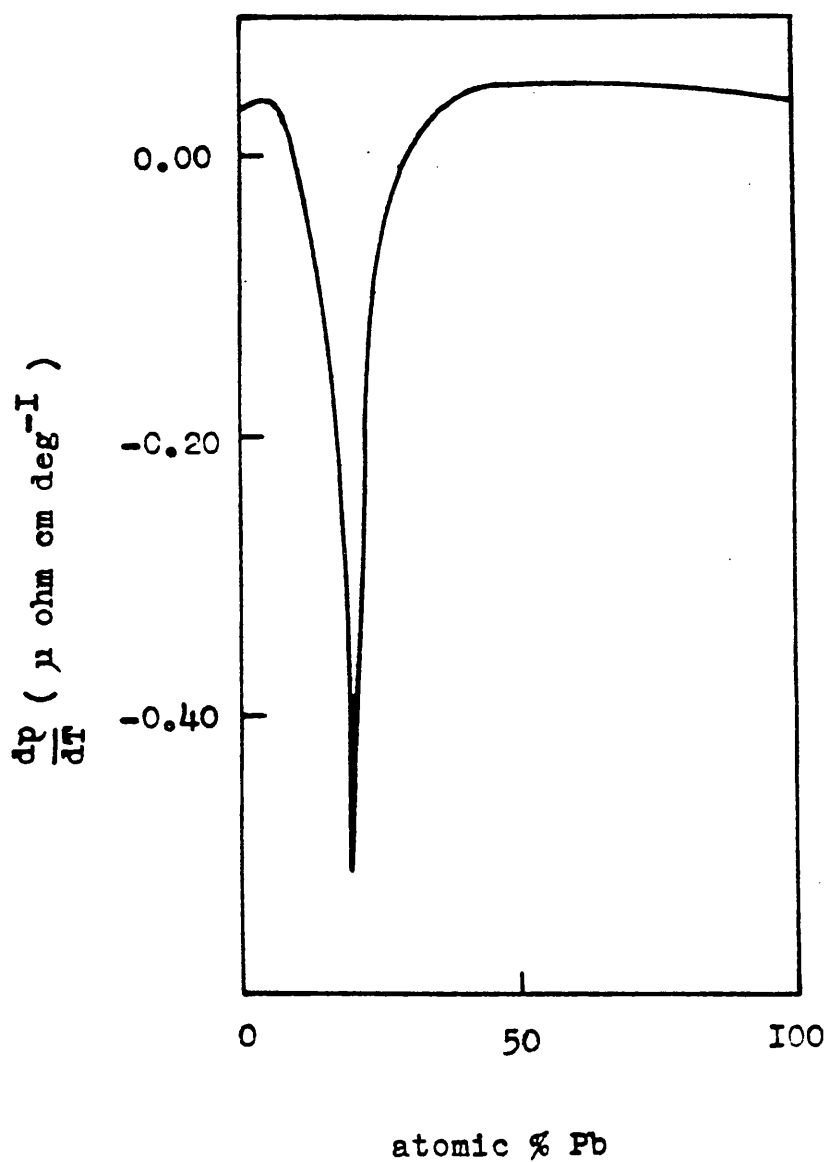
A brief summary of the structural aspect concludes that although the theoretical model of Hoshino and Young can explain many properties it contradicts the direct experimental diffraction data which indicates short range order with a strong preference for unlike nearest neighbours, a volume contraction compared to the sum of the pure components and a degree of charge transfer to the lead sites.

5.3 Electronic Properties of the Lithium-Lead and Lithium-Tin Systems

Apart from the Knight shift, there have been no reported measurements on lithium-tin in the literature and the following section will deal mainly with the properties of the lithium-lead system; the resistivity and thermoelectric power have been shown previously (figure 1-5). At the Li_4Pb composition, the conductivity value implies that the mean free path of the electrons remains fairly long and the thermoelectric power must then be interpreted within the framework of the accepted equations (section 1.9). The change in resistivity with temperature has also been reported (Nguyen and Enderby, 1977) and is reproduced (figure 5-4). Other properties covered in the literature are:-

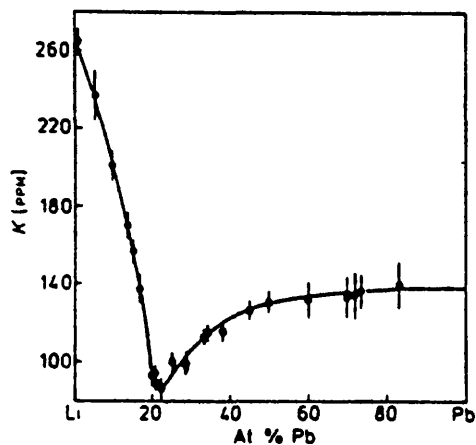
(i) The Knight Shift

The ^7Li Knight shift of liquid lithium-lead and lithium-tin alloys was reported by Van der Marel et al (1980). Their results reproduced in figure 5-5, show singularities at compositions close to Li_4X ($\text{X} = \text{Pb}$ or Sn) and a strong similarity in the behaviour of the two systems. The decrease in the Knight shift was attributed to a transfer of charge towards the more electronegative element (lead or tin)

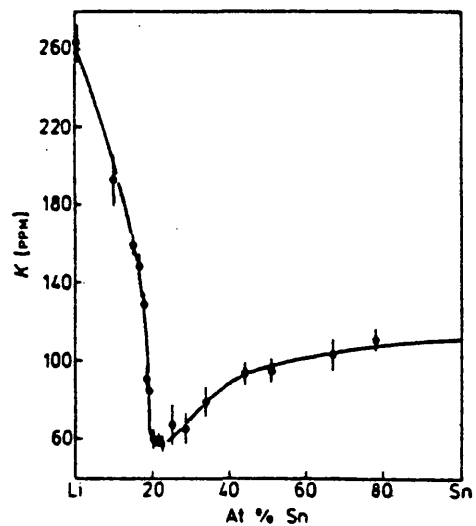


Change in resistivity with temperature
as a function of concentration for
Li-Pb system at 800°C.

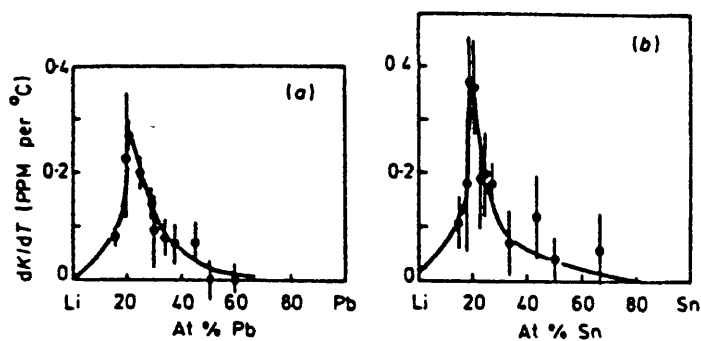
Figure 5-4



^7Li Knight shift in liquid Li-Pb alloys at the liquidus temperature.



^7Li Knight shift in liquid Li-Sn alloys at the liquidus temperature.



Temperature derivative of the ^7Li Knight shift dK/dT in: (a) liquid Li-Pb; (b) liquid Li-Sn.

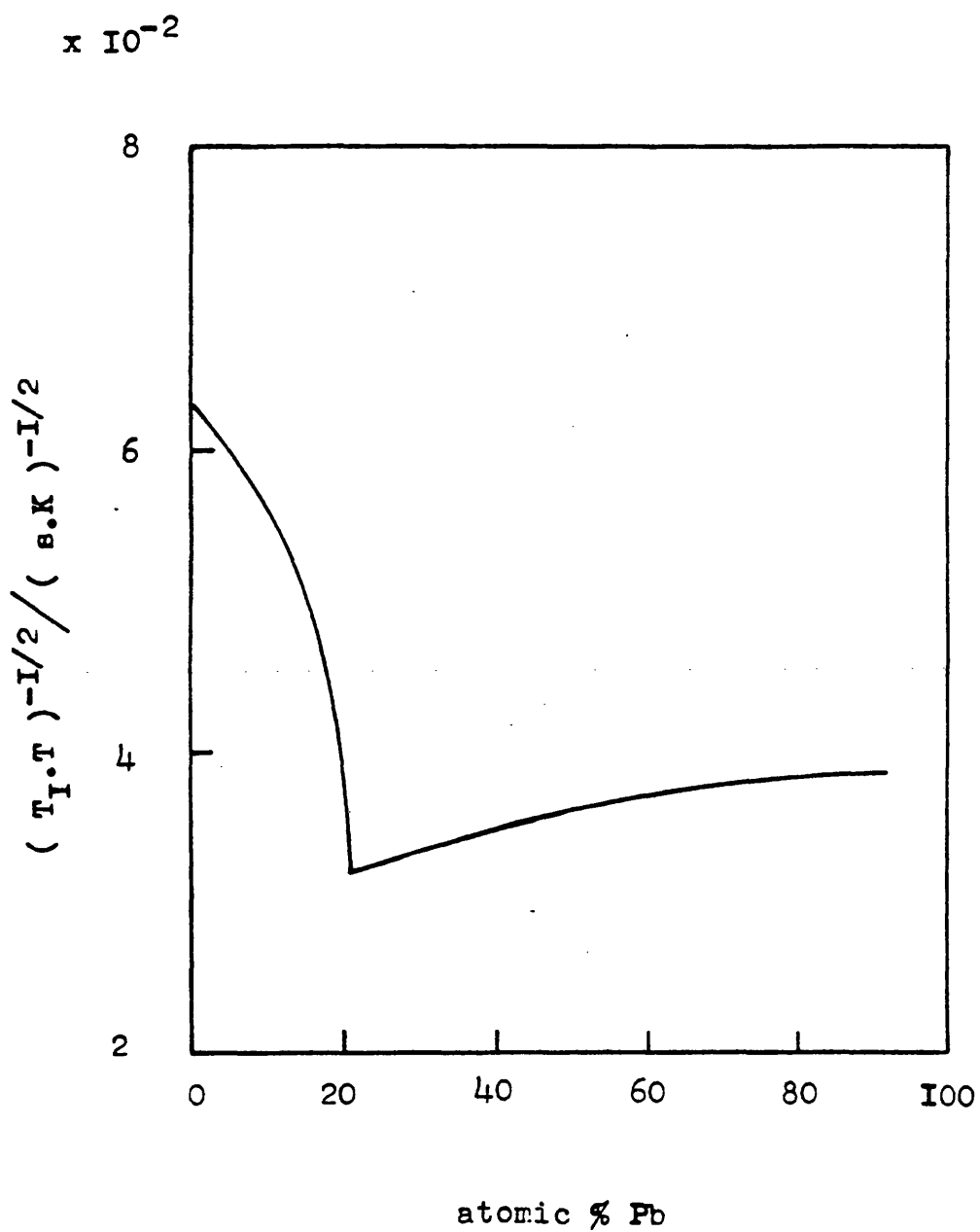
leading to a reduction of the Fermi surface average of the electron contact density at the ${}^7\text{Li}$ nuclei. The results were found to be consistent with the electronic structure model of Avci and Flynn (1979 - section 5.4) and with the prediction that $K \propto \sigma^{\frac{1}{2}}$ in the diffusive scattering regime (Mott and Davis, 1971) at the Li_4Pb composition where both the temperature derivative of the Knight shift and the temperature derivative of the conductivity show maximum values.

(ii) The Nuclear Spin-Lattice Relaxation Rate

The nuclear spin-lattice relaxation rate T_1^{-1} , which is dominated by magnetic hyperfine interaction with conduction electrons, of ${}^8\text{Li}$ in liquid lithium-lead was measured by means of the asymmetric β -decay radiation of polarized ${}^8\text{Li}$ nuclei as a function of temperature T , and solute concentration by Heitjans et al, 1980. The product $(T_1 T)^{-\frac{1}{2}}$ was found to vary about linearly with concentration in lithium-sodium and lithium-magnesium but in lithium-lead it showed a marked minimum near the Li_4Pb concentration, figure 5-6, which was ascribed to the compound forming tendency of the elements in the melt and charge transfer to the lead leading to partial ionic bonding. The inverse Korringa product (Korringa, 1950) was calculated as a function of composition which showed a significant enhancement around the Li_4Pb concentration, and the results for the enhancement of the experimental rate over the Korringa rate were compared favourably to the prediction of Warren (1971) where the enhancement factor η was related to the conductivity by the relation:-

$$\sigma \eta \approx \sigma_0 \quad (5.1)$$

where σ is the conductivity and σ_0 is a constant depending on the interatomic distance.



Concentration dependence of $(T_I.T)^{-1/2}$
of ^8Li in liquid Li-Pb at $T=1000\text{ K}$.

Figure 5-6

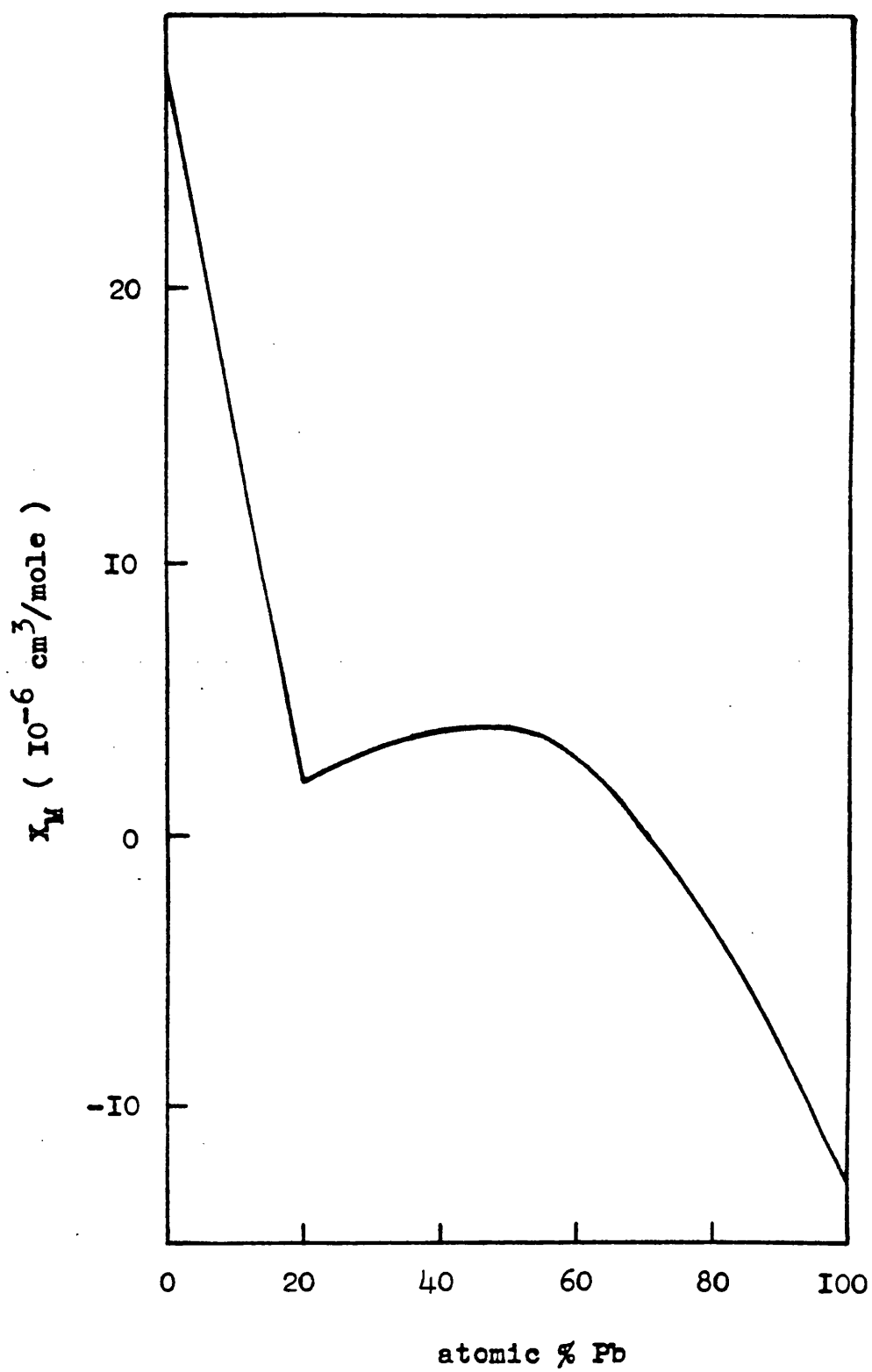
(iii) The Magnetic Susceptibility

The DC magnetic susceptibility of lithium-lead was reported by Hackstein et al (1980), which showed a diamagnetic minimum at the Li_4Pb composition (figure 5-7) and not a smooth transition between the two pure metals as would be expected from the free electron model. No analysis of the experimental data was attempted.

(iv) Theoretical Approaches to Resistivity Calculations

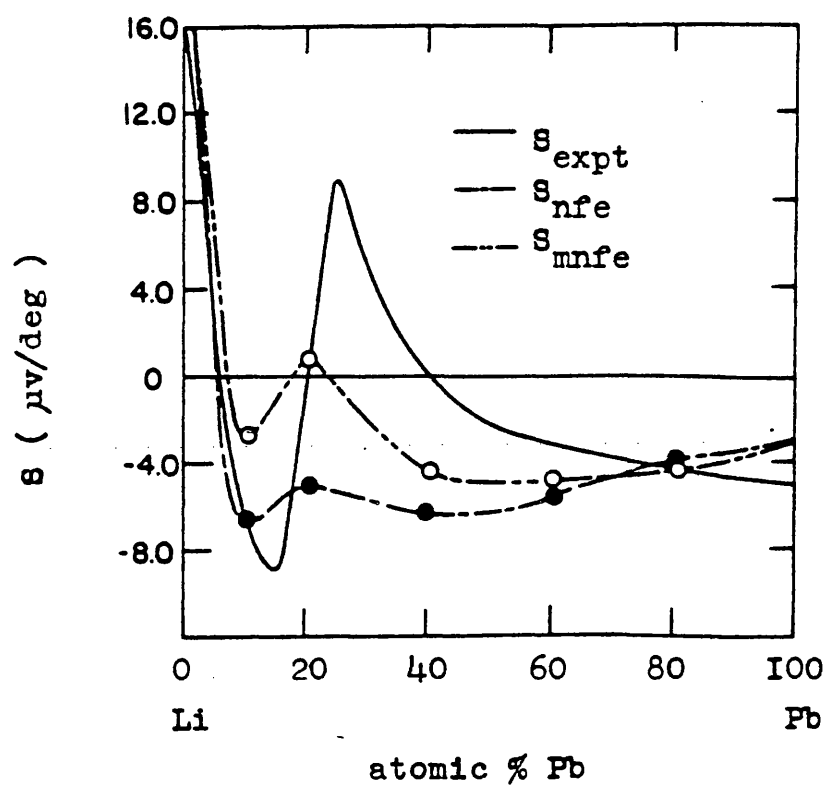
A more sophisticated calculation than that of Hoshino and Young (1980 b) was reported by Wang and Lai (1980) where a self-consistent pseudopotential theory was used to calculate the transport coefficients as a function of composition for liquid lithium-lead and the excess charge on the more electronegative (lead) ions was calculated to be ≈ 0.4 electrons (compared to Schirmacher's value of ≈ 0.8 electrons). The calculated resistivity curve was improved around the Li_4Pb composition by replacing the first order density of states effective mass by the electron density of states effective mass of the alloy at a particular concentration and it was speculated that even better agreement would be obtained by including the effect of the enhancement of the electron orbital angular momentum due to partial localization on a lead site; the resistivity being increased by the spin orbital interaction which is known to increase the resistivity of liquid lead by $\approx 7\%$ (So et al, 1978). Further evidence of charge transfer was provided by a calculation of the thermoelectric power using a modified nearly free electron formula including charge localization which showed better agreement in sign to the experimental data, figure 5-8, than the usual nearly free electron formula.

Lai and Wang (1981) considered the anomalous temperature dependence of the resistivity in lithium-lead which was attributed



Mole susceptibility of Li-Pb at 900°C .

Figure 5-7



Thermoelectric power of Li-Pb system at $T=800^\circ\text{C}$.

Figure 5-8

primarily to the significant decrease of charge localization on the more electronegative atom and computed a value for the change in resistivity with temperature for liquid Li_4Pb at 800°C of $-0.347 \mu\Omega \text{ cm deg}^{-1}$ in reasonable agreement to the experimental value of $-0.514 \mu\Omega \text{ cm deg}^{-1}$ (Nguyen and Enderby, 1977).

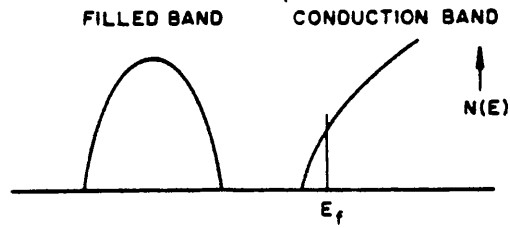
5.4 Models of the Electronic Structure

There is general agreement that the electronic structure of a liquid semiconducting alloy at the stoichiometric composition can be characterized by a pseudogap between two bands. There has been, however, some discussion as to the description of the electronic structure of alloys at nonstoichiometric compositions.

Enderby and Collings (1970) suggested a model for an alloy M_xA_{1-x} (where M refers to the more electropositive constituent) in which an excess of either M or A over the stoichiometric composition causes the valence electrons of the excess atoms to go into a rigid conduction band, figure 5-9(i). On changing composition from excess M to excess A, E_F decreases to a minimum, determined by the equilibrium concentration of the dissociated compound, and then increases. In order to explain the positive thermopower frequently found with excess A, they postulated a relatively narrow resonant scattering impurity state in the band just below E_F . This model has been criticised (Faber, 1972) for not explaining the temperature dependence of the thermopower and the change in the sign of the thermopower at the stoichiometric composition demands special behaviour of the resonance scattering.

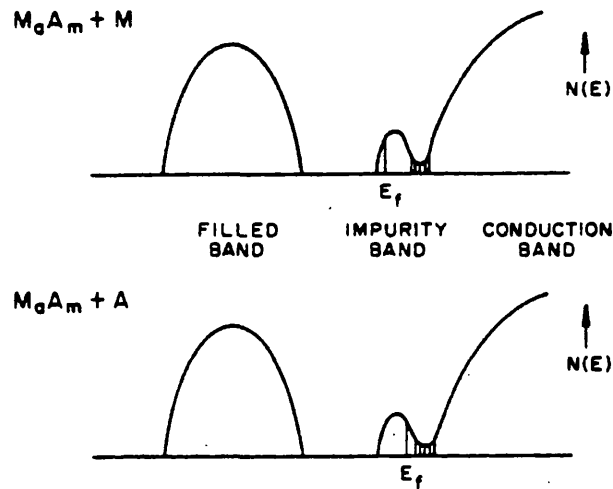
Faber modified this model by assuming that the excess element forms an impurity band below the bottom edge of the conduction band

(i)



Enderby's model for the electronic structure of an M-A alloy. E_f remains in the conduction band and bonding electrons go into the filled band.

(ii)



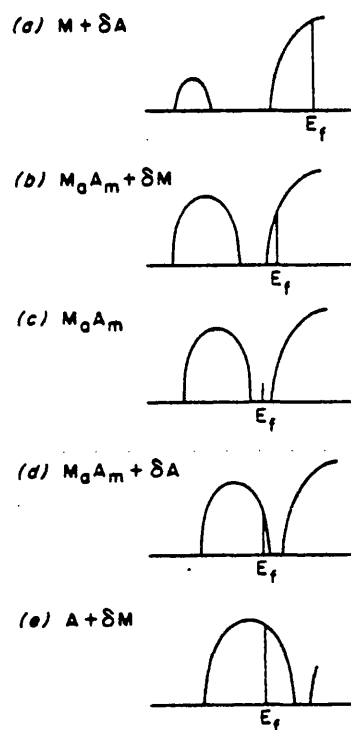
Faber's model for the electronic structure of an M-A alloy. E_f is always in the impurity band which grows with increasing concentration of excess A or M. The hatch marks denote a mobility gap between the impurity and conduction bands.

Figure 5-9

(figure 5-9(ii)) so avoiding the difficulty over the thermopower. With excess M, E_F lies below the maximum of the impurity band and with excess A, E_F is above the minimum in typical alloys. Transport is then in an impurity band near the stoichiometric composition and the impurity band grows into a true band with large concentrations of excess M or A. Cutler (1977) argued that an appreciable band gap is necessary for an impurity band not to be absorbed into the conduction band and that a distinct impurity band would be unlikely unless the minimum conductivity was lower than $100 \Omega^{-1} \text{ cm}^{-1}$.

Another model for the electronic structure proposed by Roth (1975) is shown in figure 5-10. When small quantities of A are added to M, bonding electrons go into states created below E_F which may be separated from the conduction band by a gap. This new band then grows as x decreases and E_F moves downwards in the conduction band because each atom of constituent A adds more states than electrons to the lower band. At the stoichiometric composition, E_F is near the centre of the pseudogap. An excess of constituent A causes E_F to move into the valence band and as the composition changes towards pure A, the valence band becomes a partially filled band of pure A. Such a model is likely to apply in the limit of ionic bonding. Cutler (1977) gives an extension to Roth's model assuming that excess A bonds covalently to itself; the excess A element forming bonding and antibonding states instead of adding electrons and states below E_F . Such a model is likely to apply to many binary alloys with the A constituent being tellurium or selenium.

The model of Avci and Flynn (1979) proposed that for cases of charge transfer, the valence states of the electron acceptor lie below the bottom of the band of the alkali donor, forming completely



Roth's model for the electronic structure of an M-A alloy. The lower band is due to A^{2-} ions.

Figure 5-10

localized full shells with conduction then associated with the remaining occupied states of the alkali metal. This accords with the model of Mott (private communication) to explain the Knight shift of lithium-lead and lithium-tin in which the lithium 2s band was proposed to lie above and overlap with the p bands of lead and tin. Both models are similar to that of Roth.

5.5 The Ionic Model of Liquid Semiconductors

The Caesium-Gold System

The lithium-lead system is often compared to the caesium-gold system for which there is a considerable weight of evidence suggesting ionic behaviour, forming Cs^+ and Au^- ions in the melt. Much of the available evidence is summarized in the review article by Hensel (1980). The conductivity plummets by almost four orders of magnitude to a minimum of $\approx 3\Omega^{-1}\text{ cm}^{-1}$ (figure 1-4) at the CsAu composition which is of the same order as the conductivities of molten salts and at the concentration corresponding approximately to a conductivity of $100\Omega^{-1}\text{ cm}^{-1}$ the temperature dependence changes from negative to positive. There is a similarity between the temperature dependence of the position of the optical gap (corresponding roughly to the gap between the valence and conduction bands) for caesium-gold and that of molten salts, this being consistent with the idea of predominantly ionic bonding. Direct experimental evidence that liquid caesium-gold is entirely ionic has come from an electromigration experiment (Krüger et al, 1976) in which the liquid conformed to Faraday's Law. The absolute thermoelectric power (Schmutzler et al, 1976: figure 1-4) shows that the contribution of electrons to the electrical transport in liquid caesium-gold near the stoichiometric composition must be negligibly small for instead of changing sign near this composition with peaks in the magnitude at

neighbouring compositions, the thermoelectric power remains negative with a very deep minimum at the equiatomic concentration; this large value ($> 1000 \mu\text{V}/\text{deg}$) being inconsistent with electronic transport but ascribable to ionic transport.

The electronic structure of caesium-gold has been probed by X-ray photoelectron spectroscopy (XPS) by Wertheim et al (1979 a) with results in agreement with the ultraviolet photoelectron spectroscopy (UPS) data of Norris and Walden (1970). The results were found to be in good agreement with the band structure calculations of Overhof et al (1978) and the separation of the components of the gold d-band was found to be closely equal to the free ion spin-orbit splitting of 1.52 eV (Moore, 1949) which was considered as testifying to the quasi-atomic character of the gold 5d electrons in caesium-gold, thus providing strong support for the ionic bonding formalism of the compound.

The shift of the gold $4f_{7/2}$ core level with respect to the Fermi level was measured and the core level was found to have moved deeper by 1.3 eV on forming the caesium-gold equiatomic composition alloy. The charge transfer from caesium to gold on alloying was then deduced to lie in the range 0.6 to 0.8 electrons, in accord with the band structure calculations of Overhof et al (1978) which showed the valence band of the alloy to be mainly a filled gold $6s^2$ band demanding the transfer of a large fraction of one electron to gold which has the $5d^{10} 6s^1$ configuration in the neutral state.

Theoretical calculations have been reported by Franz et al (1980) on caesium-gold using a tight-binding model including short range order and charge transfer self-consistently. The calculations of the variation of conductivity with concentration and temperature and the variation of magnetic susceptibility and Knight shift with concentration were compared to experimental data with good agreement. The charge

transfer per atom was calculated and found to be ≈ 0.7 electrons to gold at the equiatomic concentration in good agreement with the work of Wertheim et al. (1979 a).

Evans and Telo Da Gama (1980) produced structural evidence showing the ionicity of caesium-gold by modelling the equiatomic composition as fully ionized charged hard spheres and then calculating the partial structure factors in the mean spherical approximation in agreement with the experimental results of Enderby (1978) for molten alkali halides. The calculated total neutron coherent scattering cross-section was compared with the experimental data of Martin et al (1980) for the molten stoichiometric composition and showed qualitative agreement, both theory and experiment exhibited a pronounced shoulder on the low angle side of the main peak, believed to be an indicator of molten salt-like charge ordering in caesium-gold..

The evidence in the literature for the bonding in caesium-gold to be ionic is strong; the same source also shows lithium-lead to have similar properties to caesium-gold. Accordingly, photoemission results were taken from lithium-lead and lithium-tin, which is expected to show similar properties, and these are now presented and discussed.

5.6 The Photoelectron Spectra of the Lithium-Lead System

Figure 5-11 shows the energy distribution curves (EDCS) obtained with helium I (21.2 eV) radiation for the molten lithium-lead system. The curves show the respective pure metals and alloys held at $\approx 30^\circ\text{C}$ above their melting temperatures, plotted against the energy of the initial state with the Fermi energy, E_F , set at zero electron volts

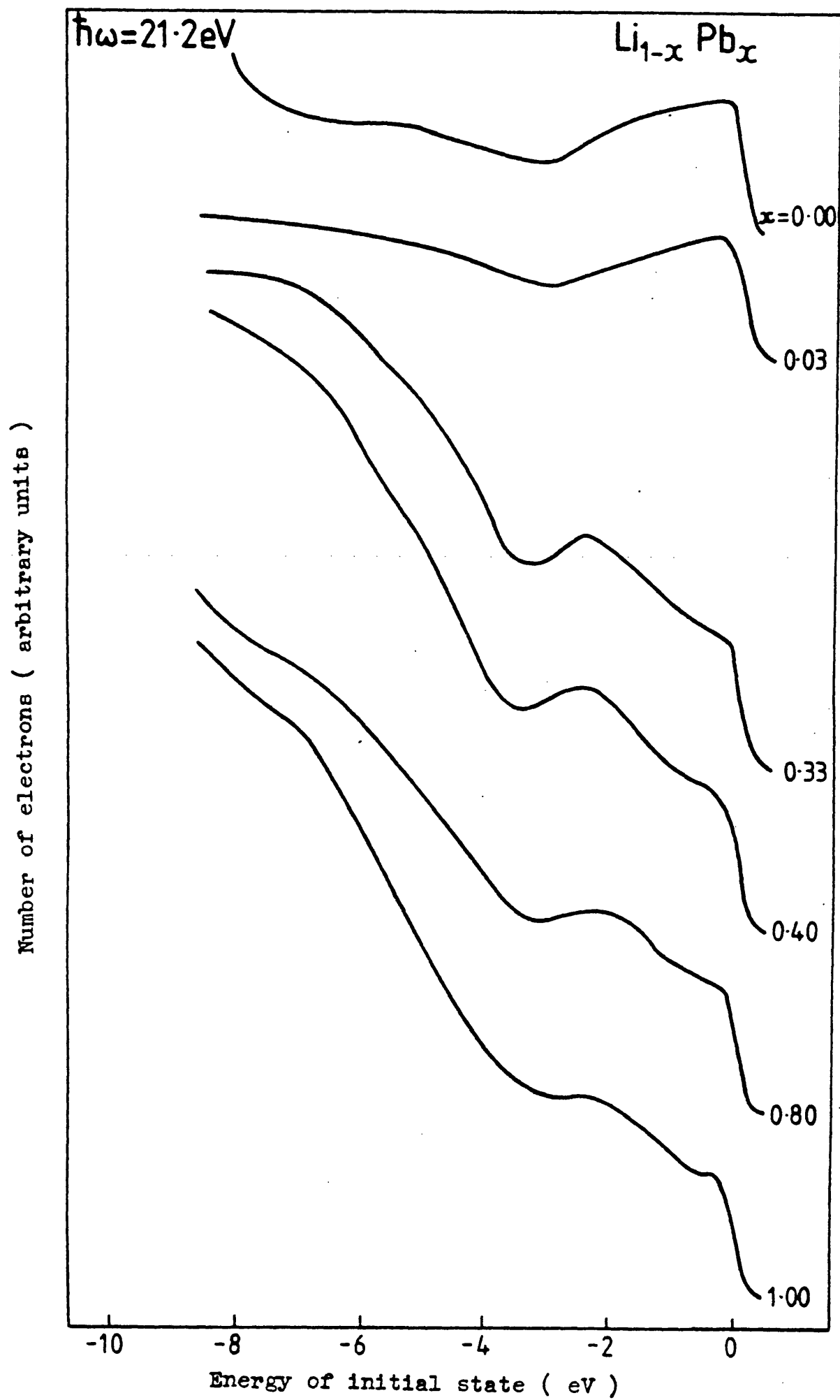


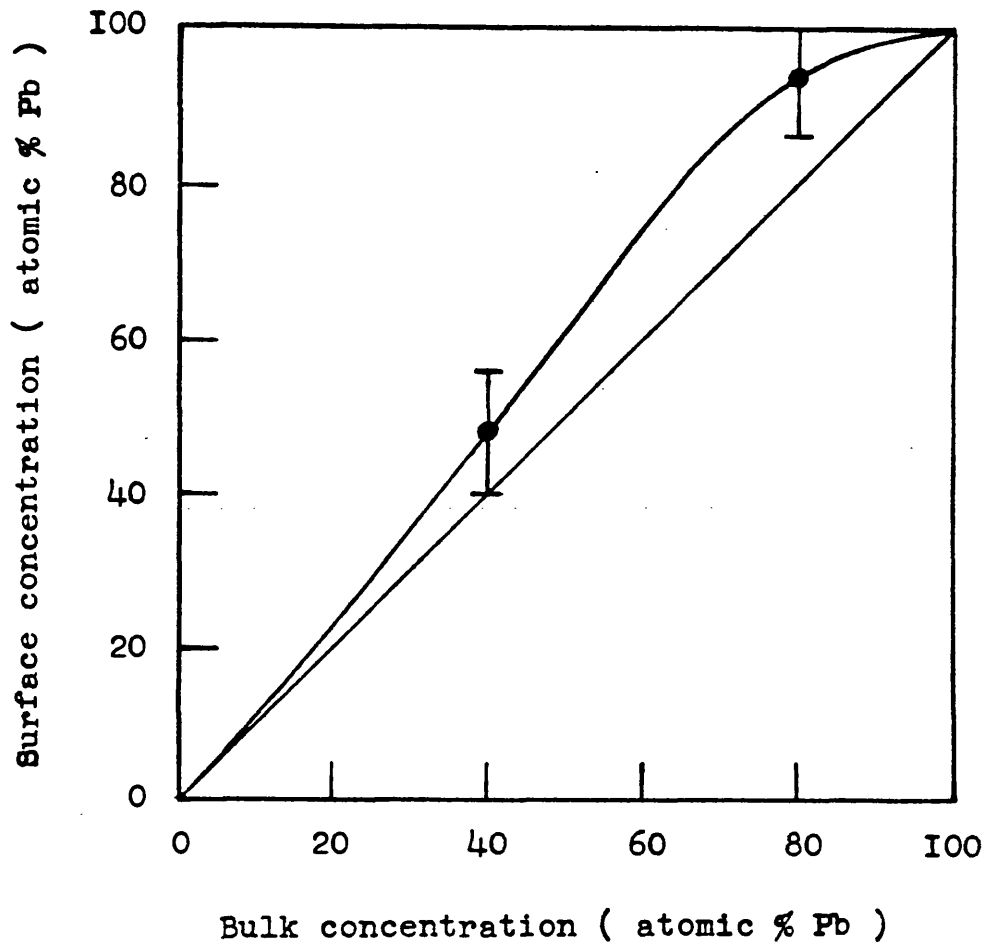
Figure 5-II

and normalised to give the same intensity at the Fermi energy.

Surface segregation is a characteristic of alloy systems in equilibrium (Gibbs, 1875) and predictions have been made from thermodynamic data (Jablonski, 1977) and bulk phase diagrams (Burton and Machlin, 1976). An estimate of the surface concentration was made by monitoring the intensity of the lead $5d_{5/2}$ core level, excited by helium II (40.8 eV) radiation, in pure lead and the alloy with the result of figure 5-12 which shows small lead enrichment, in agreement with the strain theory (McLean, 1957). The small degree of enrichment (compared to the gold-nickel system; Williams and Boudart, 1973) is expected as lead and lithium have similar surface tensions (Weast, 1979).

Molten lead shows two separate bands superposed on the background of secondary electrons in agreement with the photoemission data of Wotherspoon et al (1979) and the augmented plane wave calculation of Loucks (1965). Structure ascribable to transitions from the spin-orbit split 6p band is visible from E_F to ≈ -3.0 eV and also the 6s band, the bottom of which lies at ≈ -8.5 eV. This structure reinforces the view of Norris (1977) that the photoelectron spectra of some simple liquid metals cannot be explained by a (nearly) free electron density of states.

The $Li_{20}Pb_{80}$ curve shows an increase in width of the 6p band measured from E_F to the dip from ≈ 2.8 eV in lead to ≈ 3.2 eV and an enhancement at -2.3 eV leading to a strengthening of the dip between the 6p and 6s band which is unchanged by alloying. Pure lead shows a step from E_F to -0.7 eV which may be associated with the dip visible in the 6p band of the alloy at -1.1 eV.



Measured surface enrichment of
the Li-Pb system.

Figure 5-I2

$\text{Li}_{60}\text{Pb}_{40}$ shows a further increase in width of the 6p band to ≈ 3.5 eV and an increasing enhancement centred at -2.5 eV which accentuates the dip between the 6s and 6p bands. The 6s band remains unchanged and the dip in the 6p band remains visible although it has become less distinct.

$\text{Li}_{67}\text{Pb}_{33}$ continues the trend; the dip between the two bands is more pronounced because of the growth at -2.5 eV and the dip in the 6p band, which has narrowed slightly to ≈ 3.4 eV, is only just discernable. The 6s band remains unchanged by alloying.

Two factors prevented the experimental probing of alloys with higher lithium concentrations:-

(1) the vapour pressure became too high (section 5.1) and (2) the alloys with a high lithium content crept over the sides of the crucibles causing electrical failures.

An attempt was made to produce the intermetallic in the solid phase by evaporating lithium and lead onto a clean molybdenum substrate to form the most stable composition (Li_4Pb) as was done for caesium-gold (Norris and Walden, 1970), but the experiment failed because the film was found to be oxygen contaminated.

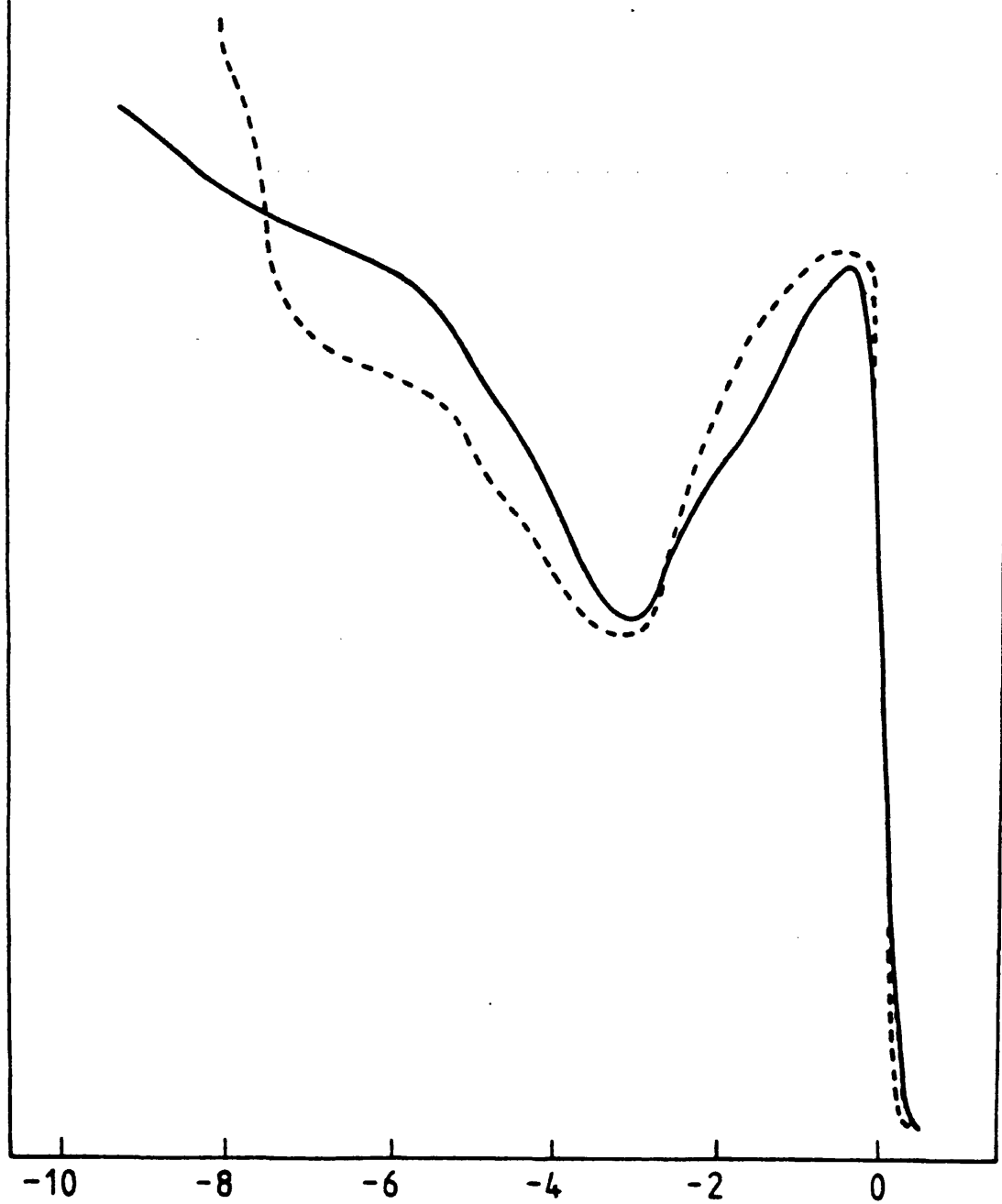
Figure 5-13 allows a close comparison to be made between lithium and the $\text{Li}_{97}\text{Pb}_3$ alloy. The main features of the lithium curve are transitions from the 2s band from E_F to ≈ -3.2 eV and a plasmon peak at ≈ -5.3 eV. The curve for the alloy shows a wider distribution at E_F but this is explained by the broadening effect of the Fermi probability distribution which contributes $2.77k_B T$ to the width. Accurate measurements allowing for this effect show the alloy and lithium have the same measured width at E_F . The band of the alloy

Number of electrons (arbitrary units)

$$\hbar\omega = 21.2 \text{ eV}$$

----- Li

———— Li₉₇ Pb₃



Energy of initial state (eV)

Figure 5-I3

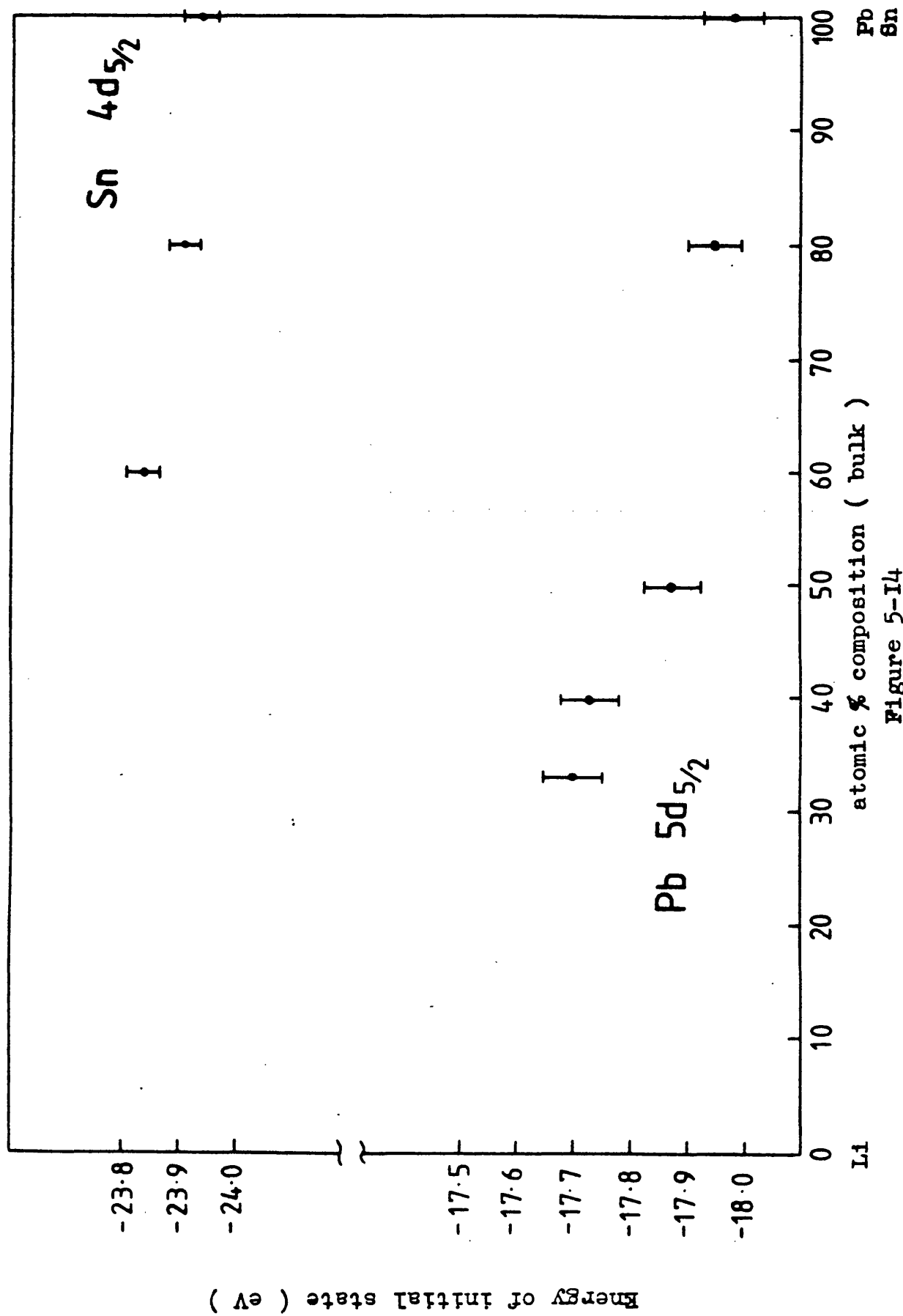
shows a change in shape from the pure metal showing the genesis of a feature at ≈ -2.1 eV and a contraction of 0.15 eV measured from E_F to the dip near -3 eV. The plasmon peak is also seen to have moved deeper in initial state energy to -5.6 eV.

Figure 5-14 shows the core level shifts for the lithium-lead and lithium-tin systems; the binding energies were measured relative to E_F . The binding energy of the $5d_{5/2}$ core level of solid lead, -18.11 eV, obtained by Bancroft et al (1978) compares favourably to the measured value from molten lead, -17.98 eV. The graph shows a monotonic decrease in the binding energy of the core levels for both alloy systems with increasing lithium concentration which although small was detectable confirming that the metals alloyed together when coupled to the fact that the measured widths of the core levels did not change.

5.7 The Photoelectron Spectra of the Lithium-Tin System

Figure 5-15 shows the energy distribution curves obtained with helium I radiation for the molten lithium-tin system. The curves show the respective pure metals and alloys held at $\approx 30^\circ\text{C}$ above their melting temperatures, plotted against the energy of the initial state with the Fermi energy set at zero electron volts and normalised to give the same intensity at the Fermi energy.

The surface concentration of tin in the $\text{Li}_{20}\text{Sn}_{80}$ alloy was estimated by comparing the intensities of the principal tin Auger electron lines from the alloy and the pure metal yielding a tin value of 71% ($\pm 8\%$); a small deviation was expected because the surface tensions of tin and lithium are similar (Weast, 1979). A different method was used from lithium-lead because the excited tin core level lies in the valence band.



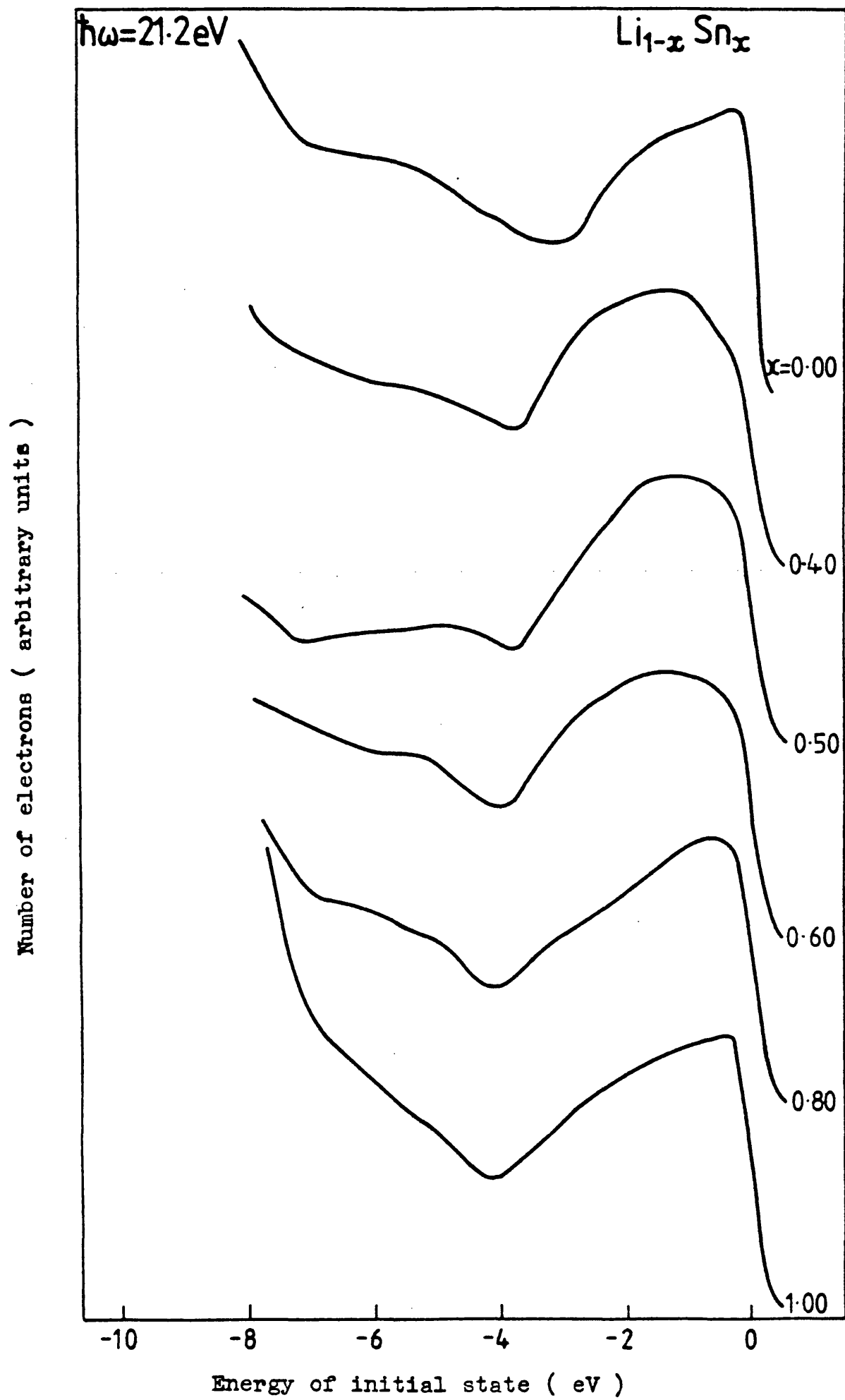


Figure 5-I5

Molten tin (section 5.11) shows transitions from the tin 5s and 5p bands from ≈ -10.0 eV to ≈ -4.2 eV and from -4.2 eV to E_F . The resolving of the s-p valence band into two peaks agrees with the XPS data of Pollak et al (1972) from a single tin crystal. It was not possible to monitor changes in the 5s band through the alloy series because the background secondary electrons suffered interference from thermionic electrons from the tungsten wire crucible heater, but changes in the 5p structure can be seen.

$\text{Li}_{20}\text{Sn}_{80}$ shows two changes over the tin spectrum; the EDC is seen to be more rounded at E_F and there is evidence for a weak peak centred at ≈ -3.0 eV but the 5p band remains at the same width, ≈ 4.2 eV.

$\text{Li}_{40}\text{Sn}_{60}$ shows the 5p band to have narrowed to ≈ 4.0 eV and to have undergone a change in shape, peaking at ≈ -1.4 eV and showing a pronounced curvature over its width. The EDC shows a very small peak centred at ≈ -2.9 eV.

The 5p band narrows further to ≈ 3.8 eV in $\text{Li}_{50}\text{Sn}_{50}$ making the band more strongly peaked at ≈ -1.3 eV.

$\text{Li}_{60}\text{Sn}_{40}$ shows a pronounced curvature over the width of the 5p band which remains at the same width as in the preceding alloy. The EDC shows the trend of the alloy series of the curvature of the 5p band making the location of E_F progressively more difficult.

A comparison of the trends in the EDCS of lithium-lead and lithium-tin excited by helium I light shows that in the former the lead 6p band increases in width and a new feature appears which grows in intensity near the bottom of the band with increasing lithium concentration, whereas in the latter there is a decrease in the width

of the tin 5p band which changes shape becoming rounded over its width. There is thus a dissimilarity in behaviour.

Figure 5-16 shows EDCS obtained using neon I light (16.8 eV) from molten lithium-tin. Molten tin shows transitions from the tin 5p band which has a different width (3.7 eV) and a slightly different shape than the EDC obtained using helium I. This is attributed to a change in the secondary electron background and a change in the matrix elements with photon energy.

$\text{Li}_{20}\text{Sn}_{80}$ shows two changes in the curve; the EDC changes shape and becomes more rounded at energies just below E_F .

$\text{Li}_{40}\text{Sn}_{60}$ exhibits the pronounced curvature over the width of the 5p band as in the EDC taken using helium I light, and shows evidence of a peak at ≈ -2.9 eV.

$\text{Li}_{50}\text{Sn}_{50}$ exhibits the continuance of the trend expected from the helium I data; the EDC is rounded over the width of the 5p band making the accurate location of E_F progressively more difficult.

The binding energy shifts of the tin $4d_{5/2}$ core level are shown in figure 5-14. An analysis of the sign and magnitude of the shifts is reserved for the next section. The binding energy of this core level for tin, -23.94 eV, compares favourably to the value of -24.04 eV obtained by van Attekum and Trooster (1979) by XPS from an evaporated film.

5.8 A Discussion and Interpretation of the Photoemission Data of the Lithium-Lead and Lithium-Tin Systems

The addition of 3 atomic % lead to lithium causes the contraction

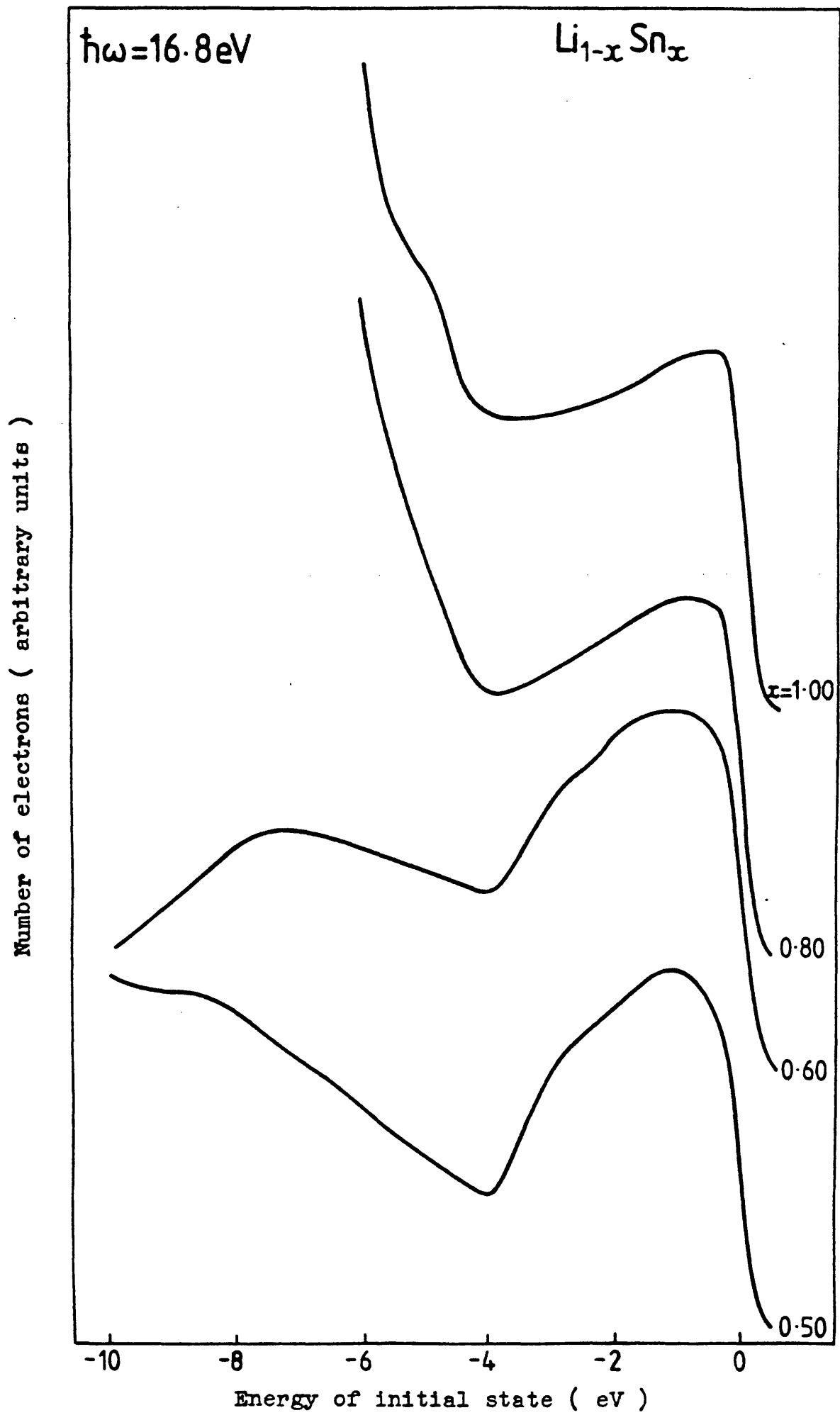


Figure 5-I6

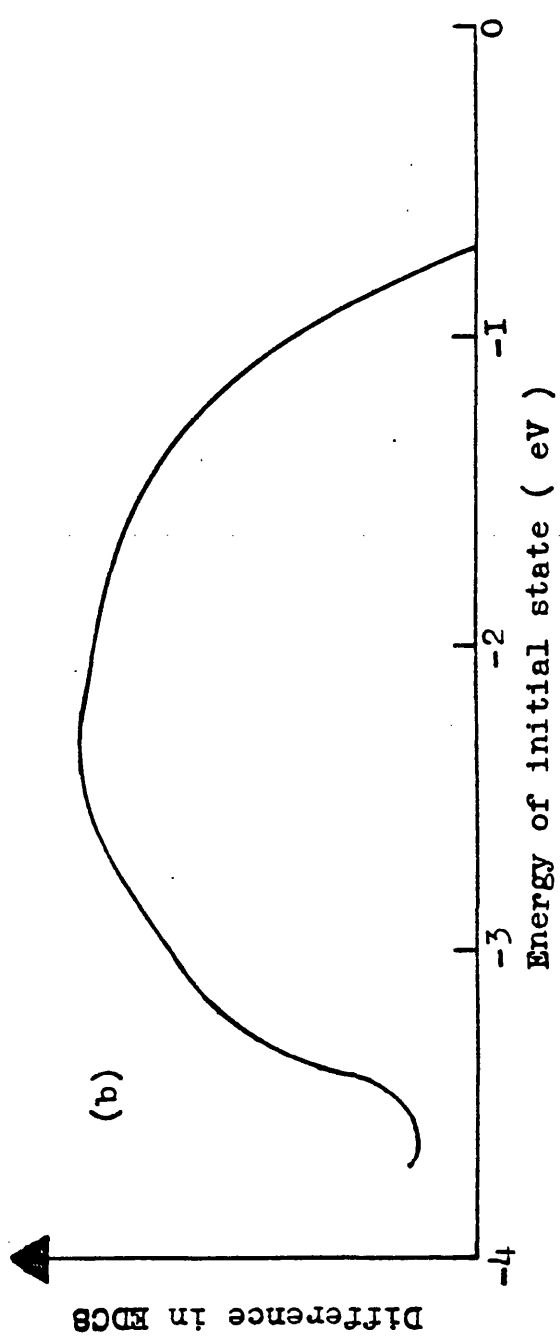
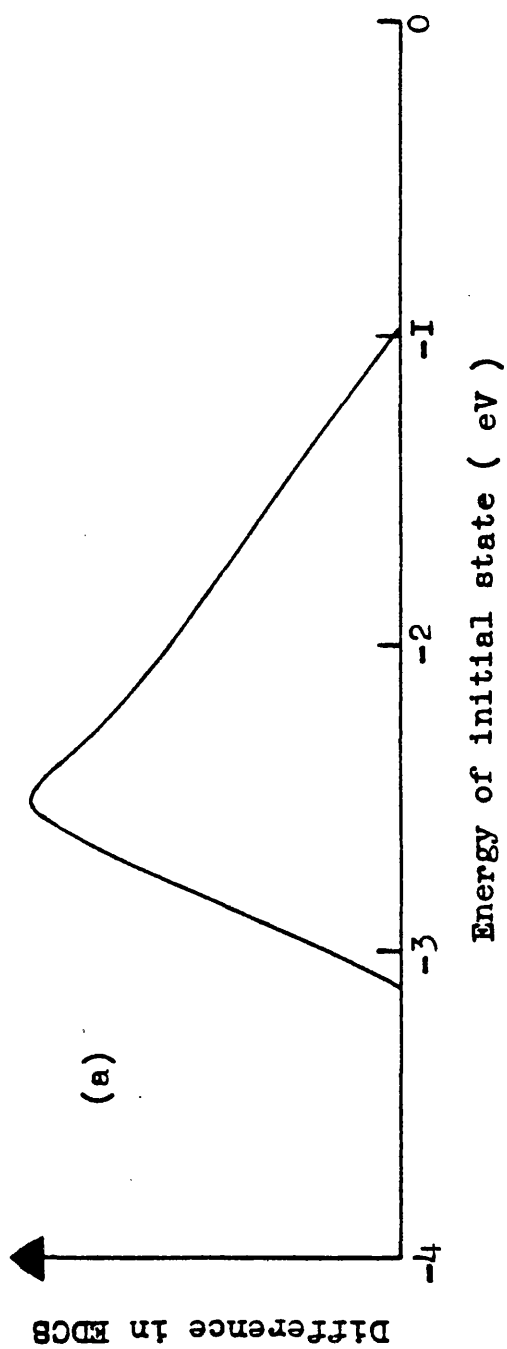
of the lithium 2s band (figure 5-13) eliminating a free electron interpretation in which the bandwidth would increase with the three extra electrons added per lead atom. A crude estimation of charge transfer to the lead sites can be made from the contraction assuming both bands to be free electron like and the band of the alloy to be predominantly lithium which has lost charge, yielding a value of ≈ 2 electrons. This is only a very rough value because the Knight shift shows the sharp change in the s electron behaviour of the band of the alloy with the addition of lead.

An interpretation of the lithium-lead EDCS within the rigid band model is difficult because two opposing factors are operating. The loss of three electrons per atom upon the addition of lithium to lead should infer the unobserved contraction of the band and a resemblance of one of the EDCS to liquid thallium but no similarity was found on examination of known data (Wotherspoon et al, 1979).

The opposing factor is that of charge transfer which should result in a filling of the lead 6p band and the resemblance of one of the EDCS to liquid bismuth. The $\text{Li}_{20} \text{Pb}_{80}$ EDC shows some similarity to known data (Wotherspoon et al, 1979) but is compressed on the energy scale.

Figure 5-17 shows difference spectra for:

- (a) the $\text{Li}_{67} \text{Pb}_{33}$ alloy and pure lead and
- (b) the $\text{Li}_{60} \text{Sn}_{40}$ alloy and pure tin. These spectra show the enhancement in the EDCS, the maximum occurring at ≈ -2.5 eV for each one. If the off-stoichiometric composition alloys are taken to be mixtures of the pure metals and stoichiometric compositions, then the difference spectra represent the EDCS expected from the latter.



Difference spectra for (a) $L1_{67}Pb_{33}$ and Pb and (b) $L1_{60}Sn_{40}$ and Sn

Figure 5-I7

The interpretation of the lithium-tin EDCS in the rigid band model is the same as for lithium-lead. Charge depletion on the addition of lithium to tin infers a similarity of one of the EDCS to liquid indium but comparison to known data (Rodway, 1978) shows no agreement.

Charge transfer from lithium to tin should infer a filling of the tin 5p band and a similarity of one of the EDCS to molten antimony. No curve for liquid antimony has been reported but the alloy EDCS show no similarity to the XPS results from an evaporated film (van Attekum and Trooster, 1979) or polycrystalline antimony (Vesely and Kingston, 1974).

The complex problem of interpreting core electron binding energy shifts to yield information on charge transfer has been covered by Chou et al (1976), Sham et al (1979), Wertheim et al (1979 a, 1979 b) and Briggs (1978). Charge transfer is an initial state effect which affects the binding energy of core electrons by the Coulomb potential produced within the atom by the gain or loss of charge by outer orbitals. Binding energies are, however, a property of the hole state produced by removal of a core electron and are strongly influenced by the final state relaxation and screening response of the sample to the formation of a core hole. Since the extra-atomic relaxation may well be affected by alloying, it must be included in a formulation of the problem. Relaxation causes all other energy levels to adjust to the new potential caused by the creation of a core hole in order to minimise the total energy. In addition there is a shift of electron density in surrounding atoms to screen the core hole charge. The total relaxation of a system will reduce the energy of the system and

will thus always increase the kinetic energy of the emitted electron which will result in a decrease of the measured binding energy relative to the value given by Koopmans' rule (Koopmans, 1934), which assumes that the binding energy of a core electron is equal to the one electron energy of the ionised level if all other orbitals remain frozen during photoionisation.

Following Wertheim et al (1979 b), the core electron binding energy shift, δE_i , resulting from alloy formation may be expressed in terms of four major contributions:

$$\delta E_i = \sum_j F(i, j) \delta z_j - M \delta z_j - \delta R - e \delta \phi \quad (5.2)$$

where the first term describes the Coulombic effect on an electron in the i^{th} shell by charge δz_j added to the j^{th} valence shell.

$F(i, j)$ is a Coulomb integral, generally of the order of 1 Ry and often taken to be inversely proportional to the atomic radius, M is the Madelung potential due to the charges on the other atomic sites, δR is the change in final state relaxation energy from metal to alloy and $\delta \phi$ is the change in Fermi energy on alloy formation. The application of this equation encounters several problems. The first arises from a substantial cancellation between the poorly known values of F and M . For an ordered structure, M may be calculated as the Madelung potential due to point charges at the lattice sites although in disordered alloys it should be substantially reduced. The relaxation energy is also not known with high accuracy; in the present case the required knowledge necessary for an interpretation of the core electron binding energy shift is the difference between the relaxation energies appropriate for the formation of the alloy and the constituent metals. Another problem emanates from the volume contraction which is known to

occur in the lithium-lead system, which, with the resulting smaller interatomic separations reduces the Fermi energy hence changing the values of the binding energies. The effect of a volume change has been considered by Watson and Perlman (1975). It is thus not easy to calculate charge transfer from binding energy shifts.

Wertheim et al (1979 a), however, estimated the charge transfer in the ionic caesium-gold system (section 5.5) although their calculation may be criticised at several stages. The difference between the intra-atomic relaxation energies of a neutral gold atom and a negative gold ion was assumed negligible. The extra-atomic relaxation in the metal where the core hole is screened by conduction electrons was estimated by a comparison to mercury and by a comparison to caesium iodide in the semiconductor where it arises from the polarization of neighbouring ions. The size of the gold ion was estimated from the lattice constant and the Coulomb integral was scaled incorrectly using the inverse radii of the gold atom and gold ion.

Although the magnitude of their calculated charge transfer may be in error, the principle is true that substantial charge transfer in an alloy leads to an increase in the binding energies of the core levels of the more electronegative component as exemplified by caesium-gold. This fact was used by Norris and Williams (1978) to calculate charge transfer in copper alloys using the simple equation:

$$\Delta\epsilon = \frac{\Delta z}{g(E_F)} \quad (5.3)$$

where Δz is the charge transferred to a site, $\Delta\epsilon$ is the binding energy shift (relative to E_F) and $g(E_F)$ is the density of states at the top of the occupied distribution.

Pauling (1960) defined a scale for the ionicity of a bond based on the electronegativity difference which is shown in table 5.1 for the systems caesium-gold, lithium-lead and lithium-tin using the values of Gordy and Thomas (1956). The small binding energy shift measured in both lithium-lead and lithium-tin (which had a maximum value of 0.28 eV in lithium-lead although not measured at the stoichiometric composition) when compared to that in caesium-gold is incorrect in sign and magnitude with the simple ionic model so eliminating a large degree of charge transfer in these systems. The much smaller electronegativity difference in these alloys suggests significant charge transfer is absent. This conclusion eliminates the model of Roth (1975) and similar models which demand a large degree of charge transfer as was proposed by Enderby (1971) for liquid semi-conductors. From this photoemission work, Robertson (1981 and 1983) proposed the ionic charges $\text{Li}^{0.05+}$ and $\text{Pb}^{0.2-}$ which are more compatible with the measured binding energy shifts than the value of ≈ 2 electrons calculated in this section.

5.9 A Model for Lithium-Lead and Lithium-Tin

The combination of the diffraction data and this photoemission work suggests a model for molten lithium-lead at the stoichiometric composition similar to the intermetallic structure in which on average each lead atom is surrounded by eight lithium atoms, the bonding between the lead and lithium being more covalent than ionic with a resonating character to satisfy valence considerations. The feature near the bottom of the lead 6p band can then be associated with this bonding state and the singularities in the electronic properties at the Li_4Pb composition can be explained by electrons becoming involved in bonding; the breaking of bonds with temperature accounting for the

Element	Electronegativity
Li	0.95
Pb	1.8
Sn	1.8
Cs	0.8
Au	2.3
System	Electronegativity difference
Li - Pb	0.85
Li - Sn	0.85
Cs - Au	1.5

Table 5.I

increase of conductivity with temperature.. The off-stoichiometric compositions consist of a similar structure but with the excess component dispersed throughout the matrix.

Although the evidence is less conclusive, a similar structure seems likely for lithium-tin, the enhancement in figure 5-17(b) being associated with a similar bonding state.

5.10 The Optical Density of States of Liquid Lead at 21.2 eV

The optical density of states (ODS) of liquid lead was extracted from the photoemission EDC using the model described in chapter two which Wotherspoon (1978) used with excellent results at low photon energies ($\hbar\omega < 10.2$ eV) although he found the secondary electron background to be incorrectly predicted for molten lead at 21.2 eV. The model has subsequently been modified to allow for plasmon decay and was used to analyse the lead EDC, producing an ODS which represents an improvement over that of Wotherspoon. Figure 5-18 shows the experimental EDC corrected for the transmission function of the analyser compared to two computed spectra from the best fit ODS function. Despite the improvement of the computer model, the agreement remains imperfect at low electron kinetic energies, although the experimental EDC may be truncated by the stray magnetic field caused by the tungsten wire sample heater.

Input parameters for the computation were taken from Weast (1979) for the work function, from Ashton and Green (1973) for the absorption coefficient and from Lemonnier et al (1973) for the bulk plasmon energy. The last two parameters were taken from evaporated films and were used as being the only data available. The inelastic mean free path of the electrons for the normalisation constant L_0 was estimated

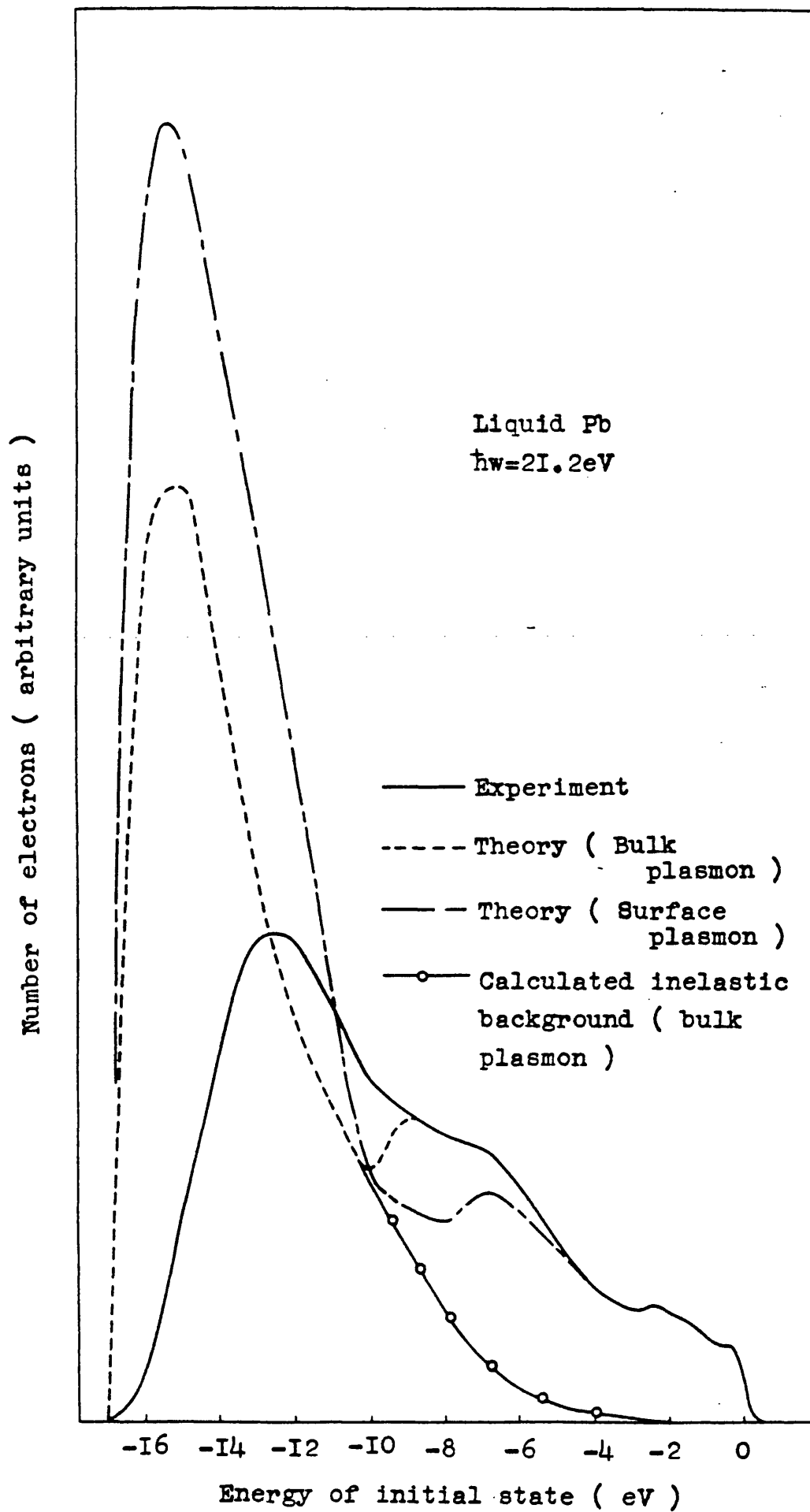


Figure 5-I8

from the universal curve (Seah and Dench, 1978). The surface plasmon energy was calculated from the bulk plasmon energy, which gave the best fit to the experimental EDC, using the simple $\sqrt{2}$ relationship (Wooten, 1972), and is shown for comparison.

The optimised ODS function is shown in figure 5-19 compared to the free electron curve and the calculation of Itami and Shimoji (1972) of the liquid lead density of states curve, which shows only a weak deviation from the free electron parabola. Both calculated curves show little agreement to the ODS function in overall shape, although Itami and Shimoji's result exhibits a weak peak near -6.0 eV in agreement with the peak of the ODS and the bandwidths agree to within 0.4 eV.

Figure 5-20 shows the ODS function compared to the calculated density of states of the liquid phase and the tight binding calculation of the density of states of the solid phase (McFeely et al, 1975). The XPS spectrum of solid lead obtained by Ley et al (1972) is also shown for comparison.

Examination of the figures shows that the experimental ODS resembles more the solid phase calculated density of states rather than the liquid phase calculated density of states. The XPS spectrum from solid lead is in good agreement with the calculation of the solid phase density of states, reproducing the two peaks at ≈ -7.5 eV and ≈ -2.0 eV although the dip at ≈ -1.0 eV is slightly displaced. The experimental ODS shows a peak near -2.0 eV in close agreement to the solid state calculation but the peak at higher binding energies is displaced by ≈ 1.2 eV.

The data reinforces the view of Wotherspoon (1978) who found

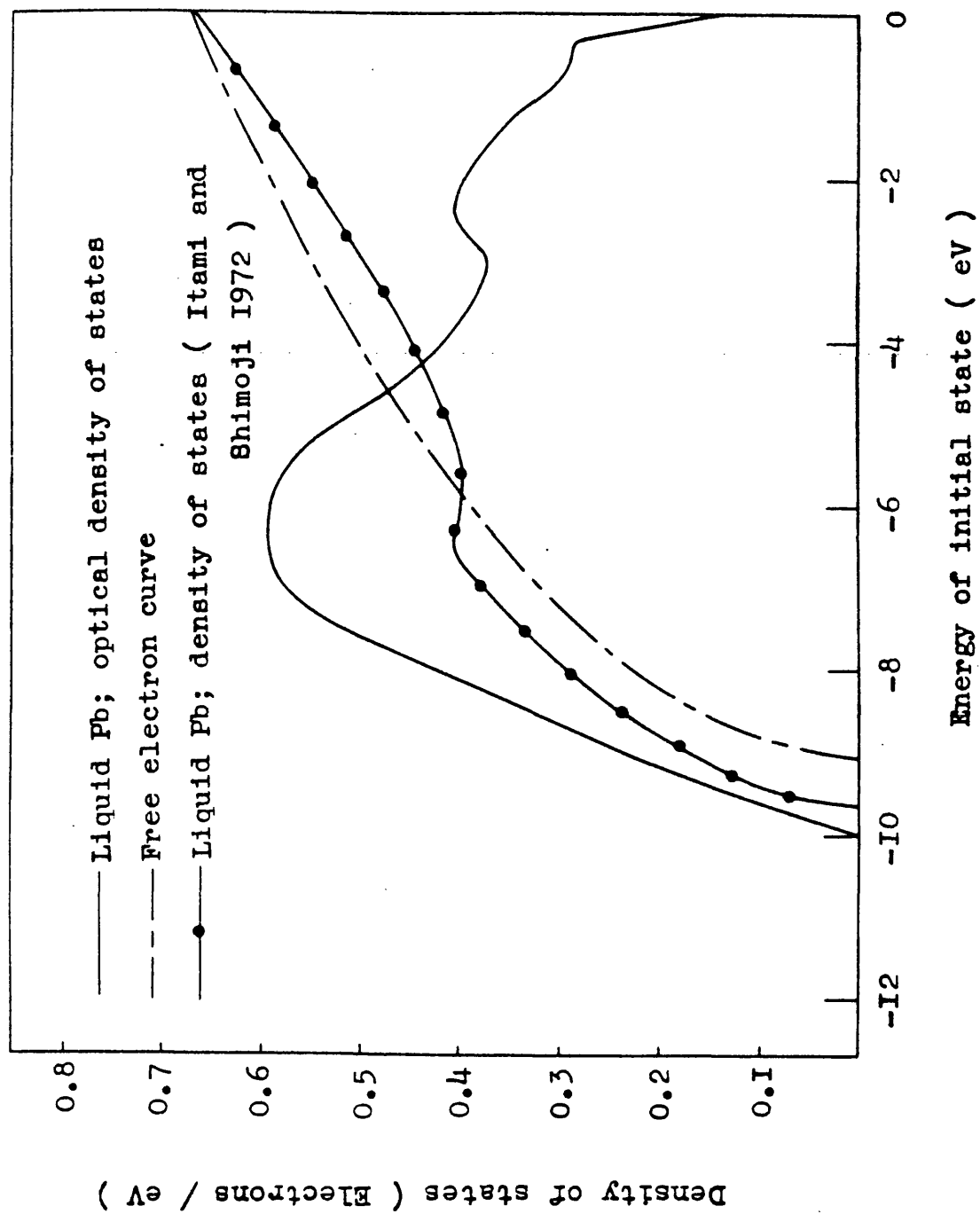


Figure 5-I9

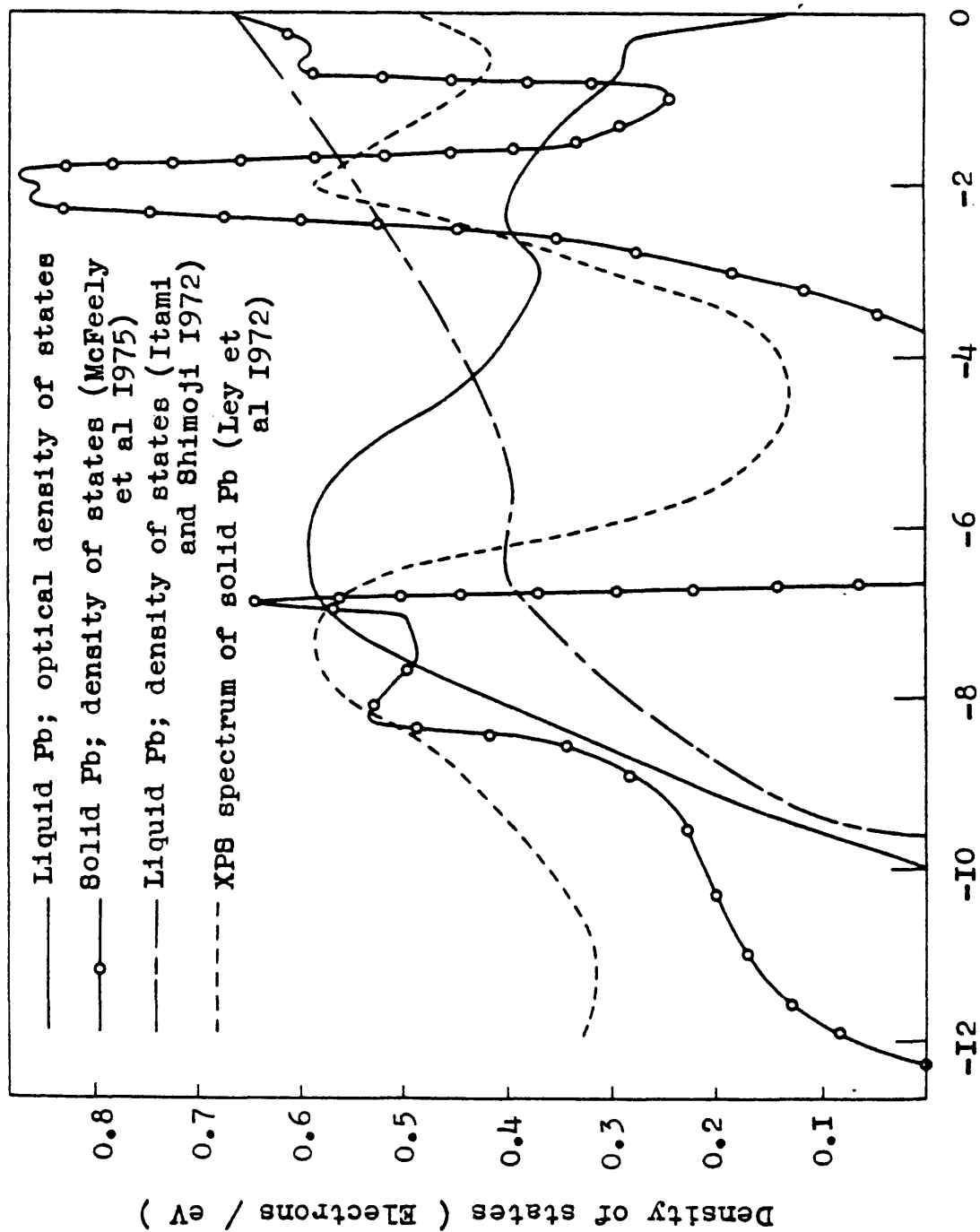


Figure 5-20

that for liquid lead the experimental ODS more clearly resembles the corresponding solid phase picture than either the free electron parabola or a liquid state curve based on a weak scattering approach in contradiction to the prediction of the NFE model.

Figure 5-21 shows a comparison between the ODS of Wotherspoon (1978) and the result of this analysis, normalised to be the same intensity at the s-band maximum near -6.0 eV. The pronounced dip between the bands near -4.0 eV of the earlier analysis can be explained by an overestimation of the contribution of the scattered electrons to the total EDC at that energy.

5.11 The Optical Density of States of Liquid Tin at 21.2 eV and 16.8 eV

The same procedure was used to extract the ODS function of liquid tin as for liquid lead. Figure 5-22 shows the experimental EDC corrected for the analyser's transmission function compared to two computed curves from the best fit ODS with bulk and surface plasmon energies. As for lead, the secondary electron background was incorrectly computed and the best fit was obtained by using the bulk plasmon energy.

Input parameters for the calculation were taken from Weast (1979) for the work function and from MacRae et al (1967) for the absorption coefficient, surface and bulk plasmon energies. These values from evaporated films were used as being the only available data. The electron inelastic mean free path for the constant L_0 was estimated from the universal curve (Seah and Dench, 1978).

Figure 5-23 shows the optimised ODS function of liquid tin compared to the free electron curve and the calculation of the density

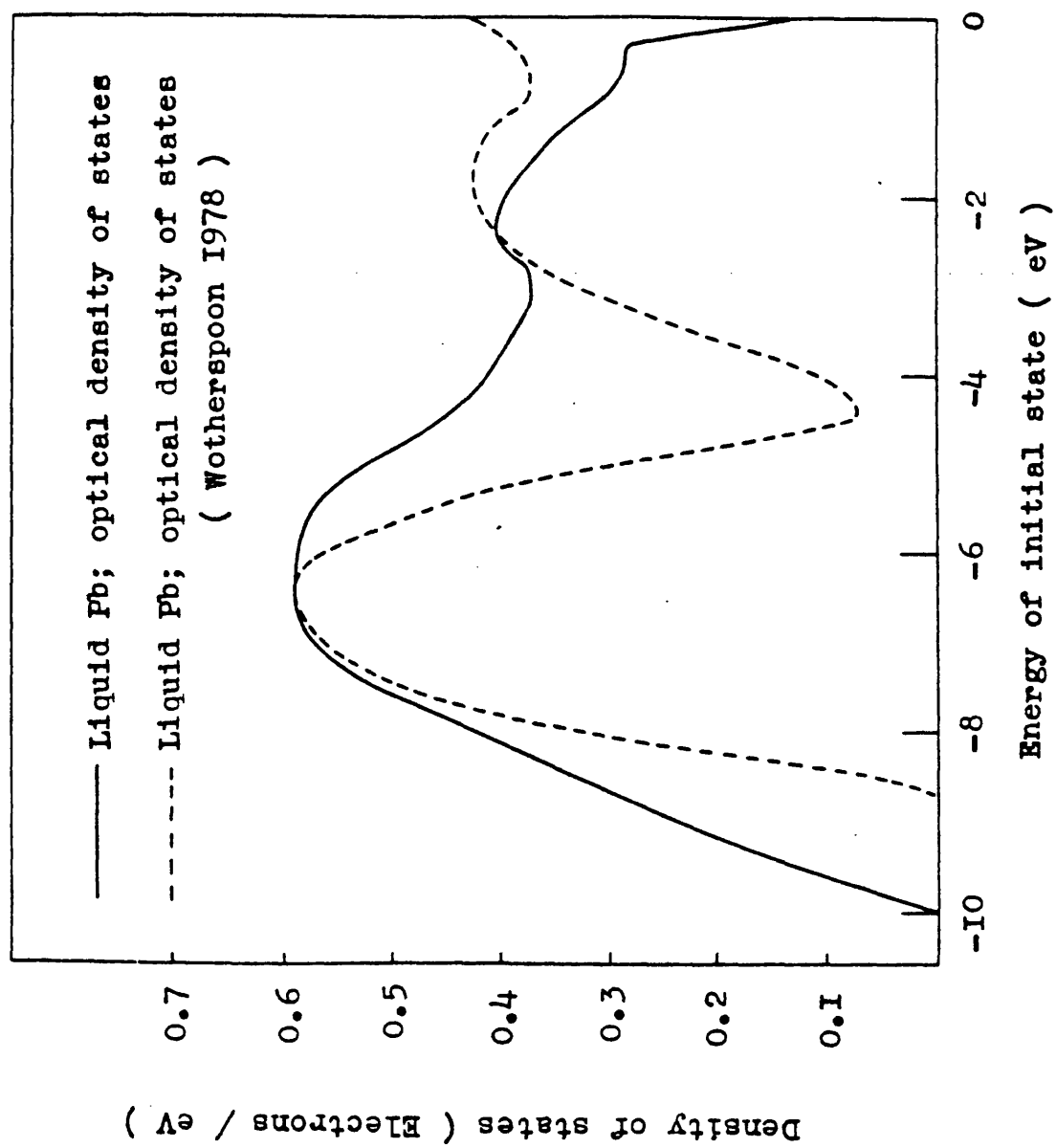


Figure 5-2I

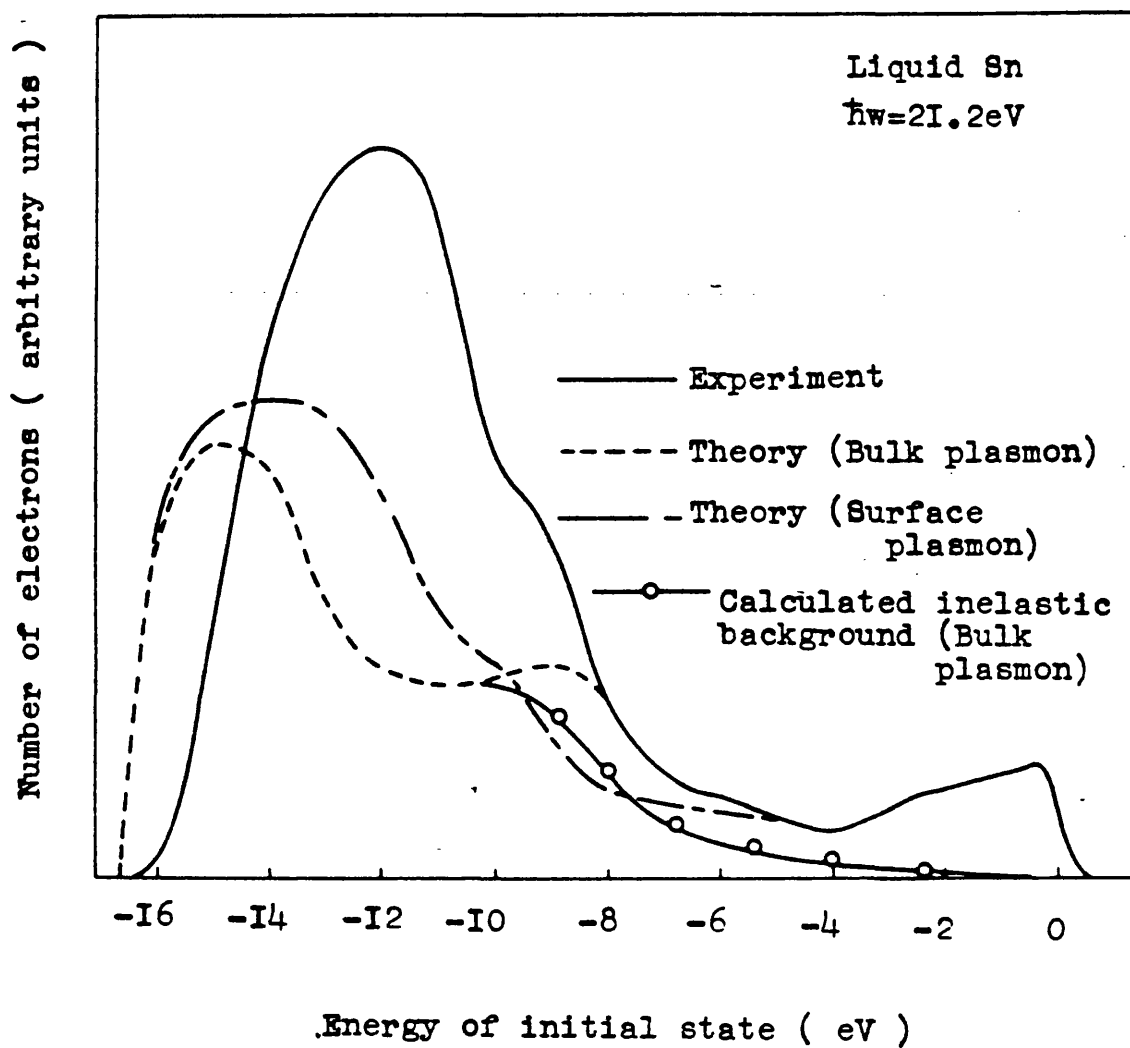


Figure 5-22

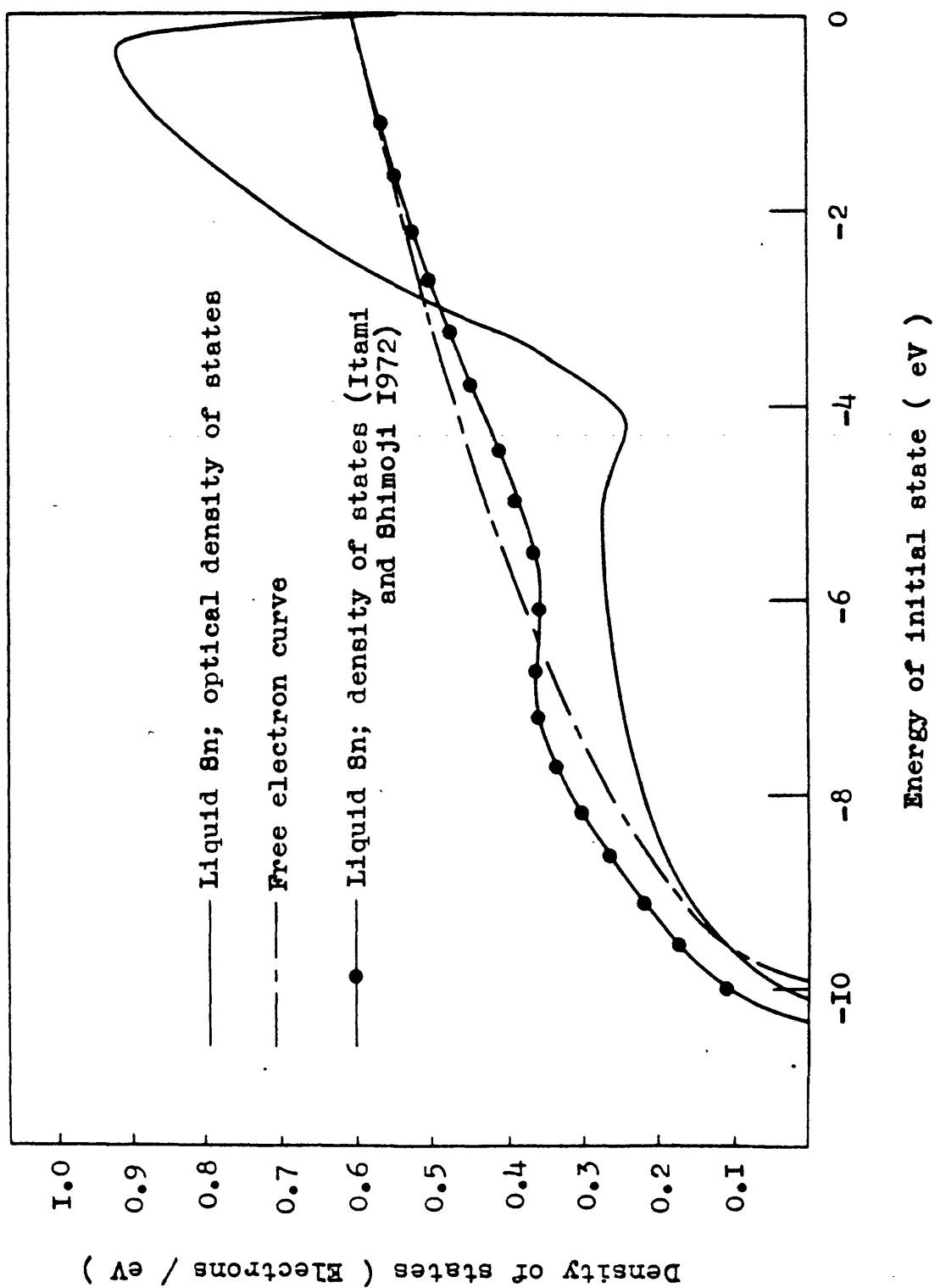


Figure 5-23

of states of liquid tin by Itami and Shimoji (1972) which exhibits only a weak deviation from the free electron parabola.

The calculated curve is in agreement with the bandwidth of the ODS to within 0.25 eV and the free electron curve agrees within 0.2 eV but neither theoretical curve for the liquid state reproduces the features of the experimentally derived curve which exhibits a strong dip at ≈ -4.2 eV. The calculated curve shows a weak dip but this is located at ≈ -6.2 eV.

Figure 5-24 shows the ODS function compared to the calculated density of states of solid tin by Ament and de Vroomen (1974) and the XPS curve of an evaporated tin film obtained by van Attekum and Trooster (1979) is also shown for comparison. The XPS curve exhibits a dip at ≈ -4.9 eV which lies near the centre of a broad dip in the solid density of states function, and the overall agreement between the two is good.

There is a better correlation between the ODS function and the calculated solid density of states rather than the corresponding liquid curve; the result for the solid exhibiting a strong minimum which is in better agreement with the experimental curve than the dip in the calculated liquid curve.

It is interesting to note that although for both lead and tin the features of the experimentally derived ODS functions show a closer resemblance to the solid density of states curves, the experimental bandwidth for each metal shows better agreement to the calculated value for the liquid. Thus the experimental curves are hybrids of the solid and liquid state calculations.

Figure 5-25 shows the experimental EDC of liquid tin taken using

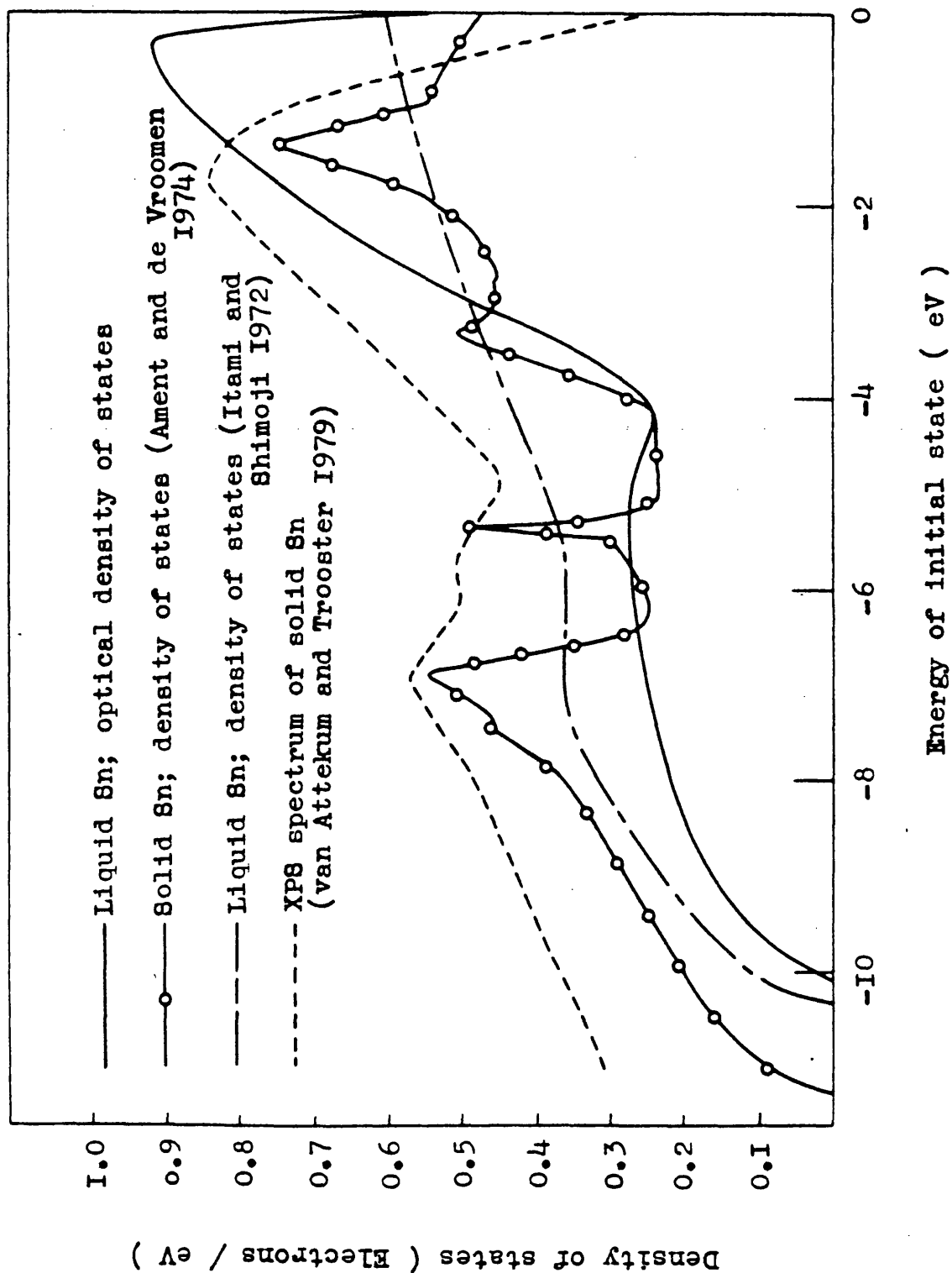


Figure 5-24

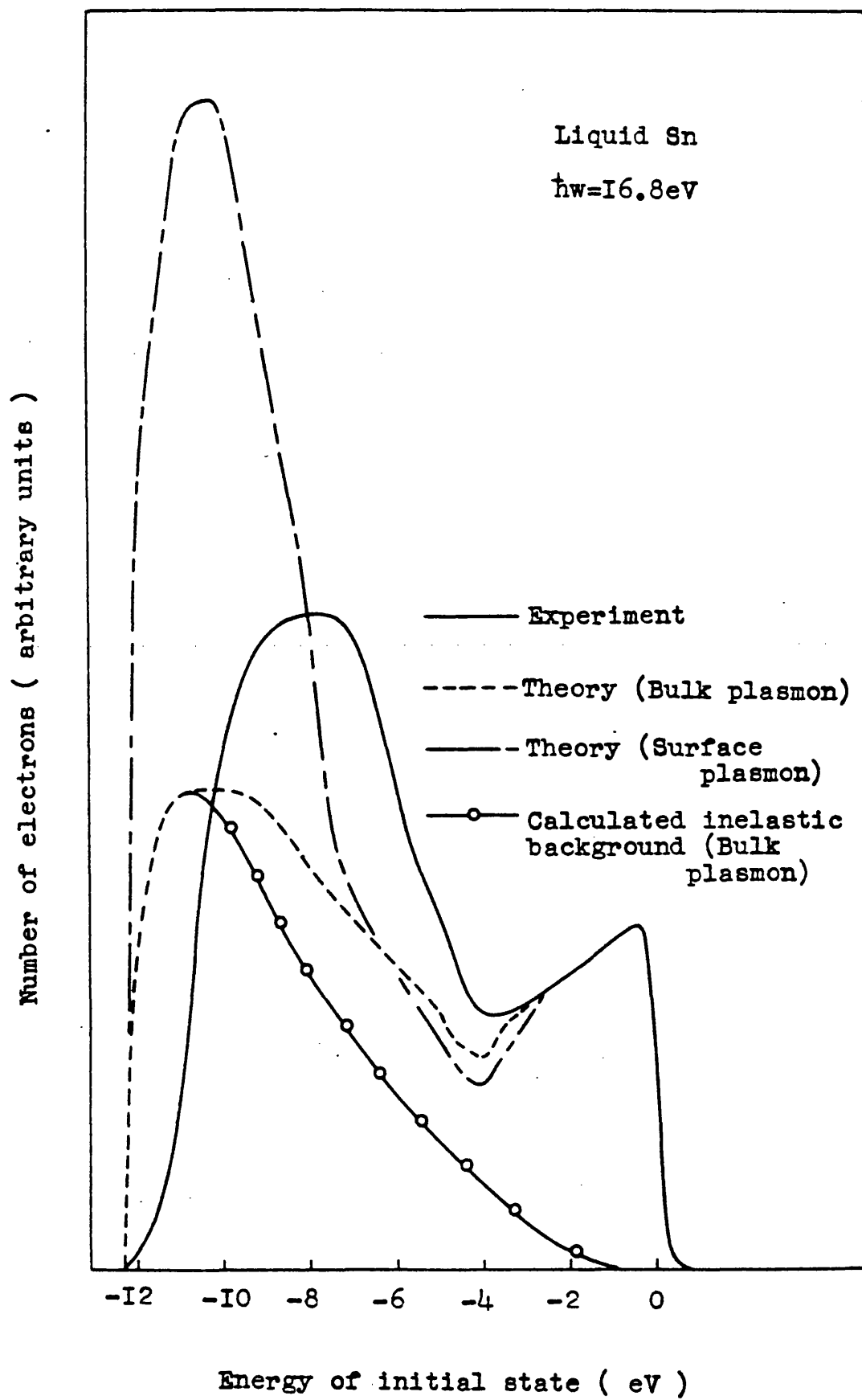


Figure 5-25

neon I light ($\hbar\omega = 16.8$ eV), corrected for the analyser's transmission function, compared to two computed curves using input parameters from the sources quoted previously and the optimised ODS function derived using helium I radiation ($\hbar\omega = 21.2$ eV). Better agreement was obtained by using the bulk plasmon energy, but even so the computed curve only shows a correlation to the experimental EDC from E_F to ≈ -3.0 eV whereas for liquid tin at 21.2 eV (figure 5-22) agreement was obtained from E_F to ≈ -8.0 eV.

This discrepancy can be explained by a change in the matrix elements with photon energy which were assumed to be constant in the computation.

In summary, this data for lead and tin in the liquid phase represents for the former an improvement over the analysis of Wotherspoon (1978) at 21.2 eV and for the latter a presentation of photoemission data which supersedes that of Norris et al (1972). The derived ODS functions of liquid lead and tin are seen to retain some of the structure of the solid phase density of states when the metals are in the liquid phase. This conclusion supports the work of Wotherspoon (1978) and is in contradiction to the NFE model of electronic structure for liquid simple metals.

CHAPTER 6

GERMANIUM, SILVER AND SILVER-GERMANIUM

Photoemission spectra for liquid and solid germanium are presented and discussed in terms of the structural changes that accompany the crystalline - amorphous and crystalline - liquid transition. The derived optical density of states of liquid germanium is compared with the results of theoretical calculations. New photoelectron spectra of liquid silver are given. The properties of the liquid silver-germanium system are reviewed as a preliminary to a discussion of new photoemission spectra.

6.1 Germanium:- Structure and Other Properties

Table 6.1 summarises the structure of germanium in the crystalline, amorphous and liquid states. Germanium crystallises in the diamond structure with each atom covalently bonded to four other atoms arranged tetrahedrally. The space lattice is face centred cubic with two atoms associated with each point. The separation of nearest neighbours is 2.45 \AA along a $[111]$ direction and the dimension of the unit cell is 5.66 \AA . Figure 6-1 shows the band structure calculated by Chelikowsky and Cohen (1976) using the non local empirical pseudopotential method. The band extending from $\approx -13 \text{ eV}$ to $\approx -4.5 \text{ eV}$ is predominantly derived from 4s states and the upper band extending from $\approx -4.5 \text{ eV}$ to above the Fermi level is mainly derived from 4p states. The crystal potential causes a repulsion between the bonding (lower) and antibonding (upper) 4p states to produce a small (0.67 eV) indirect gap at the Fermi level. This gap is responsible for the semiconducting properties of crystalline germanium.

Upon melting the ordered structure collapses and contracts with a 4.5% increase in density and a change to metallic behaviour (figure 6-2). Although the coordination number (6.8) increases it is still lower than that of a typical liquid simple metal such as aluminium (11.5) and lead (10.9), (Waseda, 1976), suggesting that some degree of local order is maintained. From diffraction measurements Orton (1980) concluded that the directional nature of the bonds is weakened in the liquid state but not completely lost. Waseda and Suzuki (1975) reached the same conclusion and suggested that the local atomic arrangement is similar to that of white tin, namely a flattened diamond grouping with four neighbours along the distorted tetrahedral axes and two more

Phase	Density (g/cm ³)	Number of nearest neighbours	Nearest neighbour distance (Å)
Crystalline ⁺ (fcc)	5.32	4	2.45
Liquid [*]	5.56	6.8	2.82
Amorphous ⁺	3.8 - 5.3	3.79 - 3.91 (T _s 150°C-350°C)	2.47

References

* Waseda, (1976)

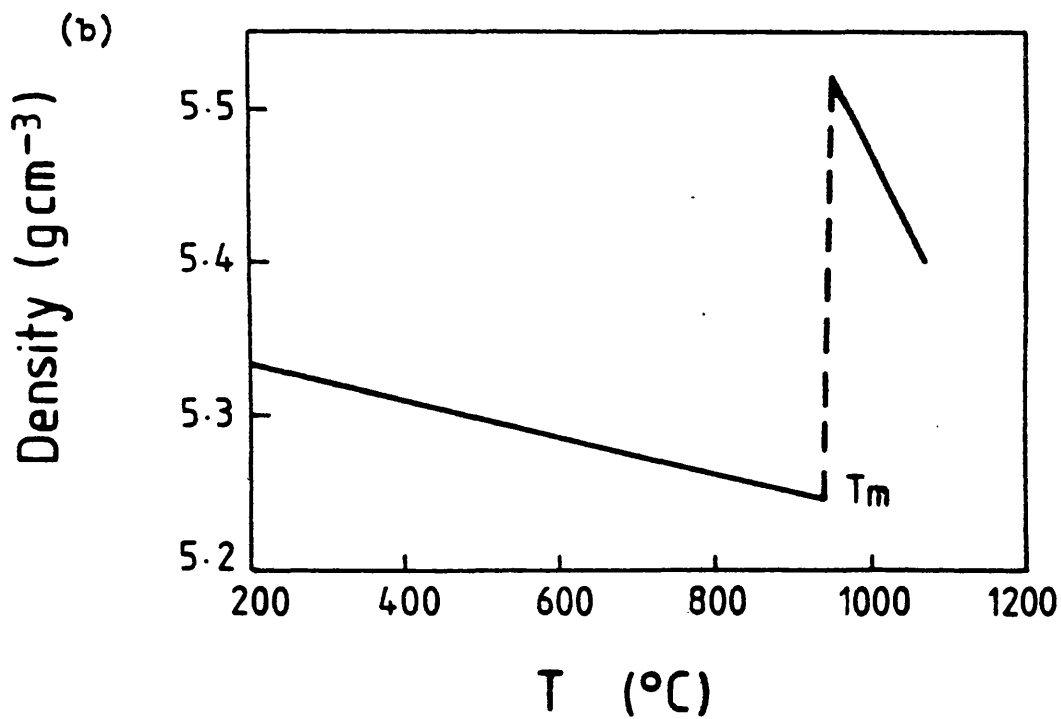
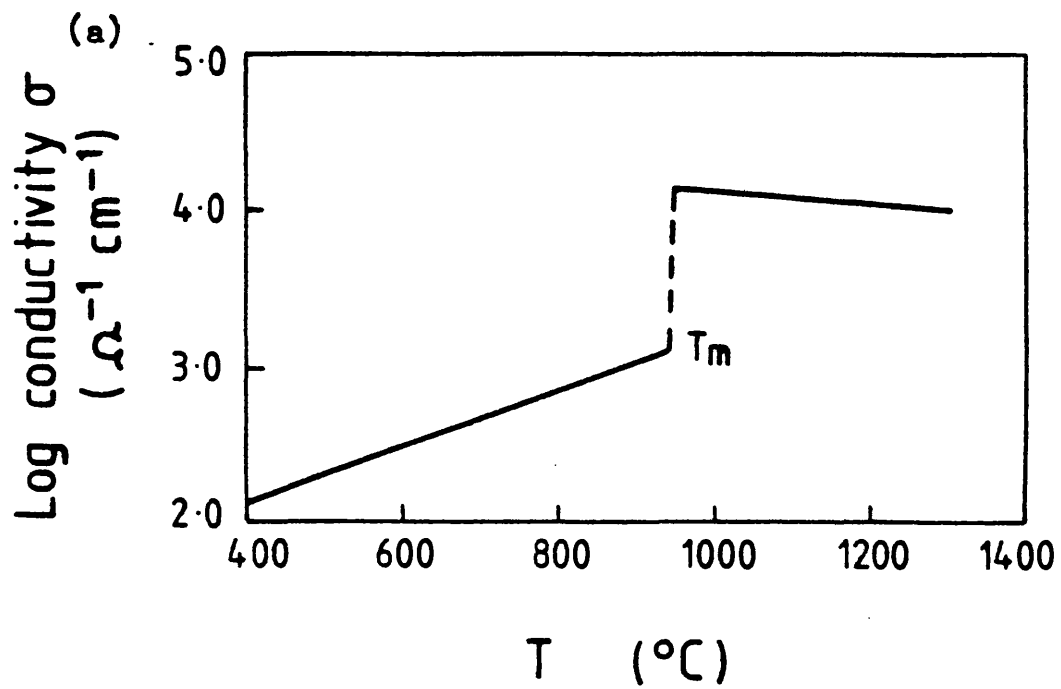
+ Paul et al., (1973)

T_s denotes temperature of substrate

Table 6.I



Figure 6-I



Change in (a) conductivity and (b) density of germanium at the melting point

Figure 6-2

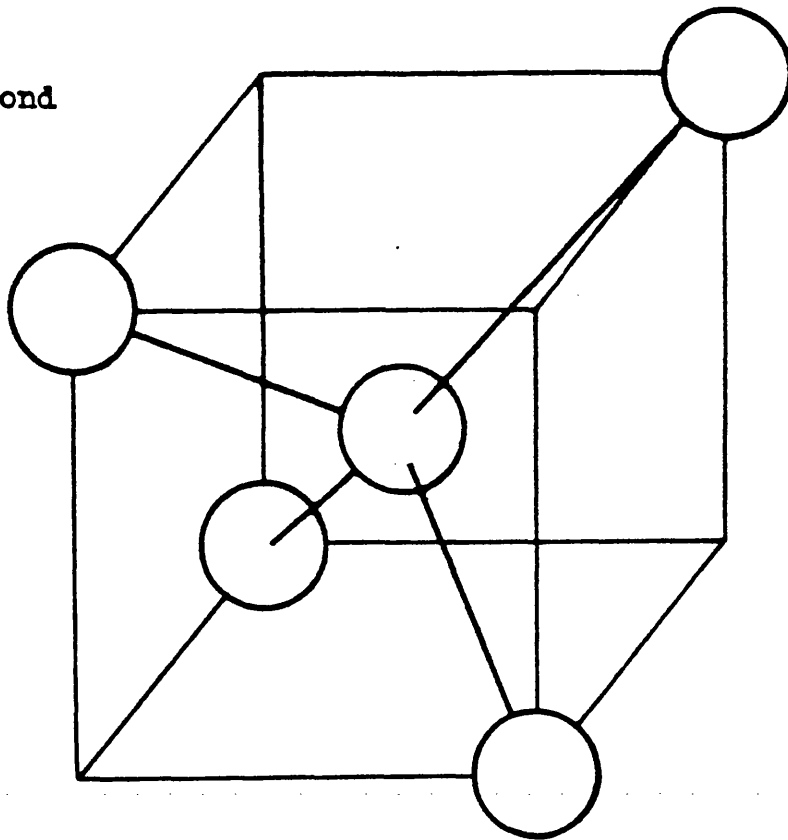
slightly further away along the c-axis, (figure 6-3). Calculations of the liquid density of electronic states have been reported by Halder (1980) and by Choo et al (1974).

Amorphous germanium may be prepared by several techniques including:- vapour deposition, sputtering, electrolytic deposition, ion bombardment and decomposition of germane (Ge H_4). Measurements of the structure are preparation dependent as indicated in table 6.1 although the wide variation in density is due to voids rather than to changes in the local atomic arrangement. The mean nearest neighbour distance of amorphous germanium (2.47 \AA) is close to that of the crystalline form (2.45 \AA). X-ray (Paul et al, 1973) and neutron (Etherington et al, 1982) diffraction measurements of vapour deposited films agree with each other and are consistent with models based on continuous random networks (CRN) of four fold tetrahedrally arranged units, such as those of Polk (1971) and Polk and Boudreaux (1973). The agreement is, however, not perfect and they cannot distinguish between different four fold coordinated CRN structures. Amorphous germanium is still a semiconductor and theoretical calculations have confirmed that this is a consequence of the well defined tetrahedral local arrangement rather than to long range order (Ley et al, 1979).

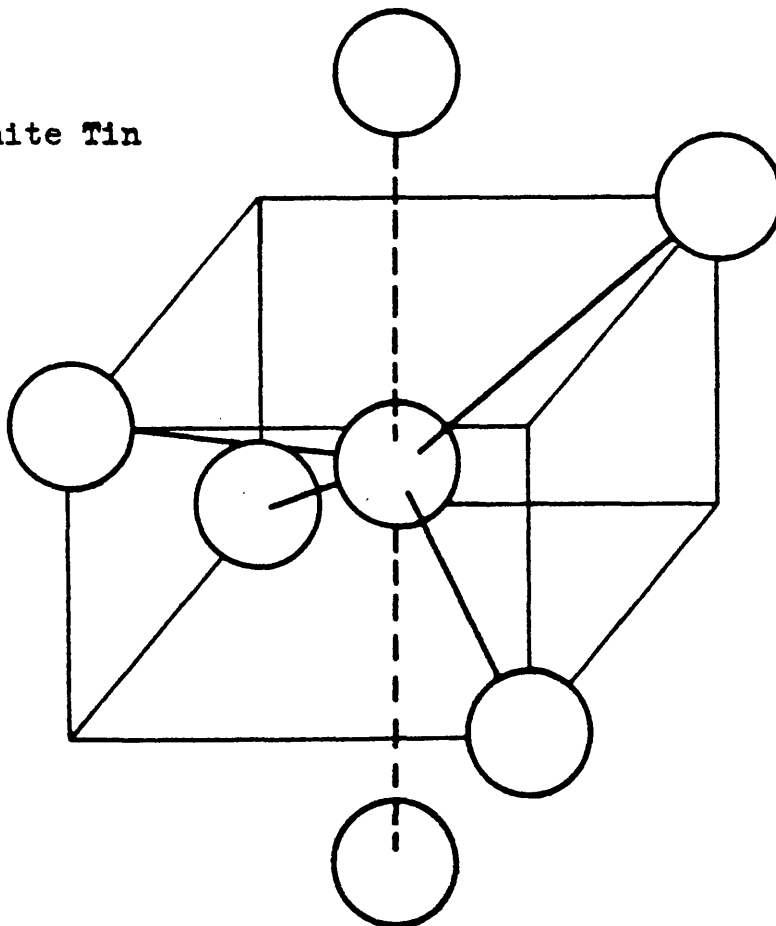
6.2 Photoemission Spectra

Figure 6-4 shows photoemission curves obtained using helium I radiation from liquid and solid (polycrystalline) germanium superposed on a background of secondary electrons and compared to the data from crystalline and amorphous germanium of Eastman et al (1974 a) excited using light of energy $h\nu = 25 \text{ eV}$. The x-axis shows the energy of the initial state in electron volts with the Fermi energy set at zero eV;

(a) Diamond

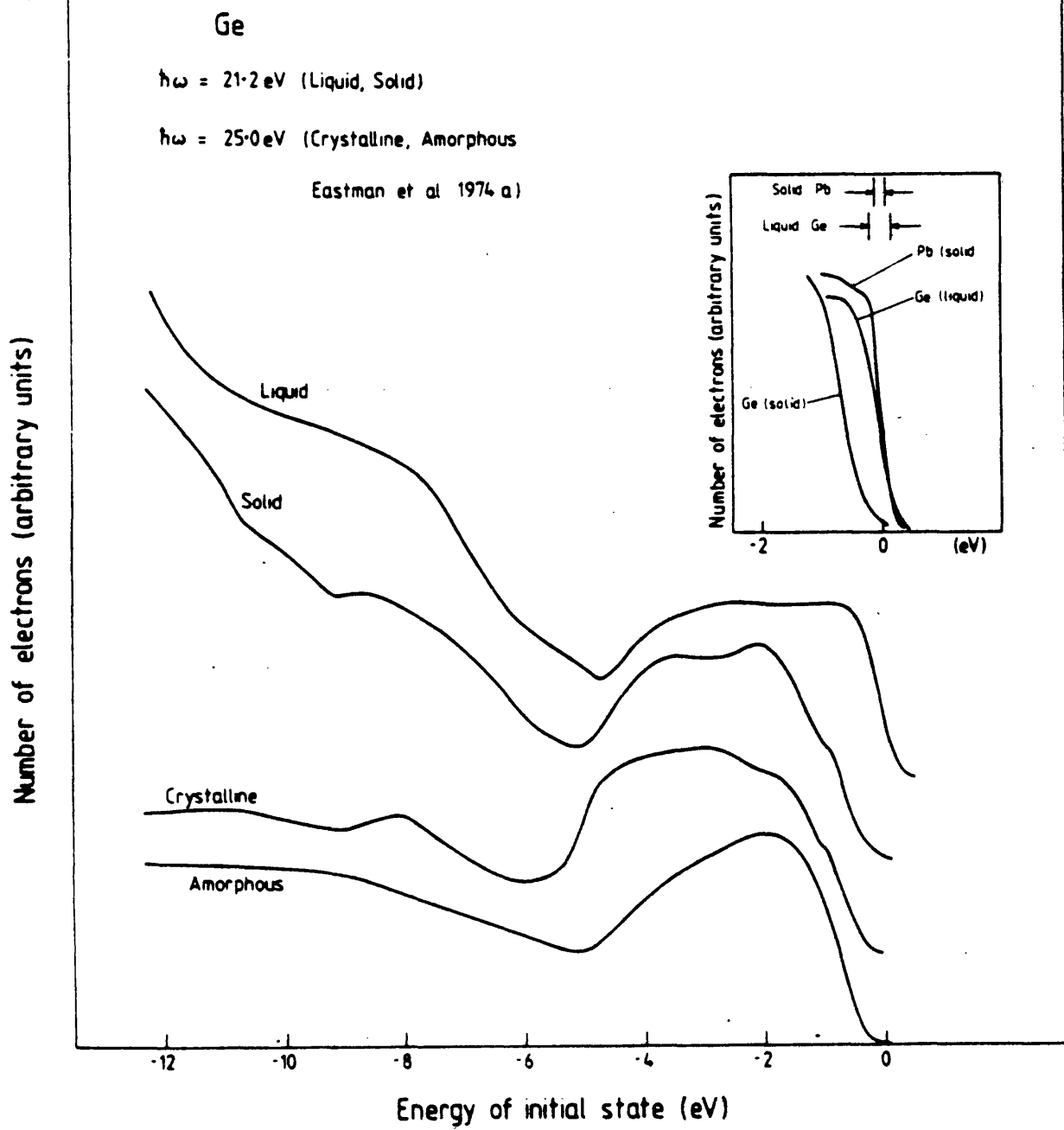


(b) White Tin



Comparison of structures of diamond and white tin

Figure 6-3



EDCS of germanium

Figure 6-4

the y-axis shows the number of electrons in arbitrary units. The Fermi energy was located in these measurements by evaporating a layer of lead metal onto the frozen germanium sample at the conclusion of the experiment; the valence band edge was extrapolated from the leading edge of the solid sample spectrum and was used to locate the crystalline and amorphous spectra on the energy scale. The inset figure shows the photoemission curves from solid and liquid germanium compared to the spectrum obtained from a solid (evaporated) lead film.

The valence spectrum of crystalline germanium consists of three bands which can be correlated to the calculated density of states shown by Eastman et al, (1974 b). The least tightly bound band is of 4p-type character with a width of ≈ 5 eV and a maximum at ≈ -3 eV. Some evidence of the fine structure present in the calculated spectrum is also observable although the shoulder at ≈ -1.0 eV is attributed to surface states (Eastman and Grobman, 1972). This band is separated from two further bands of 4s character by a well defined minimum at ≈ -6.1 eV. These bands have maxima at ≈ -8.0 eV and ≈ -11.0 eV in reasonable agreement with the theoretical result which shows peaks at ≈ -7.3 eV and ≈ -10.3 eV.

The EDC of the solid (polycrystalline) sample shows a resemblance to that of the crystalline material; the surface state feature is visible, the 4p-like band is structured and there is a clear dip visible at ≈ -9.0 eV indicating that the lower band is split.

The EDC for amorphous germanium shows changes from that of the crystalline material which may be summarised as:-

- (1) The two lower lying peaks of the crystalline EDC merge to become one in the amorphous sample.
- (2) The upper 4p-like states become less structured, the surface state

feature is lost and there is a distinct steepening of the leading edge of the amorphous EDC (figure 6-5). The dip separating the 4p-like states from the lower bands moves towards the Fermi energy by ≈ 0.9 eV in the amorphous sample.

Upon melting there are large changes visible in the EDC. Liquid germanium exhibits a finite density of states at the Fermi energy. The structure of the 4p-like band is lost as is the surface state feature and the EDC has no peak but a plateau which begins at ≈ -0.7 eV and finishes at ≈ -2.8 eV. The 4p-like band is separated from the lower band by a well defined minimum at ≈ -4.7 eV. The lower band is not split but exhibits a broad maximum at ≈ -7.7 eV with a total width of ≈ 6.5 eV in reasonable agreement with the EDC of the amorphous sample which may be expected as both are disordered systems lacking long range order.

6.3 The Optical Density of States of Liquid Germanium

The optical density of states of liquid germanium was derived from the EDC of figure 6-4 using the procedure described in chapter two. The work function was taken from Weast (1979) and the absorption coefficient was determined from the results of LaVilla and Mendlowitz (1969) for an evaporated film. The electron inelastic scattering length for the normalisation constant was estimated at 17 \AA from the universal curve (Seah and Dench, 1978) and the bulk plasmon energy was taken from Mott and Davis (1979). Figure 6-6 compares the EDC calculated from the optimised optical density of states, shown in figure 6-5, with the measured EDC.

Figure 6-5 shows the spectra of Eastman et al (1974 a) of crystalline and amorphous germanium minus the secondary electron

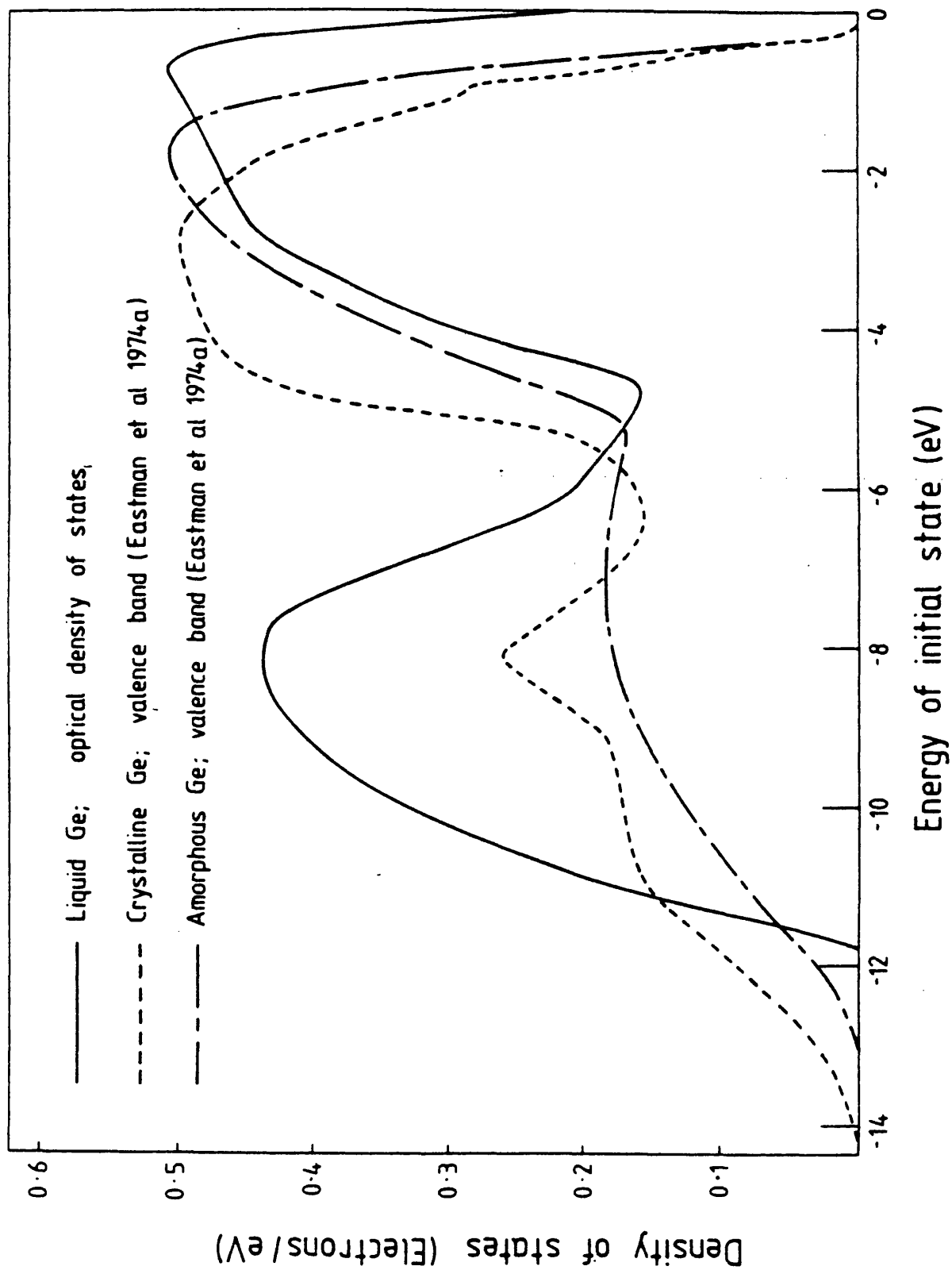
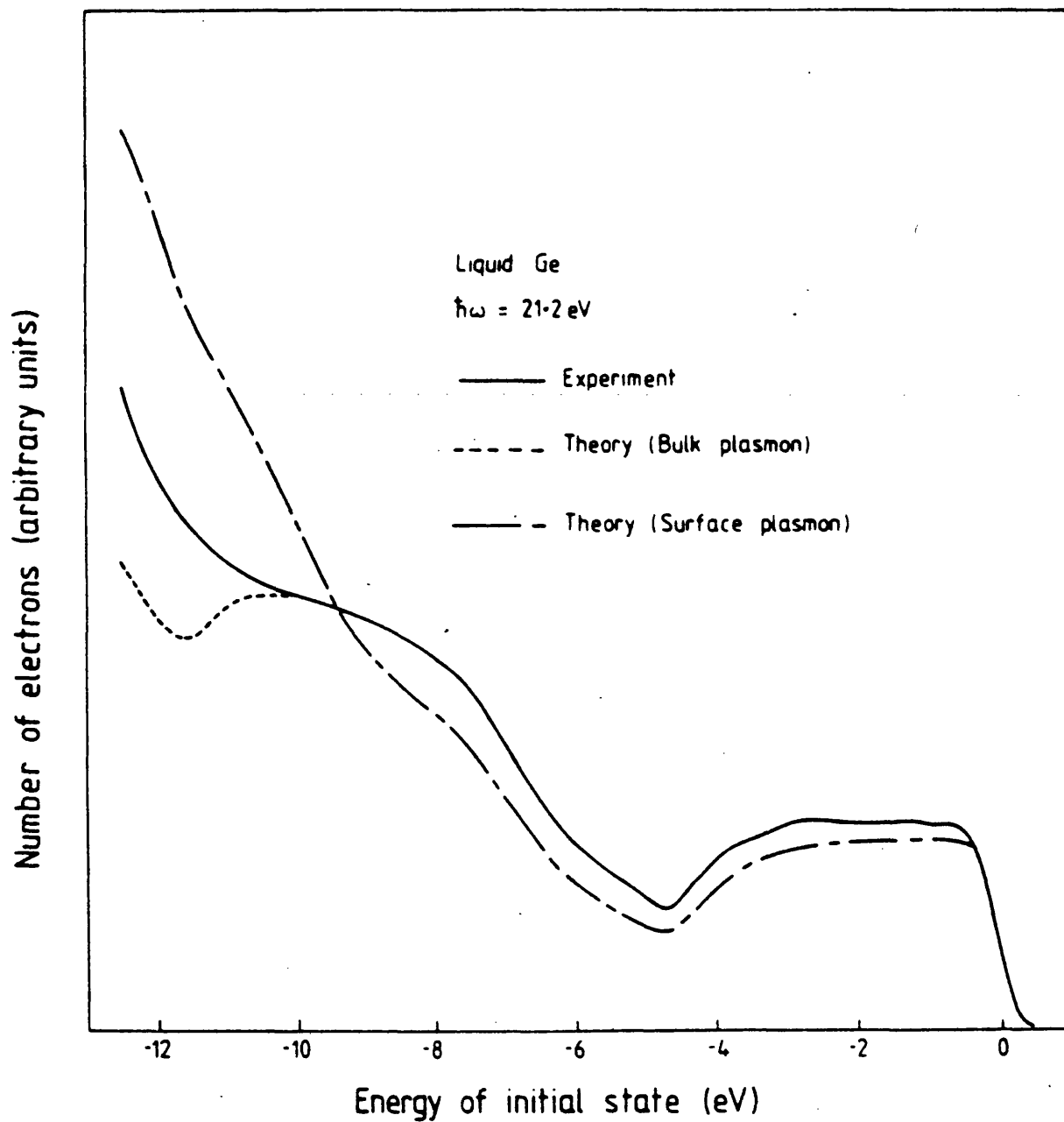


Figure 6-5



Comparison of theoretical and experimental
EDCS for liquid germanium

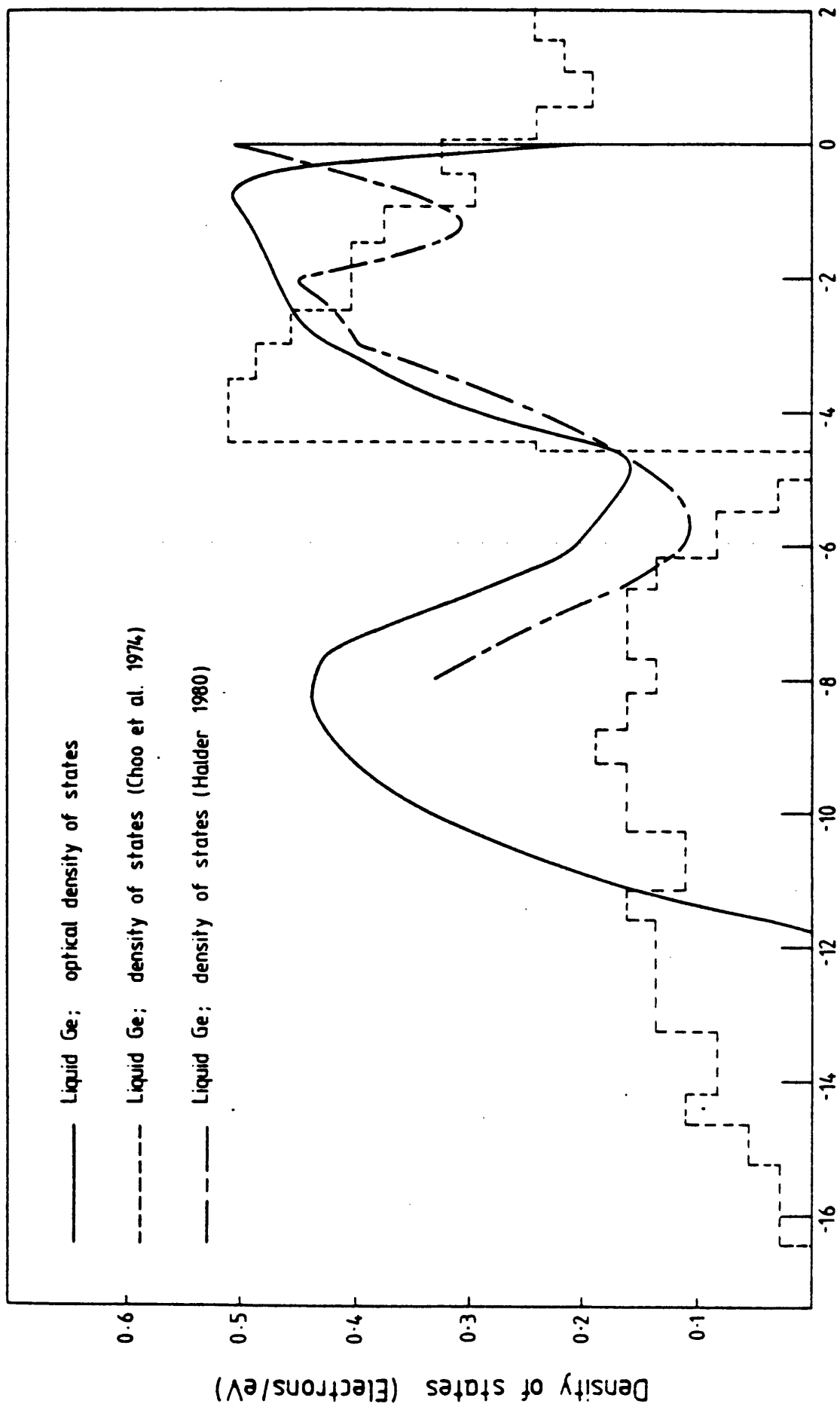
Figure 6-6

background compared to the optical density of states of liquid germanium. The curves were normalised to be of the same intensity at the peak of the 4p like band. The curves for amorphous and crystalline germanium have been discussed and analysed in detail by Eastman et al, (1974 a). The optical density of states of liquid germanium exhibits a finite density of states at E_F and an overall structure which is comparable to amorphous germanium, namely a minimum at ≈ -5 eV separating the upper 4p like states from the lower 4s like states, both curves being smooth and showing no splitting of the lower band.

Figure 6-7 shows the optical density of states compared to the calculations of the density of states of liquid germanium by Choo et al (1974) using the extended Hückel theory and Halder (1980) using an application of a molecular liquid model. The calculations were normalised to the intensity of the experimental data at the maximum of the 4p like states.

Both calculations reproduce the dip between the two bands at ≈ -5.0 eV although the calculation of Choo et al shows a gap and that of Halder displaces the minimum by ≈ 0.9 eV. Halder's calculation shows structure at ≈ -3.0 eV where the experimental curve shows a shoulder, but it also shows a dip at ≈ -1.0 eV which is not reproduced by the experimental curve. The calculation of Choo et al shows a falling density of states at E_F which will be considered in the following section: it is instructive to note that if Halder's calculation is displaced so that the minimum at ≈ -1.0 eV then lies at E_F there is better agreement to the experimental result.

Figure 6-8 shows the optical density of states compared to the calculation of the density of states of liquid germanium by Robertson



Energy of initial state (eV)

Figure 6-7

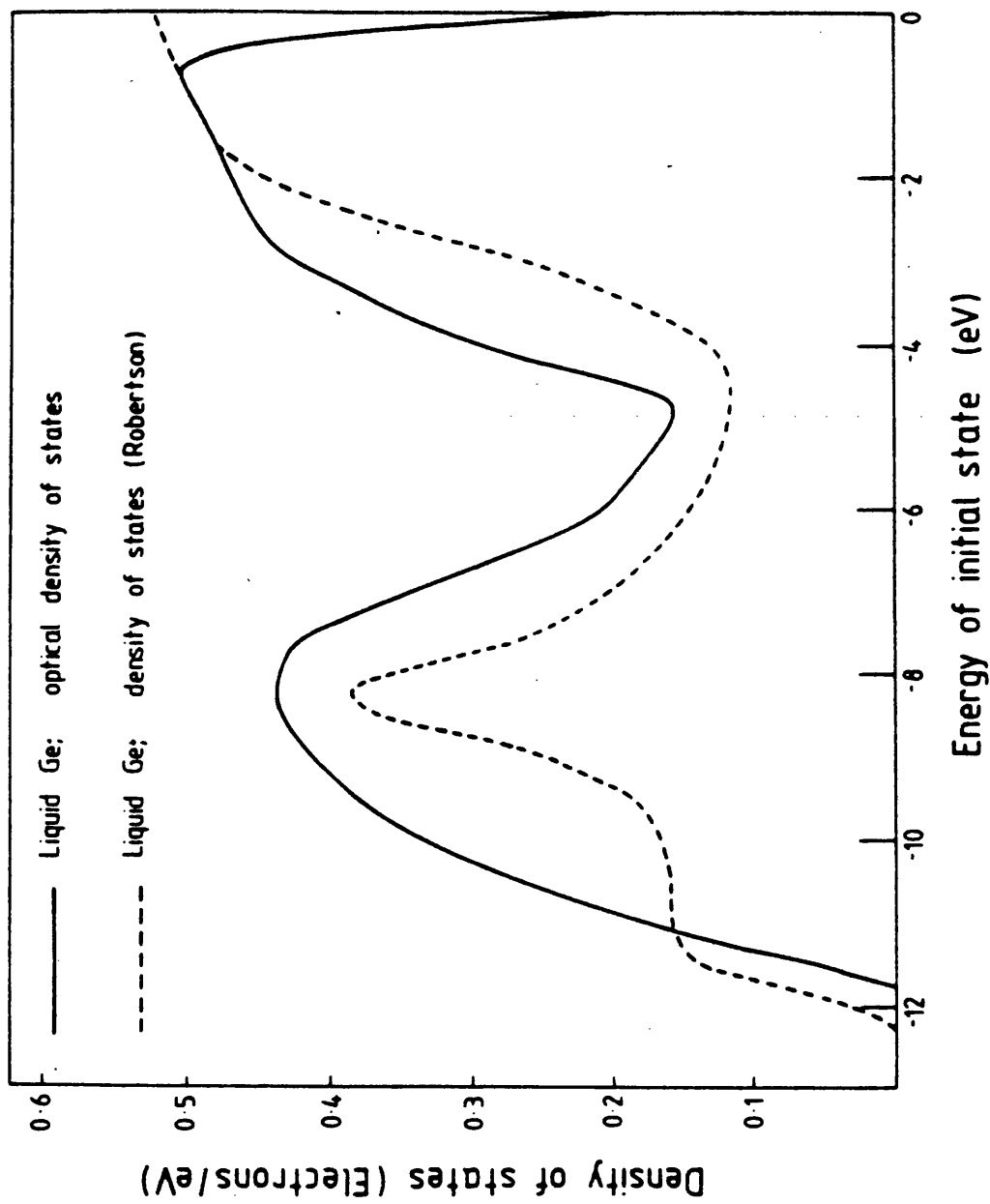


Figure 6-8

(private communication), using the recursion method. The curves were normalised to be of the same intensity at ≈ -1.0 eV. There is good overall agreement; the calculation reproduces well the bandwidth and the position of the major features but does not show the shoulder at ≈ -3.0 eV or a falling density of states at E_F .

6.4 Photoemission and Structure and Concluding Remarks

The sensitivity of valence electronic structure to local atomic order of covalently bonded materials has prompted speculation that photoelectron spectroscopy could be used to complement more direct structural probes such as Extended X-ray Absorption Fine Structure Spectroscopy (EXAFS) and X-ray and neutron diffraction (Brodsky and Cardona, 1978 and Ley et al, 1979). The sensitivity arises from the directional nature of the bonds and the dependence of the electron states on more than the first neighbour shell. For more localised d-orbitals in the transition and noble metals it is only the coordination number and near neighbour separation which is significant (Norris, 1977).

The most documented example of the interrelation of electron states and the details of the atomic environment is the loss of the double peaked structure in the silicon 3s and germanium 4s bands on passing from the crystalline to the amorphous phase. Joannopoulos and Cohen (1973) showed that the existence of two well defined peaks is a consequence of six membered rings, a ring being defined as the least number of bonds that must be traversed on leaving a given atom before returning to the same atom. For five and seven fold rings the density of states peaks near the centre of the band. In the diamond structure, only six fold rings occur, two rings intersecting at each atom, whereas the Polk CRN model possesses on average 0.38 five fold, 0.91 six fold

and 1.04 seven fold rings. Photoemission was thus able to distinguish between this and other models of the amorphous structure such as that due to Connell and Temkin (1974) which though lacking long range order was constructed of only six fold rings. Other examples where photoemission has usefully pointed to specific structures are described by Brodsky and Cardona (1978) and by Ley et al (1979).

Turning to figure 6-4 it can be seen that the structure present in the 4s band for the polycrystalline film and frozen solid is lost for the amorphous film and also for the liquid as expected. The XPS data of Ley et al (1972) clearly shows the coalescing of the two lower peaks in amorphous germanium compared to their separation in a sample of cleaved germanium. Of more interest is the behaviour of the structure near the Fermi level. Thorpe and Weaire (1971) pointed out that the semiconducting gap in the group IV elements is a consequence of the well defined tetrahedral local environment. Thus even in the amorphous case the loss of long range order does not remove the gap since four fold coordination is retained and although defect states due to unsatisfied "dangling bonds" cause some tailing into the gap region, the essential feature remains. For the liquid in which the well defined local structure is lost, the gap disappears and a metallic behaviour results.

The inset diagram of figure 6-4 compares the region of the Fermi energy for lead and solid and liquid germanium. The increase of the width of the molten germanium curve at E_F can be exactly explained by the broadening effect with temperature of the Fermi probability distribution which contributes $2.77 k_B T$ to the width. Accurate measurements allowing for the difference in temperature between molten germanium and a lead film at room temperature show the two curves have the same measured width within error limits, hence there is no evidence

of a dip in the density of states at E_F for liquid germanium which thus behaves as a simple metal.

It may be thought that because liquid germanium retains some short range order, ie:- all the covalent bonds are not broken and the liquid is not completely free electron like, that a dip in the density of states at E_F might be expected. The calculation of Choo et al (section 6.3) shows a falling density of states at E_F . Waseda and Suzuki (1975) from diffraction data suggested that liquid germanium has a white tin like arrangement of atoms and the density of states calculation of white tin (Ament and de Vroomen, 1974) shows a dip at the Fermi level. Such a dip may also be expected for liquid germanium as tin and germanium both lie in the same column of the periodic table so having a similar valence electronic structure. However, if liquid germanium does show a dip at E_F , then photoemission spectroscopy is unable to detect it.

6.5 Silver : Introduction

In the solid phase, silver has a cubic close packed structure with the atoms arranged in a face centred array like lead (figure 5-2). For silver, each atom has twelve nearest neighbours, the cell edge is 4.0862 \AA in length and the nearest neighbour distance is therefore 2.89 \AA (Wyckoff, 1963). In the molten phase, the nearest neighbour distance falls slightly to 2.87 \AA and the coordination number is 11.3 (Waseda, 1976), suggesting that the local order remains largely unchanged despite the change of phase.

Silver, unlike lead or tin, cannot be regarded as a simple metal because of the full 4d band which lies close to the conduction band; electrons in d-bands tending to be more localized and consequently less

mobile than their counterparts in s and p shells, but the valence electrons are s-like and behave like nearly free electrons.

The band structure of silver has been calculated by Fong et al (1975) using the empirical pseudopotential method and by Christensen (1972) using the relativistic augmented plane wave method. The density of states functions derived from these band structures show good agreement with each other in terms of their major features. Keller et al (1979) used the multiple scattering cluster method to calculate the density of states for silver, the result being a curve showing the silver 4d band and 5s valence band but with no sharp structure visible.

The only calculation reported of the density of states of liquid silver is that of Itami and Shimoji (1972) which reveals a deviation from the free electron parabola but which fails to reproduce any of the structure associated with transitions from the silver 4d band as seen in the experimental data (next section).

Experimental photoemission measurements have previously been reported (Williams and Norris, 1976) from liquid silver and the measurements reported in the next section serve to reinforce the validity and conclusions of the earlier data.

6.6 The Photoemission Spectrum of Liquid Silver

Figure 6-9 shows the photoemission curve obtained from liquid silver using helium I radiation ($h\nu = 21.2$ eV). The x-axis shows the energy of the initial state in eV with the Fermi energy set at zero eV, the y-axis shows the number of photoelectrons emitted and the curve is shown superposed on a background of secondary electrons. The curve is

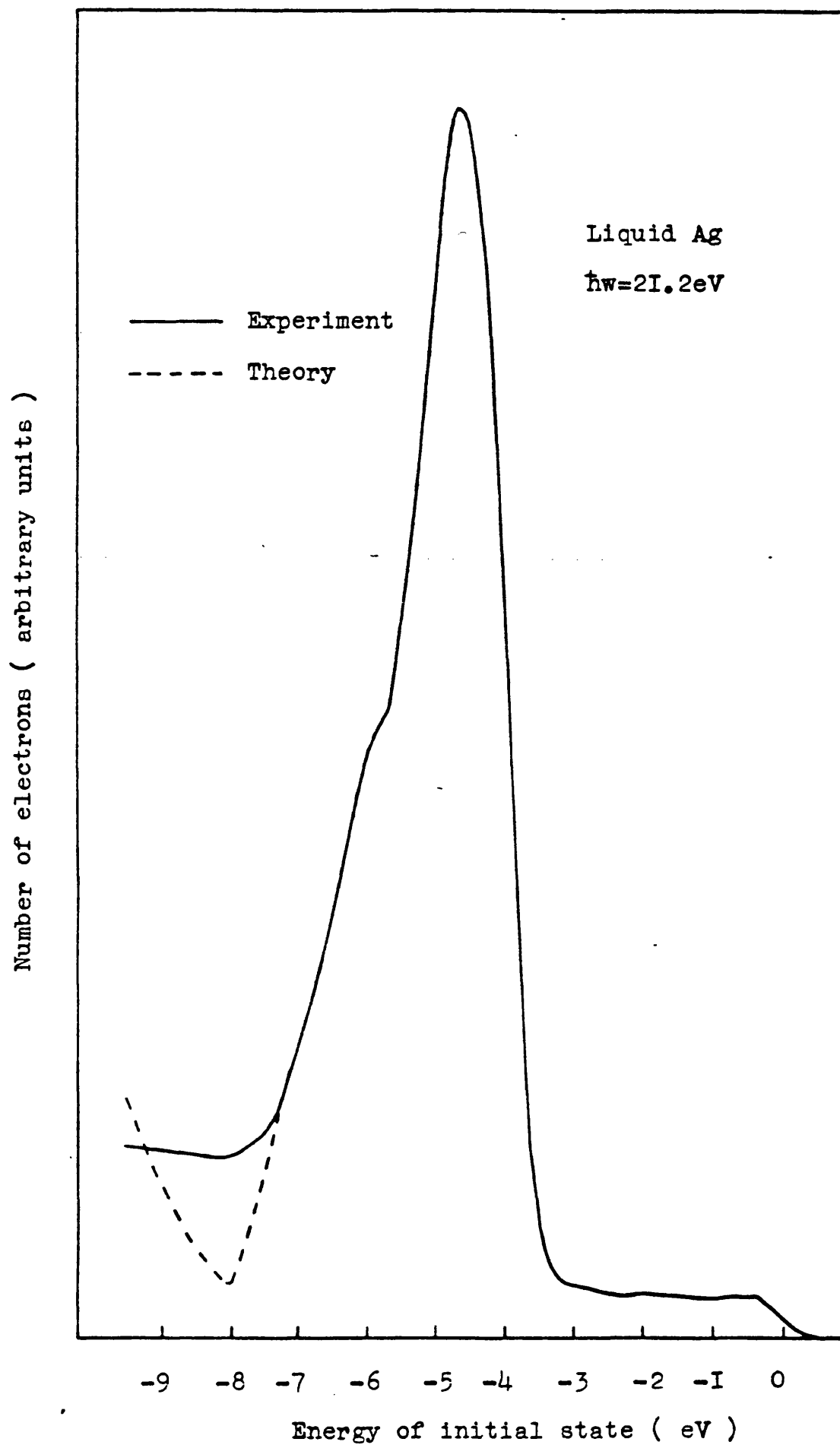


Figure 6-9

dominated by transitions ascribable to the filled silver 4d band from ≈ -7.5 eV to ≈ -3.5 eV and transitions from the silver 5s band are visible from ≈ -3.5 eV to E_F . The silver 4d band shows a shoulder at ≈ -5.8 eV which is evidence of a peaked structure which is not well resolved, although other noble metals (eg: liquid copper) show stronger evidence of a double peaked structure (Williams and Norris, 1976).

A computer routine was employed to remove the effects of the helium I satellite line (table 3-1) which otherwise causes a feature in the EDC between ≈ -2 eV to ≈ -3.5 eV generated by excitation by the satellite line ($h\nu = 23.086$ eV) of the silver 4d band.

6.7 The Optical Density of States of Liquid Silver

The optical density of states (ODS) function of liquid silver was extracted from the photoemission data using the model of chapter two. The computer simulated EDC from the optimised ODS function is shown in figure 6-9 compared to the experimental EDC which has been corrected for the transmission function of the analyser. The agreement is very good from E_F to ≈ -7.3 eV where the simulation underestimates the contribution of secondary electrons. This may be attributed to the presence of thermionic electrons in the experimental EDC for which the computer model makes no allowance.

Input parameters for the calculation were taken from Weast (1979) for the work function and the absorption coefficient was obtained from Hagemann et al (1975) from an evaporated film which was used as being the only available data. The scattering length for the normalisation constant L_0 was obtained from the universal curve (Seah and Dench, 1978) and the bulk plasmon energy was taken from the data of Zacharias and

Kliwer (1976) from a polycrystalline foil as being the only available data.

Figure 6-10 shows the optimised ODS function compared to the density of states calculation of solid silver by Christensen (1972). This comparison is reasonable, because the valence state is dominated by the semi-localized 4d band which should be well described by a tight binding method taking account of only the nearest neighbour shell, and the short range order as indicated by the number and separation of nearest neighbours changes little on melting, as argued by Norris (1976 and section 6.4). Figure 6-10 shows the result which is intuitively expected; the experimentally derived curve for the liquid is a smeared version of the solid state curve showing none of the sharp features, although the principal minimum for the solid very closely coincides with the point of inflection in the liquid spectrum.

6.8 The Photoemission Spectrum of Liquid Silver at $h\nu = 16.8$ eV

Photoemission measurements were also made on liquid silver using the neon I ($h\nu = 16.8$ eV) line as shown in figure 6-11. This energising line has the advantage that there is no satellite; the validity of the computer routine for removing the feature caused by the satellite line in the helium data may be seen in the good agreement between figures 6-9 and 6-11, in the range from E_F to ≈ -3.5 eV. The similarity of the upper valence band of liquid silver taken with the two different photon energies is evidence for non-direct transitions and supports the assumption of chapter two that the experimental EDC is dominated by the initial electron structure.

However, the imperfections of the simple model may be seen in figure 6-11 where the experimental EDC, corrected for the transmission

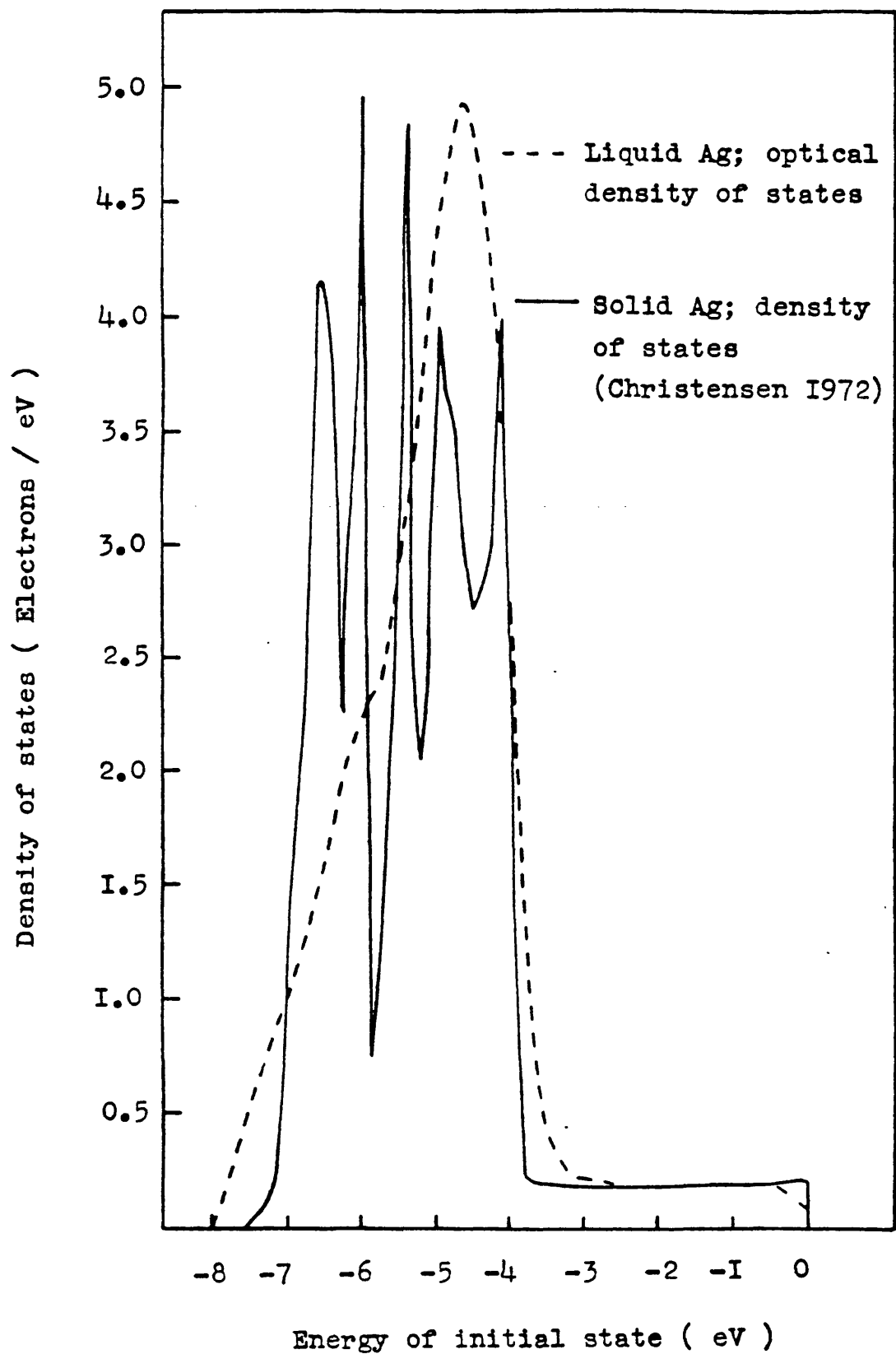


Figure 6-10

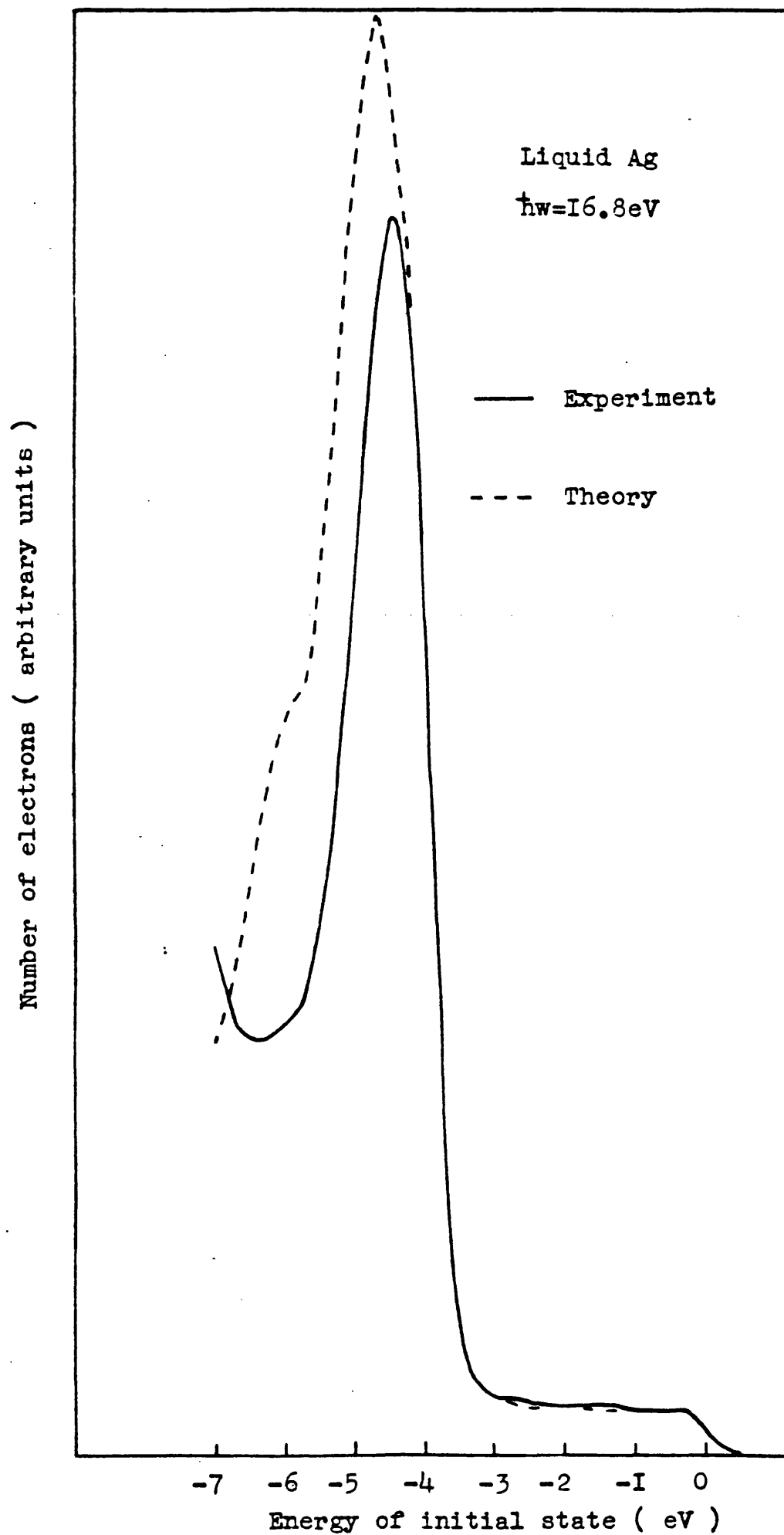


Figure 6-II

function of the analyser, is shown compared to the computer simulation of an EDC of liquid silver using a photon energy of 16.8 eV and the optimised ODS function extracted from the helium I data. The computer simulation predicts a greater intensity of the silver 4d band than is experimentally observed and also shows the point of inflection at ≈ -5.8 eV which is not seen in the experimental EDC because of the secondary electron background which the computer simulation fails to correctly predict. The experimental EDC is also influenced by the presence of thermionic electrons. The change in the secondary electron background can also explain the slight movement of the peak of the silver 4d band between the theoretical and experimental result by ≈ 0.2 eV.

In conclusion, these photoemission results from liquid silver are in good agreement with earlier published data, revealing EDCS dominated by transitions from the filled silver 4d band with the 5s valence band also visible. Structural data reveals a similarity in short range order characteristics between the solid and liquid phases and the optical density of states function extracted from the liquid photoemission data, reveals some similarity to the solid density of states function without reproducing the sharp features. The similarity of the liquid silver EDCS taken with two different photon energies in the upper valence band region is typical for non-direct transitions and supports the assumption that the EDC is dominated by the initial electron structure.

6.9 Metallic Glasses and the Silver-Germanium System

As considered in section 1.10, the system silver-germanium is of interest because it is expected to show enhanced glass forming abilities at the eutectic composition (Donald and Davies, 1978). The system

silver-germanium was chosen for study because it was judged (and proved to be) capable of yielding photoemission measurements over the full concentration range, and hence any re-arrangement of the valence electronic structure as a function of composition should show in the spectra taken.

It has long been a subject for debate as to why such binary alloys with a deep eutectic composition show enhanced glass forming qualities. Turnbull (1973) presented a summary of amorphous solid formation for monatomic systems as well as binary alloys which have a eutectic composition which included but little information as to why the glass forming ability is enhanced at or near the eutectic; the effects stressed were the possible importance of the difference between the atomic sizes of the alloy constituents (as specified by the Wigner-Seitz volumes), the potentials being of such magnitude that the energy of the system is lowered by unlike atom pairing, and the preferred separation of unlike atoms being substantially smaller than one half of the sum of the Wigner-Seitz separations of the component species.

Suryanarayana (1980) gave a later review, predominantly concerned with liquid-quenched metal-metal glasses, which also reached similar conclusions but which contained no hypothesis for the reasons for the formation of metallic glasses. The formation and characterization of amorphous metals has been covered in the review by Giessen and Whang (1980) and the article by Gilman (1980) summarises the production and engineering aspects (eg: high strength and ductility, corrosion resistance and low magnetic losses) of metallic glasses.

Tauc and Nagel (1976 a and 1976 b) have reported a theory based on a nearly free electron calculation to explain the formation of an amorphous alloy at the eutectic composition of a noble metal and a

member of group IVa or Va, the key being that the Fermi energy, E_F , must lie at a minimum of the density of states curve. An argument was presented to show that an energy barrier to nucleation would arise if the liquid were to crystallize thus explaining the enhanced glass forming quality, and also it was postulated that the eutectic temperature is lowered further by the minimum in the density of states thus increasing the glass forming tendency as well. This theory should be applicable to the silver-germanium system and will be considered later in this chapter.

As mentioned in chapter one, there has been some structural work reported on silver-germanium. The neutron diffraction study of the silver-germanium eutectic by Bellissent-Funel et al (1977) revealed predominant unlike atom interactions. This was deduced from the measurements which showed that for the liquid eutectic the silver-germanium separation (2.66 \AA) was smaller than the silver-silver separation (2.92 \AA) and the germanium-germanium separation (3.12 \AA). Similar bonding characteristics with mean closest distances for neighbouring atoms smaller than that for pure gold were reported by Waghorne et al (1976) for the similar systems gold-silicon and gold-germanium.

Bellissent-Funel et al (1979) reported small angle neutron scattering experiments on silver-germanium alloys. The q-dependent small angle scattering was found to be incompatible with theoretical predictions of the density and concentration fluctuation effects of a classical binary liquid alloy and was interpreted in terms of scattering by heteroatomic chains of atoms in the disordered metallic matrix which were postulated to exist at the eutectic composition; the volumic percentage of the chains was shown to decrease with the increase of

germanium concentration beyond the eutectic composition. This structural data will be mentioned later in this chapter in relation to the photoemission data.

The optical and electrical properties of thin films of silver-germanium have been investigated by Nguyen Van et al (1982) but the data contains no useful information concerning the properties of the liquid alloys.

It should be noted that it is not definitely known whether silver-germanium can be quenched from the liquid to form an amorphous solid alloy (Gallagher - private communication, 1983). Agarwal and Herman (1977) presented work on liquid quenched silver-germanium where small isolated areas of their foil showed the presence of an amorphous phase. They reported, however, that despite repeated efforts it was not possible to obtain a uniform amorphous phase.

The system silver-germanium was probed by photoemission spectroscopy to investigate any changes in valence electronic structure. The photoemission data is now presented and discussed in relation to the known properties of the silver-germanium system.

6.10 The Photoelectron Spectra of the Silver-Germanium System

Figure 6-12 shows the photoelectron spectra obtained from the liquid silver-germanium system excited using helium I radiation. The curves are shown with the samples held at $\approx 30^\circ\text{C}$ above their melting temperatures and are plotted against the energy of the initial state with the Fermi energy set at zero electron volts. The curves are normalised so that the intensity of the maximum of the silver 4d band is the same for each EDC apart from the liquid germanium curve which is shown for comparison and completion. The same computer routine was

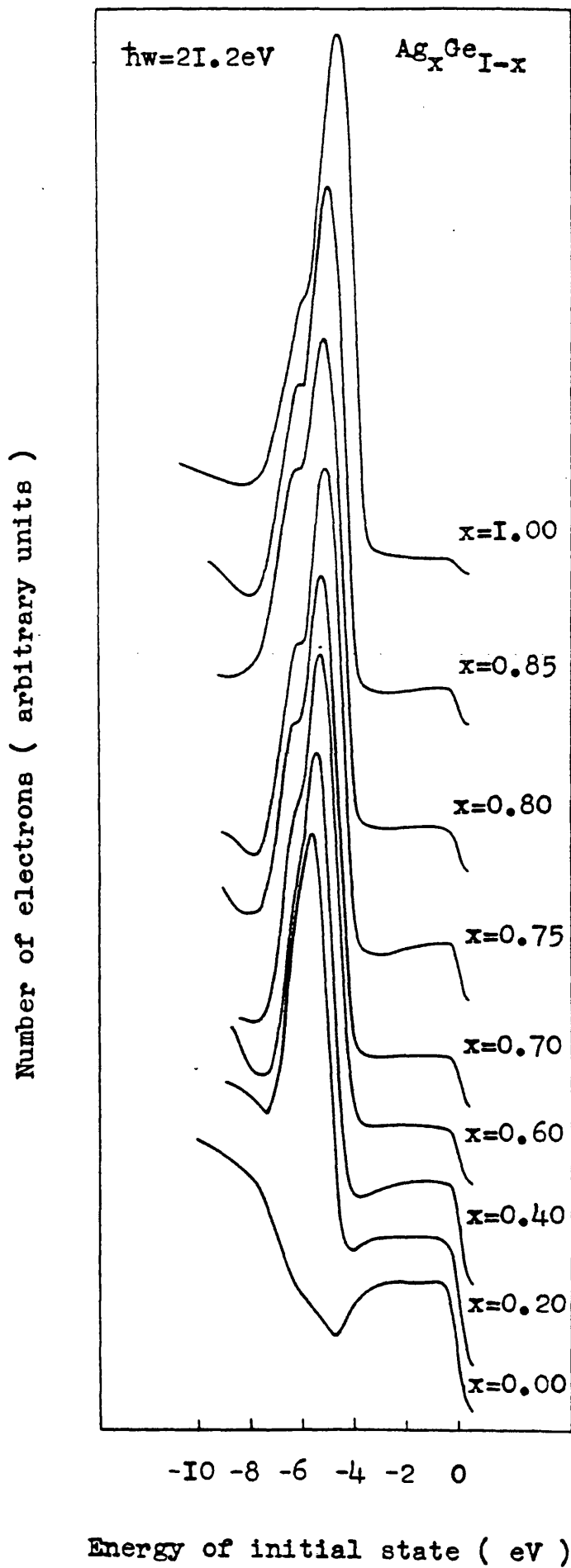


Figure 6-I2

used to remove the effects of the helium I satellite line for the silver alloys as for pure silver (section 6.6).

The curves are shown labelled with the compositions of the bulk alloys. It was not possible to monitor any surface segregation in these alloys because of the lack of a convenient core level to excite using helium II radiation and the Auger system described in section 3.9 was not installed at that time. Nevertheless the effects of surface segregation should not be too large because the surface tensions of liquid germanium and liquid silver are not too dissimilar (Weast, 1979).

6.11 A Discussion and Interpretation of the Photoemission Data of the Silver-Germanium System

The principal features of the EDCS of pure liquid silver and pure liquid germanium have previously been well described. The EDCS of figure 6-12 are dominated by the silver 4d band and show no dramatic change as a function of composition, but close inspection reveals some changes as germanium is added to silver.

Pure silver shows evidence at ≈ -5.8 eV of a second peak which is not well resolved. This splitting is caused by the (interatomic) d-d overlap between atoms rather than the (intra atomic) effect of spin orbit splitting which is also too small (≈ 0.3 eV; Christensen, 1972). The addition of germanium to silver up to the alloy $\text{Ag}_{70}\text{Ge}_{30}$ causes an enhancement of the shoulder; the addition of further germanium then weakens the shoulder until the EDC of $\text{Ag}_{20}\text{Ge}_{80}$ fails to show it.

Measurements were made of the full width at half maximum of the silver 4d band as a function of composition as shown in figure 6-13. This parameter shows an interesting variation with a maximum value at $\text{Ag}_{80}\text{Ge}_{20}$, ie: near the eutectic composition.

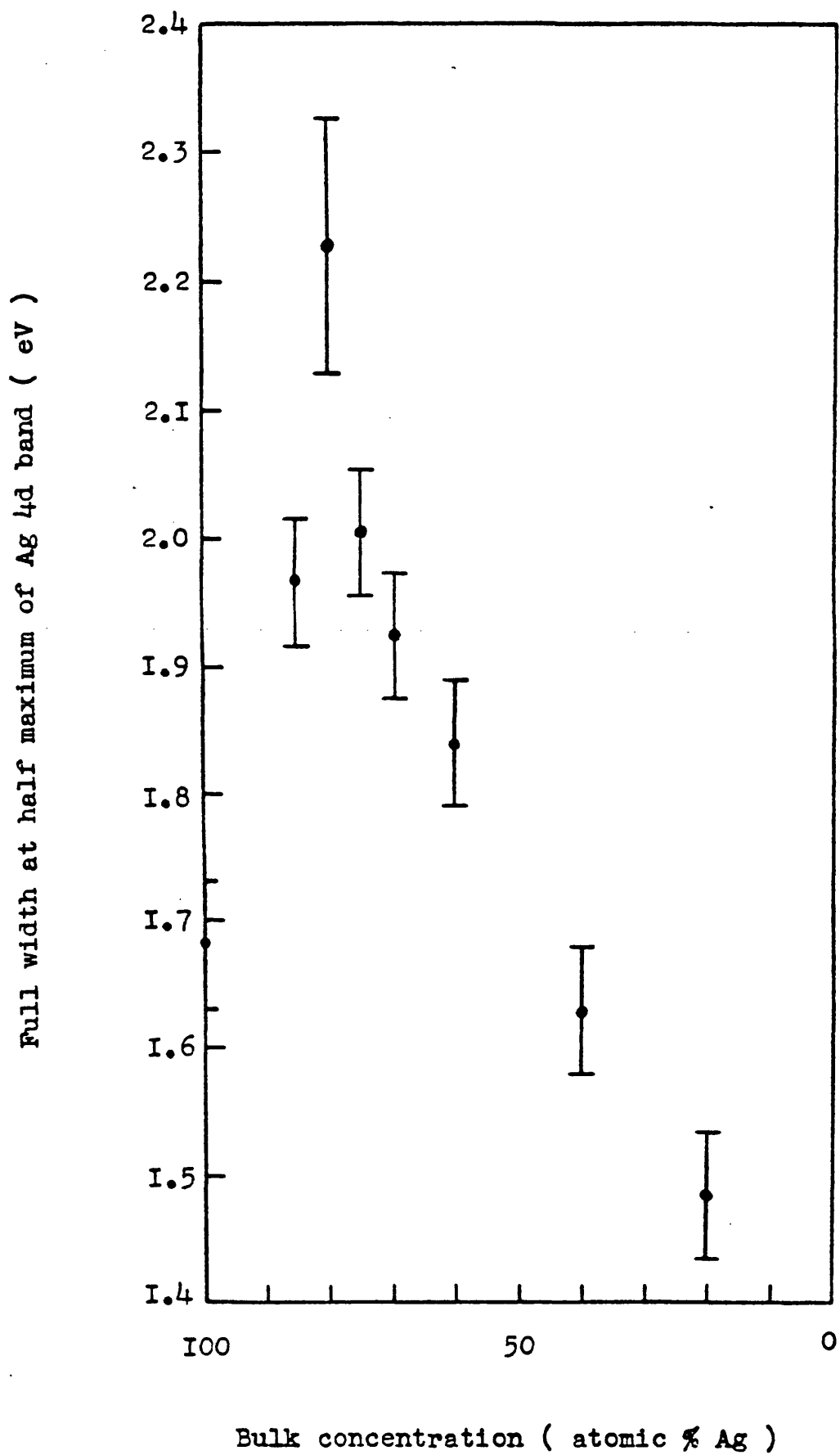


Figure 6-13

Some predictions have been made to quantify the variation of the width of the d band of a noble metal upon dilution. Velicky et al (1968) showed that the width, Δ , may be expressed by the relation:-

$$\Delta \sim \sqrt{\text{concentration}} \quad (6.1)$$

and Heine (1967) showed that the width, Δ , depends upon the interatomic separation, R as:-

$$\Delta \sim 1/R^5 \quad (6.2)$$

These two simple formulae predict that the width of the silver 4d band at the eutectic composition should decrease compared to the width of the band in pure silver because of the decrease in silver concentration and the increase in the interatomic separation of the silver atoms in the eutectic alloy (2.92 Å) compared to pure silver (2.85 Å; Bellissent - Funel et al, 1977), whereas the experimental data shows the reverse to be true. The addition of more germanium to the eutectic composition results in the expected decreasing of the width of the silver 4d band as the silver atoms become "diluted" and move further apart.

The greater width of the silver 4d band at the eutectic composition may be explained by reference to figure 6-14 which shows the variation with composition of the binding energy of the silver 4d band. This figure shows that as germanium is added to silver, the binding energy of the silver 4d band increases which indicates transfer of electronic charge from germanium to the silver 5s band. Although it is a difficult problem to calculate an exact value for the charge transfer, it can be said that the charge transfer must be substantial because the shift of the silver 4d band is large. It is also interesting to note that the gradient of figure 6-14 shows a change in value at a

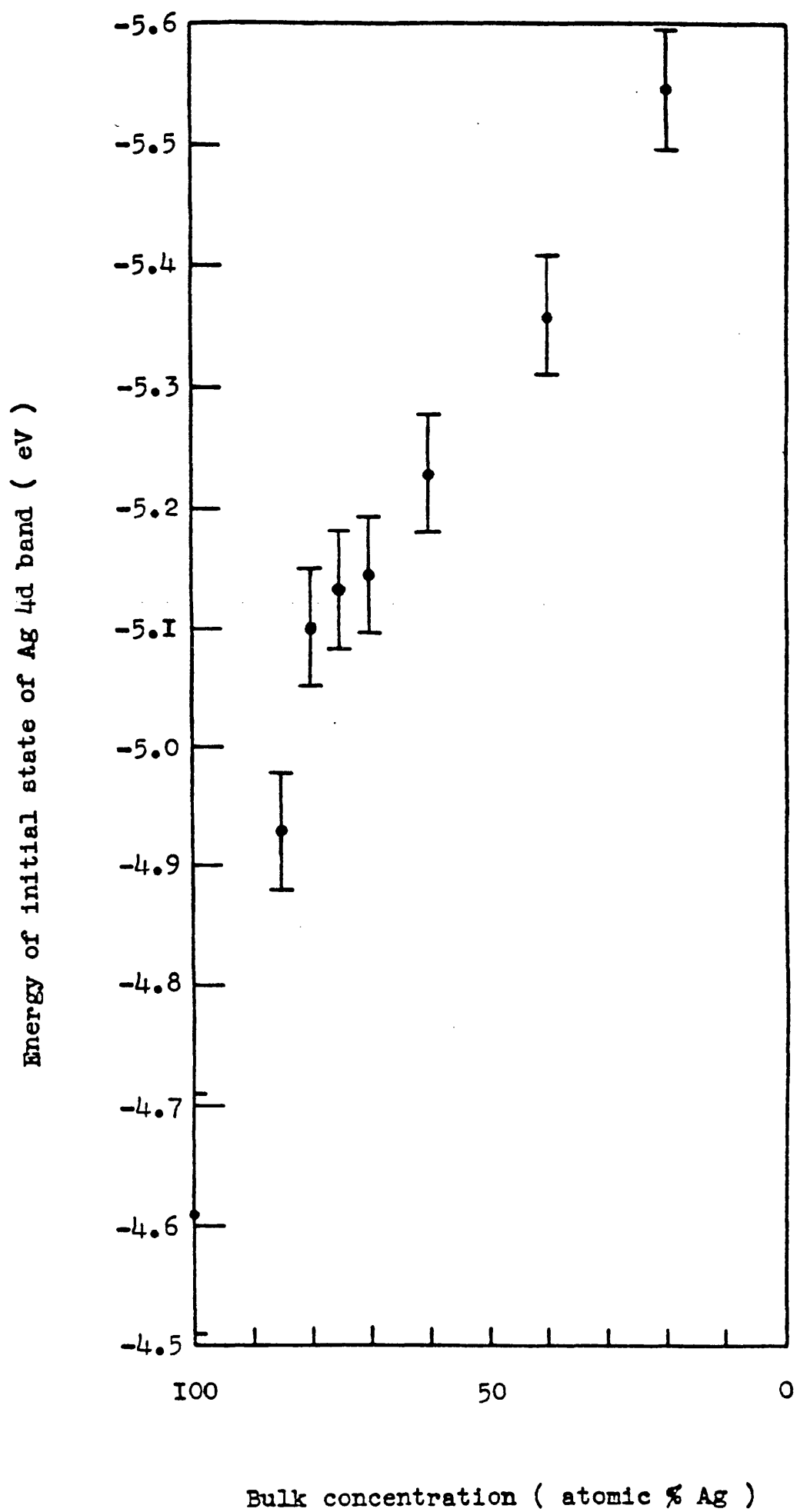


Figure 6-I4

composition close to the eutectic.

The greater width of the silver 4d band at the eutectic composition can then be simply explained by assuming that the EDC results from a mixture of more than one component, ie: a silver or a high silver content "alloy" mixed with a high germanium content "alloy". Bellissent-Funel et al (1979) postulated the existence of chains of atoms in the melt at the eutectic composition, the composition of the chains being identical to that of the matrix, but the calculated maximum volumic percentage of the chains (5%) would seem to be too small to have a large effect on the photoemission EDCS. The change in the EDCS on adding more germanium to the eutectic composition as shown by the loss of the shoulder at ≈ -5.8 eV (ie: the loss of the second peak) and the narrowing of the silver 4d band (figure 6-13) indicates that the melt becomes homogeneous with increasing germanium concentration.

The valence band region from E_F to ≈ -4 eV shows little variation with composition. The high germanium content alloys show a dip forming at ≈ -4 eV which is caused by the increasing influence of the germanium 4p band. There is no evidence of a minimum in the EDC of the eutectic composition at E_F which is to be expected from the theory of Tauc and Nagel (1976 a and 1976 b) and careful measurements on enlargements of the width of the Fermi edge allowing for the effects of temperature show no widening and hence no evidence of a dip forming at E_F at the eutectic composition within the limits of experimental error. Thus, these photoemission measurements eliminate Tauc and Nagel's model for the silver-germanium system.

In conclusion, these photoemission measurements on the silver-germanium system reveal no dramatic change in the valence electronic

structure as a function of composition despite the presence of the eutectic point in the melting curve which indicates structural and bonding changes. There is substantial transfer of electronic charge from germanium to silver sites which is not to be expected from a simple model because the electronegativities of silver and germanium are the same (1.8: Gordy and Thomas, 1956). No evidence is found of a dip in the density of states at E_F of the eutectic composition as predicted by the theory of Tauc and Nagel (1976 a and 1976 b). The increase of the width of the silver 4d band at the eutectic composition is incompatible with that predicted from tight binding theory from knowledge of the silver concentration and interatomic separation and suggests that the eutectic is a mixture of silver rich and germanium rich species. The decrease of the width of the silver 4d band as germanium is added to the eutectic then suggests that the melt becomes more homogeneous with increasing germanium concentration. However, the measured EDCS provide no clue as to why the silver-germanium system forms a eutectic composition.

CHAPTER 7

SUMMARY, CONCLUSIONS AND SUGGESTIONS FOR FURTHER WORK

The conclusions reached at stages throughout this work are collected together and briefly summarised. Suggestions are made for further experimental work. Proposals are made for improvements to the experimental apparatus.

The data presented in this work shows that a comparatively simple sample preparation technique, extended and improved over that of Wotherspoon (1978), is capable of producing clean surfaces which allow meaningful photoemission measurements to be made. The interpretation of these results within the three step model of photoemission, as presented in chapter two, is however questionable. Although Wotherspoon found it was possible to model accurately photoemission data taken at $\hbar\omega = 10.2$ eV, he found the same analysis technique lacked agreement to experimental results taken at a higher exciting energy ($\hbar\omega = 21.2$ eV). Wotherspoon suggested the effects of plasmon decay may be able to account for this discrepancy but inclusion of a term allowing for this process into the computer program (Appendix A) has failed to resolve the discrepancy. This lack of a perfect agreement suggests a more sophisticated model is necessary, and as a preliminary it would be worthwhile to extend to higher orders the higher order losses term (2.6 (V)), the limiting factor being the availability of extended computer facilities. For a complete analysis of the secondary electron background for samples with high melting points, it would also be more satisfactory to include terms to allow for thermionic emission which causes a large number of electrons to be counted at low kinetic energies.

The results from liquid lithium, however, suggest that the three step model itself needs modification to accommodate non-constant matrix elements and surface photoemission, although the bulk photoemission process was found to dominate for the other samples considered. Both Wotherspoon and Rodway (1978) found no evidence of these twin effects; therefore the work presented here gives the first evidence that a more complete theory is necessary to analyse photoemission data from liquid

metals.

Nevertheless, the three step model has been used to analyse the EDCS from the liquid metals considered and has been shown capable of yielding useful conclusions. Liquid lithium reveals a deviation from the free electron parabola but is the most free electron like of all the metals considered. Its ODS is compared to calculations of the liquid density of states; the calculation with the best agreement to the ODS being that of Shaw and Smith (1969). Both lead and tin reveal deviations from the NFE formulism and the derived ODS shows in both cases a closer agreement to the solid phase calculated density of states rather than the liquid phase calculated density of states based on a weak scattering approach. This suggests that some band structure effects persist into the liquid phase and, as detailed by Wotherspoon, stresses the need for more sophisticated methods of calculation of the liquid density of states of simple metals.

For liquid silver, the ODS is dominated by transitions from the silver 4d band and shows a broad similarity to the solid phase calculated density of states without showing the fine details of the latter. This is intuitively expected because the short range order characteristics remain largely unchanged despite melting.

Photoemission measurements have been presented from liquid germanium. The valence band EDC has been compared with similar measurements taken from amorphous and crystalline germanium in terms of local order and ring structure. This work illustrates how powerful a tool photoemission spectroscopy is, not only for elucidating electronic structure but also for providing information on local atomic structure. Although deductions from structural studies show that liquid germanium may have a dip in the density of states at the Fermi level,

no such feature was found experimentally.

The molten alloys lithium-lead and lithium-tin have been probed as a function of composition within experimental limitations by photoemission. The measured shifts of electronic core states of lead and tin have been shown to be not in accord with the simple ionic charge transfer model postulated for these systems, either in magnitude or direction. In conjunction with the EDCS from the valence bands of the alloys, a model has been proposed in which the unlike atom bonding is more covalent than ionic in character with the liquid structure at the stoichiometric composition resembling the corresponding inter-metallic for lithium-lead and also, by virtue of the similarity between the two systems, for lithium-tin. Further photoemission experiments would help to clarify the behaviour of the systems by using a variable energy photon source (eg: synchrotron radiation) to differentiate between the contributions to the EDCS of the alloys of the valence bands of the constituents although there is no reason to use an angle resolved facility because a liquid has no preferred orientation. A further structure sensitive technique such as EXAFS could also be usefully employed to elucidate short range order characteristics.

Alloys of silver and germanium have also been investigated by photoemission. The EDCS of the valence bands of the alloys have been shown to change little with composition and no evidence was found for a dip in the density of states at the eutectic composition as predicted by theory. The measured binding energy shift of the silver 4d band suggests a transfer of electronic charge from germanium to silver but the photoemission data overall contains no indication as to why silver-germanium possesses a deep eutectic.

The spectrometer as described in chapter three offers the possibilities of performing much more experimental work on liquids. It would be interesting to make photoemission measurements on other liquid simple alkali metals (eg:- sodium and potassium) to test their adherence or deviation from the free electron model.

Many other liquid semiconductor systems also offer themselves for experimental probing, at least over fractions of the concentration ranges. Cutler (1977) contains a list of such systems. It would be interesting to repeat the attempt to manufacture the stoichiometric compositions of lithium-lead and lithium-tin in the solid by co-evaporation; an attempt was made but failed (chapter five). The EDCS from the resultant films would then give a good indication of the EDCS expected from the liquid phase and hence provide information on the liquid stoichiometric electronic structure.

Other alloys possessing deep eutectics and hence enhanced glass forming capabilities would be instructive to probe, eg:- the systems gold-silicon and gold-germanium. Measurements made on such systems could be compared and contrasted to the data in this work on silver-germanium and would allow a fuller testing of the theory of Tauc and Nagel (1976 a and 1976 b).

The recent addition of an X-ray source to the spectrometer would aid a study of the proposed systems by allowing the probing of core levels inaccessible to helium II radiation, and by acting as a complement to the Auger system for the detection of impurities. The multi-scanning system as described (section 3.8), although operational, contains imperfections which limit its usefulness (as described) and

the spectrometer would benefit from having a computer based data taking facility which overcomes the faults of the present system. A flexible system would allow the multi-scanning of not only UPS spectra but also Auger and XPS spectra, making the detection of impurities easier and allowing the recording of valence band data excited by high energy photons.

A further benefit would be for an improved sample moving device between the two chambers allowing precise location of a sample underneath the analyser; the present system contains too much mechanical slack and the analyser's performance is known to be sample position dependent (truncation of low energy electrons is known to occur periodically). This effect could be fully investigated using a standard electron source, eg:- a tungsten wire carrying a DC current.

Finally, if the samples could be melted under the analyser using electron bombardment heating, then measurements of liquid transition metals are feasible (eg:- iron, cobalt, nickel). Such a procedure necessitates the organisation of heating and data taking in alternate cycles and the apparatus necessary for such a system has been suggested (Krizek - private communication).

REFERENCES

- 1) Agarwal, S.C. and Herman, H., J. Mater. Sci., 12, 2021, 1977.
- 2) Ament, M.A.E.A. and de Vroomen, A.R., J. Phys. F., 4, 1359, 1974.
- 3) Anderson, P. W., Phys. Rev., 109, 1492, 1958.
- 4) Ashcroft, N.W. and Lekner, J., Phys. Rev., 145, 83, 1966.
- 5) Ashton, A.M. and Green, G.W., J. Phys. F., 3, 179, 1973.
- 6) Auger, P., J. Phys. Radium, 6, 1925.
- 7) Avci, R. and Flynn, C.P., Phys. Rev. B., 19, 5967, 1979.
- 8) Ballentine, L.E., Can. J. Phys., 44, 2533, 1966.
- 9) Bancroft, G.M., Gudat, W. and Eastman, D.E., Phys. Rev. B., 17, 4499, 1978.
- 10) Bellissent-Funel, M.C., Desre', P.J., Bellissent, R. and Tourand, G., J. Phys. F., 7, 2485, 1977.
- 11) Bellissent-Funel, M.C., Roth, M. and Desre', P., J. Phys. F., 9, 987, 1979.
- 12) Berglund, C.N. and Spicer, W.E., Phys. Rev., 136, 1030, 1964.
- 13) Bernal, J.D., Liquids: Structure, Properties, Solid Interactions, Amsterdam, Elsevier, ed: Hughel, 1965.
- 14) Bhatia, A.B. and Krishnan, K.S., Proc. Roy. Soc. A, 194, 185, 1948.
- 15) Bhatia, A.B., Hargrove, W.H. and Thornton, D.E., Phys. Rev. B., 9, 435, 1974.
- 16) Binns, C., Ph.D. Thesis, University of Leicester, 1981.
- 17) Bradley, C.C., Faber, T.E., Wilson, E.G. and Ziman, J.M., Phil. Mag., 7, 865, 1962.
- 18) Briggs, D., Handbook of X-ray and Ultraviolet Photoelectron Spectroscopy, Heyden, 1978.
- 19) Brodsky, M.H. and Cardona, M., J. Non-cryst. Solids, 31, 81, 1978.
- 20) Burton, J.J. and Machlin, E.S., Phys. Rev. Lett., 37, 1433, 1976.
- 21) Callcott, T.A. and Arakawa, E.T., J. Opt. Soc. Am., 64, 839, 1974.
- 22) Canfield, L.R., Hass, G. and Hunter, W.R., J. de Physique, 25, 124, 1964.
- 23) Caroli, C., Lederer-Rozenblatt, D., Roulet, B. and Saint-James, D., Phys. Rev. B., 8, 4552, 1973.

- 24) Castanet, R., Claire, Y. and Laffitte, M., J. Chim. Phys., 66, 1276, 1969.
- 25) Chan, T. and Ballentine, L.E., Can. J. Phys., 50, 813, 1972.
- 26) Chang, C.C., Surf. Sci., 25, 53, 1971.
- 27) Chelikowsky, J.R. and Cohen, M.L., Phys. Rev. B., 14, 556, 1976.
- 28) Choo, F.C., Tong, B.Y. and Swenson, J.R., Phys. Letts., 50A, 255, 1974.
- 29) Chou, T.S., Perlman, M.L. and Watson, R.E., Phys. Rev. B., 14, 3248, 1976.
- 30) Christensen, N.E., Phys. Stat. Sol. (b), 54, 551, 1972.
- 31) Chung, M.S. and Everhart, T.E., Phys. Rev. B., 15, 4699, 1977.
- 32) Chung, M.F. and Jenkins, L.H., Surf. Sci., 22, 479, 1970.
- 33) Cohen, M.H. and Heine, V., Solid State Physics, eds: Ehrenreich, Seitz and Turnbull, 24, 37, Academic Press, 1970.
- 34) Cohen, M.H. and Sak, J., J. Non-cryst. Solids, 8-10, 696, 1972.
- 35) Connell, G.A.N. and Temkin, R.J., Tetrahedrally Bonded Amorphous Semiconductors, American Institute of Physics, New York, 1974.
- 36) Cutler, M., Phil. Mag., 24, 381, 1971
- 37) Cutler, M., Liquid Semiconductors, Academic Press, 1977.
- 38) Demidov, A.I., Morachevskii, A.G. and Gerasimenko, L.N., Sov. Phys. Electrochem., 9, 813, 1973.
- 39) Donald, I.W. and Davies, H.A., J. Non-cryst. Solids, 30, 77, 1978.
- 40) Eastman, D.E. and Grobman, W.D., Proceedings of the Eleventh International Conference on Semiconductors, Warsaw, 1972.
- 41) Eastman, D.E., Freeouf, J.L. and Erbudak, M., AIP Conference Proceedings, Yorktown Heights, 1974 a.
- 42) Eastman, D.E., Grobman, W.D., Freeouf, J.L. and Erbudak, M., Phys. Rev. B., 9, 3473, 1974 b.
- 43) Enderby, J.E., Physics of Simple Liquids, North-Holland Publ. Co., chap. 14, 1969.
- 44) Enderby, J.E. and Collings, E.W., J. Non-cryst. Solids, 4, 161, 1970.
- 45) Enderby, J.E., Paper presented at the Conference on Band-structure Spectroscopy of Metals and Alloys, Strathclyde, 1971.

- 46) Enderby, J.E., Liquid Metals, ed: Beer, chap. 14, Marcel Dekker, New York, 1972.
- 47) Enderby, J.E., The Metal-Nonmetal Transition in Disordered Systems, eds: Friedman and Tunstall, University of Edinburgh Press, p 425, 1978.
- 48) Endriz, J.G., Phys. Rev. B., 7, 3464, 1973.
- 49) Etherington, G., Wright, A.C., Wenzel, J.T., Dore, J.C., Clarke, J.H. and Sinclair, R.N., J. Non-Cryst. Solids, 48, 265, 1982.
- 50) Evans, R., J. Phys. C., Suppl. 2, S137, 1970.
- 51) Evans, R. and Telo Da Gama, M.M., Phil. Mag. B., 41, 351, 1980.
- 52) Faber, T.E., Introduction to the Theory of Liquid Metals, Cambridge Univ. Press, 1972.
- 53) Fong, C.Y., Walter, J.P. and Cohen, M.L., Phys. Rev. B., 11, 2759, 1975.
- 54) Franz, J.R., Brouers, F. and Holzhey, C., J. Phys. F., 10, 235, 1980.
- 55) Gibbs, J.W., Trans. Connecticut Acad. Sci. 3, 108, 1875/76; 343, 1977/78.
- 56) Giessen, B.C. and Whang, S., Proceedings of the Fourth International Conference on Liquid and Amorphous Metals, Grenoble, France, 1980.
- 57) Gilman, J.J., Proceedings of the Fourth International Conference on Liquid and Amorphous Metals, Grenoble, France, 1980.
- 58) Glazov, V.M., Chizhevskaya, S.N. and Glagoleva, N.N., Liquid Semiconductors, Plenum Press, New York, 1969.
- 59) Gobrecht, H., Gawlik, D. and Mahdjuri, F., Phys. Kondens. Mater., 13, 156, 1971.
- 60) Gordy, W. and Thomas, W.J.O., J. Chem. Phys., 24, 439, 1956.
- 61) Green, M.S., Handbuch der Physik, 10, 1, Berlin, Springer-Verlag, 1960.
- 62) Grube, G. and Klaiber, H., Z. Elektrochem., 40, 745, 1934.
- 63) Hackstein, K., Sotier, S. and Luscher, E., Proceedings of the Fourth International Conference on Liquid and Amorphous Metals, Grenoble, France, 1980.
- 64) Hagemann, H.J., Gudat, W. and Kunz, C., J. Opt. Soc. Am., 65, 742, 1975.

- 65) Halder, N.C., Phys. Rev. B., 21, 783, 1980.
- 66) Ham, F.S., Phys. Rev., 128, 82, 1962.
- 67) Hansen, M., Constitution of Binary Alloys, McGraw-Hill, 1958.
- 68) Harris, L.A., J. App. Phys., 39, 1419, 1968.
- 69) Heine, V., Phys. Rev., 153, 673, 1967.
- 70) Heine, V., Solid State Physics, eds: Ehrenreich, Seitz and Turnbull, 24, 1, New York, Academic Press, 1970.
- 71) Heitjans, P., Kiese, G., Ackermann, H., Bader, B., Buttler, W., Dörr, K., Fujara, F., Grupp, H., Körblein, A. and Stöckmann, H.J., Proceedings of the Fourth International Conference on Liquid and Amorphous Metals, Grenoble, France, 1980.
- 72) Hensel, F., Liquid Metals and Liquid Semiconductors, Angew. Chem. Int., ed: Engl, 19, 593, 1980.
- 73) Hoshino, K. and Young, W.H., J. Phys. F., 10, 1365, 1980 a.
- 74) Hoshino, K. and Young, W.H., J. Phys. F., 10, L193, 1980 b.
- 75) Hudgings, D.W. and Dragt, A.J., Am. J. Phys., 40, 1206, 1972.
- 76) Ichikawa, K., Phil. Mag., 27, 177, 1973.
- 77) Ioffe, A.F. and Regel, A.R., Progr. Semicond., 4, 238, 1960.
- 78) Itami, T. and Shimoji, M., Phil. Mag., 25, 229, 1972.
- 79) Jablonski, A., Adv. Colloid and Interface Sci., 8, 213, 1977.
- 80) Jacucci, G., Klein, M.L. and Taylor, R., Sol. Stat. Comm., 19, 657, 1976.
- 81) Joannopoulos, J.D. and Cohen, M.L., Phys. Rev., 7, 2644, 1973.
- 82) Kane, E.O., Phys. Rev., 159, 624, 1967.
- 83) Keller, J., Pisanty, A., Del Carmen De Teresa, M. and Erbudak, M., Phys. Letts., 71A, 90, 1979.
- 84) Kennedy, D.J. and Manson, S.T., Phys. Rev. A., 5, 227, 1972.
- 85) Kittel, C., Introduction to Solid State Physics, John Wiley and Sons, 5th edition, 1976.
- 86) Knight, W.D., Solid State Physics, eds: Seitz and Turnbull, 2, 93, New York, Academic Press, 1956.
- 87) Knight, W.D., Berger, A. and Heine, V., Ann. Phys., 8, 173, 1959.
- 88) Koopmans, T., Physica, 1, 104, 1934.

- 89) Korringa, J., *Physica*, 16, 601, 1950.
- 90) Kowalczyk, S.P., Ley, L., McFeely, F.R., Pollak, R.A. and Shirley, D.A., *Phys. Rev. B.*, 8, 3583, 1973.
- 91) Koyama, R.Y. and Spicer, W.E., *Phys. Rev. B.*, 4, 4318, 1971.
- 92) Krolikowski, W.F., Ph.D. Thesis, Stanford University, 1967.
- 93) Krolikowski, W.F. and Spicer, W.E., *Phys. Rev. B.*, 1, 478, 1970.
- 94) Krüger, K.D. and Schmutzler, R.W., *Ber. Bunsenges. Phys. Chem.*, 80, 816, 1976.
- 95) Kuroha, M. and Suzuki, K., *Phys. Letts.*, 47A, 329, 1974.
- 96) Lai, S.K. and Wang, S., *Phys. Letts.*, 85A, 239, 1981.
- 97) Lander, J.J., *Phys. Rev.*, 91, 1382, 1953.
- 98) LaVilla, R.E. and Mendlowitz, H., *J. App. Phys.*, 40, 3297, 1969.
- 99) Lee, P.A. and Beni, G., *Phys. Rev. B.*, 15, 2862, 1977.
- 100) Lemaignan, C. and Malmejac, Y., *J. Cryst. Growth*, 46, 771, 1979.
- 101) Lemaignan, C., Cheynet, M.C. and Eustathopoulos, N., *J. Cryst. Growth*, 50, 720, 1980.
- 102) Lemonnier, J.C., Priol, M. and Robin, S., *Phys. Rev. B.*, 8, 5452, 1973.
- 103) Ley, L., Kowalczyk, S., Pollak, R. and Shirley, D.A., *Phys. Rev. Letts.*, 29, 1088, 1972.
- 104) Ley, L., Pollak, R., Kowalczyk, S. and Shirley, D.A., *Phys. Letts.*, 41A, 429, 1972.
- 105) Ley, L., Cardona, M. and Pollak, R.A., *Topics in Applied Physics*, 27, Springer-Verlag, 1979.
- 106) *Liquid Metal Handbook*, ed: Jackson, Washington: Atomic Energy Commission and U.S. Navy, 1955.
- 107) Loucks, T.L., *Phys. Rev. Letts.*, 14, 1072, 1965.
- 108) MacRae, R.A., Arakawa, E.T. and Williams, M.W., *Phys. Rev.*, 162, 615, 1967.
- 109) Mahan, G.D., *Phys. Rev. B.*, 2, 4334, 1970.
- 110) Martin, W., Freyland, W., Lamparter, P. and Steeb, S., *Phys. and Chem. Liq.*, 10, 61, 1980.
- 111) Martin-Garin, L., Gomez, M., Bedon, P. and Desre, P., *J. Less-Common Metals*, 41, 65, 1975.

- 112) Mathewson, A.G. and Myers, H.P., Phil. Mag., 25, 853, 1972.
- 113) McFeely, F.R., Ley, L., Kowalczyk, S.P. and Shirley, D.A., Sol. Stat. Comm., 17, 1415, 1975.
- 114) McLean, D., Grain Boundaries in Metals, Oxford University Press, 118, 1957.
- 115) Moore, C.E., Atomic Energy Levels, NBS Circular No. 467, U.S.G.P.O., Washington D.C., 1949.
- 116) Mott, N.F. and Davis, E.A., Electronic Processes in Non-Crystalline Materials, Oxford, Clarendon, 1971.
- 117) Mott, N.F. and Davis, E.A., Electronic Processes in Non-Crystalline Materials, 2nd edition, Clarendon Press, 1979.
- 118) Nguyen, V.T. and Enderby, J.E., Phil. Mag., 35, 1013, 1977.
- 119) Nguyen Van, V., Fisson, S. and Theye, M.L., Thin Solid Films, 89, 315, 1982.
- 120) Norris, C., Proceedings of the Third International Conference on Liquid Metals, Conference Series No. 30, The Institute of Physics, Bristol and London, 1977.
- 121) Norris, C., Rodway, D.C. and Williams, G.P., Proceedings of the Second International Conference on Liquid Metals, Tokyo, 1972.
- 122) Norris, C., Rodway, D.C. and Williams, G.P., Proc. of Structures Metalliques Desordonnees, Strasbourg, 61, 1973.
- 123) Norris, C., Rodway, D.C. and Williams, G.P., J. Physique, C4, 61, 1974.
- 124) Norris, C. and Walden, L., Phys. Status Solidi (a), 2, 381, 1970.
- 125) Norris, C. and Williams, G.P., Phys. Status Solidi (b), 85, 325, 1978.
- 126) O'Keefe, P.M. and Goddard, W.A., Phys. Rev., 180, 747, 1969.
- 127) Orton, B.R., Proceedings of the Fourth International Conference on Liquid and Amorphous Metals, Grenoble, France, 1980.
- 128) Overhof, H., Knecht, J., Fischer, R. and Hensel, F., J. Phys. F., 8, 1607, 1978.
- 129) Paul, W., Connell, G.A.N. and Temkin, R.J., Adv. in Phys., 22, 531, 1973.
- 130) Pauling, L., The Nature of the Chemical Bond, 3rd edition, Cornell Univ. Press, Ithaca, New York, 1960.
- 131) Pendry, J.B., Surf. Sci., 57, 679, 1976.

- 132) Petersen, H., Phys. Rev. Letts., 35, 1363, 1975.
- 133) Petersen, H., Z. Phys., 31, 171, 1978.
- 134) Petersen, H. and Hagström, S.B.M., Phys. Rev. Letts., 41, 1314, 1978.
- 135) Petersen, H. and Hagström, S.B.M., Stanford Synchrotron Radiation Laboratory Activity Report, VII - 8, 1980.
- 136) Petersen, H. and Kunz, C., Vacuum Ultraviolet Radiation Physics, eds: Koch, Haensel and Kunz, Pergamon Vieweg, 587, 1974.
- 137) Petersen, H. and Kunz, C., J. Phys. F., 7, 2495, 1977.
- 138) Placzek, G., Phys. Rev., 86, 377, 1952.
- 139) Polk, D.E., J. Non-cryst. Solids, 5, 365, 1971.
- 140) Polk, D.E. and Boudreaux, D.S., Phys. Rev. Letts., 31, 92, 1973.
- 141) Pollak, R.A., Kowalczyk, S., Ley, L. and Shirley, D.A., Phys. Rev. Letts., 29, 274, 1972.
- 142) Quinn, J.J., Phys. Rev., 126, 1453, 1962.
- 143) Rasigni, M. and Rasigni, G., J. Opt. Soc. Am., 66, 826, 1976.
- 144) Robertson, J., Phil. Mag. B., 44, 239, 1981.
- 145) Robertson, J., The Electronic Structure and Metal-Nonmetal Transition in Liquid CsAu and Cs₃Sb, pre-print, 1983.
- 146) Rodway, D.C., Ph.D. Thesis, University of Leicester, 1978.
- 147) Roth, L.M., Proc. Liquid Met. Conf., Mexico, January 7-11, 1975.
- 148) Rudge, W.E., Phys. Rev., 181, 1024, 1969.
- 149) Ruppertsberg, H. and Egger, H., J. Chem. Phys., 63, 4095, 1975.
- 150) Ruppertsberg, H. and Speicher, W., Z. Naturf., 31a, 47, 1976.
- 151) Saboungi, M.L., Marr, J. and Blander, M., J. Chem. Phys., 68, 1375, 1978.
- 152) Samson, J., Techniques of Vacuum Ultraviolet Spectroscopy, John Wiley and Sons, 1967.
- 153) Schaich, W.L. and Ashcroft, N.W., Sol. Stat. Comm., 8, 1959, 1970.
- 154) Schirmacher, W., J. Non-cryst. Solids, 35, 1301, 1980.
- 155) Schmutzler, R.W., Hoshino, H., Fischer, R. and Hensel, F., Ber. Bunsenges., 80, 107, 1976.
- 156) Seah, M.P. and Dench, W.A., N.P.L. Report Chem. 82, April, 1978.

- 157) Sham, T.K., Perlman, M.L. and Watson, R.E., Phys. Rev. B., 19, 539, 1979.
- 158) Shaw, R.W. and Smith, N.V., Phys. Rev., 178, 985, 1969.
- 159) Shevchik, N.J., Phys. Rev. B., 16, 3428, 1977.
- 160) Shimoji, M., Liquid Metals, Academic Press, 1977.
- 161) Smith, N.V. and Spicer, W.E., Phys. Rev. Letts., 23, 769, 1969 a.
- 162) Smith, N.V. and Spicer, W.E., Phys. Rev., 188, 593, 1969 b.
- 163) So, C.B., Moore, R.A. and Wang, S., J. Phys. F., 8, 785, 1978.
- 164) Spicer, W.E. and Krolikowski, W.F., Phys. Rev. B., 1, 478, 1970.
- 165) Stocks, G.M., Williams, R.W. and Faulkner, J.S., J. Phys. F., 3 1688, 1973.
- 166) Sundström, L.J., Phil. Mag., 11, 657, 1965.
- 167) Suryanarayana, C., Supplement to Sci. Rep. RITU, A, March, 1980.
- 168) Tauc, J. and Nagel, S.R., Comments Sol. Stat. Phys., 7, 69, 1976 a.
- 169) Tauc, J. and Nagel, S.R., Proceedings of the Third International Conference on Liquid Metals, Conference Series No. 30, The Institute of Physics, Bristol and London, 1976 b.
- 170) Thorpe, M.F. and Weaire, D., Phys. Rev. Letts., 27, 1581, 1971.
- 171) Tjèche, Y. and Zareba, A., Phys. Kondens. Mater., 1, 402, 1963.
- 172) Turnbull, D., Journal de Physique, Structures Métalliques Désordonnées, Strasbourg, 1973.
- 173) Turner, R., J. Phys. F., 3, 457, 1973.
- 174) Van Attekum, P.M.Th.M. and Trooster, J.M., J. Phys. F., 9, 2287, 1979.
- 175) Van der Marel, C., Geertsma, W. and Van der Lugt, W., J. Phys. F., 10, 2305, 1980.
- 176) Velicky, B., Kirkpatrick, S. and Ehrenreich, H., Phys. Rev., 175, 747, 1968.
- 177) Vesely, C.J. and Kingston, D.L., Phys. Stat. Sol. (b), 61, 337, 1974.
- 178) Waghorne, R.M., Rivlin, V.G. and Williams, G.I., J. Phys. F., 6, 147, 1976.
- 179) Wagner, C., Thermodynamik Metallischer Mehrstoffsysteme in Handbuch der Metallphysik, ed: G. Masing, Akad Verlagsgesellschaft, Leipzig, 1940, vol. 1, sec. 2, p1.

- 180) Wang, S. and Lai, S.K., Proceedings of the Fourth International Conference on Liquid and Amorphous Metals, Grenoble, France, 1980.
- 181) Warren, W.W., Phys. Rev. B., 3, 3708, 1971.
- 182) Waseda, Y., Proceedings of the Third International Conference on Liquid Metals, Conference Series No. 30, The Institute of Physics, Bristol and London, 1976.
- 183) Waseda, Y. and Suzuki, K., Z. Physik., B20, 339, 1975.
- 184) Watson, R.E. and Perlman, M.L., Structure and Bonding, 24, 83, Springer, Berlin, 1975.
- 185) Weast, R.C., CRC Handbook of Chemistry and Physics, CRC Press, 60th Edition, 1979.
- 186) Wertheim, G.K., Bates, C.W. and Buchanan, D.N.E., Sol. Stat. Comm., 30, 473, 1979 a.
- 187) Wertheim, G.K., Cohen, R.L., Crecelius, G., West, K.W. and Wernick, J. H., Phys. Rev. B., 20, 860, 1979 b.
- 188) Williams, F.L. and Boudart, M., J. Catal., 30, 438, 1973.
- 189) Williams, G.P. and Norris, C., Proceedings of the International Conference on the Electronic and Magnetic Properties of Liquid Metals, Mexico, ed: J. Keller, 1975.
- 190) Williams, G.P. and Norris, C., Phil. Mag., 34, 851, 1976.
- 191) Wooten, F., Optical Properties of Solids, Academic Press, 1972.
- 192) Wotherspoon, J., Ph.D. Thesis, University of Leicester, 1978.
- 193) Wotherspoon, J.T.M., Rodway, D.C. and Norris, C., Phil. Mag. B., 40, 51, 1979.
- 194) Wyckoff, R.W.G., Crystal Structures, Interscience Publishers, 1963.
- 195) Zacharias, P. and Kliever, K.L., Sol. Stat. Comm., 18, 23, 1976.
- 196) Zalkin, A. and Ramsey, W.J., J. Phys. Chem., 62, 689, 1958.
- 197) Ziman, J.M., Phil. Mag., 6, 1013, 1961.

APPENDIX A

The parameters inputted in the calculation are:-

- 1) work function X 10 (eV)
- 2) number of data points -1 (bandwidth)
- 3) absorption coefficient (cm^{-1})
- 4) photon energy X 10 (eV)
- 5) number of valence electrons
- 6) scattering length constant (\AA)
- 7) plasmon energy X 10 (eV)

Symbols in the program are as given by Wotherspoon (1978). The program is listed.

```

      PROGRAM AUGER(JTMDAT,INPUT,OUTPUT,TAPE1=INPUT,TAPE2=OUTPUT
C   JTMAUG   EDC CALCULATION WITH FULL BACKGROUND
      1      ,TAPE3=JTMDAT,CANOUT,TAPE4=CANOUT)
      REAL N05,NP
      DIMENSION V(220), C(220),PS(220),SEE(220),HL(220)
      1      ,D(220),X(220),T(220),TF2(220),P01(220),C2(220)
      2      ,DHOLE(220),DAUG(220),PL(220),TL(220),DPLAS(220),N05(220)
      3      ,TER(220),P02(220)

C
      DATA C2/220*0.0/
      DATA P01/220*0.0/
      DATA TER/220*0.0/
      DATA DPLAS/220*0.0/
      DATA D/220*0.0/
      DATA V/220*0.0/
      DATA N05/220*0.0/
      CCCCCCCCC INPUT DATA ON THE ELECTRONIC STRUCTURE CCCCCCCCCCCCCC
C
      N8=86
      WRITE(2,232)
      READ(1,*)N1,N3,A,IH
      WRITE(2,*)N1,N3,A,IH
      WRITE(2,709)
      READ(1,*) NVAL
      WRITE(2,*)NVAL
      WRITE(4,723) N3,A
      N4=N3
      IF(IH.GT.N3) N4=IH
      N4=N4+5
      IF(N4.LT.N8) N4=N8

```



```

CCCCCCCCC NORMALIZE THE DENSITY OF STATES CCCCCCCCCCCCCCCCCC
C
      SUM=0.
      DO 10 J=1,N3
        READ(3,600) V(J)
      10 SUM=SUM+V(J)*0.1
      DO 11 J=1,N3
        11 V(J)=V(J)/SUM*NUAL
C
CCCCCCCCC FIT FREE ELECTRON DENSITY OF STATES ABOVE FERMJ ENERGY
C
      N5=N3+1
      DO 30 J=1,N4
        PAN3=FLOAT(J+N3)/N3
      30 C(J)=V(1)*SQRT(PAN3)
C
CCCCCCCCC CALCULATE THE INELASTIC E-E SCATTERING LENGTH CCCCCCCC
C
      MM=N4+1
      DO 666 J=3,MM
        U2=0
        K=J-2
        DO 777 I=1,K
          USUM=0
          MN=(J-I)/2
          DO 555 L2=1,MN
            555 USUM=.01*(C(L2)*C(J-I-L2)*V(I))+USUM
          777 U2=U2+USUM
          PFN3=J+N3
          X(J)=(SQRT(PFN3)/U2)
        666 CONTINUE

```

```

CCCCCCCCC NORMALIZE THE E-E SCATTERING LENGTH AT 8.6 EV, CCCCCC
C
      WRITE(2,401)
      READ(1,*) N9
      WRITE(2,*) N9
      P5=X(N8)
      DO 60 J=3,MM
      FNORM=N9/(P5*100000000)
      60 X(J)=X(J)*FNORM
C
CCCCCCCCC CALCULATE THE PLASMON SCATTERING LENGTH
C
      WRITE(2,643)
      READ(1,*) NP
      WRITE(2,*) NP
      WP=NP*0.1
      NA=NP+1.
      EF=(N3-1)*0.1
      IF(NA.GT.N4) GO TO 645
      DO 641 I=NA,N4
      E=(N3+I-1)*0.1
      DENOM=ALOG((SQRT(WP+EF)-SQRT(EF))/(SQRT(E)-SQRT(E-WP)))
      PL(I)=1.0582/WP*E/DENOM*1.E-8
      TL(I)=1./(1./PL(I)+1./X(I))
      641 CONTINUE
      645 NLIM=NP
      IF(NP.GT.N4) NLIM=N4
      DO 642 I=3,NLIM
      TL(I)=X(I)
      642 CONTINUE

```

```

CCCCCCCCC CALCULATE THE SEMICLASSICAL THRESHOLD FUNCTION CCCCCC
C
      DO 40 J=N1,N4
      TF2(J)=FLOAT(N1+N3)/FLOAT(J+N3)
      40 T(J)=(1-SQRT(TF2(J)))/2
C
CCCCCCCCC CALCULATE THE NORMALIZED ENERGY DISTRIBUTION OF
      EXCITED ELECTRONS CCCCCCCCCCCCCC
C
      SUM=0.
      DO 800 J=1,IH
      SUM=SUM+C(J)*V(IH-J+1)*0.1
      800 CONTINUE
      ANS=SUM
      DO 900 J=1,IH
      P01(J)=C(J)*V(IH-J+1)/SUM
      900 CONTINUE
C
CCCCCCCCC CALCULATE THE EFFECTIVE THRESHOLD FUNCTION CCCCCCCCCC
C
      IY=N1+1
      DO 700 J=IY,N4
      AL=A*TL(J)
      PX=(1.+AL)/(1.+AL-2.*AL*T(J))
      TF2(J)=T(J)*(1.-ALOG(PX)/(2.*AL*T(J)))
      700 CONTINUE

```

CCCCCCCCC CALCULATE THE SECONDARY ELECTRON DISTRIBUTION CCCCCCCCCC
C

```

      IHH=IH-1
      DO 151 IQ=N1,IH
      SUM1=0.
      NIQ=IQ-1
      DO 152 IA=1,NIQ
      NN=IQ-IA
      SUM2=0.
      DO 153 N=1,NN
      SUM2=SUM2+V(NN+1-N)*C(N)*0.1
153 CONTINUE
      PS(IA)=SUM2*C(IA)
      SUM1=SUM1+PS(IA)*0.1
152 CONTINUE
      DO 154 IA=1,NIQ
      SEE(IA)=2.*PS(IA)/SUM1
154 CONTINUE
      DO 155 IA=IQ,IHH
      SEE(IA)=0.
155 CONTINUE
      IQQ=IQ+1
      DO 156 J=3,IQ
      AL=A*TL(IQ)
      RL=X(J)/TL(IQ)
      R2=RL*(ALOG(1.+1./RL))
      R1=ALOG(1.+AL)/AL
      C2(J)=(R1+R2)/2.
156 CONTINUE
      DO 157 J=IQQ,IHH
      C2(J)=0.
157 CONTINUE
      XX=C(IQ)*V(IH-IQ+1)/SUM
      DO 158 I=N1,IHH
      D(I)=D(I)+SEE(I)*XX*C2(I)*0.1
158 CONTINUE
151 CONTINUE

```

```

CCCCCCCCC CALCULATE THE SCATTERING LENGTH FOR HOLES CCCCCCCCCC
C
      DO 838 IHOLE=2,N3
      BSUM=0.
      IMOD1=IHOLE-1
      DO 837 IFIN=1,IMOD1
      IMOD2=(IHOLE-IFIN+1)/2
      ASUM=0.
      DO 836 IINT=1,IMOD2
      ASUM=ASUM+0.1*(IINT)*V(IHOLE-IFIN+1-IINT)
836 CONTINUE
      BSUM=BSUM+0.1*(IFIN)*ASUM
837 CONTINUE
      HL(IHOLE)=SQRT(FLOAT(N3+1-IHOLE))*FNORM/BSUM
      DHOLE(IHOLE)=BSUM
838 CONTINUE
C
CCCCCCCCC CALCULATE THE DISTRIBUTION OF AUGER ELECTRONS CCCCCCCC
C
      IMOD7=IH
      IF(IH.GT.N3) IMOD3=N3
      DO 935 IFIN=1Y,IHH
      IMOD=IFIN+1
      XELEC=VL(IFIN)
      SUM=0.
      IF(IMOD.GT.IMOD3) GO TO 1001
      DO 937 IHOLE=IMOD,IMOD3
      SHE=0.0
      IMOD2=(IHOLE-IFIN+1)/2
      XHOLE=HL(IHOLE)
      DO 936 IINT=1,IMOD2
      SHE=SHE+0.1*(IINT)*V(IHOLE-IFIN+1-IINT)
936 CONTINUE
      SHE=SHE*(IFIN)/DHOLE(IHOLE)
      C2H=0.5*(ALOG(1.+A*XHOLE)/A/XHOLE+ALOG(1.+XHOLE/XELEC)
      1 *XELEC/XHOLE)

```

```

SUM=SUM+0.1*SHF*C2H*P01(IH-IHOLE+1)
937 CONTINUE
1001 CONTINUE
SUM=SUM*TF2(IFIN)
DAUG(IFIN)=SUM
935 CONTINUE
DAUG(IH)=0.
C
CCCCCCCCC CALCULATE PLASMON LOSS TERM CCCCCCCCCC
C
DO 671 I=IY,IH
SUM=0.0
IF(NA.GT,IH) GO TO 673
DO 672 INP=NA,IH
EXPON=(INP-I-NP)**2*0.01
IF(EXPON.GT,50.) EXPON=50.
GD=EXP(-EXPON)/1.77245
ALP=A*PL(INP)
RAT=PL(INP)/TL(I)
C2P=0.5*(ALOG(1.+ALP)/ALP+ALOG(1.+RAT)/RAT)
SUM=SUM+0.1*C2P*GD*P01(INP)
672 CONTINUE
673 CONTINUE
DPLAS(I)=SUM*TF2(I)
671 CONTINUE
C
CCCCCCCCC CALCULATE THE TERTIARY ELECTRON DISTRIBUTION CCCCCCCCCC
C
DO 814 I=IY,IH
P02(I)=D(I)+(DPLAS(I)+DAUG(I))/TF2(I)
814 CONTINUE
IHH=IH-1
DO 475 IQ=IY,IH
SUM1=0.
NIQ=IQ-1
DO 200 IA=1,NIQ

```

```

NN=IQ-IA
SUM2=0.
DO 100 N=1,NN
SUM2=SUM2+V(NN+1-N)*C(N)*0.1
100 CONTINUE
PS(IA)=SUM2*C(IA)
SUM1=SUM1+PS(IA)*0.1
200 CONTINUE
DO 300 IA=1,NIQ
SEE(IA)=2.*PS(IA)/SUM1
300 CONTINUE
DO 303 IA=IQ,IHH
SEE(IA)=0.
303 CONTINUE
IQQ=IQ+1
DO 950 J=3,IQ
AL=A*TL(IQ)
RL=X(J)/TL(IQ)
B2=RL*(ALOG(1.+1./RL))
B1=ALOG(1.+AL)/AL
C2(J)=(B1+B2)/2.
950 CONTINUE
DO 302 J=IQQ,IHH
C2(J)=0.
302 CONTINUE
DO 480 I=1Y,IHH
TER(I)=TER(I)+SEE(I)*P02(IQ)*C2(I)*0.1
480 CONTINUE
475 CONTINUE
C
C
CCCCCCCCC FLASMON DECAY PROCESS CCCCCCCCCCCCCCCCCCCCCCCCCC
C
C
SUM2=0.0
DO 1004 I=1Y,IH
1004 SUM2=SUM2+DPLAS(I)*0.1

```

```

IYY=IH-NP
DO 1002 IT=IYY,IH
  NGU=20+IT
  IF(NGU.GT.41) NGU=41
  NGL=1
  IF((IH-IT).LT.20) NGL=21-(IH-IT)
  SUM=0.0
  DO 1003 I=NGL,NGU
    EXPON=(I-21)**2*0.01
    GD=EXP(-EXPON)/1.77245
    SUM=SUM+V(IH-20-IT+I)*GD*0.1
  1003 CONTINUE
  N05(IT-IYY+1)=C(IT)*SUM*SUM2/ANS
  1002 CONTINUE
C
C
C
C
CCCCCCCCC CALCULATE THE ELECTRON DISTRIBUTIONS AND WRITE THEM OUT
C
  WRITE(2,2000)
  READ(1,*) IFLAG
  IF(IFLAG.EQ.1) WRITE(2,867)
  WRITE(4,867)
  DO 567 N=IY,IH
    PS(N)=TF2(N)*P01(N)
    C(N)=TF2(N)*D(N)
    TER(N)=TER(N)*TF2(N)
    C2(N)=PS(N)+C(N)+DAUG(N)+DPLAS(N)+TER(N)+N05(N)
    P02(N)=C2(N)-PS(N)
    IF(IFLAG.EQ.1) WRITE(2,815)N,PS(N),C(N),DAUG(N),DPLAS(N),TER(N),N05(N),C2(N)
  1
  WRITE(4,815) N,PS(N),C(N),DAUG(N),DPLAS(N),TER(N),N05(N),C2(N)
  567 CONTINUE
C
CCCCCCCCC WRITE OUT THE SCATTERING LENGTHS CCCCCC

```



```

WRITE(2,2001)
READ(1,*) JFLAG
IF(JFLAG.EQ.1) WRITE(2,384)
WRITE(4,384)
DO 382 I=3,N4
  J=I-1
  K=-(I-2)
  IF(J.GT.N3) HL(J)=0.
  IF(JFLAG.EQ.1) WRITE(2,383) I,X(I),PL(I),TL(I),TF2(I),K,HL(J)
  WRITE(4,383) I,X(I),PL(I),TL(I),TF2(I),K,HL(J)
382 CONTINUE
C
C
CCCCCCCCC CALCULATE THE YIELDS AND WRITE THEM OUT CCCCCCCCCCCCCC
C
SUM7=SUM8=SUM10=SUM11=SUM12=SUM13=0.0
DO 568 N=1,Y,IH
  SUM7=SUM7+PS(N)*0.1
  SUM8=SUM8+C(N)*0.1
  SUM10=SUM10+0.1*DAUG(N)
  SUM11=SUM11+0.1*DFLAS(N)
  SUM12=SUM12+0.1*TER(N)
  SUM13=SUM13+0.1*NO5(N)
568 CONTINUE
SUM9=SUM7+SUM8+SUM10+SUM11+SUM12+SUM13
WRITE(4,868) IH,SUM7,SUM8,SUM10,SUM11,SUM12,SUM13,SUM9
WRITE(2,868) IH,SUM7,SUM8,SUM10,SUM11,SUM12,SUM13,SUM9
C
CCCCCCCCC PLOTTING ROUTINES CCCCCCCCCCCCCCCCCCCCCCCCCCCCCC
C
WRITE(2,301)
READ(1,*) NNN
IF(NNN.NE.1) STOP
XPHOT=IH*0.1
XMAX=-N3*0.1
DO 901 I=1,N4

```

```

T(I)=- (I-1)*0.1
X(I)= -XFHOT-T(I)
901 CONTINUE
CALL PAPER(1)
CALL PSPACE(0.1,0.95,0.1,0.8)
CALL MAP(XMAX,0.1,1.,1.)
CALL CURVED(T,0,1,N3)
CALL SCALES
CALL PLACE(10,4)
CALL TYPECS(41HOPTICAL DENSITY OF STATES IN ELECTRONS/EV ,41)
CALL FRAME
CALL PSPACE(0.1,0.95,0.1,0.8)
CALL CTRMAG(5)
CALL MAP(1.,1.,1.,1.)
C2(N1)=0.0
CALL FTPLLOT(X,C2,N1,IH,30)
CALL FTPLLOT(X,DPLAS,IY,IH,23)
CALL FTPLLOT(X,DAUG,IY,IH,11)
CALL FTPLLOT(X,TER,IY,IH,03)
CALL FTPLLOT(X,FS,IY,IH,26)
CALL FTPLLOT(X,N05,IY,IH,14)
CALL REDPEN
CALL FTPLLOT(X,F02,IY,IH,12)
CALL BLKPEN
CALL FTPLLOT(X,C,IY,IH,29)
CALL FTPLLOT(X,C2,IY,IH,30)
CALL CTRMAG(20)
CALL SCALES
CALL PLACE(10,4)
CALL TYPECS(36HEDCS IN ELECTRONS/ABSORBED PHOTON/EV ,36)
CALL GREND

```

```

CCCCCCCCC FORMAT STATEMENTS ONLY BEYOND HERE CCCCCCCCCCCCCCCCCC
C
232 FORMAT(1X,/,40H INPUT THE WORKFUNCTION, BANDWIDTH: /
1 25H ABSORPTION COEFFICIENT /
2 40H AND PHOTON ENERGY /)
868 FORMAT(1X//21H FOR PHOTON ENERGY = , I6/
1 21H PRIMARY YIELD = , E12.4/
2 21H SECONDARY YIELD = , E12.4/
3 21H AUGER YIELD = , E12.4/
4 21H PLASMON LOSS YIELD = , E12.4/
5 21H TERTIARY YIELD = , E12.4/
5 21H PLASMON DECAY YIELD = , E12.4/
6 21H TOTAL YIELD = , E12.4)
815 FORMAT(I5,7E12.4)
500 FORMAT(I5,5E12.4)
600 FORMAT(F10.5)
867 FORMAT(1X//6H EV*10,2X,9H PRIMRIES,3X,9H SECNDRES,3X,
1 9H AUGERS ,3X,9HPLAS LOSS,3X,9H TERTIARY,3X,9HPLAS DECY,
2 3X,9HTOTAL EDC/)
401 FORMAT(1X//40H INPUT THE SCATTERING LENGTH AT 8.6 EV. /)
301 FORMAT(1X//29H ENTER 1 FOR GRAPHICAL OUTPUT /)
723 FORMAT(1H1,50H CALCULATED ELECTRON DISTRIBUTIONS FOR BAND OF WIDT
1 ,1HH,15,7H*0.1 EV/30H AND ABSORPTION COEFFICIENT OF ,
2 E11.4,4H/CM. //)
709 FORMAT(1X//47H INPUT THE NUMBER OF VALENCE ELECTRONS PER ATOM /)
2000 FORMAT(1X//44H INPUT 1 FOR TABLE OF ELECTRON DISTRIBUTIONS /
1 44H 0 FOR YIELDS ONLY /)
643 FORMAT(1X//26H INPUT THE PLASMON ENERGY /)
384 FORMAT(1X//6H EV*10,2X,9H ELEC-HOLE,3X,9H ELEC-PLAS:
1 3X,9H TOTAL ,3X,9H THRESH FN,5X,6H EV*10:
1 2X,9H HOLE-HOLE/)
383 FORMAT(I5,4E12.4,19,E12.4)
2001 FORMAT(1X//40H INPUT 1 FOR TABLE OF SCATTERING LENGTHS
1 / 40H 0 FOR YIELDS ONLY /)
STOP
END

```

APPENDIX B

Program for Microprocessor

The memory of the microprocessor was organised into 2 blocks:-

- (i) 0000 - 0FFF : for collection of data.
- (ii) 2000 - 2FFF : for program storage.

The start of the data collection is specified at location 0010 by the program. The end of data storage, which determines the energy scan width in eV, is also set by the program to be 0356 for a 20 eV scan. The program locations which determine the scan width are 2048 (upper byte) and 2049 (lower byte). All numbers are in hexadecimal. The program counter must be set to 20 (upper byte) and 00 (lower byte) at locations A048 and A049 before running the program - this tells the computer which location to begin at. The program is initiated by pressing G on the keyboard and stopped by pressing reset on the microprocessor. Each energy channel occupies 2 memory locations, eg: the number of pulses in the first channel is stored at locations 0010 (upper byte) and 0011 (lower byte). For a 20 eV scan, the number of memory locations used = $0356 - 0010 = 346_{\text{HEX}} = 838_{\text{DEC}}$. So the number of energy channels = $838/2 = 419$. Hence the energy resolution is $20/419 = 0.048$ eV/channel. This resolution is independent of the width of the scan.

THE PROGRAMVariables and Definitions

MEMS	=	Starting memory address of scan.
MEMF	=	Finishing memory address of scan.
MEM	=	Current memory address during scan.
PIA	=	Peripheral Interface Adaptor.
I/R	=	Index Register.
x	=	Contents of index register.
Acc A	=	Accumulator A.
Acc B	=	Accumulator B.

MEMORY
LOCATION

2000	4F		Clears Acc A.
2001	CE	0FFF	Loads I/R with 0FFF.
2004	6F	00	Clears memory location stored in I/R.
2006	09		Decrements I/R (to 0FFE).
2007	2E	FB	Branch to 2004 (FB \equiv 4 steps back).

2000 to 2007 clears the memory block
0FFF to 0000 for data storage.

2009	CE	20A0	Loads I/R with 20A0 (the interrupt vector).
200C	FF	A000	Stores I/R contents at locations A000 and A001.

The interrupt vector defines the location
which divides the program between the
display section and the data collection
section.

200F	7F	800D	PIA1AC	Clear instruction.
2012	7F	800C	PIA1A0	Clear instruction.
2015	73	800C	PIA1A0	Set to 11.
2018	86	34	34	Load Acc A with 34.
201A	B7	800D	PIA1AC	Transfer 34 to 800D.
201D	7F	8015	PIA2AC	Clear instruction.
2020	7F	8014	PIA2A0	Clear instruction.
2023	73	8014	PIA2A0	Set to 11.
2026	B7	8015	PIA2AC	Transfer 34 to 8015.
2029	7F	8017	PIA2BC	Clear instruction.
202C	7F	8016	PIA2B0	Clear instruction.
202F	73	8016	PIA2B0	Set to 11.
2032	B7	8017	PIA2BC	Transfer 34 to 8017.
2035	7F	800F	PIA1BC	Clear instruction.
2038	7F	800E	PIA1B1	Clear instruction.
203B	86	37	37	Load Acc A with 37.
203D	B7	800F	PIA1BC	Transfer 37 to 800F.

This part of the program from 200F to 203F sets the peripheral interface adaptors to act as input or output.

2040	CE	0010	Loads I/R with 0010 (the first data storage location)	
2043	DF	00	Stores number in I/R at 0000 and 0001.	
2045	DF	02	Stores 0010 at locations 0002 and 0003.	
2047	CE	0356	Loads 0356 in I/R; (0356 defines the scan width).	
204A	DF	04	Stores 0356 at locations 0004 and 0005.	
204C	0E		Enable interrupts now.	
204D	DE	02	Loads I/R with number at locations 0002 and 0003.	
204F	7F	8014	Clear instruction	Clears PIA's.
2052	7F	8016	Clear instruction	
2055	A6	01	Loads Acc A with number at address given by (x + 1) ie: lower byte of data in a channel.	
2057	B7	0FFF	Transfers lower byte of data to 0FFF.	
205A	E6	00	Loads Acc B with number at address given by x ie: higher byte of data in a channel.	
205C	F7	0FFE	Transfers higher byte of data to 0FFE.	

205F	27	1A	
2061	0C		This part of the program from 2040 to 209F
2062	76	OFFE	drives the oscilloscope display. The index
2065	76	OFFF	register carries (as x) the number of the
2068	7C	OFFC	memory location the program is at which starts
206B	B6	OFFC	as 0010. It is incremented by 2 in each loop
206E	B1	OFFD	and is compared to MEMF where MEMF is defined
2071	2F	03	to be the last memory location. All values
2073	7C	OFFD	of data for the y-axis are repeatedly divided by 2
2076	B6	OFFE	until they are all < 256 before being outputted.
2079	26	E6	This is necessary because the output PIA is an 8-bit
207B	B6	OFFC	and cannot handle numbers > 256. The division is
207E	B1	OFFD	achieved by transferring data to locations
2081	2D	DE	OFFC, OFFD, OFFE and OFFF. The main memory is
2083	7F	OFFC	unaffected by this operation.
2086	B6	OFFF	
2089	B7	800C	Transfers numbers in Acc A to PIA1A0 ie: y-axis output.
208C	DF	07	Stores I/R contents at locations 0007 and 0008.
208E	D6	07	Loads Acc B with number at location 0007.
2090	96	08	Loads Acc A with number at location 0008.
2092	B7	8014	This number is outputted for x-axis display,
2095	F7	8016	by PIA2A0 and PIA2B0.
2098	08		Increments contents of I/R by 2
2099	08		
209A	9C	04	Compares I/R contents to MEMF:- Tests for end of scan.
209C	26	B7	Branching instructions; branch to 2055
209E	20	AD	then always to 204D.
20A0	C6	34	Loads Acc B with 34
20A2	F7	800D	Transfers contents of Acc B (34) to PIA1AC -
			the change later to 3C resets the ramp.
20A5	5F		Clears Acc B
20A6	B6	800E	Loads Acc A with last data inputted to PIA1B1
20A9	DE	00	Loads I/R with MEM (stored at locations 0000 and
			0001) ie: 0010.
20AB	AB	01	Adds data in Acc A to data in location given by
			(x + 1), ie: lower byte of data.

20AD	E9	00	Adds "carry" from previous addition to higher byte.
20AF	25	25	Tests for overflow of data collection, branches if carry set on higher byte to 20D6.
20B1	E7	00	Stores higher byte in MEM.
20B3	A7	01	Stores lower byte in MEM + 1.
20B5	DE	00	Loads I/R with MEM.
20B7	9C	04	Compares I/R contents (ie MEM) to MEMF.
20B9	26	0C	Branch instruction; if not equal go to 20C7.
20BB	7C	0006	Increments scan counter by 1.
20BE	C6	3C	Loads Acc B with 3C then outputs it to PIA1AC;
20c0	F7	800D	this transition causes the ramp to reset.
20C3	DE	02	Loads I/R with MEMS.
20C5	20	02	Branch instruction to 20C9.
20C7	08		Increments contents of I/R by 2.
20C8	08		
20C9	DF	00	Set MEM = MEMS.
20CB	C6	3F	Loads Acc B with 3F.
20CD	F7	800F	Outputs number 3F to PIA1BC - resets the input counter.
20D0	C6	37	Loads Acc B with 37.
20D2	F7	800F	Outputs 37 to PIA1BC - resets PIA
20D5	3B		Return from intercept - returns machine to oscilloscope display section of the program.

This part of the program from 20AD to 20D5 collects the new values of the data, adds it to the old data in the correct channel, and when a scan is completed (by testing if MEM = MEMF) resets the ramp and begins a new scan.

20D6	0F		Interrupts rendered inoperative - machine ignores all external signals.
20D7	86	FF	Loads Acc A with FF.
20D9	97	00	Prevents data resetting to 0 - on overflow any data remains as FFFF and is not reset.
20DB	97	01	
20DD	86	07	Small subroutine - rings data terminal bell indicating data overflow.
20DF	BD	EIDI	
20E2	20	F9	Branch always to 20DD.

This last section of the program from 20D6 to 20E3 prevents data resetting to zero in the event of data overflow occurring. The data is set to FFFF and the data terminal bell activated.

Hexadecimal to Decimal Number Conversion Routine

On completion of a multi-scan spectrum, the data was outputted to magnetic tape using a further routine stored in the microprocessor which converted the data from hexadecimal numbers to decimal. The program for the conversion routine was stored on magnetic tape and was read in to the microprocessor along with the program for multiple scanning.

To run the conversion routine, the program counter had to be reset to 253A at locations A048 (upper byte) and A049 (lower byte). It was also necessary to define the start location and finish location of the data storage at locations 2500 to 2503 inclusive. An example for a 20 eV scan is shown below:-

Location	Input	
2500	00	Higher byte of start address.
2501	10	Lower byte of start address.
2502	03	Higher byte of finish address.
2503	56	Lower byte of finish address.

Initiation of the conversion routine was achieved by pressing G on the terminal keyboard.

APPENDIX C

The Electropolishing of Molybdenum

The electropolishing solution was made up from 204 cm³ of methanol and 85 cm³ of concentrated sulphuric acid. The methanol was put into the electropolishing vessel which was then immersed in an ice bath for 15 minutes. The acid was added very slowly and very carefully to the methanol. The reaction is exothermic and time was allowed for the solution to settle and cool before adding more acid. This operation was performed while wearing gloves in a fume cupboard with most of the protective glass screen pulled down.

The item to be polished was made the anode and was suspended in the electropolishing solution with a copper wire. The cathode was a copper plate wrapped around the inside of the electropolishing bath. A "Coutant" power supply was used to drive the electropolishing process. In practice a current of 3 amps for a time of 3 minutes sufficed to polish all pieces of molybdenum to a bright finish. The corresponding voltage varied from 3 to 10 volts depending on the size of the electropolished article. After polishing the item was washed in hot running tap water for several minutes and then ultrasonically washed for 20 minutes total time in acetone then methanol (equal periods) before being finally dried with a warm air blower. The stage of ultrasonic washing was found necessary to remove all traces of the electropolishing solution.

PHOTOELECTRON SPECTROSCOPY OF SOME
METALS AND ALLOYS IN THE LIQUID STATE

MARTYN K. GARDINER

ABSTRACT

Ultraviolet photoelectron spectroscopy measurements are presented from a variety of metals and alloys in the liquid state. For the metals, the optical density of states function is extracted from the photoemission data, by using an extended version of the three step model of Berglund and Spicer and compared to theoretical liquid density of states calculations based on a weak scattering approach which show only small deviations from the free electron parabola. The experimentally derived results for liquid lead and liquid tin reveal deviations from the simple picture with some of the solid state density of states features persisting into the liquid phase. By contrast, liquid lithium is shown to adhere more closely to the free electron model, showing a weaker deviation from the parabolic form for its experimentally derived density of states, while the same function for liquid silver is shown to be a smeared version of the solid state curve which, as explained, is not unexpected because of structural considerations. Photoemission data from liquid germanium is presented and discussed in comparison with published data for crystalline and amorphous germanium in terms of local atomic ordering.

Data is presented from the liquid semiconducting lithium-lead alloy system and the similar lithium-tin alloy system which is shown incompatible with a simple ionic bonding model, and a stoichiometric structure is proposed where the unlike atom bonding is taken to be more covalent in character.

Photoemission spectra are also presented from the silver-germanium alloy system which has a deep eutectic composition indicating enhanced glass forming qualities. Some change with composition can be seen in the valence band region but this cannot account for the above behaviour.